The role of glutaredoxin S15 in the transfer of Fe–S clusters and their consumption by lipoyl synthase in Arabidopsis mitochondria

Dissertation

zur

Erlangung des Doktorgrades (Dr. rer. nat.)

der

Mathematisch-Naturwissenschaftlichen Fakultät

der

Rheinischen Friedrich-Wilhelms-Universität Bonn

vorgelegt von

Luca Pedroletti

aus Camposampiero, Italien

Bonn, September 2023

Angefertigt mit Genehmigung der Mathematisch-Naturwissenschaftlichen Fakultät der
Rheinischen Friedrich-Wilhelms-Universität Bonn

Erstgutachter: **Prof. Dr. Andreas Meyer**
Chemical Signalling
Institut für Nutzpflanzenwissenschaften und Ressourcenschutz
Universität Bonn
Friedrich-Ebert-Allee 144
53113 Bonn, Germany

Zweitgutachter: **Prof. Dr. Peter Dörmann**
Molekulare Biotechnologie/Biochemie
Institut für Molekulare Physiologie und Biotechnologie der Pflanzen
Universität Bonn
Karlrobert-Kreiten-Str. 13
53115 Bonn, Germany

Tag der Promotion: 24.11.2023

Erscheinungsjahr: 2024

Table of contents

Summary

Iron–sulfur (Fe–S) clusters are vital cofactors in all domains of life. The mitochondrial Fe–S cluster biogenesis occurs through two major steps: the initial construction of [2Fe–2S] clusters, followed by their assembly into [4Fe–4S] clusters. However, how the clusters are distributed among the respective apoproteins is still not fully understood. In the presented thesis, we investigate the Fe–S cluster-dependent metabolism within plant mitochondria, using *Arabidopsis thaliana* as a model organism.

First, we summarise the existing knowledge on Fe–S cluster biogenesis and trafficking. We then discuss the metabolic consequences of compromised Fe–S cluster availability. In addition, we speculate about the potential release of sulfide and estimate the amount that might be set free by the continuous turnover of Fe–S cluster-containing proteins.

Furthermore, we studied the function of the glutaredoxin S15 (GRXS15). In contrast with other organisms, plants contain only GRXS15, as single class II GRX, within the mitochondria. We thus examined the distinct roles of the two main class I and class II GRXs, revealing key structural differences that determine their oxidoreductase and cluster-transferring functions. Specifically, we biochemically characterised GRXS15, to understand whether it can have catalytic activity besides its function in Fe–S cluster transfer.

With a genetic approach, we then investigated the physiological consequences of reduced GRXS15 activity *in planta.* Exploiting *grxs15* knockdown mutants and partially complemented lines, we show that the GRXS15 diminished activity mainly affects the function of lipoyl synthase (LIP1). LIP1 has a low copy number per mitochondrion and requires a constant flux of [4Fe–4S] clusters for its catalytic activity. By knocking out aconitase 3 – the most abundant mitochondrial [4Fe–4S]-dependent enzyme – we observed the suppression of the dwarfism in the *grxs15* mutants. Similarly, we obtained analogous results by overexpression of LIP1. With these experiments, we demonstrate that LIP1 is not able to compete with other enzymes for receiving [4Fe–4S] clusters when the upstream delivery system is impaired.

Unexpectedly, the overexpression of LIP1 was deleterious for wild-type plants. After having characterised this novel dwarf mutant we demonstrated that overexpression of LIP1 leads to the release of toxic amounts of sulfide, causing poisoning of the mitochondrial electron transport chain. Strikingly, we showed that this toxic effect can be alleviated by overexpression of *O*-acetylserine-(thiol)-lyase C, a component of the cysteine biosynthesis complex (CSC). We thus provide compelling evidence that the CSC acts as a sulfide detoxification system in the mitochondrion. Overall, this thesis contributes to refining the general overview of the entire pathway of mitochondrial Fe–S clusters, from assembly to consumption.

1 | Introduction

1.1 | The iron-sulfur clusters in life

Iron-sulfur (Fe–S) clusters are ancient and essential cofactors found in all domains of life. They consist of iron and sulfur atoms coordinated in specific arrangements, forming stable clusters with unique electronic and redox properties. With the partially filled *d* orbital of the transition metal iron, Fe–S clusters play key roles in electron transfer reactions such as respiratory and photosynthetic electron transport chains. Furthermore, Fe–S clusters are involved in important pathways like sulfur and nitrogen assimilation, the synthesis of co-enzymes such as biotin and lipoic acid, nucleotide metabolism, DNA synthesis, repair and gene expression regulation (Balk and Pilon, 2011; Przybyla-Toscano *et al.*, 2021). The presence of Fe–S clusters in both aerobic and anaerobic archaea, bacteria, and eukaryotes suggests their integration into central metabolic pathways early in the evolution of life, where iron sulfide is considered the most plausible source of reducing power in the "Fe–S World" (Wächtershäuser, 1992; Garcia *et al.*, 2022).

Enzymes containing Fe–S clusters can be found in different compartments of the cell, including the cytosol, nucleus, mitochondrion and, for photosynthetic organisms, also in the plastid (Balk and Pilon, 2011; Przybyla-Toscano *et al.*, 2021). In the free form, the clusters are intrinsically unstable and highly prone to oxidation by molecular oxygen (O_2), reactive oxygen species (ROS), and reactive nitrogen species like nitric oxide (NO) (Imlay, 2013). In particular, superoxide (O_2^-) and hydrogen peroxide (H_2O_2) are major causes of damage and cluster instability (Imlay, 2013). Therefore, it is crucial for all aerobic organisms to protect Fe–S clusters inside proteins, which shield the clusters from the surrounding environment and therefore prevent their disassembly. For this reason, Fe–S clusters cannot be transported across membranes and must be synthesized separately in all compartments in which they are required (Fig.1.1a).

Under anaerobic conditions, Fe–S clusters can be spontaneously assembled from the required components, iron and sulfur (Hagen *et al.,* 1981). However, it would most likely not happen efficiently *in vivo* and specialized assembly machineries are required for the *de novo* synthesis and insertion of Fe–S cluster into the respective apoproteins. In plants, the three dedicated assembly pathways are: the mitochondrial iron–sulfur cluster (ISC), the plastidic sulfur mobilization (SUF), and the cytosolic iron-sulfur protein assembly (CIA) (Balk and Pilon, 2011; Pedroletti *et al.*, 2023a). However, this last pathway depends on the mitochondrial ISC because it relies on the export of a yet unidentified sulfur compound that is transported from mitochondria to the cytosol (Lill *et al.*, 2015; Pandey *et al.*, 2019). The nucleus constitutes an exception since fully folded Fe–S holoproteins can move from the cytosol through nuclear pores to reach their destination in the nucleoplasm.

To date, there is no *in vivo* evidence for Fe–S holoproteins in other subcellular compartments like the secretory pathway, peroxisomes and apoplast (Przybyla-Toscano *et al.*, 2021).

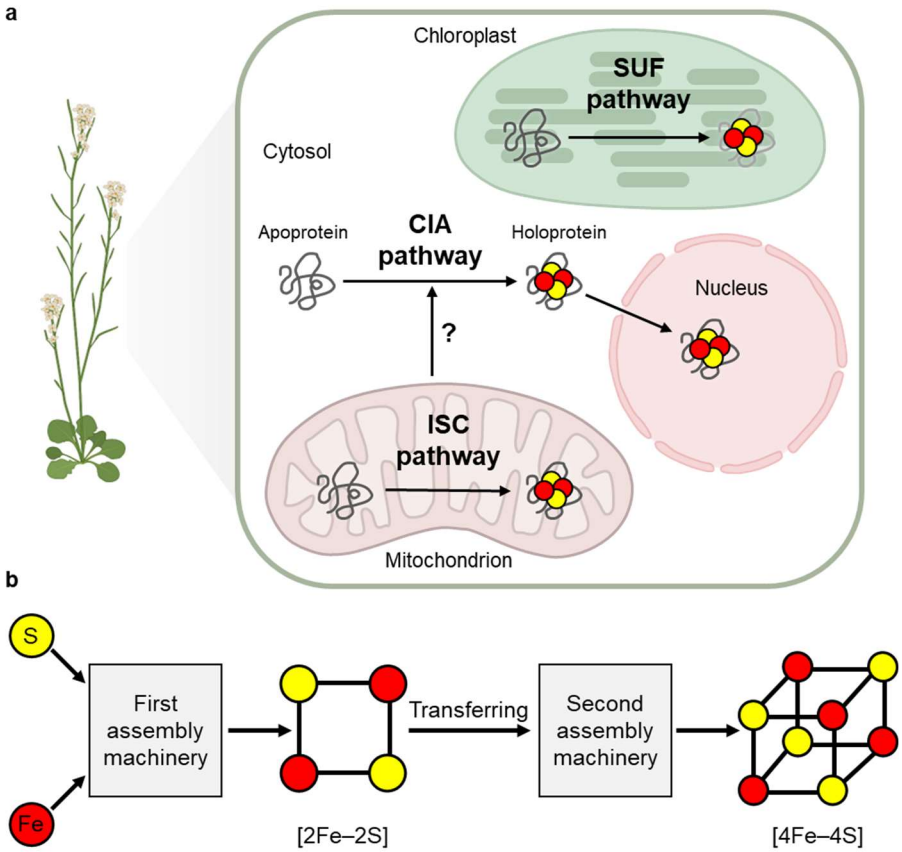

Fig. 1.1 | Iron–sulfur cluster assembly machineries in Arabidopsis. a The mitochondrial ISC (iron–sulfur cluster) and the plastidic SUF (sulfur mobilization) are independent pathways, while the cytosolic CIA (cytosolic iron–sulfur protein assembly) relies on a mitochondrial ISC unidentified sulfur compound. To date, no Fe–S machineries are identified within the nucleus, however, Fe–S holoproteins can move through nuclear pores. The Arabidopsis image has been created with BioRender (https://biorender.com). **b** Simplified scheme of the general concept for assembly and transfer of [2Fe–2S] and [4Fe–4S] clusters in mitochondria. A first assembly machinery fuses iron and sulfur atoms to build [2Fe–2S] clusters, which are transferred to a second machinery dedicated to the assembly of [4Fe–4S] clusters.

The inorganic cluster consists of iron cations (Fe^{2+}/Fe^{3+}) and sulfide anions (S^{2-}) and, even though it can vary in structure and stereochemistry, the rhombic [2Fe–2S] and cubic [4Fe–4S] conformations are the most common (Beinert, 2000). In all instances, the generation of Fe–S clusters occurs in two distinct steps: a first machinery is responsible to form [2Fe–2S] clusters which are subsequently transferred to a second machinery for the assembly of [4Fe–4S] clusters (Fig. 1.1b) (Braymer *et al.*, 2021; Pedroletti *et al.,* 2023a).

In plants, the entire machinery for the *de novo* assembly and transfer of Fe–S clusters to acceptor apoproteins consists of at least 7 proteins in the cytosol, 15 proteins in plastids and 27 proteins in mitochondria. These include proteins providing sulfur and iron atoms, scaffold

proteins for cluster assembly and several maturation factors including dedicated chaperons, co-chaperons and transfer proteins (Couturier *et al.*, 2013; Przybyla-Toscano *et al.*, 2021).

Despite the progress achieved in understanding the assembly process, our information on how Fe–S clusters are transferred and distributed among their respective apoproteins remains rudimental. In the review presented in Chapter 2 (Pedroletti *et al.,* 2023a), we summarize current knowledge about the assembly, transfer and distribution of [2Fe–2S] and [4Fe–4S] clusters, with emphasis on plant mitochondria.

Furthermore, we explore a topic that had received relatively little attention: the fate of Fe–S clusters. Continuous protein turnover results in the disintegration of Fe–S clusters, leading to the release of free iron and sulfur; as well, we highlighted how biotin synthase and lipoyl synthase utilise Fe–S clusters as a sulfur source, with sacrificial destruction of clusters and consequent sulfur release.

1.2 | Oxidative stress

Fe–S clusters can be easily damaged and disintegrated by oxidants (Imlay, 2013), which are largely abundant in mitochondria, where ROS are generated as a by-product of the electron transport chain (Møller *et al.,* 2007). In general, protein thiolates are susceptible to oxidation. Since the dissociation constant (pKa) in many proteins is rather acidic, the sulfhydryl residues (-SH) exist preferentially in the deprotonated form as a thiolate anion ($R\text{-}S^-$), which is highly nucleophilic (Alvarez and Salinas, 2022). Thus, cysteinyl residues can relatively easily undergo unwanted and harmful post-transcriptional modification by reacting with H_2O_2, resulting in the formation of sulfenic acids (R-SOH). Further reaction with H_2O_2 leads to irreversible oxidation, with the formation of sulfinic ($R\text{-}SO_2H$) and sulfonic ($R\text{-}SO_3H$) acids and irrecoverable protein (Fig. 1.2) (Gupta and Carroll, 2014; Zaffagnini *et al.*, 2019).

To prevent oxidative damage, ROS oxidation is counteracted by low molecular weight antioxidants like ascorbate and glutathione, which keep the majority of protein thiolates in a reduced form (Schwarzländer *et al.*, 2008; Foye and Noctor, 2013). Besides uncatalyzed reactions, a large set of enzymes is involved in redox modifications via a thiol-switching mechanism as regulatory mechanisms that allow to protect proteins in respond to changes in the cellular redox state, preventing irreversible oxidative damage (Buchanan and Balmer, 2005; Gupta and Carroll, 2014). These enzymes include superoxide dismutases, catalases, peroxidases and more than a hundred proteins belonging to the thioredoxin (TRX) superfamily (Dumanović *et al.*, 2021). Among the latter, there is the family of glutaredoxins, which further separates into different subfamilies (see Section 1.3).

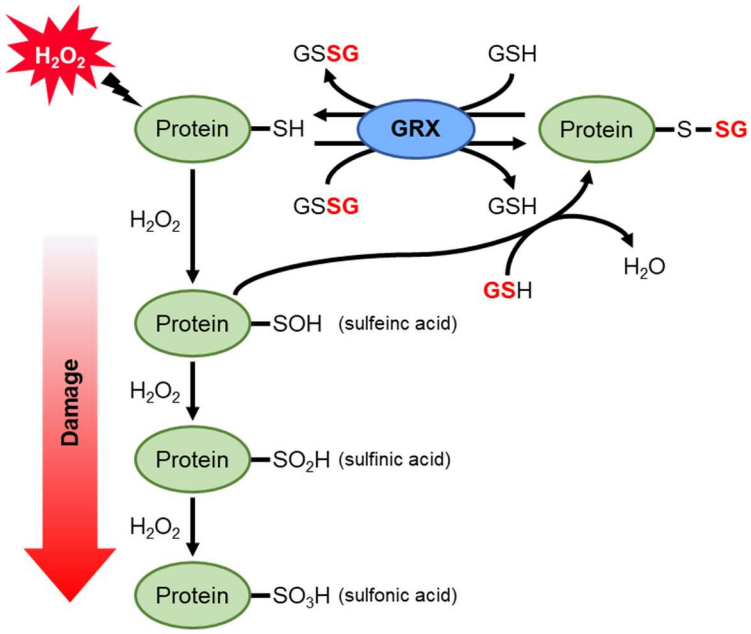

Fig. 1.2 | Types of oxidative damage and how glutaredoxins protect protein thiols. ROS (reactive oxygen species) such as hydrogen peroxide (H_2O_2) can attack cysteinyl residues, resulting in the formation of sulfenic (R-SOH) acid. Glutaredoxins (GRX) can protect protein thiols from uncontrolled oxidation via reversible glutathionylation. Also, glutathione (GSH) can spontaneously scavenge sulfenic acids through a nucleophilic attack and substitution of the hydroxyl residue along with the release of a water molecule. Further reaction of sulfenic acids with H_2O_2 leads to irreversible oxidation, with the formation of sulfinic ($-SO_2H$) and sulfonic ($-SO_3H$) acids, causing the protein irrecoverable.

1.3 | The glutaredoxin family

Glutaredoxins (GRXs) are small ubiquitous proteins and constitute a subfamily of the thioredoxin superfamily of oxidoreductases. The unifying structural motif that is present in virtually all family members is the so-called thioredoxin fold. This motif is a highly conserved core structure that is typically 11-13 kDa large and consists of four β-strands and three α-helices (Martin, 1995).

GRXs were first identified in *Escherichia coli* due to their capacity to catalyse the hydrogen donation necessary for reducing ribonucleotides to deoxyribonucleotides with glutathione (GSH) acting as the reducing equivalent (Holmgren, 1976). GRXs indeed have a binding site for glutathione, located between the active site motif and the helix α2, where the thiol group of glutathione is oriented towards the active site (Deponte, 2013). Their activity of reduction or formation of protein disulfides is mediated by glutathionylation and deglutathionylation reactions (Fig. 1.2) (Gravina and Mieyal, 1993; Lillig *et al.,* 2008; Deponte, 2013).

Initially, the GRXs classification of non-plant organisms was based on the specific active site motif, resulting in generally defining two main categories (Rodríguez-Manzaneque *et al.*, 1999). Class I GRXs, known as dithiol GRXs, are characterized by the consensus “CxxC”

motif, which often is present as “CPYC”. On the other hand, class II GRXs, referred to as monothiol GRXs, possess a highly conserved “CGFS” motif (Lillig *et al.,* 2008; Deponte, 2013).

Class I GRXs exhibit distinct oxidoreductase activities. The precise catalytic mechanism includes a complex series of intermediate steps that can differ between different GRXs (Lillig *et al.,* 2008; Deponte, 2013). For some GRXs, the reaction does not rely on the second thiol within the consensus “CxxC” but instead they directly utilise the thiol of reduced glutathione (GSH) as resolving thiol (Fernandes and Holmgreen, 2004; Zimmermann *et al.*, 2020). Other class I GRXs (so-called “monothiol class I GRXs”) do not even possess the second cysteine in the catalytic site; however, an additional semi-conserved cysteine in the C-terminal region allows the enzyme to form an intramolecular disulfide bond, facilitating the reduction of the protein after de-glutathionylation of a substrate, mimicking the dithiol mechanism (Mesecke *et al.*, 2008; Zannini *et al.*, 2019; Zimmermann *et al.*, 2020).

On the contrary, class II GRXs are mostly inactive in redox reactions and instead are involved in Fe–S cluster transfer (Deponte, 2013). This class is well known to be able to coordinate [2Fe–2S] clusters at the interface of a dimeric complex, through the cysteine residue in the highly conserved “CGFS” motif and the thiol of a non-covalently bound molecule of glutathione (see Section 1.3 and Chapter 3a) (Johansson *et al.*, 2007; Picciocchi *et al.*, 2007; Iwema *et al.*, 2009; Rouhier *et al.*, 2010; Li and Outten, 2012). Some class I GRXs can coordinate [2Fe–2S] clusters *in vitro* and *in vivo*, in an analogue way to class II GRXs (Lillig *et al.*, 2005; Rouhier *et al.*, 2007; Hoff *et al.*, 2009; Scalcon *et al.*, 2019); however, these proteins are unable to efficiently transfer the cluster to the respective apoproteins (Trnka *et al.*, 2020). Moreover, certain class II GRXs have been demonstrated to have residual oxidoreductase activity, although the catalysis is relatively slow and often limited to oxidation, with no detectable reduction activity (Zaffagnini *et al.*, 2008; Gao *et al.*, 2010; Moseler *et al.*, 2015; Zannini *et al.*, 2019). The *in vivo* relevance of this activity remains a topic of debate.

Despite sharing a similar structure based on the TRX fold, for decades it remained elusive why class I GRXs are efficient oxidoreductases while class II GRXs are essentially dedicated to iron–sulfur clusters transfer. The evolutionary significance behind the development of distinct types of GRXs, as well as the specific reasons that explain the differences between these classes, is not completely resolved.

In the research paper presented in Chapter 3a (Trnka *et al.*, 2020), we investigate the structural differences between classes I and II GRXs in-depth. We demonstrate that the primary distinction is the length of amino acids that separate a conserved lysine on the strand β1 from the active site on helix α1. In fact, class I GRXs possess a spacer of only two amino acids while class II GRXs have seven amino acids. The extended sequence in class II GRXs forms a loop structure which alters the orientation of the conserved lysyl residue, which determines

the properties of the enzyme. Hence, the loop structure diminishes the redox activity of class II GRXs, while it allows them to form a looser coordination with the [2Fe–2S] cluster which may be a prerequisite for its efficient transfer to specific apoprotein. The knowledge acquired in Chapter 3a (Trnka *et al.*, 2020) is applied to characterise the mitochondrial glutaredoxin S15 of Arabidopsis *in vitro*, in Chapter 4 (Moseler *et al.*, 2021).

1.4 | Glutaredoxins in Arabidopsis

The publication of the *Arabidopsis thaliana* genome (The Arabidopsis Genome Initiative, 2000) revealed an unexpectedly high number of genes coding for GRXs. Arabidopsis indeed contains at least 31 genes encoding GRXs (Rouhier *et al.,* 2004) compared to only eight in *Saccharomyces cerevisiae* and four in humans (Herrero *et al.,* 2011; Abdalla *et al.,* 2018; Ogata *et al.*, 2021). In contrast to non-plant species, which have only the classical class I and class II GRXs, plants possess an additional class III. Within the conventional classes, six members belong to class I and four members belong to class II (Fig. 1.3). However, while the "CGFS" active site is consistently conserved among all members of class II GRXs, the "CPYC" consensus deviates for three members of class I GRXs (Appendix 1). The remaining 21 GRXs exhibit a distinct active site alignment, characterized by a "CCxC" or "CCxS" consensus sequence and are classified as CC-type or class III GRXs, which are land plant-specific. With observations mainly limited to developmental processes *e.g.*, regulation of floral, anther or petal development (Xing *et al.,* 2005; Xing *et al.,* 2008; Li *et al.*, 2009), the biological functions of class III GRXs are largely uncharacterised. Recent studies report that ROXY9 (a class III GRXs) has no GSH-dependent oxidoreductase activity *in vitro,* suggesting that class III GRXs might have different functions than class I GRXs (Mrozek *et al.*, 2023).

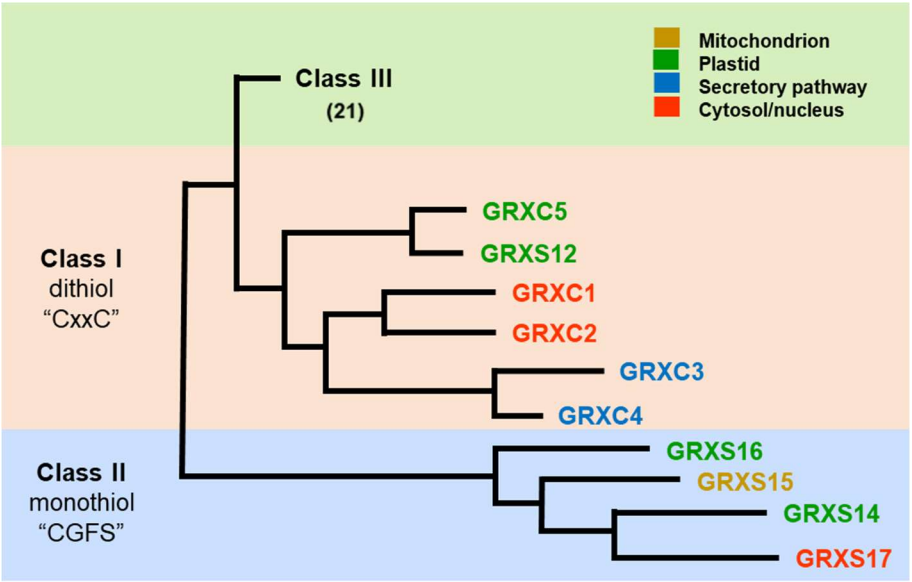

Fig. 1.3 | Phylogeny and subcellular localisation of glutaredoxins in Arabidopsis. The localisation of the respective GRXs indicated by the colour code is based on predictions from SUBA3 (https://suba.live/index.html) or evidence in the literature. The 21 poorly characterized class III GRXs are not shown for simplification. The neighbour-joining tree without distance corrections was generated by local multiple-sequence alignment (Clustal Omega, https://www.ebi.ac.uk/Tools/msa/clustalo/).

1.5 | Glutaredoxin S15 in mitochondria

In contrast to other kingdoms, plants contain only glutaredoxin S15 (GRXS15) as the sole GRX within mitochondria (Rouhier *et al.,* 2004; Moseler *et al.*, 2015; Ströher *et al.*, 2016). It belongs to the class II GRXs and possesses a single GRX domain with the conserved "CGFS" active site motif.

GRXS15 was identified as an essential component for the mitochondrial biogenesis of iron–sulfur clusters (Moseler *et al.*, 2015). First, the [2Fe–2S] is *de novo* assembled on the scaffold protein ISU1, which then forms a complex with the chaperone/co-chaperon complex HSCA1/HSCB (Xu *et al.*, 2009; Leaden *et al.,* 2014). In yeast, it has been shown that this shuttle complex can directly transfer the [2Fe–2S] cluster to *Sc*GRX5, homolog of *At*GRXS15 (Uzarska *et al.*, 2013). Although there is no direct evidence, the high degree of evolutionary conservation suggests that this mechanism might be preserved in human and plant mitochondria with *Hs*Grx5 (Lill and Freibert, 2020) and *At*GRXS15 (Moseler *et al.*, 2015), respectively.

Despite the lack of GRXS15 crystal structure, it can still be compared by analogy with other Arabidopsis class II GRXs (Li *et al.*, 2010) and homologs in bacteria, yeast and human (Iwema *et al.*, 2009; Johansson *et al.*, 2011; Abdalla *et al.*, 2016). It is therefore assumed that two GRXS15 non-covalently harbour a molecule of GSH each, in the respective binding site, and cooperatively coordinate a single [2Fe–2S] cluster through the cysteinyl residues of the two GSH molecules and the two cysteinyl residues of the "CGFS" motifs (Fig. 1.4). This model is supported by spectroscopic evidence (Picciocchi *et al.*, 2007; Moseler *et al.*, 2015).

After receiving the cluster, the homodimeric complex GRXS15–[2Fe–2S]–GRXS15 delivers it to the second machinery, for the assembly of [4Fe–4S] clusters. The core of the second assembly machinery in Arabidopsis mitochondria is constituted by the proteins ISCA1a/b, ISCA2 and IBA57. It has been experimentally confirmed that GRXS15 directly interacts with ISCA proteins and transfers the [2Fe–2S] cluster as a building block for the assembly of [4Fe–4S] clusters (Azam *et al.*, 2020). A similar observation was done for other systems such as yeast (Mühlenhoff *et al.*, 2011) and human (Brancaccio *et al.*, 2014).

In addition to [2Fe–2S] cluster transfer, GRXS15 displays a slow oxidation activity and lacks reduction activity, when assessed through standard GSH-dependent *in vitro* enzymatic assays

e.g., HED assay and roGFP2 assay (see Section 1.6) (Moseler *et al.*, 2015). This observation is particularly noteworthy since the mitochondrion is a cellular compartment characterized by a high GSH-dependent metabolism and possibly GSH-dependent redox signalling (Schwarzländer *et al.*, 2008; Zannini *et al.*, 2019). However, the reasons behind the absence of efficient oxidoreductases class I GRXs in plant mitochondria remain unclear.

To understand whether GRXS15 can fulfil the functions of the class I GRXs, in Chapter 3b we focus on characterizing the *in vitro* properties of this protein. In particular, we measure its oxidoreductase activity by exploiting the roGFP2 interaction assay (see Section 1.6).

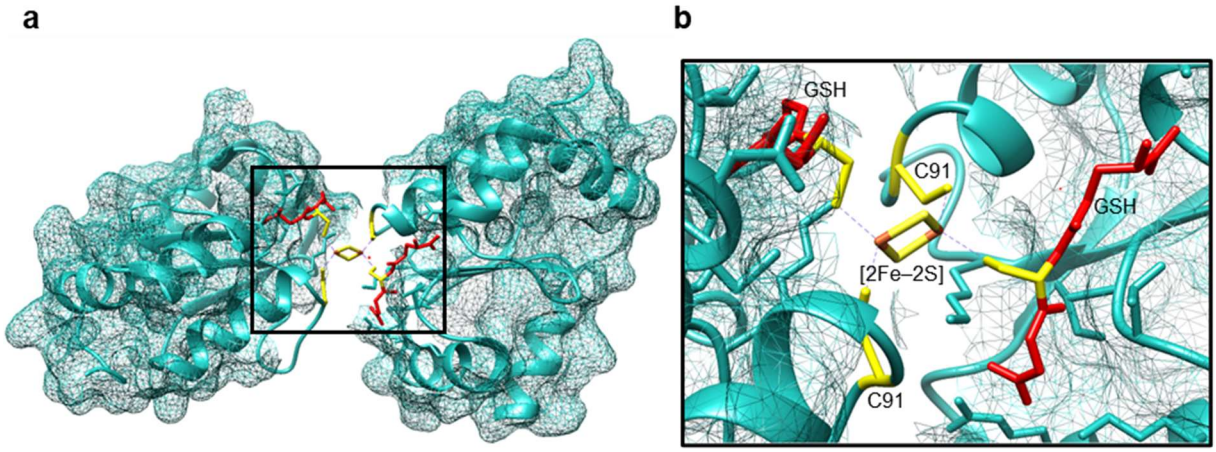

Fig. 1.4 | GRXS15 homodimer forms a complex with GSH to coordinate [2Fe–2S] cluster. a Working model for the cluster coordination by Arabidopsis glutaredoxin S15 (GRXS15). The model is generated by the Phyre2 web portal (Kelley *et al.*, 2016) and it is based on the crystal structure of the human glutaredoxin 5 deposited by Johansson *et al.* (2011) (PDB: 2WUL). **b** Detail of the coordination of the [2Fe–2S] cluster (yellow and orange). The cysteines of GRXS15 (C91) are highlighted in yellow, the glutathione molecules (GSH) in red, with their cysteinyl residue in yellow.

1.6 | roGFP2 assay to test *in vitro* oxidoreductase activity of glutaredoxins

Since the discovery of GRXs, several assays have been developed to investigate and measure their enzymatic activity (Lillig *et al.,* 2008). The most commonly used *in vitro* assay is the bis-(2-hydroxyethyl)-disulfide (HED) assay (Holmgreen and Aslund, 1995; Begas *et al.,* 2015). It is based on a double-step reaction: first, the small artificial substrate HED is reduced by GSH and GRXs, causing the formation of glutathione disulfide (GSSG). Subsequently, GSSG is reduced by glutathione reductase (GR), by using NADPH as electron donor, which can finally be monitored spectrophotometrically (Fig. 1.5) (Luthman and Holmgren, 1982; Begas, Staudacher and Deponte, 2015). However, the HED assay is a relatively complex enzymatic assay with two coupled forward reactions and a non-catalysed background reaction (Fig. 1.5) that necessitates considerable technical expertise to ensure its reliability and robustness. In addition, the assay has some limitations as it is restricted to only unidirectional reactions. Thus,

the HED assay can provide information on the reducing activity of the GRXs but not on their oxidising abilities.

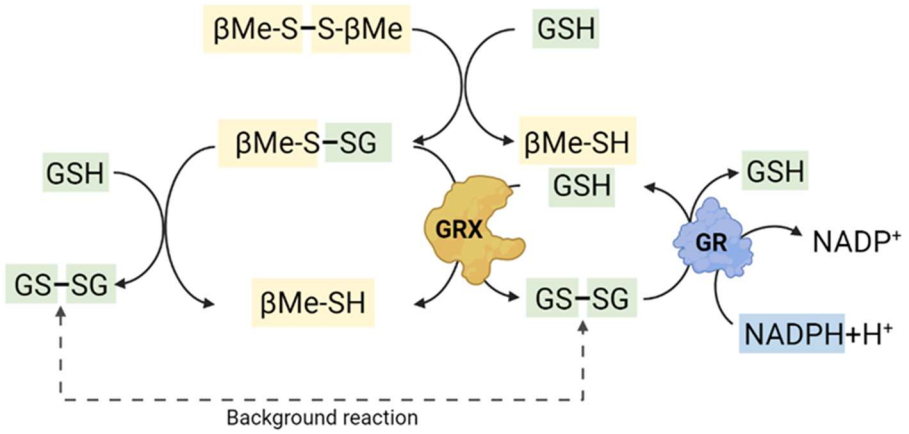

Fig. 1.5 | Schematic representation of the HED assay. The reaction is initiated when a molecule of reduced glutathione (GSH) attacks a molecule of HED (βMe-S–S-βMe), resulting in the formation of two molecules of 2-mercaptoethanol (βMe-SH), one of which is glutathionylated (βMe-S–SG). The glutaredoxin (GRX) catalyses the de-glutathionylation of βMe-S–SG, releasing a molecule of glutathione disulfide (GS–SG). GS–SG is a substrate for glutathione reductase (GR) that reduces it in two molecules of GSH using NADPH as final electron donor. The consumption of NADPH can be monitored by measuring the absorbance at 340 nm. In addition, βMe-S–SG spontaneously interacts with a second molecule of GSH, producing GS–SG, which is reduced by GR in a background reaction that is independent of GRX.

An alternative *in vitro* enzymatic assay, which allows not only the measurement of the reducing activity of GRXs but also the oxidising activity, is the roGFP2 interaction assay. This enzymatic test exploits the redox-sensitive green fluorescent protein 2 (roGFP2), a GFP variant which possesses two engineered cysteine residues (C147 and C204) that can dynamically form a disulfide bridge or undergo reduction in response to changes in the redox potential of its surrounding environment (Fig. 1.6) (Hanson *et al.*, 2004).

roGFP2 has two fluorescence excitation peaks at about 400 and 490 nm (Fig. 1.6) and exhibits rapid and reversible ratiometric changes in fluorescence intensity, according to the redox state of the disulfide bridge between the two cysteines. Those cysteines can be attacked by GRXs (Meyer *et al.*, 2007) which, depending on the redox potential of the surrounding glutathione buffer and the oxidoreductase abilities of the enzyme, catalyse the oxidation of the two cysteines leading to the formation of the disulfide bridge or on the contrary resolve it, leading to the reduction of the disulfide. The transition from the oxidised to the reduced form, and *vice versa*, mediates changes in roGFP2 structure, which causes shifts in its spectral properties, which are detectable in the excitation spectrum (Fig. 1.6). The continuous equilibration of the redox status of the disulfide bridge regulated by GRXs indicates that the reaction can proceed

in both directions. Thus, it is possible to assess both the oxidizing and reducing activities of GRXs (Meyer *et al.*, 2007).

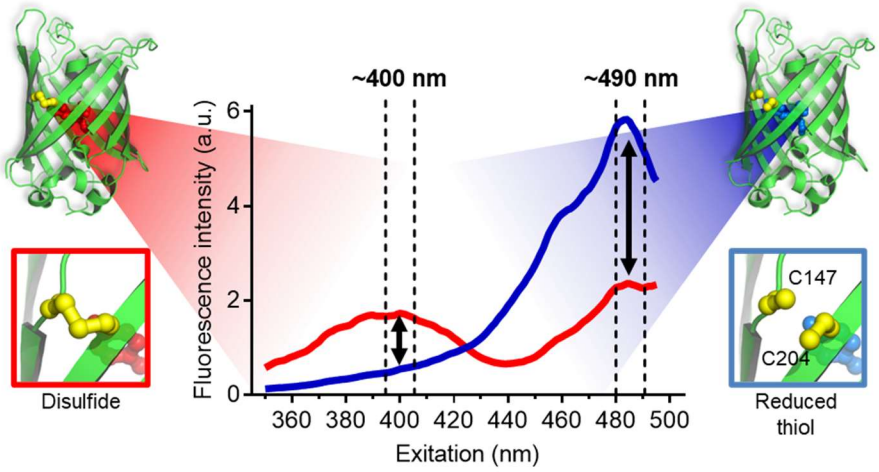

Fig. 1.6 | Structural changes of reduced and oxidized roGFP2. The structural changes of oxidised or reduced roGFP2 are a result of the intramolecular formation of a disulfide bridge between cysteine 147 and cysteine 204 or its dissolution, respectively. Specifically, the protonated form of the tyrosine 66 in the chromophore exhibits an excitation peak at about 400 nm, whereas the deprotonated form exhibits an excitation peak at about 490 nm, enabling ratiometric sensor read-out. Oxidized and reduced roGFP2 are represented in red and blue, respectively. Sulfur atoms are depicted in yellow. Modified from Morgan and Schwarzländer (2016).

roGFP2 and derivatives have been extensively utilized in various biological studies, including investigations of oxidative stress, redox signalling, cellular or mitochondrial responses to environmental changes *in planta* (Meyer *et al.*, 2007; Aller *et al.,* 2013; Nietzel *et al.*, 2019; Müller-Schüssele *et al.,* 2021; Ugalde *et al.*, 2021, 2022). It offers a dynamic non-invasive approach to assess intracellular redox changes, providing valuable information about the cellular glutathione redox potential. In addition to the application in live cells, the roGFP2 can also be adapted for *in vitro* measurements. In the *in vitro* assay, purified roGFP2 is used as an artificial substrate protein for GRXs. The redox state of the sensor is then measured using a fluorescence spectrophotometer, providing information on the redox activity of the GRX. This assay is largely exploited in Chapter 3a and Chapter 3b to determine the activity of various GRXs from human and Arabidopsis. The application of the roGFP2/GRX assay is a highly valuable tool for exploring mutated versions of GRXs, providing insights into the biochemical characteristics and functions of GRXs.

Generally, two different reactions are performed to investigate the reduction or oxidation of roGFP2. To investigate the reduction abilities of a GRX, the protein is mixed in a buffer containing fully oxidised roGFP2. The reaction is triggered by injection of GSH, which reduces the roGFP2 disulfide bridge. Although this reduction is spontaneous, the reverse reaction is

more rapid, reconverting the roGFP2 back to its oxidised form (Fig. 1.7a). In fact, the equilibrium between the oxidised and reduced roGFP2 is mainly established by the glutathione redox potential, which is determined by the standard concentration of GSH injected in the assay (2 mM). Considering also the presence of molecular oxygen in the buffer, the equilibrium is eventually shifted to the oxidised roGFP2. However, the GRX can subtract the intermediate glutathionylated roGFP2 by efficiently catalysing its de-glutathionylation and fully reducing the sensor (Fig. 1.7a). By doing so, GRX is eventually glutathionylated. In this state, the protein can use a second molecule of GSH to self-regenerate, releasing a molecule of GSSG (Fig. 1.7a). Given that even a small amount of GSSG significantly affects the glutathione redox potential, it becomes necessary to convert it back to its reduced form by GR, which uses NADPH as final electron donor (Fig. 1.7a).

To investigate the oxidation abilities of a GRX, a second experimental configuration is employed. The roGFP2 is first fully reduced by incubation with dithiothreitol (DTT) and subsequently desalted to remove excess DTT (Fig. 1.7b). The reaction is then initiated by adding GSSG, which initially attacks the GRX, by forming its glutathionylated form. Hence, the glutathionylated GRX transfers the glutathione group to the reduced sensor through a thiol-disulfide exchange reaction. Subsequently, roGFP2 spontaneously forms the disulfide bridge, leading to the release of a GSH molecule (Fig. 1.7b).

By continuously measuring the specific roGFP2 fluorescent wavelengths at 520 nm after excitation at 400 nm and 490 nm, it is possible to monitor its redox state dynamically over time and calculate the time course of the glutaredoxin-mediated reaction.

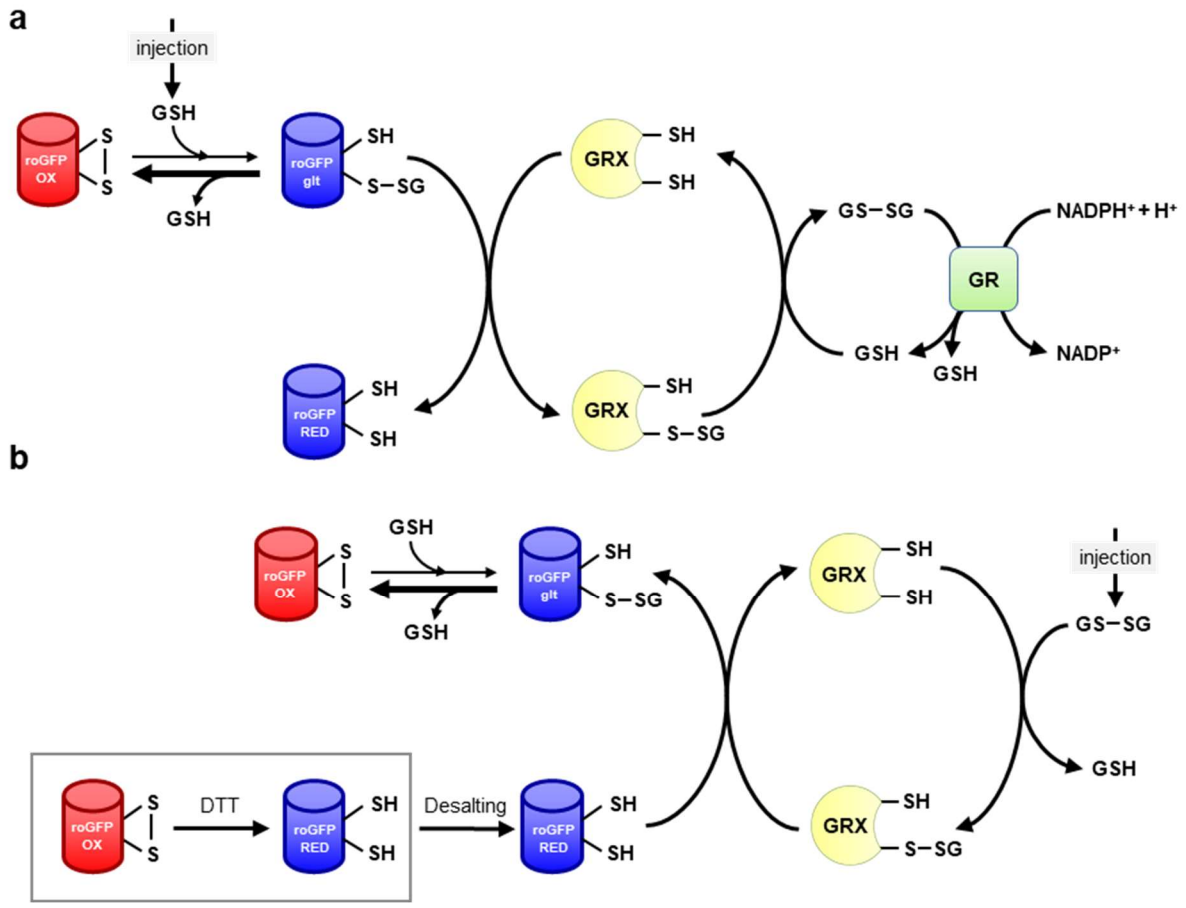

Fig. 1.7 | Proposed reaction scheme for the reduction and oxidation of roGFP2 mediated by glutaredoxin. a Reduction of roGFP2 catalysed by a glutaredoxin (GRX, here depicted as dithiol GRX). The reduced glutathione (GSH) is injected into the reaction mix to start the reaction. An equilibrium between oxidised and glutathionylated roGFP2 is established. The intermediate glutathionylated roGFP2 is recognized by the GRX that catalyses its deglutathionylation and fully reduces the sensor. The GRX is de-glutathionylated with the consequent formation of glutathione disulfide (GSSG). Glutathione reductase (GR) reconverts GSSG in GSH, consuming a molecule of NADPH as a final electron donor. **b** Oxidation of roGFP2 catalysed by a GRX. The sensor is pre-reduced by dithiothreitol (DTT) and desalted to remove excess DTT (here depicted in the grey box). The reaction is started by GSSG. The glutathionylated GRX transfers the GSH group to the reduced sensor with the spontaneous formation of the disulfide bridge and release of a GSH molecule. The GRX is then glutathionylated again to start the next catalytic cycle.

1.7 | Metabolic consequences of diminished GRXS15 activity

In yeast, the lack of the mitochondrial *Sc*Grx5, homolog of *At*GRXS15, is non-lethal but results in continuous oxidative damage, accumulation of cellular iron and inactivation of Fe–S-dependent enzymes (Bellí *et al.*, 2002; Rodríguez-Manzaneque *et al.*, 2002). A similar impact was observed in zebrafish and humans, where impairment in heme biosynthesis and erythropoiesis was reported (Wingert *et al.*, 2005; Camaschella *et al.*, 2007). In Arabidopsis, knockout lines for the single GRXS15 are instead embryo-lethal (Moseler *et al.*, 2015), while

knockdown lines with residual GRXS15 are viable but display a dwarf phenotype (Ströher *et al.*, 2016; Moseler *et al.*, 2021).

Null mutants *grxs15* can be complemented through the overexpression of mutated GRXS15 K83A. However, this rescue leads to an extremely dwarf phenotype (Moseler *et al.*, 2015). The GRXS15 K83A mutant protein consists of GRXS15 where the highly conserved lysine residue 83 (K83) is substituted with an alanine. Since the K83 is important for the stabilization of the thiolate form of the cysteine in the active site and thus for the coordination of the GSH, the result is a protein with a compromised ability to coordinate a [2Fe–2S] cluster. The consequence is that GRXS15 K83A is less efficient in transferring the cluster from the first to the second assembly machinery (Moseler *et al.*, 2015).

Despite GRXS15 being an early participant in the mitochondrial Fe–S cluster assembly and transfer system, no significant global metabolic effects were observed in *grxs15* mutants (Moseler *et al.*, 2015; Ströher *et al.*, 2016) suggesting that the bottleneck generated by GRXS15 inefficiency in the supply of [2Fe–2S] clusters to the second assembly machinery may not necessarily affect all [4Fe–4S]-dependent proteins to a similar extent. In Chapter 4 (Moseler *et al.*, 2021) we investigate the physiological consequences of this bottleneck, exploring the *in planta* consequences of diminished activity of GRXS15 by systematically analysing several pathways and proteins relying on mitochondrial Fe–S clusters.

In accordance with previous observations (Moseler *et al.*, 2015; Ströher *et al.*, 2016), in Chapter 4 (Moseler *et al.*, 2021) we have identified that the reduced function of GRXS15 leads to a deficiency in protein lipoylation. In fact, both *grxs15* knockdown lines and *grxs15 K83A* mutants show evident metabolite accumulation, notably: pyruvate, 2-oxoglutarate glycine, and α-ketoacids. These are substrates of four mitochondrial dehydrogenase complexes, pyruvate dehydrogenase complex (PDC), 2-oxoglutarate dehydrogenase complex (OGDC), glycine dehydrogenase complex (GDC), and branched-chain α-keto acid (BCKA) dehydrogenase complex (BCKDC). Their activity relies on lipoic acid, a prosthetic group attached to the E2-subunits of PDC, OGDC, BCKDC, and to the H-protein of GDC (see Section 1.8) (Taylor *et al.*, 2004; Solmonson and DeBerardinis, 2018). These findings serve as bases for the hypotheses discussed in Chapter 5 (Pedroletti *et al.*, 2023b).

1.8 | Lipoyl synthase

The highly conserved lipoyl synthase (LIP1) belongs to the superfamily of radical *S*-adenosylmethionine (SAM) enzymes. These proteins are characterized by a cysteine-rich motif “CxxxCxxC” which allows the coordination of a [4Fe–4S] radical SAM (RS) cluster that provides electrons to catalyse the formation of 5′-deoxyadenosyl radicals (dAdo•) (Booker and Lloyd, 2022). LIP1 carries an additional “auxiliary” [4Fe–4S] cluster which is used as sulfur

source for the synthesis of lipoic acid (Fig. 1.8) (Cicchillo *et al.*, 2004; Lanz and Booker, 2015; McLaughlin *et al.*, 2016; McCarthy and Booker, 2017).

Although Arabidopsis LIP1 has not been biochemically characterized, the conservation of residues and motifs for the Fe–S cluster coordination suggests that the catalytic mechanism is similar to LIP1 orthologues from different species (Przybyla-Toscano *et al.*, 2022). Through two consecutive steps, the RS cluster supplies two electrons to cleave two molecules of SAM into methionines and dAdo• radicals. These radicals abstract hydrogen atoms from the C6 and C8 carbons of an octanoyl residue attached to carrier proteins (usually the H-protein of GDC). Subsequently, the resultant carbon radicals attack two of the four sulfur atoms of the [4Fe–4S] auxiliary cluster, forming covalent C–S bonds and thus the lipoic acid (Fig. 1.8) (McCarthy and Booker, 2017; Booker and Lloyd, 2022). Hence, LIP1 sacrifices the auxiliary cluster as a sulfur source.

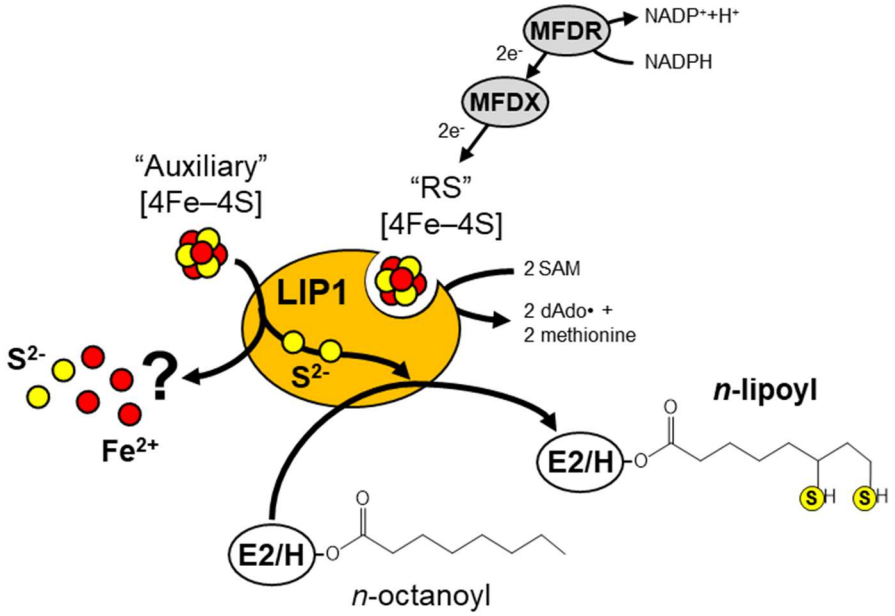

Fig. 1.8 | Working model of lipoic acid biosynthesis by LIP1. Lipoyl synthase (LIP1) contains two [4Fe–4S] clusters: the "auxiliary" cluster and radical SAM ("RS") cluster. LIP1 transfers two sulfur atoms from the auxiliary cluster to the *n*-octanoyl residue attached to E2 or H subunits of the mitochondrial dehydrogenases for its conversion to the *n*-lipoyl prosthetic group. The electrons for the reduction of two molecules of *S*-adenosylmethionine (SAM) are provided through the NADPH/MFDR/MFDX (mitochondrial ferredoxin/ferredoxin reductase) cascade. Cleavage of SAM molecules results in two methionines and dAdo• (5′-deoxyadenosyl) radicals, which serve to abstract H atoms from the *n*-octanoyl. Whether the auxiliary clusters after extraction of sulfur atoms fall apart and release sulfide or whether they can be repaired is not known.

The fate of the fragmentary auxiliary cluster after the abstraction of two sulfur atoms is not known. *In vitro* evidence has suggested that the bacterial carrier protein *Ec*NfuA (homolog of *At*NFU5/6) might efficiently reconstitute the cluster on *Ec*LipA (homolog of *At*LIP1), allowing to use of all the sulfur atoms of the [4Fe–4S] cluster (McCarthy and Booker, 2017). This

observation is consistent with results from *in vitro* assays with the human homologous proteins *Hs*NFU1 and *Hs*LIAS (Warui *et al.*, 2022).

In both yeast and Arabidopsis, *in vivo* evidence has highlighted the central role of NFUs proteins for LIP1 activity, as NFUs delivery [4Fe–4S] clusters from the second assembly machinery to the lipoyl synthase (Melber *et al.*, 2016; Przybyla-Toscano *et al.*, 2022). However, in the absence of a confirmed mechanism for repairing the remnants of the auxiliary cluster, we assume that LIP1 catalytic activity leads to sacrificial destruction of the [4Fe–4S] clusters, and the fragmentary [4Fe–2S] clusters fall apart and release free iron and sulfide.

In Chapter 5 (Pedroletti *et al.*, 2023b), we investigate the distribution of iron–sulfur clusters among different apoproteins in Arabidopsis mitochondria and unravel the link between the reduced activity of LIP1 and the cluster transfer activity via GRXS15. Furthermore, we bring *in vivo* evidence that the activity of LIP1 results in the release of sulfide as a highly toxic by-product. As is already underlined in Chapter 2 (Pedroletti *et al.,* 2023a), we demonstrate the key role of mitochondrial cysteine biosynthesis as a crucial salvage pathway. Indeed, the immediate refixation of sulfide through incorporation into cysteine is not only essential for the spontaneous degradation of cluster-containing holoproteins – which inevitably are a source of free sulfide – but also is essential to face the destructive activity of lipoyl synthase.

Aim of this study

Fe–S clusters play a key role as essential co-factors across all forms of life. For instance, they are exploited by many proteins for essential metabolic functions and biosynthetic pathways. In the review paper presented in Chapter 2 (Pedroletti *et al.,* 2023a), we summarise the latest discoveries about the processes of assembly, distribution, and fate of Fe–S clusters in plant mitochondria. In particular, we investigate the need for a local sulfide detoxification system within the mitochondrion.

In the research paper presented in Chapter 3a (Trnka *et al.*, 2020), we analyse the molecular structure and the oxidoreductase activity of class I and class II GRXs to investigate the features that determine the different activity of the two main GRX classes.

In Chapter 3b, we exploit the insights from Chapter 3a to characterize the catalytic ability of GRXS15 *in vitro*, to understand whether the only GRX localized in Arabidopsis mitochondria can have an oxidoreductase activity and can fulfil the function of class I GRXs.

In the research paper presented in Chapter 4 (Moseler *et al.*, 2021), we study the role of GRXS15 as transferase for [2Fe–2S] clusters *in planta*. We especially investigate the physiological consequences of diminished activity of GRXS15, systematically analysing several pathways and proteins reliant on mitochondrial Fe–S clusters.

The results achieved in Chapter 4 served as the cornerstone for the hypothesis that we explore in Chapter 5 (Pedroletti *et al.*, 2023b). In this last part, we present an unpublished research paper, in which we uncover why compromised Fe–S cluster transfer via GRXS15 mainly impacts LIP1. With a genetic approach, we characterise the effects of LIP1 overexpression and investigate the mitochondrial cysteine biosynthesis for the key role in the refixation of excessive sulfide generated in mitochondria.

2 | Assembly, transfer, and fate of mitochondrial iron–sulfur clusters

This chapter presents the review paper published in *Journal of Experimental Botany* in 2023:

***Luca Pedroletti**, Anna Moseler and Andreas Meyer. (2023)*
Journal of Experimental Botany, 74(11), pp. 3328–3344. doi: 10.1093/jxb/erad062.

2.1 | Summary and personal contribution

Iron–sulfur (Fe–S) clusters are crucial cofactors of many proteins involved in indispensable metabolic activities and biosynthetic processes. In this review, we provide current knowledge about the processes involved in Fe–S cluster assembly in plant mitochondria. We focus particularly on Fe–S-cluster fluxes and on two specific enzymes, biotin synthase (BIO2) and lipoic acid synthase (LIP1), because they both use Fe–S clusters as a sulfur source. To draw a larger and more consistent picture, we compared the established plant processes with the respective knowledge of other species such as yeast, human and bacteria.

In the first part of the review, we describe how Fe–S clusters are assembled, delivered and inserted as essential co-factors into the respective apoproteins. We summarize how a first assembly machinery generates [2Fe–2S] clusters and how these clusters are transferred to various subunits in the mitochondrial electron transport chain (mETC). Beyond the evidence presented in the published paper, further information and hypotheses on the generation of [4Fe–4S] clusters directly on the succinate dehydrogenase subunits are reported in Additional Information in Section 2.3.

In Pedroletti *et al.* (2023a), we highlight the crucial role of glutaredoxin S15 (GRXS15), a transferase protein, which connects the first assembly machinery to the second, and discuss the metabolic consequences of a compromised Fe–S cluster assembly machinery. A more detailed description of the cluster transfer to the GRXS15 dimer is reported in the unpublished Fig. 2.1.

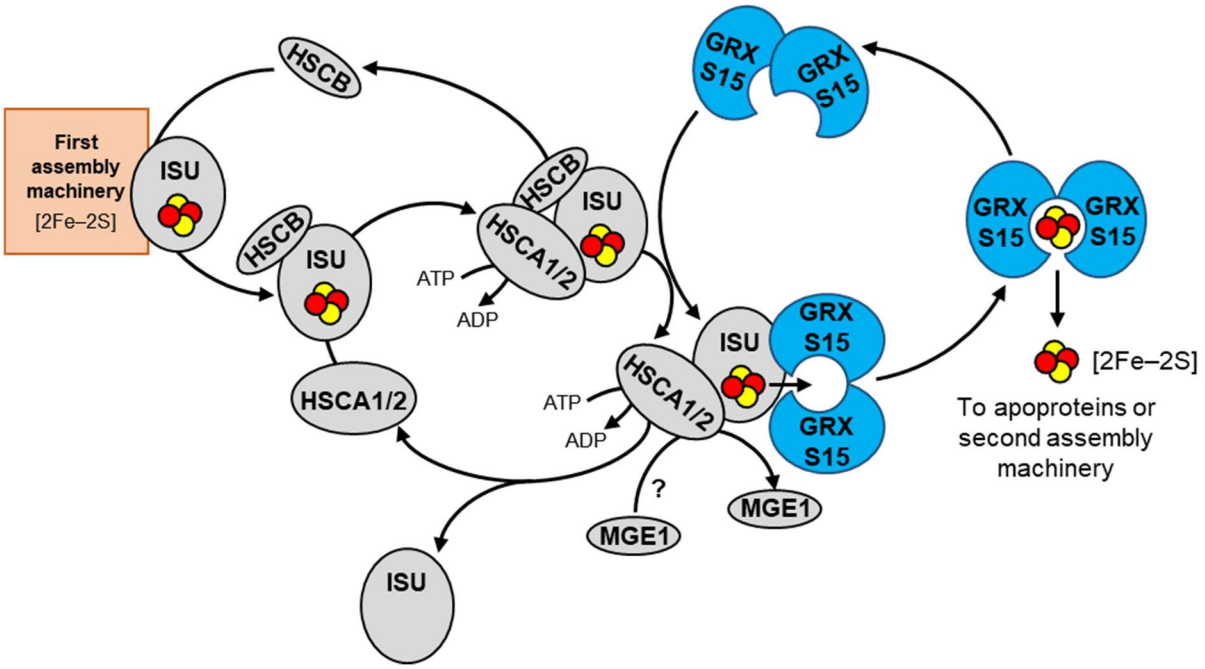

Fig. 2.1 | Working model for the transfer of [2Fe–2S] from the first assembly machinery to glutaredoxin S15 via the chaperone/co-chaperone system HSCA/HSCB. The first assembly machinery generates the [2Fe–2S] cluster on the scaffold proteins ISU1/2/3 (Iscu-like – here for simplification shown as ISU). After assembly, the scaffold protein ISU is detached from the assembly machinery by the co-chaperone HSCB (heat shock protein B), which subsequently recruits the HSCA1/2 chaperones (heat shock protein A) to form a complex for delivery of the cluster. GRXS15 (glutaredoxin S15) interacts with the complex, promoting the detachment of HSCB. HSCB and hypothetically MGE1/2 (mitochondrial GRPEs) stimulate ATP/ADP exchange activity of HSCAs leading to a conformational change between HSCAs and ISUs that favours the release of the [2Fe–2S] cluster into GRXS15 homodimer.

We further describe the second machinery for the generation of [4Fe–4S] clusters. An even more detailed update on the current hypotheses for [4Fe–4S] assembly on ISCAs proteins is reported in Additional Information (see Section 2.3).

In the second part of the review, we investigate the fate of the mitochondrial Fe–S clusters. We highlight that the continuous turnover of mitochondrial Fe–S-containing proteins not only drives the demand for newly assembled Fe–S clusters but also has an impact on the release of sulfide. The degradation of Fe–S proteins implies that the protein-bound clusters are set free and most likely disintegrate due to their instability in free form, with the concomitant release of sulfide and iron. Free sulfide is toxic, especially in mitochondria, where it can inhibit the cytochrome *c* oxidase (complex IV) in the mitochondrial electron transport chain (mETC) with major deleterious effects on energy metabolism (for more details see Chapter 5, Pedroletti *et al.* (2023b)). We thus estimate how much sulfide is released during Fe–S cluster-containing protein turnover in the mitochondrial matrix. We combine protein abundances determined for individual mitochondria from Arabidopsis suspension cultures (Fuchs *et al.*, 2020) and the rates of protein degradation determined in Arabidopsis seedlings (Li *et al.*, 2017). Although the

datasets are limited and rates may vary across tissues, developmental stages, etc., we estimate that a single Arabidopsis mitochondrion daily disassembles over 2,500 [2Fe–2S] clusters and over 5,600 [4Fe–4S] clusters due to protein degradation (Table 2.1).

Table 2.1 | Estimation of Fe–S clusters daily required/destroyed per single mitochondrion.

	Type	*Number*
Clusters disassembled/resupplied for Fe–S-dependent proteins	[2Fe–2S]	2584
	[4Fe–4S]	5638
Auxiliary clusters sacrificed by LIP1	[4Fe–4S]	1083
Auxiliary clusters sacrificed by BIO2	[2Fe–2S]	?

Estimated number of [2Fe–2S] and [4Fe–4S] clusters that are consumed in a single Arabidopsis mitochondrion per day. The calculation is based on the abundance and turnover rate of proteins containing Fe–S clusters or the turnover of lipoyl-containing proteins to estimate the clusters sacrificed by LIP1. The lack of knowledge of the abundance and turnover of biotinylated proteins does not allow us to estimate the activity of BIO2.

We also highlight two mitochondrial enzymes BIO2 and LIP1, which use Fe–S cluster as a sulfur source. Both enzymes belong to the radical SAM superfamily and sacrifice an auxiliary cluster to extract sulfur atoms to synthesise biotin and lipoic acid (see Chapter 1.8). This catalytic activity results in the destruction of their auxiliary clusters. To date, there is no established *in vivo* repair mechanism for the remains of these clusters, which may release free iron and sulfide. We thus estimate the number of clusters destroyed by LIP1 per day considering the turnover of lipoylated proteins. On the contrary, the lack of knowledge of the abundance and turnover of biotinylated proteins does not allow us to estimate the activity of BIO2. Hence, we calculate that another 1,000 auxiliary [4Fe–4S] clusters may be destroyed each day solely by LIP1 activity (Table 2.1).

Combining the approximated number of clusters released by Fe–S protein turnover, the number of sacrificed auxiliary clusters and the turnover of the lipoylated proteins, we estimate that every day, more than 31,000 sulfur atoms are set free in a single mitochondrion, of which 6% could be attributed to LIP1 alone (Table 2.2).

Table 2.2 | Sulfide release due to Fe–S cluster turnover in a single mitochondrion per day.

Source	*S^{2-} atoms*	
Fe–S-containing proteins turnover	28,896	86%
LA-dependent proteins turnover	2,301	7%
LIP1 activity	2,166	6%
BIO2 activity	?	?

Estimated sulfide ions daily released in a single Arabidopsis mitochondrion from Fe–S cluster turnover. The calculation is based on Table 2.1, with the addition of the lipoyl (LA)-dependent protein turnover

Those estimations are rather speculative, nevertheless the release of sulfide by Fe–S cluster turnover or as a toxic by-product of cofactor biosynthesis highlights the need for local sulfide detoxification systems in mitochondria.

In the last section of the review, we focus on the scavenging mechanisms of sulfide originating from Fe–S clusters. We explore the current hypotheses on the repair of clusters, highlighting the lack of *in vivo* evidence, especially for the plant kingdom. In particular, we introduce NFU (NifU-like) as a potential protein that not only delivers [4Fe–4S] cluster to LIP1 but could also repair the auxiliary cluster after extraction of two sulfur atoms for lipoyl biosynthesis. We then discuss the issue of free sulfide toxicity and its detoxification system in plant mitochondria. To date, the only known mechanism for scavenging sulfide in Arabidopsis is through the biosynthesis of cysteine via the cysteine synthase complex (CSC). Both aspects, cluster repair by NFU and sulfide detoxification by CSC, are investigated in detail in the work described in Chapter 5 and the corresponding manuscript (Pedroletti *et al.*, 2023b).

My personal contribution to this review paper included the writing of the manuscript draft, the bibliographic research and the generation of all figures. I contributed especially to the sections “Assembly and transfer of Fe–S clusters in mitochondria” and “The fate of mitochondrial Fe–S clusters” and I was involved in the entire revision process.

2.2 | Manuscript

Attached on the following pages is the manuscript published in the *Journal of Experimental Botany (doi: 10.1093/jxb/erad062)*.

SOCIETY FOR EXPERIMENTAL BIOLOGY

Journal of Experimental Botany
https://doi.org/10.1093/jxb/erad062 Advance Access Publication 27 February, 2023

REVIEW PAPER

Assembly, transfer, and fate of mitochondrial iron–sulfur clusters

Luca Pedroletti, Anna Moseler and Andreas J. Meyer*

INRES-Chemical Signalling, University of Bonn, Friedrich-Ebert-Allee 144, D-53113 Bonn, Germany
* Correspondence: andreas.meyer@uni-bonn.de

Received 9 December 2022; Editorial decision 7 February 2023; Accepted 13 February 2023

Editor: Hideki Takahashi, Michigan State University, USA

Abstract

Since the discovery of an autonomous iron–sulfur cluster (Fe–S) assembly machinery in mitochondria, significant efforts to examine the nature of this process have been made. The assembly of Fe–S clusters occurs in two distinct steps with the initial synthesis of [2Fe–2S] clusters by a first machinery followed by a subsequent assembly into [4Fe–4S] clusters by a second machinery. Despite this knowledge, we still have only a rudimentary understanding of how Fe–S clusters are transferred and distributed among their respective apoproteins. In particular, demand created by continuous protein turnover and the sacrificial destruction of clusters for synthesis of biotin and lipoic acid reveal possible bottlenecks in the supply chain of Fe–S clusters. Taking available information from other species into consideration, this review explores the mitochondrial assembly machinery of Arabidopsis and provides current knowledge about the respective transfer steps to apoproteins. Furthermore, this review highlights biotin synthase and lipoyl synthase, which both utilize Fe–S clusters as a sulfur source. After extraction of sulfur atoms from these clusters, the remains of the clusters probably fall apart, releasing sulfide as a highly toxic by-product. Immediate refixation through local cysteine biosynthesis is therefore an essential salvage pathway and emphasizes the physiological need for cysteine biosynthesis in plant mitochondria.

Keywords: Biotin synthase, dehydrogenase complexes, glutaredoxin S15, iron–sulfur cluster, lipoic acid, lipoyl synthase, mitochondria, respiratory electron transport chain, sulfide.

Introduction

Iron–sulfur (Fe–S) clusters are essential cofactors of many proteins involved in electron transfer reactions in the photosynthetic and respiratory electron transport chains (ETCs) or of enzymes involved in metabolic activities and biosynthetic processes. Moreover, Fe–S-dependent enzymes play a role in multiple processes involved in nucleotide metabolism and DNA synthesis, DNA repair, and regulation of gene expression. Enzymes containing Fe–S clusters are present in the cytosol and the nucleus, as well as in plastids and mitochondria (Fig. 1A) (Balk and Schaedler, 2014; Przybyla-Toscano *et al.*, 2021a). The presence of Fe–S clusters in aerobic and anaerobic archaea, bacteria, and eukaryotes as well as their requirement for fundamental metabolism indicates that these clusters were probably integrated into central metabolic pathways early in the evolution of life, where iron sulfide is considered the most geochemically plausible source of reducing power for the early evolution of life in an 'Fe–S World' (Wächtershäuser, 1992; Garcia *et al.*, 2022). In free form, Fe–S clusters are inherently

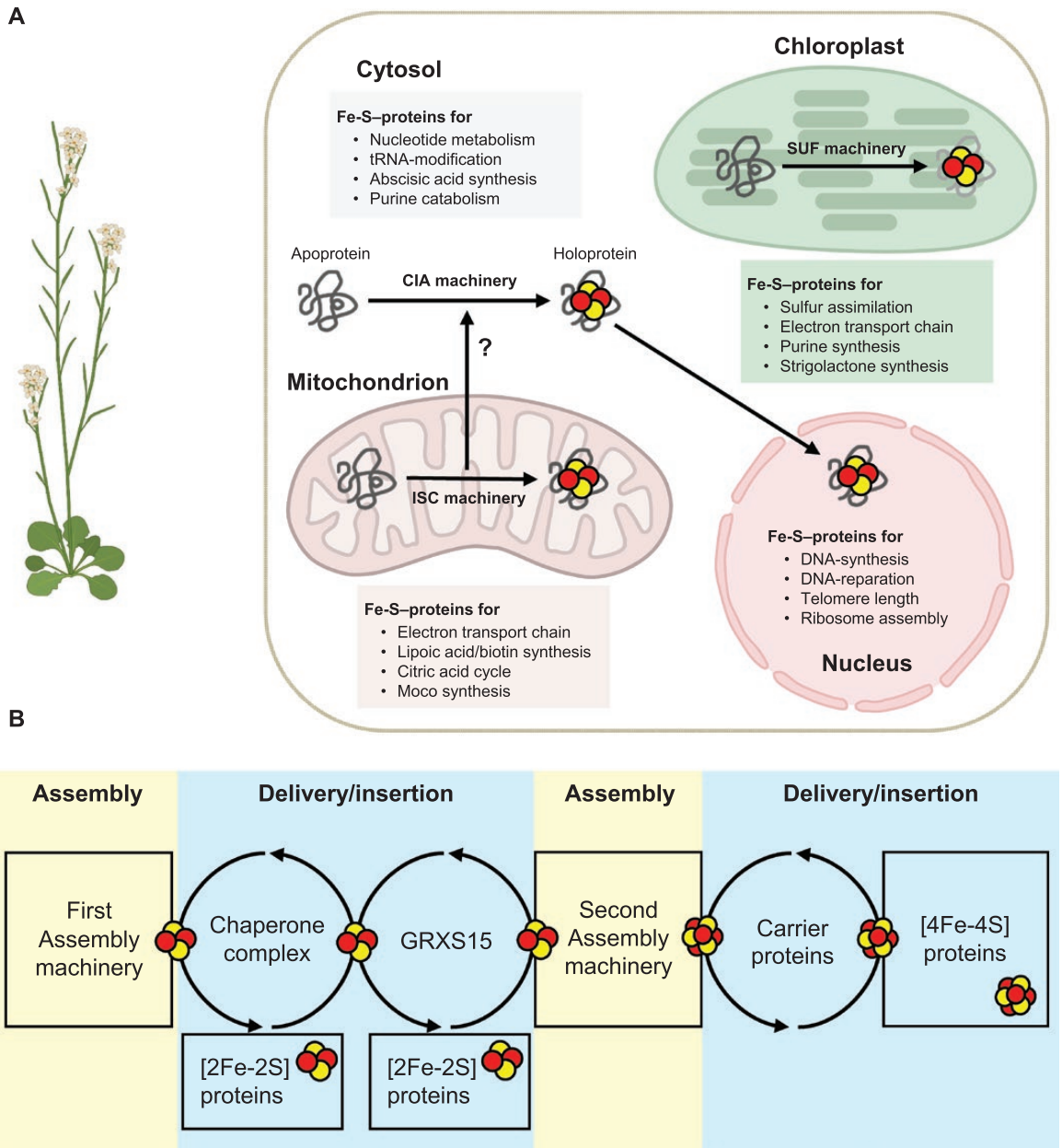

Fig. 1. Fe–S cluster assembly machineries in plants. (A) The mitochondrial iron–sulfur cluster (ISC) machinery and the plastidic sulfur mobilization (SUF) machinery are autonomous pathways, while the cytosolic iron–sulfur protein assembly (CIA) machinery depends on an unknown sulfur compound exported from mitochondria. Fe–S proteins are localized in mitochondria, plastids, cytosol, and the nucleus. The Arabidopsis image is created with BioRender (https://biorender.com). (B) Simplified scheme of assembly and transfer of [2Fe–2S] and [4Fe–4S] clusters in plant mitochondria. Yellow boxes represent the two stages for assembly of [2Fe–2S] and [4Fe–4S] clusters. Blue boxes represent the transfer systems made up of a chaperone complex and GRXS15, which specifically deliver/insert the [2Fe–2S] cluster into apoproteins, and several dedicated carrier proteins (syn. assembly factors, shuttle proteins, maturation factors), which deliver/insert [4Fe–4S] clusters into the respective apoproteins.

instable as they are highly susceptible to oxidation by molecular oxygen (O_2), reactive oxygen species (ROS), and reactive nitrogen species such as nitric oxide (NO). Superoxide (O_2^-) and H_2O_2 in particular can lead to damage and disintegration of clusters (Imlay, 2013). For all aerobic organisms it is thus mandatory to protect Fe–S clusters at all times through tight coordination by proteins that protect the clusters from solvent exposure. For this reason, Fe–S clusters also cannot be transported across membranes and need to be synthesized separately in all compartments with the iron–sulfur cluster (ISC) machinery in mitochondria, the sulfur mobilization (SUF) machinery in plastids, and the cytosolic iron–sulfur protein assembly (CIA) machinery in the cytosol (Fig. 1A) (Balk and Pilon, 2011). An exception is the nucleus to which folded

proteins containing their cofactors can be imported through the nuclear pores. The CIA machinery, however, depends on the mitochondrial ISC machinery as it relies on the export of an unknown sulfur compound transported by the ABC transporter AtATM3 in Arabidopsis or the orthologous ScATM1 in *Saccharomyces cerevisiae* in a glutathione-dependent manner (Schaedler *et al.*, 2014; Lill *et al.*, 2015). Recent results based on *in vitro* studies and computational modulations suggest that the fungal transporter CtATM1 is able to export a glutathione-coordinated [2Fe–2S] cluster (P. Li *et al.*, 2022), but *in vivo* evidence for this model is lacking.

Fe–S clusters exist in different forms, with the rhombic [2Fe–2S] and cubic [4Fe–4S] clusters being the most frequent (Beinert, 2000). In all cases, the primary assembly machineries build [2Fe–2S] clusters, which may be delivered to the respective target proteins or, alternatively, to a second machinery for assembly of higher order [4Fe–4S] clusters (Braymer *et al.*, 2021). Key proteins for protection of [2Fe–2S] clusters during delivery and transfer are monothiol glutaredoxins (GRXs), which are characterized by their CGFS (Cys–Gly–Phe–Ser) active site motif and an additional five amino acid insertion preceding this motif (Rodríguez-Manzaneque *et al.*, 2002; Trnka *et al.*, 2020). The resulting extended loop together with the active site glycine separate these specific GRXs from bona fide redox-active GRXs. Repositioning of the active site cysteine resulting from these structural differences diminishes redox activity and fosters coordination of a [2Fe–2S] cluster in a dimeric complex consisting of two GRXs, two molecules of the cofactor reduced glutathione (GSH), and one [2Fe–2S] cluster (Johansson *et al.*, 2010; Liedgens *et al.*, 2020; Trnka *et al.*, 2020).

While plastids contain multiple monothiol GRX isoforms, plant mitochondria contain only GRXS15 and thus have been proven to be accessible to genetic modification of the transfer machinery (Moseler *et al.*, 2015; Ströher *et al.*, 2016). The respective modifications together with alteration of elements of the [4Fe–4S] cluster assembly machinery have generated new insight into the flux of Fe–S clusters to different target proteins. In this review, we summarize current knowledge about the assembly machineries for [2Fe–2S] and [4Fe–4S] clusters, the transfer and distribution of clusters between different target proteins, and the turnover of Fe–S clusters with emphasis on plant mitochondria.

Assembly and transfer of Fe–S clusters in mitochondria

The first assembly machinery for [2Fe–2S] clusters

The central function of the assembly machinery is to mobilize Fe and S atoms, to assemble them into an Fe–S cluster, and to transfer the cluster to their respective apoproteins. Despite the chemical simplicity of Fe–S clusters, their biosynthesis is rather complex. Two highly conserved assembly machineries can be distinguished: the first assembly machinery for the generation of [2Fe–2S] clusters and the second assembly machinery for [4Fe–4S] clusters (Fig. 1B). In general, the first assembly complex in Arabidopsis consists of the cysteine desulfurase AtNFS1, the accessory LYRM (Leu–Tyr–Arg motif) protein AtISD11, frataxin (AtFH), and the scaffold protein AtISU (Fig. 2). Protein–protein interactions between Arabidopsis AtNFS1 and AtISD11 as well as AtNFS1 and AtFH were confirmed via pull-down assays and modelled interaction studies (Turowski *et al.*, 2012; Armas *et al.*, 2020). In yeast, it was also shown that the acyl carrier protein 1 (ScACP1) interacts with the ScNFS1–ScISD11 complex, thereby promoting the stabilization of the complex (Van Vranken *et al.*, 2016). In Arabidopsis, three mitochondrial isoforms AtACP1–AtACP3 are present and may exhibit conserved functions (Fu *et al.*, 2020); however, so far, no experimental evidence for interaction with other proteins in the first assembly machinery exists.

In a first step, the sulfur is mobilized by the class I cysteine desulfurase AtNFS1. This pyridoxal-5′-phosphate-dependent enzyme subtracts the sulfur from cysteine to form a persulfide on its catalytic cysteine while leaving alanine as a by-product (Turowski *et al.*, 2012). The persulfide is then transferred from the AtNFS1 active site through the movement of a flexible loop to AtISU for assembly of the [2Fe–2S] cluster (Marinoni *et al.*, 2012). Failure to isolate homozygous null mutants in Arabidopsis indicates mitochondrial AtNFS1 as an essential protein (Frazzon *et al.*, 2007; Fonseca *et al.*, 2020), but the exact developmental stage of lethality was not shown. The vital importance of AtNFS1 is in accordance with findings from orthologues in other organisms, where deletion of yeast ScNFS1 (Li *et al.*, 1999) or *Azotobacter vinelandii* AvIscS (Zheng *et al.*, 1998) is lethal. Similar to mitochondrial *nfs1*, no viable null mutants of the plastidic cysteine desulfurase (AtNFS2) can be isolated (Van Hoewyk *et al.*, 2007), indicating that sulfur mobilization by these cysteine desulfurases is essential in both organelles. Arabidopsis knockdown mutants of AtNFS1 show reduced root growth and chlorotic spots on the leaves and a bushy phenotype (Frazzon *et al.*, 2007; Fonseca *et al.*, 2020). Activities of the mitochondrial Fe–S proteins aconitase (ACO) and succinate dehydrogenase (SDH) were 25–40% decreased in *nfs1* knockdown lines compared with wild-type plants and 30–50% higher in *AtNFS1* overexpression lines (Armas *et al.*, 2019). Furthermore, in the knockdown lines, the activity of cytosolic aldehyde oxidases (AtAOs), which contain an FAD, a molybdenum cofactor (Moco), and two [2Fe–2S] clusters, is decreased (Frazzon *et al.*, 2007). Because the two [2Fe–2S] clusters in this case are provided by the cytosolic CIA machinery (Fig. 1A), Moco is probably the link to the mitochondrial ISC machinery. If the ISC machinery is compromised, Moco abundance may decrease because its precursor cyclic pyranopterin monophosphate (cPMP) is synthesized in the mitochondrial matrix by the [4Fe–4S]-dependent AtCNX2 (cofactor of nitrate reductase and xanthine dehydrogenase 2) and the cPMP synthase AtCNX3. cPMP is then exported to

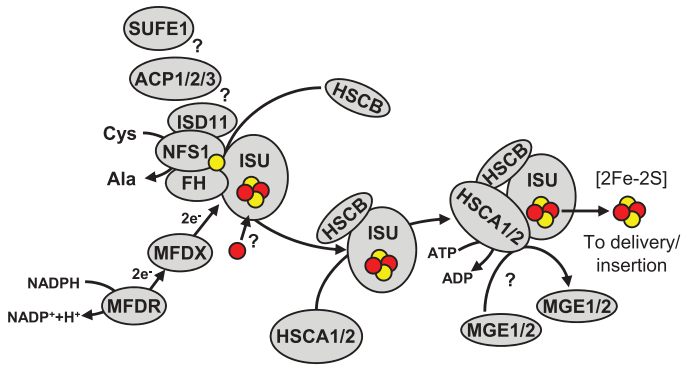

Fig. 2. The machineries for assembly and transfer of [2Fe–2S] clusters in *Arabidopsis thaliana*. ISD11 (ISC biogenesis desulfurase-interacting protein of 11 kDa) and FH (frataxin homologue) stabilize NFS1 (cysteine desulfurase), which provides the sulfur atoms (yellow circles) from cysteine desulfurization. The electrons are supplied by MFDX1/2 (mitochondrial ferredoxin—here simply depicted as MFDX without its [2Fe–2S] cluster) and MFDR (mitochondrial ferredoxin reductase), which uses NADPH as its electron donor. The [2Fe–2S] cluster is assembled on the scaffold proteins ISU1/2/3 (Iscu-like—here for simplification shown as ISU). The mode of iron supply (Fe^{2+}: red circles) is not fully resolved. Similarly, it is unclear whether SUFE1 (SufE-like 1) and ACPs (acyl carrier proteins) play a role in the assembly of [2Fe–2S] clusters in plants. After assembly, the scaffold protein ISU carrying the [2Fe–2S] cluster is detached from the assembly machinery by the co-chaperone HSCB (heat shock protein B), which subsequently also recruits the HSCA1/2 chaperones (heat shock protein A) to form a complex for delivery of the cluster. HSCB and hypothetically MGE1/2 (mitochondrial GRPEs) stimulate ATP/ADP exchange activity of HSCAs, leading to a conformational change between HSCAs and ISUs that favours the release of the [2Fe–2S] cluster to the next acceptor protein.

the cytosol for subsequent biosynthetic steps (Bittner, 2014; Kruse *et al.*, 2018). It is noteworthy that, in yeast, ScNFS1 has also been implicated as being the sulfur source of the CIA machinery, and thus essential for the maturation of cytosolic and nuclear Fe–S proteins (Mühlenhoff *et al.*, 2004). Thus, the AtAO activity in Arabidopsis *nfs1* knockdown lines might be affected by the decreased availability of both Moco and the Fe–S cluster.

Both AtNFS1 interaction partners, AtFH and AtISD11, increase the catalytic efficiency of NFS1 (Turowski *et al.*, 2012; Armas *et al.*, 2020). This positive effect on AtNFS1 activity indicates that both proteins act as AtNFS1 regulators (Fig. 2). For human frataxin, it was shown that the protein is not required for the formation of the persulfide on *Homo sapiens* HsNFS1 itself, but that it accelerates the sulfane sulfur (S^0) transfer from HsNFS1 to HsISCU (Parent *et al.*, 2015; Gervason *et al.*, 2019). Furthermore, yeast ScNFS1 is prone to aggregation in the absence of ScISD11, implying a stabilizing effect of ScISD11 (Adam *et al.*, 2006). In Arabidopsis, an *fh* null mutant is embryo lethal, while knockdown lines showed a decreased activity of Fe–S proteins such as ACO or SDH, emphasizing the important role of AtFH in the assembly machinery (Busi *et al.*, 2006; Vazzola *et al.*, 2007). No Arabidopsis mutants are characterized yet, but AtISD11 was shown to be able to complement the growth defect of the respective yeast mutant (Ivanova *et al.*, 2019). Another protein that might interact with AtNFS1 and thereby stimulate the cysteine desulfurase activity is sulfur E (AtSUFE1) (Fig. 2). Although it was shown that the respective green fluorescent protein (GFP) fusion protein is dual localized to plastids and mitochondria (Xu and Møller, 2006; Woo *et al.*, 2022), its low abundance or even absence in the mitochondrial proteome sparked a debate about the localization, and thus potential interaction with AtNFS1 (Taylor *et al.*, 2011; Fuchs *et al.*, 2020). Nevertheless, it was shown that AtSUFE1 can interact with AtNFS1 via bimolecular fluorescence complementation (BiFC) *in planta* and AtSUFE1 stimulates the AtNFS1 activity *in vitro* (Xu and Møller, 2006). The most compelling fact supporting a mitochondrial function of AtSUFE1 is that the lethality of a null mutant cannot be rescued by AtSUFE1 that is solely targeted to chloroplasts (Xu and Møller, 2006).

The transferred sulfur atom of AtNFS1 is S^0 and, consequently, the sulfur needs to be reduced to sulfide (S^{2-}) prior to the Fe–S cluster assembly. In yeast and humans, electrons are provided through a short electron supply chain consisting of a ferredoxin (FDX) and its NADPH-dependent FDX reductase (FDR) (Webert *et al.*, 2014). In plants, no direct evidence for the involvement of mitochondrial ferredoxins AtMFDX1 and AtMFDX2 or the respective reductase AtMFDR in S^0 reduction exists (Takubo *et al.*, 2003). AtMFDX1 was found in screens for genes required for the development of male and female gametophytes, indicating that the protein is essential (Pagnussat *et al.*, 2005; Boavida *et al.*, 2009).

The scaffold protein AtISU exists with three isoforms in Arabidopsis mitochondria, namely AtISU1–AtISU3 (Léon *et al.*, 2005). Knockdown lines phenocopy the *nfs1* mutant, showing a reduced growth and bushy phenotype (Frazzon *et al.*, 2007). Gene expression analysis showed that AtISU1, in contrast to the other isoforms, has the highest expression during vegetative growth, which might explain why only AtISU1 is found in the mitochondrial proteome from a heterotrophic Arabidopsis culture (Frazzon *et al.*, 2007; Fuchs *et al.*, 2020). All three isoforms, however, are able to complement the respective yeast mutant *Δisu1* (Léon *et al.*, 2005). The source of iron is unclear so far, but for the mouse homologue MmISCU it was shown that it can bind Fe^{2+} upon removal of a Zn^{2+} ion (Gervason *et al.*, 2019). ISCU employs two Cys residues, an Asp residue, and a His residue for coordinating the Fe^{2+} atom (Srour *et al.*, 2022). These residues are strictly conserved in other orthologues, which indicates a highly conserved process in general. Furthermore, it was shown that iron binding of MmISCU is a prerequisite for the formation of an Fe–S cluster in the presence of the NFS1–ISD11–ACP complex as well as the electron supply chain consisting of MmFDX2, MmFDXR, and NADPH (Fig. 2) and stoichiometric amounts of cysteine (Gervason *et al.*, 2019).

The release of the [2Fe–2S] cluster from the first assembly machinery

The newly formed [2Fe–2S] cluster needs to be delivered from the first machinery scaffold protein ISU to the respective apoproteins or to the second assembly machinery for the generation of a [4Fe–4S] cluster (Figs 1B, 2). Various studies in yeast and bacteria have proposed that the release of the cluster from the scaffold protein ScISU1 is assisted by a dedicated chaperone system involving HSP70-type proteins and a J-type co-chaperone (Dutkiewicz *et al.*, 2003; Cupp-Vickery *et al.*, 2004; Braymer *et al.*, 2021). In yeast, it was shown that the binding site of the cysteine desulfurase and the frataxin homologue on the scaffold protein ScISU1 is the same as for the chaperone system. This implies that after assembly of a [2Fe–2S] cluster the chaperone system competes with proteins of the assembly machinery and ultimately detaches the scaffold protein containing the new [2Fe–2S] cluster from the assembly machinery (Majewska *et al.*, 2013; Manicki *et al.*, 2014).

In plants, the first proteins taking care of the nascent cluster are the chaperones AtHSCA1 and AtHSCA2 (orthologues of the yeast ScSSQ1 and bacterial EcHscA) in cooperation with the co-chaperone AtHSCB (orthologue of the yeast ScJAC1 and bacterial EcHscB). It was shown by yeast two-hybrid (Y2H) and BiFC assays that AtHSCB interacts with AtISU1 (Xu *et al.*, 2009). In addition, the *hscB* mutant had a strongly decreased activity of the Fe–S cluster-dependent enzymes ACO and SDH (Xu *et al.*, 2009). In Arabidopsis, AtHSCA2 interacts with the AtISU1–AtHSCB complex, which synergistically stimulates the ATPase activity of AtHSCA2 (Xu *et al.*, 2009; Leaden *et al.*, 2014). In *Escherichia coli*, ATP hydrolysis leads to a conformational change of EcIscU that decreases the affinity for the bound [2Fe–2S] cluster and thus facilitates its dissociation (Bonomi *et al.*, 2008). A second co-chaperone was identified in yeast, with the nucleotide exchange factor ScMGE1 forming a complex with the chaperone ScSSQ1 and thereby promoting the ATP/ADP exchange on ScHSP70 (Schmidt *et al.*, 2001; Karri *et al.*, 2019). Arabidopsis possesses two homologues of ScMGE1, identified as AtMGE1 and AtMGE2 (Hu *et al.*, 2012), but evidence for direct interaction with the HSP70-type protein is still lacking (Fig. 2).

Transfer of the [2Fe–2S] cluster to complexes in the electron transport chain, glutaredoxin S15, and biotin synthase

The respiratory ETC contains several subunits in complexes I, II, and III that require Fe–S clusters for their function in electron transfer (Fig. 3). In mammals, it was proposed that the co-chaperone scaffold HsHSC20/HsHSC70/HsISCU (orthologous to AtHSCA1/AtHSCB/AtISU1 in Arabidopsis) acts as a single adaptable complex able to deliver the [2Fe–2S] cluster directly to complexes I–III based on the interaction with carrier proteins of the LYRM family, which recruit the scaffold complex and selectively guide it to the respective ETC subunit (Maio *et al.*, 2017) (Fig. 3). Recent studies have identified the plant-specific LYRM protein AtCIAF1 (complex I assembly factor 1) as an essential factor for complex I assembly. AtCIAF1 is assumed to interact with the subunit TYKY in the matrix arm of complex I and has been proposed to play a role in delivery of [2Fe–2S] to this subunit (Ivanova *et al.*, 2019; López-López *et al.*, 2022) (Fig. 3). How this [2Fe–2S] cluster is ultimately converted to a [4Fe–4S] cluster and finally inserted into the TYKY subunit remains unknown. Also for complex II, an LYRM-protein named AtSDHAF1 (SDH assembly factor 1) was identified for insertion of the [2Fe–2S] cluster (Li *et al.*, 2022). The plant SDH is composed of two membrane subunits (SDH3 and SDH4), which bind the catalytic subunits SDH1 with the coenzyme FAD, and SDH2, which coordinates three Fe–S clusters ([2Fe–2S], [3Fe–4S], and [4Fe–4S]) (Meyer *et al.*, 2019) (Fig. 3). For complex III, it was found that the human HsLYRM7 (orthologue of Arabidopsis AtLYRM7) directly binds the co-chaperone HsHSC20 on its LYRM motif. HsLYRM7 then guides the co-chaperone/scaffold to the subunit HsUQCRFS1, the Rieske Fe–S protein of complex III (Maio *et al.*, 2017). So far, no evidence for physical interaction of AtLYRM7 and AtHSCB in Arabidopsis has been reported, but a strong transcriptional co-regulation was observed for the respective genes (Przybyla-Toscano *et al.*, 2021b) (Fig. 3). Overall, it is generally accepted that the LYRM proteins guide the scaffold system to the ETC complexes for insertion of [2Fe–2S] clusters, but the transfer of the other types of Fe–S clusters is largely unresolved. For the human transfer system, Maio *et al.* (2016) proposed that a second holo-ISCU/HSC20/HSPA9 complex binds the subunit HsSDH2. The two co-chaperone/scaffold complexes brought into close proximity may then lead to the spontaneous assembly of a [4Fe–4S]. A more likely supply route for [4Fe–4S] clusters for complex I is via an iron–sulfur protein required for NADH dehydrogenase (AtINDH; in human: HsINT1, Fig. 3) (Wydro *et al.*, 2013).

The co-chaperone/scaffold complex can also transfer the [2Fe–2S] cluster to mitochondrial GRXs. Such direct transfer of a [2Fe–2S] cluster from the shuttle complex to ScGRX5 has been shown in yeast (Uzarska *et al.*, 2013). Although no direct evidence exists, the high degree of evolutionary conservation strongly suggests that this mechanism is maintained in human mitochondria with glutaredoxin HsGRLX5 (Lill and Freibert, 2020) and in plants with AtGRXS15 (Moseler *et al.*, 2015). Based on detailed characterization of the chaperoning system in human mitochondria, it is assumed that in Arabidopsis the co-chaperone AtHSCB guides ISU to the chaperone AtHSCA (isoforms 1 and 2) and stimulates its ATPase activity, which induces a tighter binding on AtISU. While AtHSCB is released, the homodimer AtGRXS15 binds AtHSCA and exchanges the cluster with AtISU. AtMGE1 is then assumed to be involved in loading and releasing the GRXS15–[2Fe–2S]–GRXS15 homodimer (Hu *et al.*, 2012).

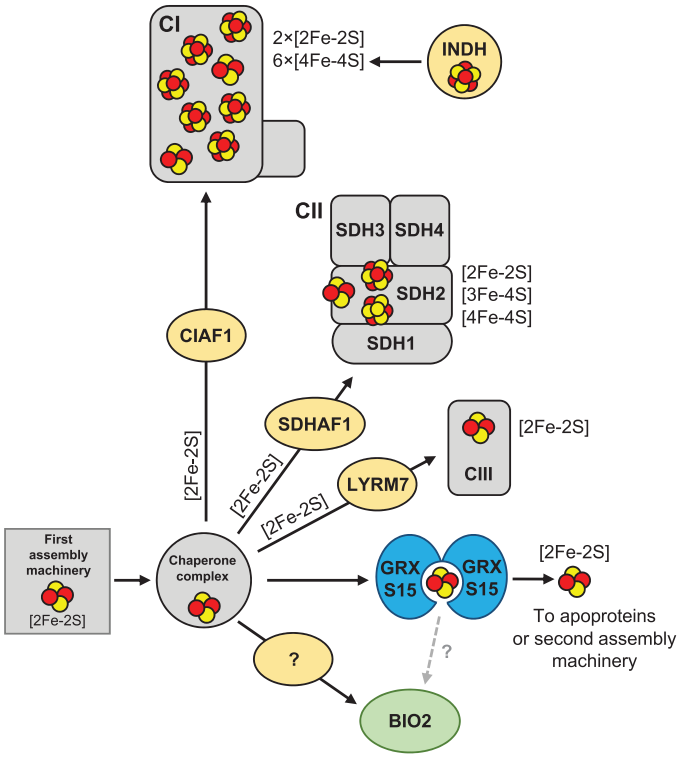

Fig. 3. Working model for the delivery of [2Fe–2S] clusters in mitochondria of *Arabidopsis thaliana*. [2Fe–2S] clusters are transferred from the first assembly machinery to the ETC complexes and the transfer to GRXS15. The [2Fe–2S] cluster built by the first assembly machinery is delivered by a chaperone complex and the carrier proteins CIAF (complex I assembly factor 1), SDHAF1 (SDH assembly factor 1), and LYRM7 (LYR motif protein 7) from the LYRM family to the ETC complexes I–III. The chaperone system can directly transfer the [2Fe–2S] cluster to GRXS15, which will deliver the cluster downstream to the next acceptor proteins. Whether the [2Fe–2S] cluster for biotin synthase 2 (BIO2) is directly inserted by the chaperone complex, by GRXS15, or via another dedicated carrier protein is still unknown (for more details, see the main text).

Another soluble Fe–S-dependent protein that contains a [2Fe–2S] cluster is biotin synthase (BIO2; in bacteria: BioB) (Sanyal *et al.*, 1994; Ugulava *et al.*, 2001). For AtBIO2 it is not clear though whether it receives its [2Fe–2S] cluster directly from the chaperone/co-chaperone complex or via AtGRXS15 and whether any additional carrier proteins might be involved in the transfer step (Fig. 3). These two possibilities and incorporation of an additional [4Fe–4S] cluster will be assessed in more detail later (see section 'LIP1 and BIO2 use Fe–S clusters as sulfur source').

Delivery of [2Fe–2S] clusters to the second machinery for assembly of [4Fe–4S] clusters

The assembly of [4Fe–4S] clusters requires a dedicated second assembly machinery that uses [2Fe–2S] clusters delivered by AtGRXS15 as building blocks. In Arabidopsis mitochondria, the core of the second assembly machinery consists of AtISCA1a/b, AtISCA2, and AtIBA57 (Fig. 4). All three AtISCAs have been experimentally confirmed to directly interact with AtGRXS15 (Azam *et al.*, 2020a). Similar to the yeast and human systems, AtISCA1a or AtISCA1b, respectively, can form heterodimers with AtISCA2, with both subunits contributing a [2Fe–2S] cluster (Mühlenhoff *et al.*, 2011; Brancaccio *et al.*, 2014; Azam *et al.*, 2020a). In all cases, two [2Fe–2S] clusters are being provided by the respective GRXs to the two ISCA proteins in the complex (Banci *et al.*, 2014). While a detailed mechanistic understanding of the exact steps in [4Fe–4S] assembly is still lacking, the presence of homologous proteins for all participating proteins in yeast and human together with strict conservation of functional domains allows a homology model to be drawn for [4Fe–4S] cluster assembly in plants (Azam *et al.*, 2020a). After binding a [2Fe–2S] cluster, HsISCA2 is assumed to bind HsIBA57 (Gourdoupis *et al.*, 2018). Whether binding of HsIBA57 to HsISCA2 occurs before or after binding the [2Fe–2S]-loaded ISCA1 is not clear at this point. The role of HsIBA57 in this process is mediating electron transfer from FDX for the reductive fusion of two [2Fe–2S] clusters to one [4Fe–4S] cluster on the ISCA1–ISCA2 heterodimer (Weiler *et al.*, 2020). The electrons for this reductive assembly are ultimately provided by NADPH through the FDR–FDX cascade. While in human mitochondria the electron transfer is mediated specifically by HsFDX2 (Schulz *et al.*, 2023), no information on isoform-specific functions is available for Arabidopsis MFDXs.

ISCAs may not be the exclusive interactors of GRXS15. In fact, it was shown by both Y2H and BiFC assays that Arabidopsis monothiol GRXs can interact with BOLA family proteins (Couturier *et al.*, 2014). However, in the literature there is conflicting information regarding the actual role of such heterodimers. Yeast ScBOLA1 and ScBOLA3 can form heterodimers with both ScGRX5 and ScNFU1, and have been proposed to act as carrier proteins for [4Fe–4S]-dependent proteins (Uzarska *et al.*, 2016). Human HsBOLA1 and HsBOLA3 instead form heterodimers with HsGRX5 and coordinate a [2Fe–2S] cluster in either the reduced, Rieske-type $[2Fe–2S]^{1+}$ form for HsBOLA1–HsGLRX5, or the oxidized, ferredoxin-like $[2Fe–2S]^{2+}$ form in the HsBOLA3–HsGLRX5 complex (Nasta *et al.*, 2017). In an alternative model for [4Fe–4S] cluster assembly, two HsGLRX5–HsBOLA3 heterodimers transfer two [2Fe–2S] clusters to HsNFU1, which is able to assemble a [4Fe–4S] cluster (Nasta *et al.*, 2020). In Arabidopsis, it was shown that BOLA4, and possibly also BOLA1, interacts with GRXS15. However, whether these heterodimers act as carrier proteins or as a delivery system to specific Fe–S-dependent proteins is still to be clarified. It is noteworthy that AtSUFE1 also contains a BOLA domain and it was shown by Y2H assay that GRXS15 can interact with this domain (Couturier *et al.*, 2014).

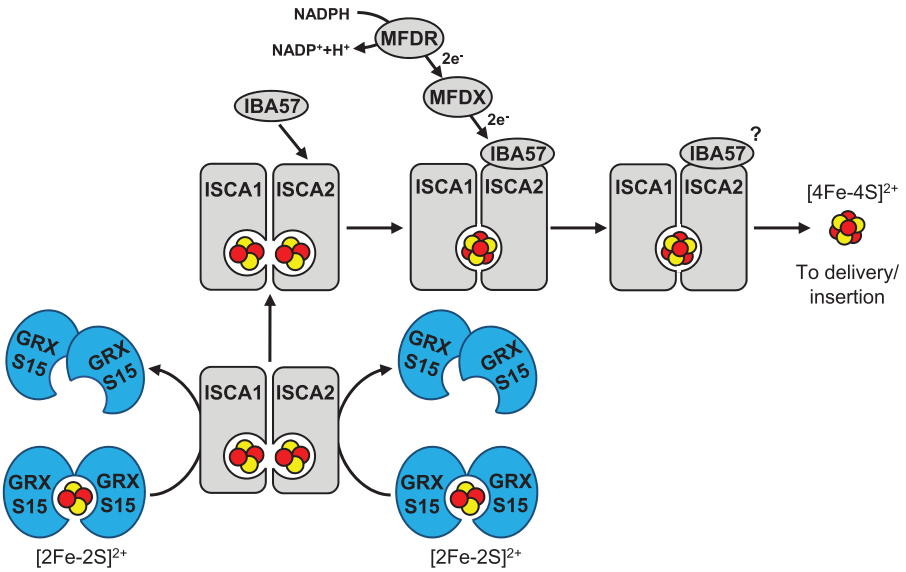

Fig. 4. The machinery for assembly of [4Fe–4S] clusters in *Arabidopsis thaliana*. GRXS15 directly transfers two [2Fe–2S] clusters to the ISCA (iron–sulfur cluster A-type carrier) proteins, but, despite several models, the precise molecular mechanism of this transfer remains unclear. The ISCA1–ISCA2 heterodimer coordinates two $[2Fe–2S]^{2+}$ clusters which are brought into close proximity. IBA57 (ISC assembly factor of 57 kDa) interacts with ISCA2 and mediates the electron transfer from the MFDX/MFDR (mitochondrial ferredoxin/ferredoxin reductase) cascade for reductive fusion of the two $[2Fe–2S]^{2+}$ clusters to one $[4Fe–4S]^{2+}$ cluster. The newly built [4Fe–4S] cluster is subsequently delivered to receiving apoproteins or further carrier proteins.

Transfer of newly assembled [4Fe–4S] clusters to apoproteins

After their assembly, the [4Fe–4S] clusters need to be delivered to the respective apoproteins. To date, only a few proteins have been identified as acceptors for [4Fe–4S] clusters from the second assembly machinery for transfer to specific apoproteins (Fig. 5). In Arabidopsis, these are the mitochondrial carrier proteins NifU-like4 (NFU4), NifU-like5 (NFU5) and INDH.

In Arabidopsis, all ISCA isoforms interact with both NFU4 and NFU5, and ISCA1a/2 heterodimers can efficiently transfer reconstituted [4Fe–4S] to both NFU4 and NFU5 *in vitro* (Azam *et al.*, 2020b). Interestingly, it was also observed that ISCA1a/2 and both NFUs are able to transfer [4Fe–4S] clusters to apo-ACO2 (Azam *et al.*, 2020b) while the human ISCA1–ISCA2–IBA57 machinery can transfer [4Fe–4S] clusters to the mitochondrial ACO directly *in vitro* (Weiler *et al.*, 2020). These findings may suggest a non-essential role for NFUs in ACO maturation *in vivo* and highlight the essential role of the mitochondrial FDX- and FDR-dependent supply of electrons. Indeed, in *nfu4 nfu5* Arabidopsis mutants, no decrease in ACO activity was observed (Przybyla-Toscano *et al.*, 2022). Hence, in the absence of *in vivo* evidence for a mechanistic role for NFUs in transferring the [4Fe–4S] cluster to ACOs, it remains an open question whether or not direct transfer of clusters to apoproteins is possible and efficient (Fig. 5). In earlier work, it was found that NFUs are linked to lipoylation in both human and yeast (Navarro-Sastre *et al.*, 2011). This model was recently confirmed in Arabidopsis for the mitochondrial AtNFU4/5 being dedicated carrier proteins for transfer of [4Fe–4S] to lipoyl synthase 1 (AtLIP1) *in vivo* (Przybyla-Toscano *et al.*, 2022).

Another putative carrier protein that might be involved in transfer of [4Fe–4S] clusters is AtINDH, which is essential for assembly of complex I and mitochondrial translation (Wydro *et al.*, 2013). This protein is an orthologue of human HsIND1 and of YlIND1 from the yeast *Yarrowia lipolytica*, which are both able to coordinate a [4Fe–4S] cluster and facilitate the assembly of complex I (Bych *et al.*, 2008; Sheftel *et al.*, 2009). Even though additional work to verify the actual role of AtINDH is needed, the available evidence indicates that INDH may be involved in [4Fe–4S] delivery to complex I in plants.

The distribution of [4Fe–4S] clusters among all recipient apoproteins depends on the relative abundance of these proteins and the efficiency of the intermediate transfer steps. The latter requires detailed kinetic information and knowledge about the interacting proteins, which is rather fragmentary at this point and thus cannot be assessed further. The abundance of recipient proteins spans a large range from >9000 estimated copies of AtACO3 down to only 85 estimated copies of AtLIP1 in a single mitochondrion (Fuchs *et al.*, 2020) (Table 1). Under the parsimonious assumption that efficiencies for the transfer of [4Fe–4S] clusters to the different apoproteins are similar, all individual proteins would have the same probability for receiving a cluster. However, for proteins that require two or more clusters, the probability for achieving their functional state is far lower than for proteins carrying only one cluster. The likelihood for maintaining AtLIP1 activity decreases further if AtLIP1 sacrifices one of the two clusters in

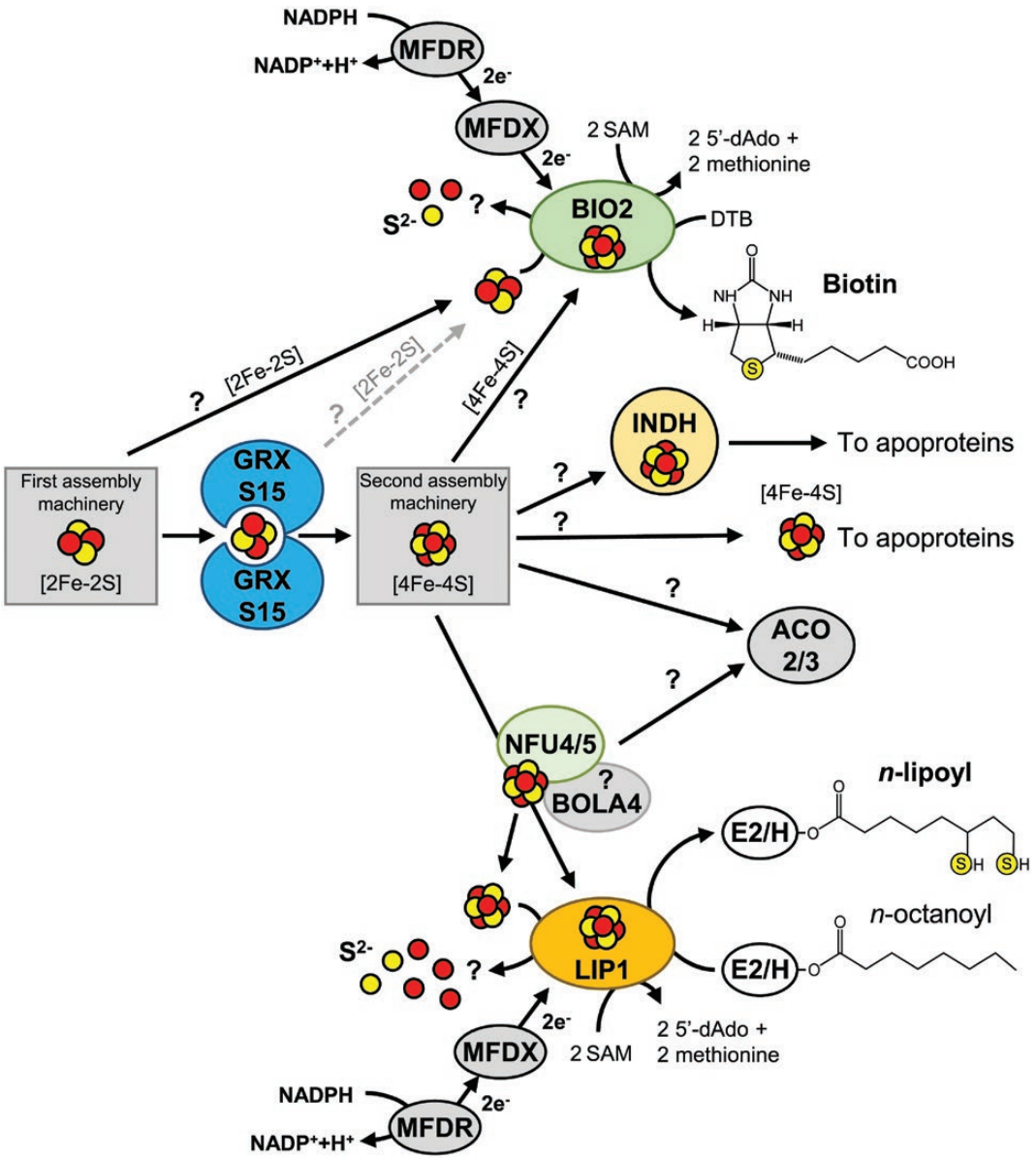

Fig. 5. Hypothetical working model for the delivery and distribution of [4Fe–4S] clusters and sacrifice of auxiliary Fe–S clusters by biotin synthase (BIO2) and lipoyl synthase (LIP1) as a sulfur source in mitochondria of *Arabidopsis thaliana*. The auxiliary [2Fe–2S] and [4Fe–4S] radical–SAM (RS) clusters for BIO2 are provided by the first and second assembly machinery, respectively. The exact modes of transfer are unknown. Transfer of the [2Fe–2S] cluster by GRXS15, however, is unlikely because severe deficiency in GRXS15 activity does not cause detectable defects in biotin synthesis. BIO2 transfers one sulfur atom from the auxiliary cluster to dethiobiotin (DTB) to produce biotin. The electrons for reduction of two molecules of *S*-adenosylmethionine (SAM) are provided through the NADPH/MFDR/MFDX (mitochondrial ferredoxin/ferredoxin reductase) cascade. The auxiliary and RS [4Fe–4S] clusters for LIP1 are both delivered by NFU4/5 (NifU-like proteins). It is still unclear whether BOLA4 or other BOLA proteins assist NFUs in this transfer process. On LIP1, two sulfur atoms are transferred from the auxiliary cluster to the *n*-octanoyl residue of the dehydrogenase subunits E2 or H for its conversion to the *n*-lipoyl prosthetic group. The electrons are provided through the NADPH/MFDR/MFDX cascade. Whether the auxiliary clusters after extraction of sulfur atoms fall apart and release sulfide or whether they can be repaired is not known. After their assembly in the second assembly machinery, the [4Fe–4S] clusters are also supplied to apoproteins either directly (e.g. aconitases ACO2/3) or indirectly via carrier proteins such as INDH (iron–sulfur protein required for NADH dehydrogenase).

each lipoylation reaction, as shown for the bacterial orthologue EcLipA (Lanz and Booker, 2015). For situations of diminished [4Fe–4S] cluster supply in particular, it can be hypothesized that the low-abundant AtLIP1 may very quickly become a severe metabolic bottleneck.

Metabolic consequences of diminished Fe–S cluster supply

The loss of specific mitochondrial Fe–S proteins frequently leads to severe metabolic alterations, ultimately causing

phenotypic effects in growth, development, and stress resilience (Roschzttardtz *et al.*, 2009; Hooks *et al.*, 2014; Kruse *et al.*, 2018). In cases where a mitochondrial Fe–S protein is involved in biosynthetic processes, such as, for example, biosynthesis of the cofactors Moco, biotin, or lipoic acid, loss of the respective proteins is lethal (Patton *et al.*, 1998; Ewald *et al.*, 2014; Kruse *et al.*, 2018). While for most proteins involved in mitochondrial Fe–S cluster assembly and transfer mutant alleles are available, so far only a few of those have been studied for potential metabolic deficiencies. In most cases, the respective null mutants have been characterized only for macroscopically visible growth defects and for embryo lethality to show that the respective proteins are essential (Busi *et al.*, 2006; Frazzon *et al.*, 2007; Balk and Schaedler, 2014). With the isolation and characterization of *grxs15* mutants by Moseler *et al.* (2015) and Ströher *et al.* (2016), the focus has shifted towards mitochondrial metabolism. Embryo-lethal *grxs15* null mutants can be rescued by overexpression of mutated GRXS15$_{K83A}$ to an extent that viable dwarf mutants can be grown under normal growth conditions (Moseler *et al.*, 2015). The K83A mutation removes a residue involved in coordination of the cofactor GSH and used for stabilizing the thiolate form of the active site cysteine of GRXS15. Together, these two effects cause a severely compromised cluster coordination (Moseler *et al.*, 2015;Trnka *et al.*, 2020). Although GRXS15 is an early player in the mitochondrial Fe–S assembly and transfer system, no global metabolic effects could be observed. First, no effect of the GRXS15 deficiency was found for biotin synthesis even though the key enzyme BIO2 contains one [4Fe–4S] cluster and one [2Fe–2S] cluster, the latter of which is continuously sacrificed as a sulfur source in each catalytic cycle (for mechanistic details see the section on the fate of mitochondrial Fe–S clusters below). Thus, BIO2 was expected to have a relatively high demand for Fe–S clusters (Moseler *et al.*, 2021). The absence of any detectable deficiencies in biotin synthesis in *GRXS15*$_{K83A}$ mutants suggests that GRXS15 is not involved in delivery of the [2Fe–2S] cluster to BIO2 and that the cluster might instead be supplied directly from the ISU chaperone complex (Fig. 3). Alternatively, it may also be possible that the large amount of low-active GRXS15$_{K83A}$ in lines overexpressing the mutated protein variant can still provide enough [2Fe–2S] clusters to BIO2. The lack of severe defects in BIO2, however, also indicates that the strong interference with GRXS15-mediated [2Fe–2S] cluster supply to the [4Fe–4S] cluster assembly machinery does not severely limit the supply of [4Fe–4S] clusters to BIO2. Similarly, Moco-dependent proteins such as nitrate reductase, AO, or xanthine dehydrogenase were also not compromised in mutants with decreased GRXS15 activity (Moseler *et al.*, 2021). Furthermore, ACO activity in whole-leaf extracts was also not significantly affected even though the mitochondrial ACOs are among the most abundant [4Fe–4S] proteins in plants (Fuchs *et al.*, 2020) (Table 1). These observations indicated already that a synthetically generated bottleneck in [2Fe–2S] cluster supply to the second assembly machinery may not necessarily affect all [4Fe–4S]-dependent proteins to a similar extent.

By investigating partially complemented null mutants (*GRXS15*$_{K83A}$) or artificial miRNA (amiR)-based knockdown mutants of GRXS15 (*GRXS15*^{amiR}), two groups independently identified specific effects of GRXS15 deficiency in protein lipoylation along with distinct metabolic changes (Moseler et al., 2015, 2021; Ströher *et al.*, 2016). Overall, both *GRXS15*^{amiR} and *GRXS15*$_{K83A}$ mutants accumulate several metabolites, especially pyruvate, 2-oxoglutarate (2-OG), glycine, and branched-chain amino acids, as well as their respective α-ketoacids (Moseler *et al.*, 2021). These metabolites are all substrates of the four mitochondrial dehydrogenase complexes pyruvate dehydrogenase complex (PDC), 2-oxoglutarate dehydrogenase complex (OGDC), glycine decarboxylase complex (GDC), and branched-chain α-keto acid (BCKA) dehydrogenase complex (BCKDC) that all depend on lipoic acid as a prosthetic group attached to dihydrolipoyl acyltransferase (E2 subunit) in PDC, OGDC, and BCKDC, and to the H-protein in GDC, respectively (Taylor *et al.*, 2004; Solmonson and DeBerardinis, 2018).

Similar defects in protein lipoylation were recently also reported for mutants deleted in the carrier proteins AtNFU4 and AtNFU5 (Przybyla-Toscano *et al.*, 2022). The metabolic signature in this case also showed increased levels of glycine, pyruvate, 2-OG, and branched-chain amino acids. In addition, succinate was also increased, which indicates that AtSDH may receive its [4Fe–4S] cluster via AtNFUs. Growth inhibition and early bleaching of *nfu4 nfu5* double mutants can be partially suppressed if photorespiratory activity is largely avoided by growing plants in a high CO_2 atmosphere. This suggests that diminished glycine catabolism in particular, resulting in high glycine levels in mutants with defects in Fe–S cluster transfer, causes deleterious effects.

The fate of mitochondrial Fe–S clusters

Turnover of Fe–S-dependent proteins

As in any other compartment, steady-state levels of mitochondrial proteins are defined by continuous synthesis and degradation. For Fe–S proteins, this implies that the protein-bound clusters are set free and most probably disintegrate due to their inherent instability in the free form. The turnover rates for specific proteins thus have implications for the demand for *de novo* assembled Fe–S clusters and also for the amount of sulfide and iron that is being released. Unfortunately, data for protein abundance and turnover are scarce and thus only a first rough approximation of turnover and the amount of sulfide released in the matrix is possible at this point. For this, we used protein abundance data determined for individual mitochondria isolated from heterotrophic Arabidopsis suspension cultures

Table 1. Overview of mitochondrial Fe–S proteins in Arabidopsis and their turnover with an estimated release of sulfide from the Fe–S clusters.

Protein type and function		AGI code	Protein symbol	Fe–S cluster	S atoms involved	Protein copies (per mitochondrion)	Degradation rates (d^{-1})	Protein degraded (d^{-1} per mitochondrion)	Sulfide released (d^{-1} per mitochondrion)
ETC	CI	At5g08530	51 kDa	[4Fe–4S]	4	6131	0.16	963	3851
		At4g02580	24 kDa	[2Fe–2S]	2	4684	0.10	461	923
		At5g37510	75 kDa	[2Fe–2S], 2×[4Fe–4S]	10	5521	0.14	751	7514
		At1g16700	TYKY	2×[4Fe–4S]	8	120	0.12	14	115
		At1g79010	TYKY isoform	2×[4Fe–4S]	8	2770	0.13	370	2961
		At5g11770	PSST (20 kDa)	[4Fe–4S]	4	3492	0.26	899	3595
	CII	At3g27380	SDH2-1	[2Fe–2S], [3Fe–4S], [4Fe–4S]	10	1003	0.09	87	866
		At5g40650	SDH2-2	[2Fe–2S], [3Fe–4S], [4Fe–4S]	10	3441	0.05	174	1737
		At5g65165	SDH2-3	[2Fe–2S], [3Fe–4S], [4Fe–4S]	10	In seeds only	NA	NA	NA
	CIII	At5g13430	RISP/ UCR1	Rieske [2Fe–2S]	2	6657	0.10	634	1268
		At5g13440	RISP/ UCR1-like	Rieske [2Fe–2S]	2	NA	NA	NA	NA
	ETC associated	At2g43400	ETFQO	[4Fe–4S]	4	313	0.12	38	150
Metabolism	TCA	At4g26970	ACO2	[4Fe–4S]	4	4222	0.07	304	1215
		At2g05710	ACO3	[4Fe–4S]	4	9898	0.09	904	3614
Cofactor synthesis	Radical SAM	At2g43360	BIO2	[4Fe–4S]+auxiliary [2Fe–2S]	4 (+2)	347	NA	NA	NA
		At2g20860	LIP1	[4Fe–4S]+auxiliary [4Fe–4S]	4 (+4)	85	NA	NA	NA
		At2g31955	CNX2	2×[4Fe–4S]	8	219	NA	NA	NA
		At5g63290	HEMN1	[4Fe–4S]	4	38	NA	NA	NA
		At1g75200	TYW1	2×[4Fe–4S]	4 (+4)	474	NA	NA	NA
		At4g05450	MFDX1	[2Fe–2S]	2	73	NA	NA	NA
		At4g21090	MFDX2	[2Fe–2S]	2	494	NA	NA	NA
		At5g23395	MIA40	[2Fe–2S]	2	NA	NA	NA	NA
		At2g35010	TRXo1	[4Fe–4S]	4	837	0.04	33	134
		At5g04140	GLU1	[3Fe–4S]	4	NA	NA	NA	NA
		At2g41220	GLU2	[3Fe–4S]	4	32	NA	NA	NA
		At3g27570	HAA-TLF1	[2Fe–2S]	2	1043	0.23	236	471
		At4g26620	HAA-TLF3	[2Fe–2S]	2	437	NA	NA	NA
		At2g44270	CTU1/ ROL5	[4Fe–4S]	4	NA	NA	NA	NA
		At1g60230	RlmN	[4Fe–4S]	4	NA	NA	NA	NA
		At5g51720	NEET	[2Fe–2S]	2	NA	NA	NA	NA

The copy numbers of proteins per single mitochondrion were retrieved from proteomic analysis of purified mitochondria from 7-day-old heterotrophic cell culture (Fuchs *et al.*, 2020). The protein degradation data are from decay rates measured in 14-day-old seedlings grown in hydroponics Li *et al.* (2017). 'NA' means not available data. The calculation of single protein degradation and the concomitant release of sulfide resulting from Fe–S cluster decay (expressed in d^{-1} mitochondrion^{-1}) is based on the previous two parameters.

(Fuchs *et al.*, 2020) and combined these with protein degradation rates determined for hydroponically grown Arabidopsis seedlings (Table 1) (Li *et al.*, 2017). From this combination, we calculated that every day >2500 [2Fe–2S] clusters and >5600 [4Fe–4S] clusters are being disassembled in a single Arabidopsis mitochondrion, due to the protein decay. Obviously, such a combination of data from different materials carries a major risk, but at this point seems to be the best possible approach to gain some estimates for the actual turnover.

LIP1 and BIO2 use Fe–S clusters as sulfur source

The four enzymes AtCNX2, coproporphyrinogen III oxidase (AtHEMN1), AtLIP1, and AtBIO2 in plant mitochondria all belong to the radical *S*-adenosylmethionine (SAM) superfamily. These proteins are characterized by a conserved CxxxCxxC motif for coordination of a [4Fe–4S] radical–SAM (RS) cluster that supplies two electrons for the reductive cleavage of two molecules of SAM into methionines and 5′-deoxyadenosyl radicals (dAdo·) with electrons provided by FDX via the [4Fe–4S] RS cluster (Booker and Lloyd, 2022). AtBIO2 and AtLIP1, however, are exceptional in that they both use an additional 'auxiliary' cluster that provides sulfur atoms for the synthesis of the sulfur-containing cofactors biotin and lipoic acid (Lanz and Booker, 2015). While in AtBIO2 the auxiliary cluster is a [2Fe–2S] cluster, the auxiliary cluster in AtLIP1 is [4Fe–4S] (Fig. 5) (Sanyal *et al.*, 1994; Cicchillo *et al.*, 2004). In AtBIO2, the dAdo· functions as an electron source to abstract two hydrogen atoms from the C6 and C9 methyl groups of dethiobiotin (DTB). The resulting carbon radicals in two consecutive steps attack a sulfur atom of the auxiliary [2Fe–2S] cluster coordinated by AtBIO2 to form covalent C–S bonds and mediate ring closure in biotin with the sulfur atom inserted between the C6 and C9 atoms (Ugulava *et al.*, 2001; Lin and Cronan, 2011). Because the intermediate 9-mercaptodethiobiotin of this reaction has been found in Arabidopsis (Baldet *et al.*, 1993), it can be assumed that the biosynthetic process for biotin is highly conserved between evolutionary distant species.

Arabidopsis LIP1 has not been biochemically characterized but the residues and motifs involved in Fe–S cluster ligation are conserved and the catalytic mechanism can be assumed to be the same as for LIP1 orthologues from other species (Przybyla-Toscano *et al.*, 2022). In addition to the [4Fe–4S] RS cluster, AtLIP1 contains a second auxiliary [4Fe–4S] cluster (Cicchillo *et al.*, 2004). In two consecutive steps, two dAdo· radicals generated on the RS cluster abstract hydrogens from the C6 and C8 carbons of a protein-bound octanoyl residue. The resulting carbon radicals then attack two sulfur atoms in the auxiliary cluster to form covalent C–S bonds (McCarthy and Booker, 2017). Like AtBIO2, AtLIP1 thus sacrifices the auxiliary cluster as a sulfur source. For *E. coli* LipA, the carrier protein EcNfuA efficiently reconstitutes the auxiliary cluster (McCarthy and Booker, 2017). This is consistent with results from *in vitro* assays with human LIP1 (Warui *et al.*, 2022) and *in vivo* evidence for a central role for NFUs in LIP1 function in yeast and Arabidopsis (Melber *et al.*, 2016; Przybyla-Toscano *et al.*, 2022). McCarthy and Booker (2017) also showed a possible [4Fe–4S] cluster transfer from EcIscU to EcLipA, which may explain why *E. coli* can grow normally without EcNfu. The severe defects in Arabidopsis mutants with diminished AtNFU activity, however, strongly argue against an efficient alternative route from AtISCA to AtLIP1 bypassing NFU in plants (Przybyla-Toscano *et al.*, 2022).

For both BIO2 and LIP1, the catalytic activity thus leads to destruction of their auxiliary Fe–S clusters. In the absence of any established repair mechanism for the remains of these clusters, it has to be assumed that they fall apart and release free iron and sulfide (Fig. 5).

Turnover of biotinylated and lipoylated proteins

The use of the auxiliary Fe–S clusters of BIO2 and LIP1 as a sulfur source for cofactor biosynthesis implies that the turnover of proteins carrying the respective cofactors also affects the amount of sulfide released from disintegrated clusters. Because it is not possible to directly measure the activity of BIO2 and LIP1 *in vivo*, we also attempted an estimation of the amount of sulfide released based on the abundance and the turnover of the biotinylated and lipoylated proteins.

Biotin is synthesized in free form and then covalently attached to conserved Lys residues on the respective apoprotein by a biotin–protein ligase (Alban, 2011). In plants, a small number of biotin-dependent enzymes are found in different organelles that play crucial cellular housekeeping roles (Table 2). These include two acetyl-CoA carboxylase isoforms in the cytosol and plastids (Alban *et al.*, 1994; Nikolau *et al.*, 2003), a geranyl-CoA carboxylase in plastids of maize (Guan *et al.*, 1999), a methylcrotonoyl-CoA carboxylase in mitochondria (Alban *et al.*, 1993), and a cytosolic seed storage biotin-protein (SBP) with an atypical biotinylation motif that was localized in pea seeds but so far is not annotated in Arabidopsis (Duval *et al.*, 1994). Because very little is known on the turnover and the copy number of biotinylated proteins, we refrain from considering this further here.

More information is available for the four mitochondrial dehydrogenase complexes PDC, OGDC, BCKDC, and GDC. The first three share the complex architecture and are organized in the three active units E1, the LA-dependent E2, and E3 (Zhou *et al.*, 2001). The GDC is organized in four associated proteins named P, T, L, and LA-dependent H (Bauwe and Kolukisaoglu, 2003; Peterhansel *et al.*, 2010). For many of these subunits, the Arabidopsis genome contains several isoforms (Table 2). The abundance of the GDC complex correlates with the photorespiration activity (Bourguignon *et al.*, 1993; Mouillon *et al.*, 1999), and thus the numbers provided for heterotrophic suspension culture cells are very probably underestimated compared with green tissues of mature plants, where GDC contributes up to 32% of the total matrix protein in pea mitochondria (Oliver *et al.*, 1990).

Table 2. Overview of LA-dependent proteins in Arabidopsis mitochondria and biotin-dependent proteins in mitochondria, the cytosol, and plastids.

Protein type		AGI code	Protein symbol	Co-factor	S atoms involved	Protein copies (per mitochondrion)	Degradation rates (d^{-1})	Protein degraded (d^{-1} per mitochondrion)	Sulfide released (d^{-1} per mitochondrion)
Mitochondrial LA-dependent subunits	GDC cleavage	At2g35370	GDC-H1	NA	NA	NA	0.02	NA	NA
		At2g35120	GDC-H2	Lipoic acid	2	2503	0.11	285	570
		At1g32470	GDC-H3	NA	NA	NA	0.01	NA	NA
	TCA cycle	At3g52200	PDC-E2-1	2× Lipoic acid[a]	4	2120	0.07	152	609
		At3g13930	PDC-E2-2	Lipoic acid	2	5592	0.03	180	360
		At1g54220	PDC-E2-3	Lipoic acid	2	557	0.00	2	5
		At4g26910	OGDC-E3-1	Lipoic acid	2	650	0.07	45	90
		At5g55070	OGDC-E3-2	Lipoic acid	2	5842	0.04	217	434
	AA catabolism	At3g06850	BCKDC-E	Lipoic acid	2	813	0.06	49	98
Biotin-dependent proteins	MCCase	At1g03090	MCCA	Biotin	1	878	0.15	134	134
	ACCase	At5g15530	BCCP2	Biotin	–	–	–	–	–
	ACCase	At5g16390	BCCP1	Biotin	–	–	–	–	–
	GCCase	not annotated	GCCase	Biotin	–	–	–	–	–
	Biotin sink	not annotated	SBP65	Biotin	–	–	–	–	–

The details of estimated protein copies, degradation rate, and the calculation of single protein degradation and the concomitant release of sulfide are described in Table 1. The number of *n*-lipoyl and biotin groups are indicated as well as the respective number of sulfur atoms required for cofactor synthesis.

The only biotinylated protein so far identified in mitochondria is the methylcrotonyl-CoA carboxylase (MCCase) MCCA. Biotinylated proteins localized in other compartments are indicated in grey. BCCP1 and BCCP2 are acetyl-CoA carboxylase (ACCase) localized in the plastid and cytosol, respectively (Alban *et al.*, 1994; Nikolau *et al.*, 2003). The geranoyl-CoA carboxylase (GCCase) was localized in maize plastids (Guan *et al.*, 1999) and the protein SBP65 was reported for pea seeds albeit without any information on the subcellular localization (Duval *et al.*, 1994); both proteins are not annotated in Arabidopsis.

[a] The PDC subunit E1 isoform 1 has a two-lipoyl domain structure (Broz *et al.*, 2014).

Estimation of LIP1 activity based on turnover of the LA-dependent subunits necessarily remains speculative. A first approximation based on protein abundance data from Fuchs *et al.* (2020) and protein decay data from Li *et al.* (2017) leads to >1000 [4Fe–4S] clusters per mitochondrion sacrificed every day by LIP1, with the release of >2000 sulfide ions (Table 2). Despite the inherent uncertainties, this information highlights that release of sulfide as a toxic by-product of cofactor biosynthesis makes it important to also consider the demand for local sulfide detoxification systems in mitochondria.

Scavenging of sulfide originating from Fe–S clusters

Repair of Fe–S clusters

The loss of sulfur atoms from the Fe–S cluster results in two possibilities. On the one hand, the Fe–S cluster can be repaired or replaced to keep the protein functional. On the other hand, the remains of a damaged cluster are released, which might result in unfolding and degradation of the protein as was shown for ACO after oxidative damage (Bulteau *et al.*, 2003). For *E. coli* EcBioB, it was shown that the enzyme can, in the absence of a supply of [2Fe–2S] clusters, still produce more than one molecule of biotin, which suggested repair of the auxiliary [2Fe–2S] cluster. This catalytic activity, however, also results in partial protein degradation (Choi-Rhee and Cronan, 2005). Based on that, the authors suggested that the observed degradation is a consequence of protein unfolding to allow the repair/replacement of the [2Fe–2S] cluster because the cluster is buried in the protein interior. Similarly, it was shown that recombinant EcLipA is catalytically active and hence able to generate several molecules of lipoic acid if EcNfuA is present and able to provide new [4Fe–4S] clusters to EcLipA (McCarthy and Booker, 2017). In combinatorial labelling assays with the sulfur

isotopes ^{34}S and ^{32}S for labelling the newly provided [4Fe–4S] clusters and free sulfide in the reaction buffer, the formation of a lipoyl group containing one ^{32}S atom and one ^{34}S atom indicated that repair of the auxiliary [4Fe–4S] cluster of EcLipA through EcNfuA had occurred (McCarthy and Booker, 2017). Similar to EcBioB and EcLipA as described above, the methylthiolase EcMiaB also sacrifices a [4Fe–4S] cluster to insert sulfur in a subset of tRNAs. The cluster in this case is also provided by EcNfuA (Boutigny *et al.*, 2013). Based on the observation that a *nfuA grx4* double mutant showed a strong decrease in methylthiolated tRNAs, the authors speculated about a potential function for EcGrx4 in the repair of the [4Fe–4S] cluster (Boutigny *et al.*, 2013). They did not consider, however, that EcGrx4 is important to provide the [2Fe–2S] cluster for the formation of [4Fe–4S]. Nevertheless, based on the ability of monothiol GRXs to incorporate a linear [3Fe–4S] cluster, it is speculated that they can either convert this cluster to a [2Fe–2S] cluster and thereby deliver sulfur for cluster repair or they are able to convert the linear cluster to the cubic [4Fe–4S] cluster, thereby scavenging at least the iron of disassembled clusters (Zhang *et al.*, 2013; Couturier *et al.*, 2015).

Free sulfide toxicity and its detoxification

A question that remains unanswered so far is regarding the fate of Fe–S clusters when proteins are degraded. Considering that the clusters are simply disassembled, the cell has to cope with free sulfide. Maintaining low sulfide levels is key to proper plant growth because sulfide binds to the copper centre of the cytochrome *c* oxidase (complex IV) in the ETC and is therefore a powerful inhibitor of respiration (Birke et al., 2012, 2015; Nicholls *et al.*, 2013). In Arabidopsis, the only known pathway to consume sulfide is the biosynthesis of cysteine. First, the acceptor of sulfide, *O*-acetylserine (OAS), is generated by serine acetyltransferase (SERAT) from serine and acetyl-CoA. Then, sulfide is used as a substrate by *O*-acetylserine(thiol)lyase (OAS-TL) to convert OAS to cysteine by replacing the acetyl group of OAS with sulfide. Both SERAT and OAS-TL are forming a so-called cysteine synthase complex (CSC). The heterooligomeric complex consists of a dimer of trimers for SERAT and of two dimers of OAS-TL (Wirtz and Hell, 2006; Jez, 2019). In Arabidopsis, the CSC is located not only in plastids, where sulfide is produced in the course of assimilatory sulfate reduction, but also in the cytosol and mitochondria (Wirtz and Hell, 2006). Interestingly, single null mutants of the cytosolic AtOAS-TL A and plastid AtOAS-TL B do not show any growth defects, while selective deletion of the mitochondrial OAS-TL isoform, AtOAS-TL C, results in mild growth retardation even though it contributes only 5% of total OAS-TL activity (Heeg *et al.*, 2008). The mitochondrial *oast-tl c* mutant does not show any defects in the maturation of Fe–S cluster proteins (Birke *et al.*, 2012), which indicates that the production of cysteine through this pathway is not substantial for the function of AtNFS1. Indeed, it has been suggested that the cytosol is the main compartment for cysteine biosynthesis, and cysteine is then transported into mitochondria (Krueger *et al.*, 2009). The mitochondrial SERAT3, however, is responsible for ~83% of the overall OAS production (Haas *et al.*, 2008). Since mitochondria need to tightly control the amount of free sulfide in the matrix, one may speculate that a high amount of OAS might serve as a backup to rapidly detoxify excessive sulfide under certain conditions.

Conclusion

Efficient provision of Fe–S-dependent proteins in mitochondria with their respective clusters is essential for maintaining many basic metabolic functions. Because Fe–S clusters cannot be imported, mitochondria contain autonomous assembly machineries for different types of clusters and the respective delivery and insertion machineries. While the target proteins are largely known and characterized in terms of their physiological functions, knowledge about the exact mechanisms of Fe–S cluster transfer between the first assembly machinery for [2Fe–2S] clusters and the second machinery for [4Fe–4S] clusters as well as carrier proteins mediating cluster insertion is still fragmentary in plants. To close these gaps in our knowledge, detailed protein–protein interaction studies complemented with genetic evidence is necessary and should be addressed in depth. Furthermore, how Fe–S clusters are distributed among the large number of receiving proteins is not widely known. It is most likely that it depends on the abundance of apoproteins, the efficiency of the individual transfer steps, the turnover of the Fe–S holoproteins, and damage or turnover of the clusters. Understanding the distribution of Fe–S clusters among target proteins and the identification of possible bottlenecks for Fe–S cluster supply thus depend on quantitative and dynamic analysis of Fe–S clusters and metabolite fluxes. Turnover of Fe–S proteins and maybe even more so self-sacrificing death of clusters donating sulfur for sulfur-containing cofactors may cause the release of potentially toxic cluster residuals. Thus, careful analysis of mechanisms for removal of free iron and sulfide will be important in future research.

Author contributions

All authors conceptualized the review and wrote the original draft together. LP designed the figures. All authors reviewed and edited the final manuscript, and approved the submitted version.

Conflict of interest

The authors declare that they have no conflict of interest with the content of this article.

Funding

This work was supported by the German Research Foundation (Deutsche Forschungsgemeinschaft) through the grant ME1567/12-1. AM is the

recipient of a Feodor Lynen Research Fellowship from the Alexander von Humboldt Foundation and wishes to thank the University of Bonn for additional financial support.

References

Adam AC, Bornhövd C, Prokisch H, Neupert W, Hell K. 2006. The Nfs1 interacting protein Isd11 has an essential role in Fe/S cluster biogenesis in mitochondria. The EMBO Journal **25**, 174–183.

Alban C. 2011. Biotin (Vitamin B8) synthesis in plants. Advances in Botanical Research **59**, 39–66.

Alban C, Baldet P, Axiotis S, Douce R. 1993. Purification and characterization of 3-methylcrotonyl-coenzyme A carboxylase from higher plant mitochondria. Plant Physiology **102**, 957–965.

Alban C, Baldet P, Douce R. 1994. Localization and characterization of two structurally different forms of acetyl-CoA carboxylase in young pea leaves, of which one is sensitive to aryloxyphenoxypropionate herbicides. The Biochemical Journal **300**, 557–565.

Armas AM, Balparda M, Terenzi A, Busi MV, Pagani MA, Gomez-Casati DF. 2020. Iron–sulfur cluster complex assembly in the mitochondria of *Arabidopsis thaliana*. Plants **9**, 1171.

Armas AM, Balparda M, Turowski VR, Busi MV, Pagani MA, Gomez-Casati DF. 2019. Altered levels of mitochondrial NFS1 affect cellular Fe and S contents in plants. Plant Cell Reports **38**, 981–990.

Azam T, Przybyla-Toscano J, Vignols F, Couturier J, Rouhier N, Johnson MK. 2020a. The Arabidopsis mitochondrial glutaredoxin GRXS15 provides [2Fe–2S] clusters for ISCA-mediated [4Fe–4S] cluster maturation. International Journal of Molecular Sciences **21**, 9237.

Azam T, Przybyla-Toscano J, Vignols F, Couturier J, Rouhier N, Johnson MK. 2020b. [4Fe–4S] cluster trafficking mediated by Arabidopsis mitochondrial ISCA and NFU proteins. Journal of Biological Chemistry **295**, 18367–18378.

Baldet P, Gerbling H, Axiotis S, Douce R. 1993. Biotin biosynthesis in higher plant cells. European Journal of Biochemistry **217**, 479–485.

Balk J, Pilon M. 2011. Ancient and essential: the assembly of iron–sulfur clusters in plants. Trends in Plant Science **16**, 218–226.

Balk J, Schaedler TA. 2014. Iron cofactor assembly in plants. Annual Review of Plant Biology **65**, 125–153.

Banci L, Brancaccio D, Ciofi-Baffoni S, Del Conte R, Gadepalli R, Mikolajczyk M, Neri S, Piccioli M, Winkelmann J. 2014. [2Fe–2S] cluster transfer in iron–sulfur protein biogenesis. Proceedings of the National Academy of Sciences, USA **111**, 6203–6208.

Bauwe H, Kolukisaoglu Ü. 2003. Genetic manipulation of glycine decarboxylation. Journal of Experimental Botany **54**, 1523–1535.

Beinert H. 2000. Iron–sulfur proteins: ancient structures, still full of surprises. Journal of Biological Inorganic Chemistry **5**, 2–15.

Birke H, De Kok LJ, Wirtz M, Hell R. 2015. The role of compartment-specific cysteine synthesis for sulfur homeostasis during H_2S exposure in Arabidopsis. Plant and Cell Physiology **56**, 358–367.

Birke H, Haas FH, De Kok LJ, Balk J, Wirtz M, Hell R. 2012. Cysteine biosynthesis, in concert with a novel mechanism, contributes to sulfide detoxification in mitochondria of *Arabidopsis thaliana*. The Biochemical Journal **445**, 275–283.

Bittner F. 2014. Molybdenum metabolism in plants and crosstalk to iron. Frontiers in Plant Science **5**, 28.

Boavida LC, Shuai B, Yu H-J, Pagnussat GC, Sundaresan V, McCormick S. 2009. A collection of Ds insertional mutants associated with defects in male gametophyte development and function in *Arabidopsis thaliana*. Genetics **181**, 1369–1385.

Bonomi F, Iametti S, Morleo A, Ta D, Vickery LE. 2008. Studies on the mechanism of catalysis of iron–sulfur cluster transfer from IscU[2Fe2S] by HscA/HscB chaperones. Biochemistry **47**, 12795–12801.

Booker SJ, Lloyd CT. 2022. Twenty years of radical SAM! The genesis of the superfamily. ACS Bio & Med Chem Au **2**, 538–547.

Bourguignon J, Vauclare P, Merand V, Forest E, Neuburger M, Douce R. 1993. Glycine decarboxylase complex from higher plants. European Journal of Biochemistry **217**, 377–386.

Boutigny S, Saini A, Baidoo EEK, Yeung N, Keasling JD, Butland G. 2013. Physical and functional interactions of a monothiol glutaredoxin and an iron sulfur cluster carrier protein with the sulfur-donating radical S-adenosyl-L-methionine enzyme MiaB. Journal of Biological Chemistry **288**, 14200–14211.

Brancaccio D, Gallo A, Mikolajczyk M, Zovo K, Palumaa P, Novellino E, Piccioli M, Ciofi-Baffoni S, Banci L. 2014. Formation of [4Fe–4S] clusters in the mitochondrial iron–sulfur cluster assembly machinery. Journal of the American Chemical Society **136**, 16240–16250.

Braymer JJ, Freibert SA, Rakwalska-Bange M, Lill R. 2021. Mechanistic concepts of iron–sulfur protein biogenesis in biology. Biochimica et Biophysica Acta **1868**, 118863.

Broz AK, Tovar-Méndez A, Mooney BP, Johnston ML, Miernyk JA, Randall DD. 2014. A novel regulatory mechanism based upon a dynamic core structure for the mitochondrial pyruvate dehydrogenase complex? Mitochondrion **19**, 144–153.

Bulteau A-L, Ikeda-Saito M, Szweda LI. 2003. Redox-dependent modulation of aconitase activity in intact mitochondria. Biochemistry **42**, 14846–14855.

Busi MV, Maliandi MV, Valdez H, Clemente M, Zabaleta EJ, Araya A, Gomez-Casati DF. 2006. Deficiency of *Arabidopsis thaliana* frataxin alters activity of mitochondrial Fe–S proteins and induces oxidative stress. The Plant Journal **48**, 873–882.

Bych K, Kerscher S, Netz DJA, Pierik AJ, Zwicker K, Huynen MA, Lill R, Brandt U, Balk J. 2008. The iron–sulphur protein Ind1 is required for effective complex I assembly. The EMBO Journal **27**, 1736–1746.

Choi-Rhee E, Cronan JE. 2005. Biotin synthase is catalytic *in vivo*, but catalysis engenders destruction of the protein. Chemistry & Biology **12**, 461–468.

Cicchillo RM, Lee K-H, Baleanu-Gogonea C, Nesbitt NM, Krebs C, Booker SJ. 2004. *Escherichia coli* lipoyl synthase binds two distinct [4Fe–4S] clusters per polypeptide. Biochemistry **43**, 11770–11781.

Couturier J, Wu H-C, Dhalleine T, Pégeot H, Sudre D, Gualberto JM, Jacquot J-P, Gaymard F, Vignols F, Rouhier N. 2014. Monothiol glutaredoxin–BolA interactions: redox control of *Arabidopsis thaliana* BolA2 and SufE1. Molecular Plant **7**, 187–205.

Couturier J, Przybyla-Toscano J, Roret T, Didierjean C, Rouhier N. 2015. The roles of glutaredoxins ligating Fe–S clusters: sensing, transfer or repair functions? Biochimica et Biophysica Acta **1853**, 1513–1527.

Cupp-Vickery JR, Peterson JC, Ta DT, Vickery LE. 2004. Crystal structure of the molecular chaperone HscA substrate binding domain complexed with the IscU recognition peptide ELPPVKIHC. Journal of Molecular Biology **342**, 1265–1278.

Dutkiewicz R, Schilke B, Knieszner H, Walter W, Craig EA, Marszalek J. 2003. Ssq1, a mitochondrial Hsp70 involved in iron–sulfur (Fe/S) center biogenesis: similarities to and differences from its bacterial counterpart. Journal of Biological Chemistry **278**, 29719–29727.

Duval M, Job C, Alban C, Douce R, Job D. 1994. Developmental patterns of free and protein-bound biotin during maturation and germination of seeds of *Pisum sativum*: characterization of a novel seed-specific biotinylated protein. The Biochemical Journal **299**, 141–150.

Ewald R, Hoffmann C, Florian A, Neuhaus E, Fernie AR, Bauwe H. 2014. Lipoate-protein ligase and octanoyltransferase are essential for protein lipoylation in mitochondria of Arabidopsis. Plant Physiology **165**, 978–990.

Fonseca JP, Lee H-K, Boschiero C, Griffiths M, Lee S, Zhao P, York LM, Mysore KS. 2020. Iron–sulfur cluster protein NITROGEN FIXATION S-LIKE1 and its interactor FRATAXIN function in plant immunity. Plant Physiology **184**, 1532–1548.

Frazzon APG, Ramirez MV, Warek U, Balk J, Frazzon J, Dean DR, Winkel BSJ. 2007. Functional analysis of Arabidopsis genes involved in mitochondrial iron–sulfur cluster assembly. Plant Molecular Biology **64**, 225–240.

Fu X, Guan X, Garlock R, Nikolau BJ. 2020. Mitochondrial fatty acid synthase utilizes multiple acyl carrier protein isoforms. Plant Physiology **183**, 547–557.

Fuchs P, Rugen N, Carrie C, *et al*. 2020. Single organelle function and organization as estimated from Arabidopsis mitochondrial proteomics. The Plant Journal **101**, 420–441.

Garcia PS, D'Angelo F, Ollagnier de Choudens S, Dussouchaud M, Bouveret E, Gribaldo S, Barras F. 2022. An early origin of iron–sulfur cluster biosynthesis machineries before Earth oxygenation. Nature Ecology & Evolution **6**, 1564–1572.

Gervason S, Larkem D, Mansour AB, *et al*. 2019. Physiologically relevant reconstitution of iron–sulfur cluster biosynthesis uncovers persulfide-processing functions of ferredoxin-2 and frataxin. Nature Communications **10**, 3566.

Gourdoupis S, Nasta V, Calderone V, Ciofi-Baffoni S, Banci L. 2018. IBA57 recruits ISCA2 to form a [2Fe–2S] cluster-mediated complex. Journal of the American Chemical Society **140**, 14401–14412.

Guan X, Diez T, Prasad TK, Nikolau BJ, Wurtele ES. 1999. Geranoyl-CoA carboxylase: a novel biotin-containing enzyme in plants. Archives of Biochemistry and Biophysics **362**, 12–21.

Haas FH, Heeg C, Queiroz R, Bauer A, Wirtz M, Hell R. 2008. Mitochondrial serine acetyltransferase functions as a pacemaker of cysteine synthesis in plant cells. Plant Physiology **148**, 1055–1067.

Heeg C, Kruse C, Jost R, Gutensohn M, Ruppert T, Wirtz M, Hell R. 2008. Analysis of the Arabidopsis O-acetylserine(thiol)lyase gene family demonstrates compartment-specific differences in the regulation of cysteine synthesis. The Plant Cell **20**, 168–185.

Hooks MA, Allwood JW, Harrison JKD, Kopka J, Erban A, Goodacre R, Balk J. 2014. Selective induction and subcellular distribution of ACONITASE 3 reveal the importance of cytosolic citrate metabolism during lipid mobilization in Arabidopsis. The Biochemical Journal **463**, 309–317.

Hu C, Lin S, Chi W, Charng Y. 2012. Recent gene duplication and subfunctionalization produced a mitochondrial GrpE, the nucleotide exchange factor of the Hsp70 complex, specialized in thermotolerance to chronic heat stress in Arabidopsis. Plant Physiology **158**, 747–758.

Imlay JA. 2013. The molecular mechanisms and physiological consequences of oxidative stress: lessons from a model bacterium. Nature Reviews. Microbiology **11**, 443–454.

Ivanova A, Gill-Hille M, Huang S, Branca RM, Kmiec B, Teixeira PF, Lehtiö J, Whelan J, Murcha MW. 2019. A mitochondrial LYR protein is required for complex I assembly. Plant Physiology **181**, 1632–1650.

Jez JM. 2019. Structural biology of plant sulfur metabolism: from sulfate to glutathione. Journal of Experimental Botany **70**, 4089–4103.

Johansson C, Roos AK, Montano SJ, Sengupta R, Filippakopoulos P, Guo K, von Delft F, Holmgren A, Oppermann U, Kavanagh KL. 2010. The crystal structure of human GLRX5: iron–sulfur cluster co-ordination, tetrameric assembly and monomer activity. The Biochemical Journal **433**, 303–311.

Karri S, Singh S, Paripati AK, Marada A, Krishnamoorthy T, Guruprasad L, Balasubramanian D, Sepuri NV. 2019. Adaptation of Mge1 to oxidative stress by local unfolding and altered interaction with mitochondrial Hsp70 and Mxr2. Mitochondrion **46**, 140–148.

Krueger S, Niehl A, Lopez Martin MC, Steinhauser D, Donath A, Hildebrandt T, Romero LC, Hoefgen R, Gotor C, Hesse H. 2009. Analysis of cytosolic and plastidic serine acetyltransferase mutants and subcellular metabolite distributions suggests interplay of the cellular compartments for cysteine biosynthesis in Arabidopsis. Plant, Cell & Environment **32**, 349–367.

Kruse I, Maclean AE, Hill L, Balk J. 2018. Genetic dissection of cyclic pyranopterin monophosphate biosynthesis in plant mitochondria. The Biochemical Journal **475**, 495–509.

Lanz ND, Booker SJ. 2015. Auxiliary iron–sulfur cofactors in radical SAM enzymes. Biochimica et Biophysica Acta **1853**, 1316–1334.

Leaden L, Busi MV, Gomez-Casati DF. 2014. The mitochondrial proteins AtHscB and AtIsu1 involved in Fe–S cluster assembly interact with the Hsp70-type chaperon AtHscA2 and modulate its catalytic activity. Mitochondrion **19**, 375–381.

Léon S, Touraine B, Briat J-F, Lobréaux S. 2005. Mitochondrial localization of *Arabidopsis thaliana* Isu Fe–S scaffold proteins. FEBS Letters **579**, 1930–1934.

Li J, Kogan M, Knight SAB, Pain D, Dancis A. 1999. Yeast mitochondrial protein, Nfs1p, coordinately regulates iron–sulfur cluster proteins, cellular iron uptake, and iron distribution. Journal of Biological Chemistry **274**, 33025–33034.

Li L, Nelson C, Fenske R, Trösch J, Pružinská A, Millar AH, Huang S. 2017. Changes in specific protein degradation rates in *Arabidopsis thaliana* reveal multiple roles of Lon1 in mitochondrial protein homeostasis. The Plant Journal **89**, 458–471.

Li P, Hendricks AL, Wang Y, Villones RLE, Lindkvist-Petersson K, Meloni G, Cowan JA, Wang K, Gourdon P. 2022. Structures of Atm1 provide insight into [2Fe–2S] cluster export from mitochondria. Nature Communications **13**, 4339.

Li Y, Belt K, Alqahtani SF, Saha S, Fenske R, Van Aken O, Whelan J, Millar AH, Murcha MW, Huang S. 2022. The mitochondrial LYR protein SDHAF1 is required for succinate dehydrogenase activity in Arabidopsis. The Plant Journal **110**, 499–512.

Liedgens L, Zimmermann J, Wäschenbach L, Geissel F, Laporte H, Gohlke H, Morgan B, Deponte M. 2020. Quantitative assessment of the determinant structural differences between redox-active and inactive glutaredoxins. Nature Communications **11**, 1725.

Lill R, Dutkiewicz R, Freibert SA, *et al*. 2015. The role of mitochondria and the CIA machinery in the maturation of cytosolic and nuclear iron–sulfur proteins. European Journal of Cell Biology **94**, 280–291.

Lill R, Freibert S-A. 2020. Mechanisms of mitochondrial iron–sulfur protein biogenesis. Annual Review of Biochemistry **89**, 471–499.

Lin S, Cronan JE. 2011. Closing in on complete pathways of biotin biosynthesis. Molecular Biosystems **7**, 1811–1821.

López-López A, Keech O, Rouhier N. 2022. Maturation and assembly of iron–sulfur cluster-containing subunits in the mitochondrial complex I from plants. Frontiers in Plant Science **13**, 916948.

Maio N, Ghezzi D, Verrigni D, Rizza T, Bertini E, Martinelli D, Zeviani M, Singh A, Carrozzo R, Rouault TA. 2016. Disease-causing SDHAF1 mutations impair transfer of Fe–S clusters to SDHB. Cell Metabolism **23**, 292–302.

Maio N, Kim KS, Singh A, Rouault TA. 2017. A single adaptable cochaperone–scaffold complex delivers nascent iron–sulfur clusters to mammalian respiratory chain complexes I–III. Cell Metabolism **25**, 945-953.

Majewska J, Ciesielski SJ, Schilke B, Kominek J, Blenska A, Delewski W, Song J-Y, Marszalek J, Craig EA, Dutkiewicz R. 2013. Binding of the chaperone Jac1 protein and cysteine desulfurase Nfs1 to the iron–sulfur cluster scaffold Isu protein is mutually exclusive. Journal of Biological Chemistry **288**, 29134–29142.

Manicki M, Majewska J, Ciesielski S, Schilke B, Blenska A, Kominek J, Marszalek J, Craig EA, Dutkiewicz R. 2014. Overlapping binding sites of the frataxin homologue assembly factor and the heat shock protein 70 transfer factor on the Isu iron–sulfur cluster scaffold protein. Journal of Biological Chemistry **289**, 30268–30278.

Marinoni EN, de Oliveira JS, Nicolet Y, Raulfs EC, Amara P, Dean DR, Fontecilla-Camps JC. 2012. $(IscS–IscU)_2$ complex structures provide insights into Fe_2S_2 biogenesis and transfer. Angewandte Chemie International Edition **51**, 5439–5442.

McCarthy EL, Booker SJ. 2017. Destruction and reformation of an iron–sulfur cluster during catalysis by lipoyl synthase. Science **358**, 373–377.

Melber A, Na U, Vashisht A, Weiler BD, Lill R, Wohlschlegel JA, Winge DR. 2016. Role of Nfu1 and Bol3 in iron–sulfur cluster transfer to mitochondrial clients. eLife **5**, e15991.

Meyer EH, Welchen E, Carrie C. 2019. Assembly of the complexes of the oxidative phosphorylation system in land plant mitochondria. Annual Review of Plant Biology **70**, 23–50.

Moseler A, Aller I, Wagner S, *et al*. 2015. The mitochondrial monothiol glutaredoxin S15 is essential for iron–sulfur protein maturation in *Arabidopsis thaliana*. Proceedings of the National Academy of Sciences, USA **112**, 13735–13740.

Moseler A, Kruse I, Maclean AE, *et al*. 2021. The function of glutaredoxin GRXS15 is required for lipoyl-dependent dehydrogenases in mitochondria. Plant Physiology **186**, 1507–1525.

Mouillon J-M, Aubert S, Bourguignon J, Gout E, Douce R, Rébeillé F. 1999. Glycine and serine catabolism in non-photosynthetic higher plant cells: their role in C1 metabolism. The Plant Journal **20**, 197–205.

Mühlenhoff U, Balk J, Richhardt N, Kaiser JT, Sipos K, Kispal G, Lill R. 2004. Functional characterization of the eukaryotic cysteine desulfurase Nfs1p from *Saccharomyces cerevisiae*. Journal of Biological Chemistry **279**, 36906–36915.

Mühlenhoff U, Richter N, Pines O, Pierik AJ, Lill R. 2011. Specialized function of yeast Isa1 and Isa2 proteins in the maturation of mitochondrial [4Fe–4S] proteins. Journal of Biological Chemistry **286**, 41205–41216.

Nasta V, Giachetti A, Ciofi-Baffoni S, Banci L. 2017. Structural insights into the molecular function of human [2Fe–2S] BOLA1–GRX5 and [2Fe–2S] BOLA3–GRX5 complexes. Biochimica et Biophysica Acta **1861**, 2119–2131.

Nasta V, Suraci D, Gourdoupis S, Ciofi-Baffoni S, Banci L. 2020. A pathway for assembling $[4Fe–4S]^{2+}$ clusters in mitochondrial iron–sulfur protein biogenesis. The FEBS Journal **287**, 2312–2327.

Navarro-Sastre A, Tort F, Stehling O, *et al*. 2011. A fatal mitochondrial disease is associated with defective NFU1 function in the maturation of a subset of mitochondrial Fe–S proteins. American Journal of Human Genetics **89**, 656–667.

Nicholls P, Marshall DC, Cooper CE, Wilson MT. 2013. Sulfide inhibition of and metabolism by cytochrome c oxidase. Biochemical Society Transactions **41**, 1312–1316.

Nikolau BJ, Ohlrogge JB, Wurtele ES. 2003. Plant biotin-containing carboxylases. Archives of Biochemistry and Biophysics **414**, 211–222.

Oliver DJ, Neuburger M, Bourguignon J, Douce R. 1990. Interaction between the component enzymes of the glycine decarboxylase multienzyme complex 1. Plant Physiology **94**, 833–839.

Pagnussat GC, Yu H-J, Ngo QA, Rajani S, Mayalagu S, Johnson CS, Capron A, Xie L-F, Ye D, Sundaresan V. 2005. Genetic and molecular identification of genes required for female gametophyte development and function in Arabidopsis. Development **132**, 603–614.

Parent A, Elduque X, Cornu D, Belot L, Le Caer J-P, Grandas A, Toledano MB, D'Autréaux B. 2015. Mammalian frataxin directly enhances sulfur transfer of NFS1 persulfide to both ISCU and free thiols. Nature Communications **6**, 5686.

Patton DA, Schetter AL, Franzmann LH, Nelson K, Ward ER, Meinke DW. 1998. An embryo-defective mutant of Arabidopsis disrupted in the final step of biotin synthesis. Plant Physiology **116**, 935–946.

Peterhansel C, Horst I, Niessen M, Blume C, Kebeish R, Kürkcüoglu S, Kreuzaler F. 2010. Photorespiration. The Arabidopsis Book **8**, e0130.

Przybyla-Toscano J, Boussardon C, Law S, Rouhier N, Keech O. 2021a. Gene atlas of iron-containing proteins in *Arabidopsis thaliana*. The Plant Journal **106**, 258–274.

Przybyla-Toscano J, Christ L, Keech O, Rouhier N. 2021b. Iron–sulfur proteins in plant mitochondria: roles and maturation. Journal of Experimental Botany **72**, 2014–2044.

Przybyla-Toscano J, Maclean AE, Franceschetti M, Liebsch D, Vignols F, Keech O, Rouhier N, Balk J. 2022. Protein lipoylation in mitochondria requires Fe–S cluster assembly factors NFU4 and NFU5. Plant Physiology **188**, 997–1013.

Rodríguez-Manzaneque MT, Tamarit J, Bellí G, Ros J, Herrero E. 2002. Grx5 is a mitochondrial glutaredoxin required for the activity of iron/sulfur enzymes. Molecular Biology of the Cell **13**, 1109–1121.

Roschzttardtz H, Fuentes I, Vásquez M, Corvalán C, León G, Gómez I, Araya A, Holuigue L, Vicente-Carbajosa J, Jordana X. 2009. A nuclear gene encoding the iron–sulfur subunit of mitochondrial complex II is regulated by B3 domain transcription factors during seed development in Arabidopsis. Plant Physiology **150**, 84–95.

Sanyal I, Cohen G, Flint DH. 1994. Biotin synthase: purification, characterization as a [2Fe–2S] cluster protein, and *in vitro* activity of the *Escherichia coli bioB* gene product. Biochemistry **33**, 3625–3631.

Schaedler TA, Thornton JD, Kruse I, Schwarzländer M, Meyer AJ, van Veen HW, Balk J. 2014. A conserved mitochondrial ATP-binding cassette transporter exports glutathione polysulfide for cytosolic metal cofactor assembly. Journal of Biological Chemistry **289**, 23264–23274.

Schmidt S, Strub A, Röttgers K, Zufall N, Voos W. 2001. The two mitochondrial heat shock proteins 70, Ssc1 and Ssq1, compete for the cochaperone Mge1. Journal of Molecular Biology **313**, 13–26.

Schulz V, Basu S, Freibert S-A, *et al*. 2023. Functional spectrum and specificity of mitochondrial ferredoxins FDX1 and FDX2. Nature Chemical Biology **19**, 206–217.

Sheftel AD, Stehling O, Pierik AJ, Netz Daili J, Kerscher S, Elsässer H-P, Wittig I, Balk J, Brandt U, Lill R. 2009. Human Ind1, an iron–sulfur cluster assembly factor for respiratory complex I. Molecular and Cellular Biology **29**, 6059–6073.

Solmonson A, DeBerardinis RJ. 2018. Lipoic acid metabolism and mitochondrial redox regulation. Journal of Biological Chemistry **293**, 7522–7530.

Srour B, Gervason S, Hoock MH, *et al*. 2022. Iron insertion at the assembly site of the ISCU scaffold protein is a conserved process initiating Fe–S cluster biosynthesis. Journal of the American Chemical Society **144**, 17496–17515.

Ströher E, Grassl J, Carrie C, Fenske R, Whelan J, Millar AH. 2016. Glutaredoxin S15 is involved in Fe–S cluster transfer in mitochondria influencing lipoic acid-dependent enzymes, plant growth, and arsenic tolerance in Arabidopsis. Plant Physiology **170**, 1284–1299.

Takubo K, Morikawa T, Nonaka Y, Mizutani M, Takenaka S, Takabe K, Takahashi M, Ohta D. 2003. Identification and molecular characterization of mitochondrial ferredoxins and ferredoxin reductase from Arabidopsis. Plant Molecular Biology **52**, 817–830.

Taylor NL, Heazlewood JL, Day DA, Millar AH. 2004. Lipoic acid-dependent oxidative catabolism of α-keto acids in mitochondria provides evidence for branched-chain amino acid catabolism in Arabidopsis. Plant Physiology **134**, 838–848.

Taylor NL, Heazlewood JL, Millar AH. 2011. The *Arabidopsis thaliana* 2-D gel mitochondrial proteome: refining the value of reference maps for assessing protein abundance, contaminants and post-translational modifications. Proteomics **11**, 1720–1733.

Trnka D, Engelke AD, Gellert M, *et al*. 2020. Molecular basis for the distinct functions of redox-active and FeS-transfering glutaredoxins. Nature Communications **11**, 3445.

Turowski VR, Busi MV, Gomez-Casati DF. 2012. Structural and functional studies of the mitochondrial cysteine desulfurase from *Arabidopsis thaliana*. Molecular Plant **5**, 1001–1010.

Ugulava NB, Sacanell CJ, Jarrett JT. 2001. Spectroscopic changes during a single turnover of biotin synthase: destruction of a [2Fe–2S] cluster accompanies sulfur insertion. Biochemistry **40**, 8352–8358.

Uzarska MA, Dutkiewicz R, Freibert S-A, Lill R, Mühlenhoff U. 2013. The mitochondrial Hsp70 chaperone Ssq1 facilitates Fe/S cluster transfer from Isu1 to Grx5 by complex formation. Molecular Biology of the Cell **24**, 1830–1841.

Uzarska MA, Nasta V, Weiler BD, Spantgar F, Ciofi-Baffoni S, Saviello MR, Gonnelli L, Mühlenhoff U, Banci L, Lill R. 2016. Mitochondrial Bol1 and Bol3 function as assembly factors for specific iron–sulfur proteins. eLife **5**, e16673.

Van Hoewyk D, Abdel-Ghany SE, Cohu CM, Herbert SK, Kugrens P, Pilon M, Pilon-Smits EAH. 2007. Chloroplast iron–sulfur cluster protein maturation requires the essential cysteine desulfurase CpNifS. Proceedings of the National Academy of Sciences, USA **104**, 5686–5691.

Van Vranken JG, Jeong M-Y, Wei P, Chen Y-C, Gygi SP, Winge DR, Rutter J. 2016. The mitochondrial acyl carrier protein (ACP) coordinates

mitochondrial fatty acid synthesis with iron sulfur cluster biogenesis. eLife **5**, e17828.

Vazzola V, Losa A, Soave C, Murgia I. 2007. Knockout of frataxin gene causes embryo lethality in Arabidopsis. FEBS Letters **581**, 667–672.

Wächtershäuser G. 1992. Groundworks for an evolutionary biochemistry: the iron-sulphur world. Progress in Biophysics and Molecular Biology **58**, 85–201.

Warui DM, Sil D, Lee K-H, Neti SS, Esakova OA, Knox HL, Krebs C, Booker SJ. 2022. *In vitro* demonstration of human lipoyl synthase catalytic activity in the presence of NFU1. ACS Bio & Med Chem Au **2**, 456–468.

Webert H, Freibert S-A, Gallo A, Heidenreich T, Linne U, Amlacher S, Hurt E, Mühlenhoff U, Banci L, Lill R. 2014. Functional reconstitution of mitochondrial Fe/S cluster synthesis on Isu1 reveals the involvement of ferredoxin. Nature Communications **5**, 5013.

Weiler BD, Brück M-C, Kothe I, Bill E, Lill R, Mühlenhoff U. 2020. Mitochondrial [4Fe–4S] protein assembly involves reductive [2Fe–2S] cluster fusion on ISCA1–ISCA2 by electron flow from ferredoxin FDX2. Proceedings of the National Academy of Sciences,USA **117**, 20555–20565.

Wirtz M, Hell R. 2006. Functional analysis of the cysteine synthase protein complex from plants: structural, biochemical and regulatory properties. Journal of Plant Physiology **163**, 273–286.

Woo S, Moon B, Hwang I. 2022. Both metaxin and Tom20 together with two mitochondria-specific motifs support mitochondrial targeting of dual-targeting AtSufE1. Journal of Integrative Plant Biology **64**, 1596–1613.

Wydro MM, Sharma P, Foster JM, Bych K, Meyer EH, Balk J. 2013. The evolutionarily conserved iron–sulfur protein INDH is required for complex I assembly and mitochondrial translation in Arabidopsis. The Plant Cell **25**, 4014–4027.

Xu XM, Lin H, Latijnhouwers M, Møller SG. 2009. Dual localized AtHscB involved in iron sulfur protein biogenesis in Arabidopsis. PLoS One **4**, e7662.

Xu XM, Møller SG. 2006. AtSufE is an essential activator of plastidic and mitochondrial desulfurases in Arabidopsis. The EMBO Journal **25**, 900–909.

Zhang B, Bandyopadhyay S, Shakamuri P, Naik SG, Huynh BH, Couturier J, Rouhier N, Johnson MK. 2013. Monothiol glutaredoxins can bind linear $[Fe3S4]^{+}$ and $[Fe4S4]^{2+}$ clusters in addition to $[Fe2S2]^{2+}$ clusters: spectroscopic characterization and functional implications. Journal of the American Chemical Society **135**, 15153–15164.

Zheng L, Cash VL, Flint DH, Dean DR. 1998. Assembly of iron–sulfur clusters: identification of an iscSUA–hscBA–fdx gene cluster from *Azotobacter vinelandii*. Journal of Biological Chemistry **273**, 13264–13272.

Zhou ZH, McCarthy DB, O'Connor CM, Reed LJ, Stoops JK. 2001. The remarkable structural and functional organization of the eukaryotic pyruvate dehydrogenase complexes. Proceedings of the National Academy of Sciences, USA **98**, 14802–14807.

2.3 | Additional Information

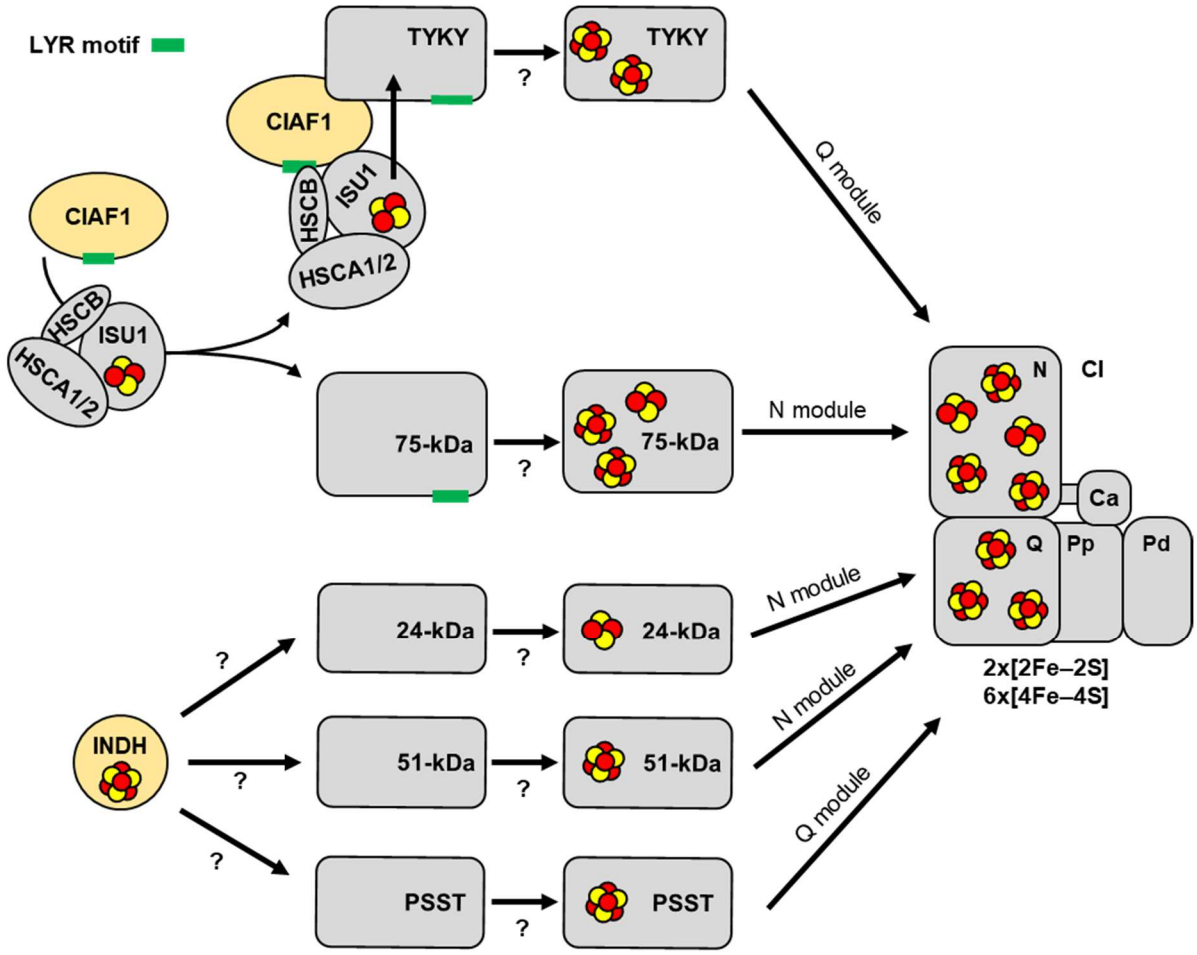

Additional Information Fig. 1 | Working model for the delivery and insertion of Fe–S clusters to mETC complex I. The complex I assembly factor 1 (CIAF1) contains an LYR (Leu–Tyr–Arg) motif (highlighted in green). CIAF1 can recruit the chaperon/co-chaperon complex (HSCA/HSCB/ISU1) via interaction with HSCB and guide it to the complex I (CI) subunits TYKY of the Q module and 75-kDa of the N module (Ivanova *et al.*, 2019). To date, it is unknown whether the [2Fe–2S] clusters delivered by CIAF1 are converted to [4Fe–4S] clusters directly on the CI subunits (similarly to the hypothesis in Additional Information Fig. 2) or whether CIAF1 can coordinate [4Fe–4S] clusters. The INDH (iron–sulfur protein required for NADH dehydrogenase) assembly factor is the homolog of human *Hs*NUBPL (Sheftel *et al.*, 2009) and yeast *Sc*Ind1 (Bych *et al.*, 2008) and belongs to a subfamily of P-loop NTPases, which can bind [4Fe–4S] clusters. It is supposed that INDH deliveries [4Fe–4S] clusters to several subunits of the CI but lack of precise evidence prevents to provide more details (Wydro *et al.*, 2013).

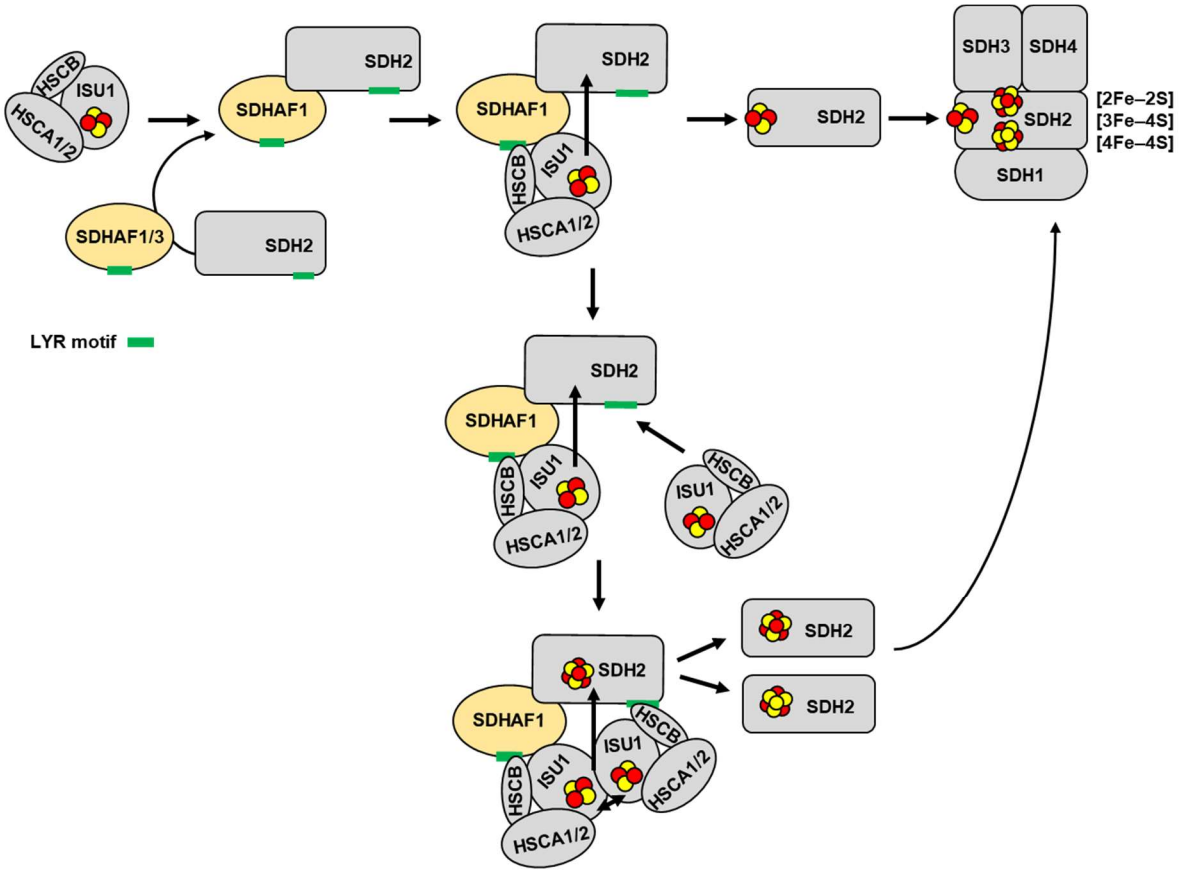

Additional Information Fig. 2 | Working model for the delivery and insertion of Fe–S clusters to mETC complex II. The succinate dehydrogenase (SDH) assembly factors 1 and 3 (SDHAF1/3) contain an LYR motif (highlighted in green). Evidence in yeast (Na *et al.*, 2014) suggests that these assembly factors can recruit the chaperon/co-chaperon complex (HSCA/HSCB/ISU1) via interaction with HSCB and guide it to the SDH subunit 2 (SDH2), where the [2Fe–2S] cluster carried by ISU1 is transferred. Maio *et al.* (2014, 2016) proposed that [4Fe–4S] clusters can be assembled directly on the SDH subunits. It was hypothesized that SDH2, which contains an LYR motif at the C-terminus, can recruit a second chaperon/co-chaperon complex through direct binding with HSCB. This should allow bringing two [2Fe–2S] clusters in close proximity, with consequent fusion to one [4Fe–4S] cluster.

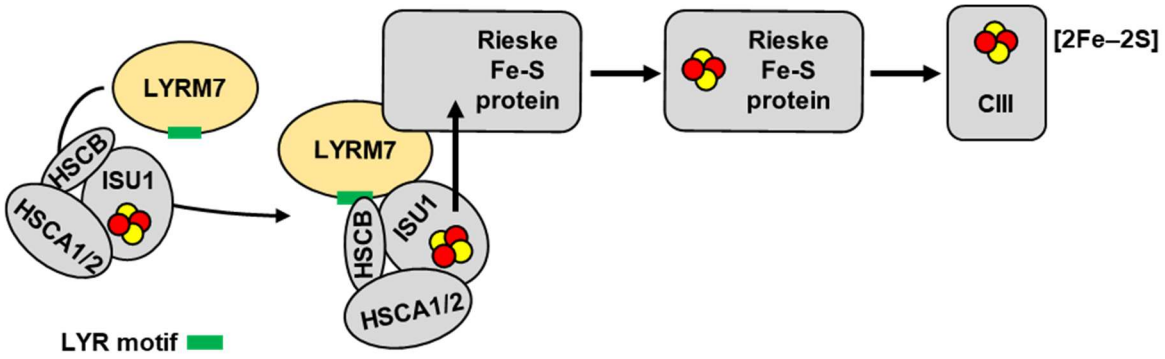

Additional Information Fig. 3 | Working model for the delivery and insertion of Fe–S clusters to mETC complex III. Evidence in human (Maio *et al.*, 2017) and yeast (Atkinson *et al.*, 2011) suggest that the assembly factor LYRM7 directly binds HSCB via its LYR motif and guides the chaperon/co-chaperon complex to the subunit UQCRFS1, the Riske-Fe–S-subunit of complex III.

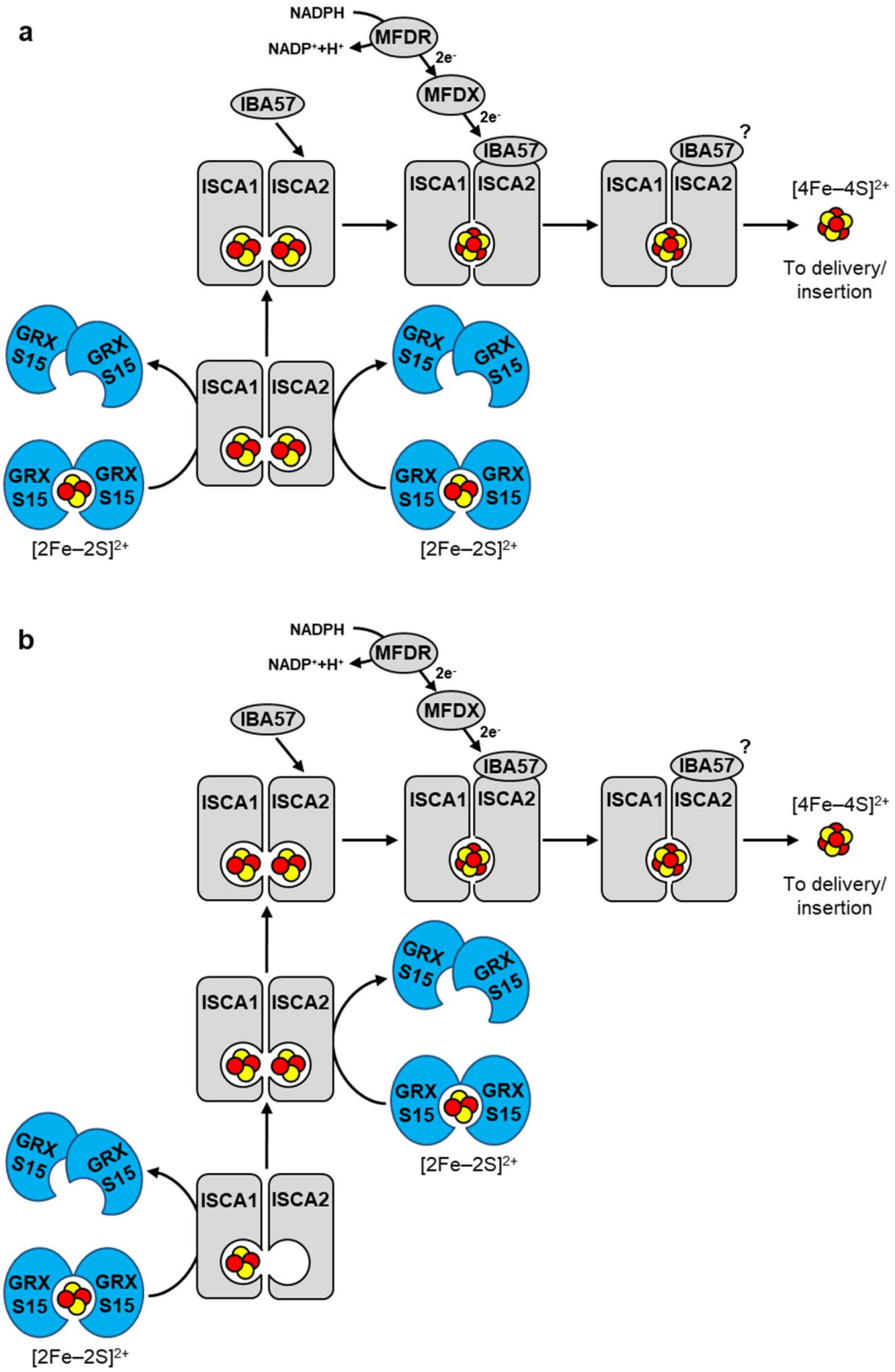

Additional Information Fig. 4 | Working model 1 for the delivery of [2Fe–2S] cluster and the assembly of [4Fe–4S] cluster. In both **a** and **b**, the two [2Fe–2S] clusters are transferred to preformed heterodimer ISCA1/ISCA2. In **a**, the clusters can be transferred to the ISCAs dimer only at the same time, in case ISCA1/ISCA2 cannot coordinate one [2Fe–2S] cluster only. In case it is possible, in **b** the [2Fe–2S] clusters are inserted one by one in the dimeric structure ISCA1/ISCA2. The models are proposed based on evidence from the respective proteins in human (Brancaccio *et al.*, 2014; Weiler *et al.*, 2020) and plants (Azam *et al.*, 2020).

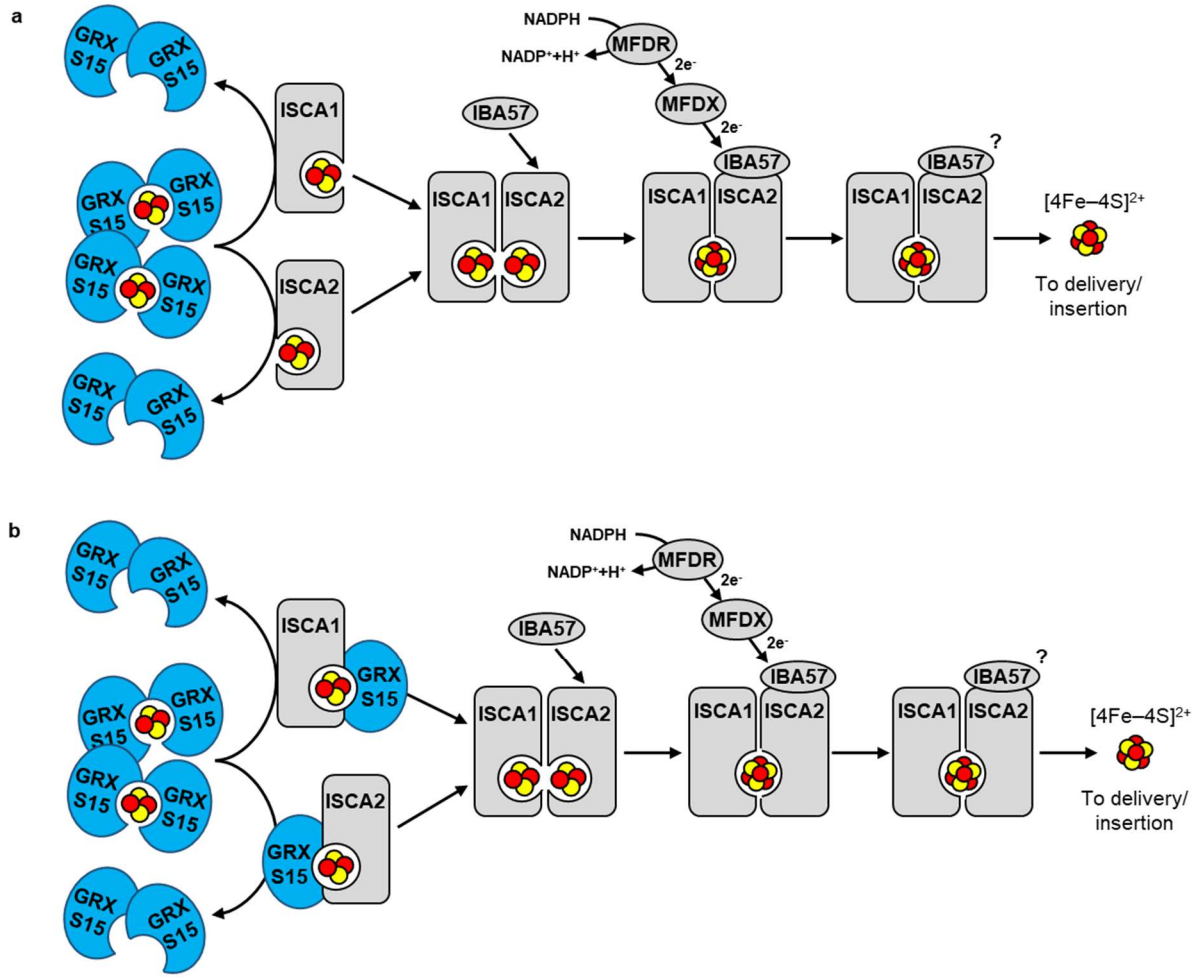

Additional Information Fig. 5 | Working model 2 for the delivery of [2Fe–2S] cluster and the assembly of [4Fe–4S] cluster. In both **a** and **b**, the two [2Fe–2S] clusters are transferred to ISCA1 and ISCA2 separately, before forming the dimeric structure. In **a** is depicted the possibility that the clusters can be coordinated by the ISCAs monomers alone. In **b**, the monomers cannot coordinate alone the [2Fe–2S] clusters and to prevent the cluster loss they need to form a heterodimeric complex with GRXS15 before the ISCA1/ISCA2 dimer formation. The models are proposed based on evidence from the respective proteins in plants (Azam *et al.*, 2020).

3a | Comparative characterization of class I and class II glutaredoxins

This chapter presents the research paper published in *Nature Communications* in 2020:

"Molecular basis for the distinct functions of redox-active and FeS-transfering glutaredoxins"

Daniel Trnka, Anna D. Engelke, Manuela Gellert, Anna Moseler, Md. Faruq Hossain, Tobias T. Lindenberg, ***Luca Pedroletti****, Benjamin Odermatt, João V. de Souza, Agnieszka K. Bronowska, Tobias P. Dick, Uli Mühlenhoff, Andreas J. Meyer, Carsten Berndt and Christopher Horst Lillig. (2020)*

Nature Communications, no. 2020; doi.org/10.1038/s41467-020-17323-0.

The complete supplementary data are available under "Supplementary information" and "Source Data" on the website:
https://www.nature.com/articles/s41467-020-17323-0#additional-information

3a.1 | Summary and personal contribution

Despite being structurally closely related, glutaredoxins (GRXs) fall into functionally different groups. In this research paper, we investigated the molecular bases that determine their functions providing fundamental insights into the mechanisms of different types of GRXs and revealing the crucial structural differences.

GRXs are typically divided into two main classes. The first class ("class I") is able to efficiently catalyse glutathione-dependent reactions, whereas the second class ("class II") is involved in the trafficking of iron–sulfur clusters (Fe–S). The plant kingdom possesses an additional "class III", for which, however, we have only limited information (Rouhier *et al.,* 2006; Mrozek *et al.*, 2023).

Class I GRXs are characterised by a consensus "CxxC" motif in their active site. Although this consensus could deviate in "CxxS" motif, these GRXs are referred to as "dithiol glutaredoxins" due to the highly conserved presence of the two cysteine residues. Class II GRXs were identified later and share a consensus "CGFS" motif in their active site. They are thus referred to as "monothiol glutaredoxins". While class I GRXs commonly possess oxidoreductase activity, class II GRXs can coordinate one [2Fe–2S] cluster at the interface of a dimeric complex with one cysteine residue from each GRX subunit and two cysteines from non-covalently bound molecules of glutathione (Fig. 3a.1) (see Chapter 1.3 and 1.4). Despite the

structural similarity based on the thioredoxin fold, it remained elusive for decades why class I GRXs are efficient oxidoreductases and class II rather not.

In this study, we re-investigated the structural differences between the two classes I and II GRXs. We focused on a short sequence of 5 amino acids that separates a highly conserved lysyl residue from the active site cysteine (Fig. 1a, Trnka *et al.* (2020)). This sequence forms a loop structure which is not highly conserved for the identity of the single amino acid residues but for their number. We demonstrated that the loop structure is the main difference between the two classes.

We interconverted the two GRXs types into each other by either inserting the extended loop of class II human glutaredoxin 5 (*Hs*Grx5) into class I human glutaredoxin 2 (*Hs*Grx2) or by deleting the extended loop of class II *Hs*Grx5 to transform it into a shorter class I-type loop. Moreover, we exchanged the monothiol active site "CGFS" motif of *Hs*Grx5 with the dithiol "CSYC" motif of *Hs*Grx2 in both the wild-type *Hs*Grx5 and in the variant lacking the loop.

Exploiting different *in vitro* techniques, such as the HED assay and the roGFP2 assay (see Chapter 1.6), we demonstrated that the enzymatic activity of the two types of proteins can be switched by the presence/absence of the loop. In particular, the modified *Hs*Grx2 with an extended *Hs*Grx5 class II-type loop was massively compromised in its reduction and oxidation capacities. On the contrary, the class II *Hs*Grx5 lacking the loop gained the completely new ability to reduce and was able to oxidize roGFP2 almost 10 times faster compared to the wild type *Hs*Grx5.

By spectroscopic analysis, we investigated whether the presence or absence of the extended loop changed the GRXs absorption bands, indicative of Fe–S cluster bound to the protein. Loop substitution indeed altered the spectral characteristics of the holo-protein complexes (the fully assembled dimer including the [2Fe–2S] cluster), aligning them more closely with the other class. Interestingly, the substitution of the *Hs*Grx5 active site with the class I "CSYC" motif did not cause significant changes in the absorbance bands of the Fe–S cluster, highlighting the role of the loop structure for the coordination with the cluster.

We also tested the *in vivo* function of the engineered proteins. Using zebrafish as a model. The endogenous mitochondrial class II *Dr*Grx5 was silenced resulting in lower embryo survival, while expression of human class I *Hs*Grx2 or *Hs*Grx5-loop (class II GRX carrying a class I-type loop) did not complement the loss of the endogenous GRX. Expression of both human *Hs*Grx5 and modified *Hs*Grx2 with an extended class II-type loop rescued the viability of the fish embryos.

Moreover, circular dichroism studies revealed that the presence or absence of the extended loop had a notable effect on the conformation of the dimeric holo-complex of *Hs*Grx2 and

*Hs*Grx5 with consequences on the orientation and stability of the coordinated [2Fe–2S] cluster. The angle of the monomers is believed to be a prerequisite for efficient transfer of the cluster and changes in the position of the components of the complex likely have significant implications for the overall functionality of the class II GRXs (Fig. 3a.1)

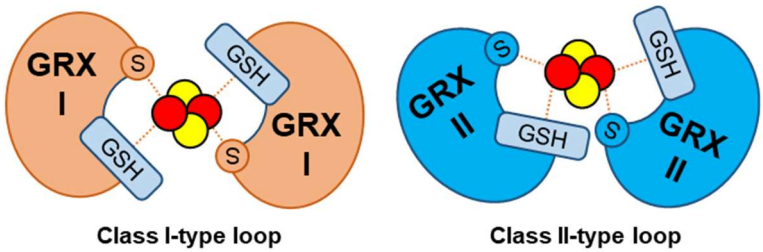

Fig. 3a.1 | Model of the holo-complexes formed by representatives of the two different glutaredoxin classes. Circular dichroism spectra suggest that the loop structure determines the conformation of the dimeric holo-complex. Hence, GRXs with class I-type loop (GRX I) can coordinate a [2Fe–2S] cluster in a more stable way but results in less cluster mobility. Class II-type loop (GRX II) instead leads to the rotation of the second monomer, inducing the shift and rotation of the coordinated [2Fe–2S] cluster. As a result, the cluster binding is less stable but more mobile.

In conclusion, our findings not only demonstrated that the absence of the loop is the key to efficient redox activity but also the presence of the loop influences the structure of the holo-dimer, critical for the iron-sulfur cluster coordination. This study represents a significant step forward in understanding *in vivo* processes such as Fe–S cluster biogenesis and trafficking.

My personal contribution to this study was the purification of recombinant Arabidopsis GRXC1, which was used as positive CxxC-type (class I) GRX control for the redox assays. In particular, I performed the HED assay to calculate the relative kinetic data shown in Table 1. The raw data of the assay are deposited in the supplementary data set available online under “Source Data”. The run is depicted in Supplementary Fig. 6, panel top-left (see Section 3a.3).

I also purified the redox-sensitive roGFP2 and its single-cysteine variant roGFP2 C204S. I performed a roGFP2 interaction assay where the pre-reduced sensor was re-oxidized by GRXC1 after addition of glutathione disulfide (GSSG) (Supplementary Fig. 3b; raw data available online under “Source Data”). I further confirmed sensor oxidation by measuring the entire sensor excitation spectra before and after the assay (Supplementary Fig. 3c, d). Moreover, I proved that the single-cysteine sensor variant cannot be oxidized and thus remains in its reduced state. Supplementary Fig. 3f shows that the single-cysteine sensor is in any case glutathionylated after reaction with GRXC1. The supplementary information I generated is provided after the manuscript, in Section 3a.3.

This research was relevant for this thesis since it gave important insights into how to engineer the class II glutaredoxin S15 of Arabidopsis, to characterize its activity *in vitro* and further

understand its *in vivo* role in plant mitochondria. The results of those findings are presented in the next Chapter 3b.

3a.2 | Manuscript

Attached on the following pages is the manuscript published in *Nature Communications (doi.org/10.1038/s41467-020-17323-0)*.

nature COMMUNICATIONS

ARTICLE

https://doi.org/10.1038/s41467-020-17323-0 OPEN

Molecular basis for the distinct functions of redox-active and FeS-transfering glutaredoxins

Daniel Trnka[1,9], Anna D. Engelke[2,9], Manuela Gellert[1,9], Anna Moseler[3,8], Md Faruq Hossain[1], Tobias T. Lindenberg[4], Luca Pedroletti[3], Benjamin Odermatt[4], João V. de Souza[5], Agnieszka K. Bronowska[5], Tobias P. Dick[6], Uli Mühlenhoff[7], Andreas J. Meyer[3], Carsten Berndt[2] & Christopher Horst Lillig[1✉]

Despite their very close structural similarity, CxxC/S-type (class I) glutaredoxins (Grxs) act as oxidoreductases, while CGFS-type (class II) Grxs act as FeS cluster transferases. Here we show that the key determinant of Grx function is a distinct loop structure adjacent to the active site. Engineering of a CxxC/S-type Grx with a CGFS-type loop switched its function from oxidoreductase to FeS transferase. Engineering of a CGFS-type Grx with a CxxC/S-type loop abolished FeS transferase activity and activated the oxidative half reaction of the oxidoreductase. The reductive half-reaction, requiring the interaction with a second GSH molecule, was enabled by switching additional residues in the active site. We explain how subtle structural differences, mostly depending on the structure of one particular loop, act in concert to determine Grx function.

[1] Institute for Medical Biochemistry and Molecular Biology, University Medicine, University of Greifswald, Greifswald, Germany. [2] Department of Neurology, Medical Faculty, Heinrich-Heine University Düsseldorf, Düsseldorf, Germany. [3] Institute of Crop Science and Resource Conservation, University of Bonn, Bonn, Germany. [4] Institute of Neuroanatomy, University Clinics, University of Bonn, Bonn, Germany. [5] Chemistry, School of Natural and Environmental Sciences, Newcastle University, Newcastle NE1 7RU, UK. [6] Division of Redox Regulation, DKFZ-ZMBH Alliance, German Cancer Research Center (DKFZ), Heidelberg, Germany. [7] Institute for Cytobiology and Cytopathology, Philipps University Marburg, Marburg, Germany. [8] Present address: UMR 1136 Interactions Arbres/Microorganismes, Université de Lorraine, Vandoeuvre-lès-Nancy, France. [9] These authors contributed equally: Daniel Trnka, Anna D. Engelke, Manuela Gellert. ✉email: horst@lillig.de

Glutaredoxins (Grxs) were first described as electron donors for essential metabolic processes, such as the reduction of ribonucleotides and activated sulfate[1–3]. These initially described Grxs (also known as class I or dithiol Grxs), herein termed CxxC/S-type Grxs, share a consensus CPYC active site motif that enables the proteins to catalyze the glutathione (GSH)-dependent reduction of protein disulfides. Later on, these Grxs were also recognized for their ability to specifically reduce mixed disulfides formed between protein thiols and GSH, a reaction termed de-glutathionylation[4]. A subgroup of the CxxC/S-type Grxs in which the prolyl residue in the active site is replaced by seryl or glycyl residues (C(S/G)YC) can complex a Fe_2S_2 cluster at the interface of a dimeric complex of two Grxs ligated by the two N-terminal active site thiols and the thiols of two non-covalently bound GSH molecules[5–9].The de-glutathionylation reaction requires only the more N-terminal cysteinyl residue in the active site of the CxxC/S-type Grxs and was thus termed the monothiol reaction mechanism. In brief, the reaction is initiated by a nucleophilic attack of the thiolate of this cysteinyl residue on the glutathione moiety of the glutathionylated protein. This results in the reduction of the protein substrate and a mixed disulfide between the N-terminal cysteinyl residue of the Grx active site and GSH (Grx-S-SG). Subsequently, this disulfide is reduced by a second molecule of GSH. The basis for this reduction of the mixed disulfide is a second GSH binding site on the Grxs that was suggested to activate GSH as the reducing agent[10]. In general, most CxxC/S-type Grxs also catalyze the direct reduction of protein disulfides in a thiol−disulfide exchange reaction (termed dithiol reaction mechanism, summarized, e.g., in ref. [11]). In some cases, for instance the reduction of mammalian ribonucleotide reductase by Grx1, protein disulfides may react with GSH first yielding a glutathionylated protein that is subsequently reduced by the Grx in the monothiol reaction mechanism[12]. It is important to state that all these reactions and steps are reversible equilibrium reactions, the direction of which is defined by thermodynamic constrains, i.e. the concentrations and redox potential of the GSH/glutathione disulfide (GSSG) redox couple. Under conditions that lead to a transient increase in the amounts of GSSG, Grxs will catalyze the glutathionylation of proteins at the expense of GSSG. In fact, the oxidation of the engineered redox-sensitive roGFP2 disulfide by GSSG was suggested to be catalyzed in the monothiol reaction mechanism[13].

Around 30 years following the first description of the CxxC/S-type Grxs, a second group of Grxs came into focus. These proteins share a consensus CGFS active site motif and are also known as class II or monothiol Grxs, herein termed CGFS-type Grxs. These proteins function in iron metabolism, i.e. bacterial, mitochondrial, or plastidal FeS cluster biogenesis[14–19] and the trafficking of iron in the cytosol of eukaryotic cells[20,21]. These functions critically depend on the ability of the CGFS-type Grxs to bind a Fe_2S_2 cluster in a mode similar to those of the CxxC/S-type Grxs[22,23]. Still, the function of the CGFS-type Grxs could not be rescued by FeS-coordinating CxxC/S-type Grxs in a yeast Δ*grx5* mutant, indicating different roles of the coordinated clusters for the functions of both classes of Grxs[15]. Both Grx classes share the same basic fold, including all motifs required for the interaction with GSH moieties[24]. The more N-terminal active site cysteinyl residue is fully conserved between all classes of Grxs. Despite of the presence of all these features required for the activity as GSH-dependent oxidoreductase, CGFS-type Grxs lack significant activity with established model substrates or physiological substrates of the CxxC/S-type Grxs (summarized, e.g., in ref. [25]).

In this study, we re-investigated the structural differences of the two main classes of Grxs to solve the mystery of the missing FeS transferase activity of the CxxC/S-type and the lack of oxidoreductase activity of the CGFS-type Grxs. We hypothesized that not a radically different substrate specificity accounts for the lack of activity, but rather slightly different modes of GSH binding. The validity of our hypothesis was analyzed in vitro and in vivo using engineered mutants from both Grx subfamilies.

Results

Major differences in substrate specificity are unlikely. One proposed explanation for the lack of significant oxidoreductase activity of the CGFS-type Grxs may be that their substrate specificity differs radically from those of the CxxC/S-type Grxs. Substrate recognition and interaction of the Grxs is largely determined by their electrostatic properties[26]. We have compared the electrostatic properties of both the types of Grxs from various species (Supplementary Fig. 1). These demonstrate a considerable degree of similarity between the surface potential at and surrounding the active sites. These features, together with the conservation of all four motifs required for GSH binding[24], do not support a radically different substrate specificity or reaction mechanisms as the reason for the lack in oxidoreductase activity of the CGFS-type Grxs.

Alternative loop structures are the main difference. Next, we re-evaluated the structural differences between two Grx classes in more detail (Fig. 1). The general fold in both classes of Grxs is very similar following the classical thioredoxin fold[27]. This is also true for the binding of GSH. Figure 1b, c depict GSH bound to the surfaces of human Grx2 (CxxC/S-type, b) and human Grx5 (CGFS-type, c) from the structures of the Fe_2S_2 holo-complexes deposited in the PDB. As discussed earlier[10,24], both classes use the same four motifs to bind GSH non-covalently for the ligation of the FeS cluster and redox reactions, respectively. The largest deviation between the substrate binding sites of both Grxs was identified in the loop region directly adjacent to the more N-terminal active site cysteinyl residue. All CGFS-type Grxs contain an extension in this loop of 5 amino acid residues (Fig. 1a, yellow box). The N-terminal anchor point of this loop is a lysyl residue (Fig. 1a, red). This lysyl or (very rarely) an alternative arginyl residue is strictly conserved in all Grxs. In CxxC/S-type Grxs, the positive charge electrostatically interacts with the carboxyl group of the C-terminal glycyl residue of the GSH molecule. In the CGFS-type Grxs, however, the conformation of the extended loop following this residue shifts the orientation of the ε-amino group towards the thiol of the GSH molecule by 0.2 nm. This causes a re-orientation of the GSH thiol towards the amino group (Fig. 1d, e); in the CxxC/S-type Grxs this distance is >0.88 nm. This structural difference is not restricted to the two human mitochondrial Grxs. In fact, all deposited structures of CGFS-type and CxxC/S-type Grxs with non-covalently bound GSH show the same distinct features (Fig. 1e, blue: CxxC/S-type Grxs, gray: CGFS-type Grxs). The re-orientation of the lysine side chain is not dependent on binding of GSH, it is a feature present in all experimentally solved structures of the CGFS-type Grxs (Fig. 1f). Another conserved difference between the structures of the two classes is the orientation of the active site phenylalanyl and tyrosyl residues in the active sites, respectively (Fig. 1g). The position of the Phe side chain in the CGFS-type Grxs would, in fact, clash with the thiol of the GSH as bound in the CxxC/S-type Grxs. It will thus contribute to the different orientation of the GSH thiol groups in both classes of Grxs. These different orientations do profoundly affect the ligation and orientation of the Fe_2S_2 clusters and thus the overall conformation of the holo-complexes. Moreover, they will also affect the reactivity of the GSH thiol, and thus the formation of the mixed disulfide with the N-terminal active site thiol of the Grx. The alternative orientations of the active site phenylalanyl versus tyrosyl residues, together with the different orientation of the GSH thiols, will also affect the attack of the second

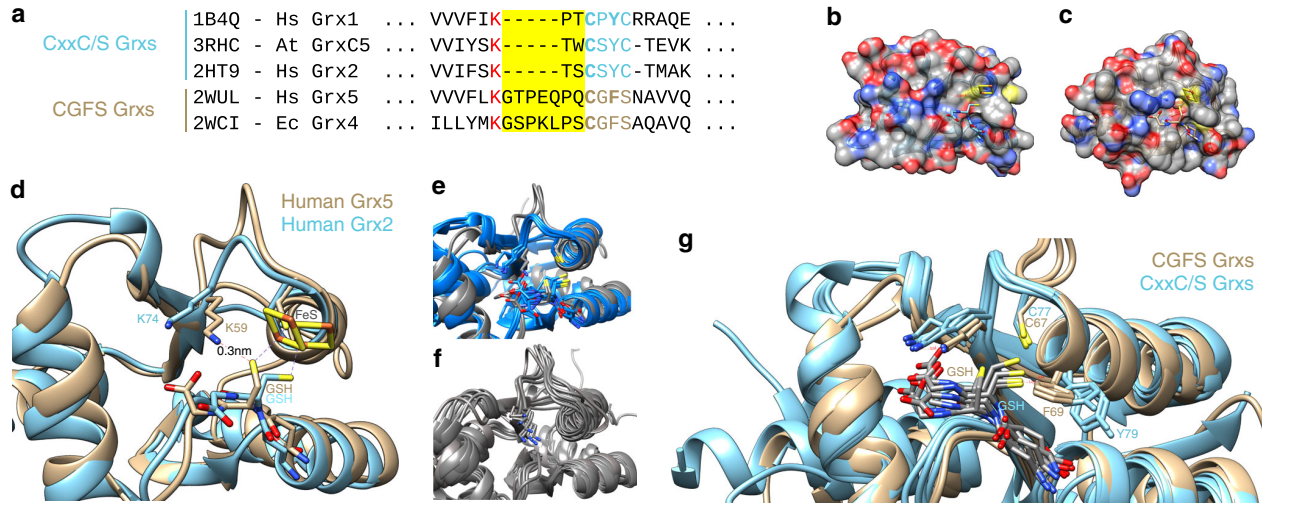

Fig. 1 Structural analysis of CxxC/S- and CGFS-type glutaredoxins. a Primary structure comparison of glutaredoxins from both classes around the active site: CxxC/S-type: Homo sapiens (Hs) Grx1 (gene glrx1, PDB 1B4Q), *Arabidopsis thaliana* (At) GrxC5 (gene GrxC5, PDB 3RHB), and Hs Grx2 (GLRX2, PDB 2HT9). CGFS-type: Hs Grx5 (GLRX5, PDB 2WUL) and *Escherichia coli* (Ec) Grx4 (grxD, PDB 1YKA). The alignment was generated by super-positioning of the 3D structures of the PDB entries. The critical lysyl residue is highlighted in red, the yellow box the class-specific loops, the active sites are shown in blue and brown according to the class. **b** Surface representation of one monomer of the human Grx2 holo-complex with bound GSH and Fe_2S_2 cluster (PDB 2HT9). **c** Surface representation of one monomer of the human Grx5 holo-complex with bound GSH and Fe_2S_2 cluster (PDB 2WUL). **d** Super-positioning of the structures of the CxxC/S-type human Grx2 (blue) and the CGFS-type human Grx5 (brown) including their bound FeS clusters and glutathione. **e** Comparison of the structures of all CxxC/S-type (blue) and CGFS-type (gray) Grxs with non-covalently bound GSH (PDB entries used: CGFS-type Grxs, 2XCI, 2WUL, 3RHC, and 5J3R; CxxC/S-type Grxs, 1B4Q, 2E7P, and 2HT9). **f** Comparison of the critical lysyl residue in all structures of CGFS-type Grxs (PDB entries: 2LKU, 2MNZ, 2WCI, 2WUL, 2YAN, 3GX8, 2IPZ, and 2ZYW). **g** Position of the phenylalanyl and tyrosyl residues in CGFS- (brown) and CxxC/S-type (blue) Grxs in relation to the GSH thiol (PDB entries used: CGFS-type Grxs, 2WUL and 3RHC; CxxC/S-type Grxs, 1B4Q, 2E7P, and 2HT9.

GSH on a Grx-GSH mixed disulfide intermediate, as this has to occur in an angle of 180°[28].

We performed all-atom molecular dynamics (MD) simulations with Grx2 and Grx5 as apo proteins and non-covalent Grx:GSH complexes for 100 ns. The results obtained confirm the distinct orientations of the GSH thiols and the conserved lysyl residues in both classes of Grxs (Fig. 2). Moreover, the simulations also indicate that the alternative orientation of the lysyl amino group is independent of GSH binding. The distance of the amino nitrogen of the lysyl residue in Grx2 to the more N-terminal active site thiol is either around 0.5 nm or around 0.8 nm (Fig. 2e), the larger distance is stabilized in the Grx2:GSH complex (Fig. 2a, g). For Grx5 it is stable around 0.5 nm independent of GSH binding (Fig. 2b, f, h). As seen in the crystal and NMR structures (Fig. 1d–f), the distance of the amino nitrogen to the GSH thiol is significantly larger in Grx2 (up to 2 nm, Fig. 2a, i) than in Grx5 (around 0.5 nm, Fig. 2b, j). The different orientations of the Phe versus Tyr residues in the active sites may be the result of the glycyl residue in the CGFS active site. This allows for alternative backbone conformations and favors slightly shifted phi-psi bond angles compared to the seryl residue in Grx2 (Fig. 2k, l). Noteworthy, in Grx5, but not Grx2, the orientation of the N-terminal active side thiol is locked in the presence of GSH (Fig. 2c). Our simulations also indicate that Grx5 binds GSH with higher binding energy, in fact the non-covalent Grx2:GSH complex partially dissociated during the simulation (Fig. 2d).

Based on our structural analyses, we proposed that alternative loop and active site structures are the molecular basis for the lack of activities of the CGFS-type Grxs as oxidoreductases and the CxxC/S-type Grxs as FeS transferases.

Mutants mimicking the alternative loop structures. To test our hypothesis, we have generated mutants of both human Grx2 and Grx5 (Supplementary Table 1). First, we have inserted the five amino acid extension GTPEQ into the structure of the CxxC/S-type Grx2 (Grx2-loop; Grx2 with a CGFS-type loop). Secondly, we shortened the loop in the CGFS-type Grx5 to enforce a CxxC/S-type conformation of the lysl side chain (Grx5-loop; Grx5 with a CxxC/S-type loop). In addition, we exchanged the CGFS active site of Grx5 to the Grx2 CSYC motif in both wild-type (Grx5-AS) and CxxC/S-type loop modified Grx5 (Grx5-loop/AS). All proteins were expressed recombinantly and purified as His-tagged proteins. Their structural stability was confirmed by differential scanning fluorimetry (thermofluor assay, Supplementary Fig. 2). All proteins were found to be thermally stable at the designated assay temperatures of 25 °C (activity assays) and 28 °C (zebrafish), the T_m for their denaturation was in between 35 °C and 57 °C.

Redox activity of the engineered proteins. We analyzed the oxidoreductase activity of the wild-type and mutant proteins using three different assays (Table 1, Fig. 3). The redox sensitive roGFP2[29] allows to follow both the oxidation and the reduction of a target protein. The reaction is thought to occur in three reversible steps through the glutathionylation of the protein before the formation of an intra-molecular disulfide:

$$\mathrm{Grx-SH + GSSG \rightleftharpoons Grx-S-SG + GSH} \quad (1)$$

$$\mathrm{Grx-S-SG + roGFP2-(SH)_2 \rightleftharpoons Grx-SH + roGFP2-S-SG} \quad (2)$$

$$\mathrm{roGFP2-S-SG \rightleftharpoons roGFP2-(S-S) + GSH} \quad (3)$$

We have confirmed this reaction sequence using mass spectrometry and a roGFP2 mutant lacking the second cysteinyl residue required for the reaction (Eq. 2) to trap the

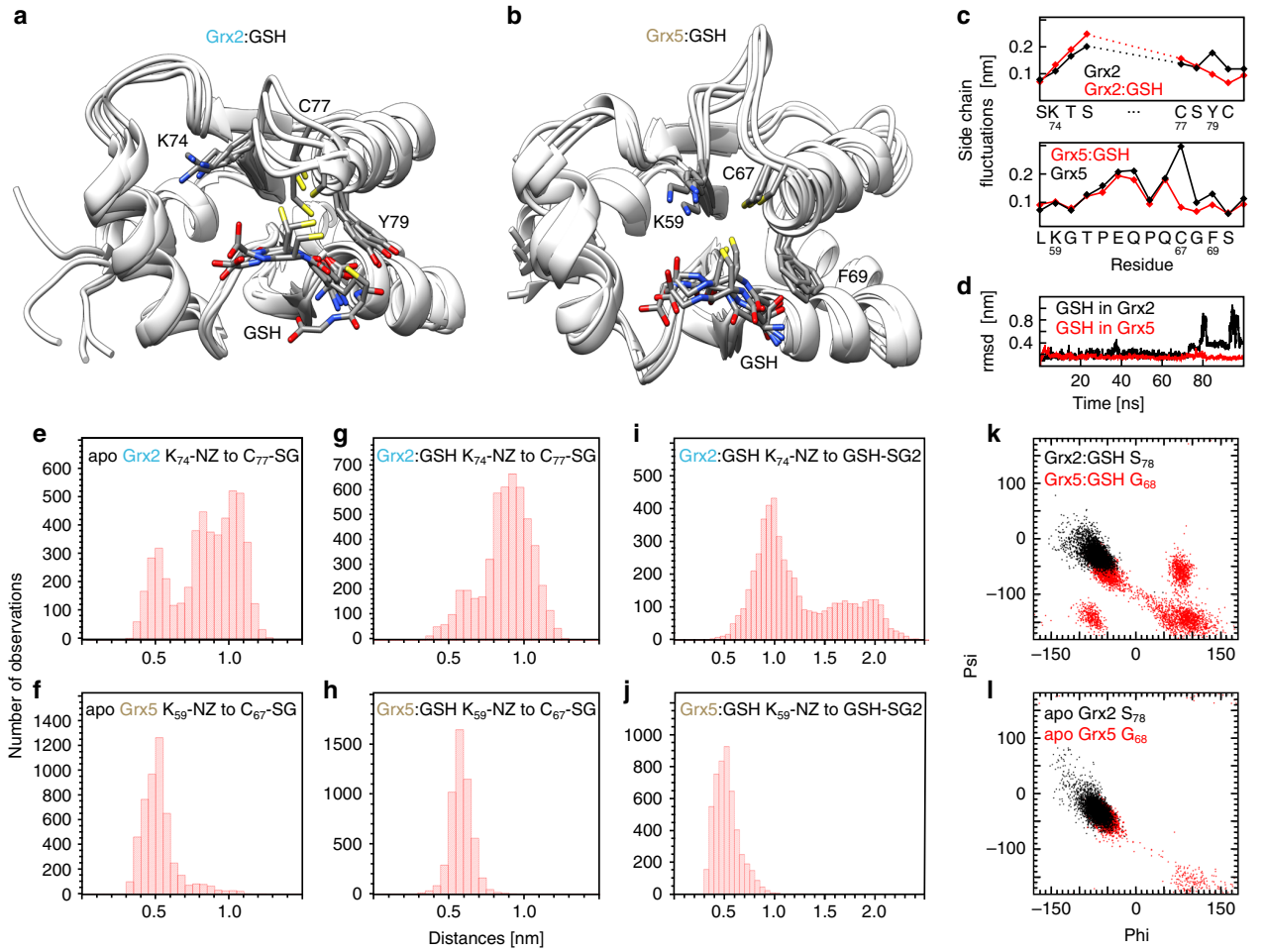

Fig. 2 Molecular dynamics simulations of human Grx2 and Grx5 GSH complexes. a, **b** The four most representative structures of the simulations runs of the Grx2:GSH (**a**) and the Grx5:GSH (**b**) complexes. The structures were identified with the UCSF chimera 'Ensemble Cluster tool' and represent 76% (Grx2:GSH) and 65% (Grx5:Grx) of all structures. **c** Side chain fluctuations of the residues of the loops and active sides in the Grx2:GSH complex and the Grx5:GSH complex, black squares: apo Grxs, red squares: Grx:GSH complexes. **d** Root mean square deviation (rmsd) of the GSH molecule bound in the complexes, black line: Grx2, red line: Grx5. **e**–**j** Distribution of distances of the indicated atom pairs over three independent simulations of 100 ns each. **e**–**h** Distances of the amino nitrogen atom of the strictly conserved lysyl residue to the thiol sulfur of the more N-terminal active site cysteinyl residue in apo Grx2 (**e**), apo Grx5 (**f**), the Grx2:GSH complex (**g**), and the Grx5:GSH complex (**h**). **i**, **j** Distances between the amino nitrogen atom of the strictly conserved lysyl residue to the thiol sulfur of the non-covalently bound GSH in the Grx2:GSH complex (**e**) and the Grx5:GSH complex (**f**). **k**–**l** Distribution of phi and psi angles of the active site seryl residue in Grx2 (black) and the respective glycyl residue in Grx5 (red) in the Ramachandran plots for the Grx:GSH complexes (**k**) and the apo proteins (**l**).

Table 1 Kinetic data of the proteins analyzed.

Protein	HED assay			roGFP2 reduction	roGFP2 oxidation
	$K_{m\ app}$ (HED)	k_{cat}	$k_{cat}{\cdot}K_m^{-1}$	k_{cat}	k_{cat}
	μM	s^{-1}	$M^{-1}s^{-1}$	min^{-1}	min^{-1}
AtGrxC1	773 ± 164	4.25 ± 0.27	5.50 × 103	(1.80 ± 0.28) × 10^{-1}	(4.49 ± 0.23) × 10^{-2}
Grx2-wt	165 ± 12	0.91 ± 0.03	5.54 × 103	(6.55 ± 0.17) × 10^{-2}	(8.35 ± 0.26) × 10^{-3}
Grx2-loop	317 ± 32	0.180 ± 0.01	5.68 × 102	(3.38 ± 0.24) × 10^{-4}	(2.11 ± 0.11) × 10^{-3}
Grx5-wt	-	0	-	0	(3.50 ± 0.07) × 10^{-3}
Grx5-AS	771 ± 64	0.07 ± 0.00	8.50 × 101	(6.68 ± 0.09) × 10^{-4}	(1.79 ± 0.13) × 10^{-2}
Grx5-loop	818 ± 51	0.02 ± 0.00	2.80 × 101	(1.09 ± 0.23) × 10^{-3}	(2.38 ± 0.08) × 10^{-2}
Grx5-loop/AS	924 ± 54	0.13 ± 0.00	1.45 × 102	(1.14 ± 0.02) × 10^{-3}	(2.81 ± 0.06) × 10^{-2}

All data are shown as mean ± sd (n = 7–8 for the HED assay, n = 4 (with 3 technical replicates) for the roGFP2 assays. Source data are provided as a Source data file.

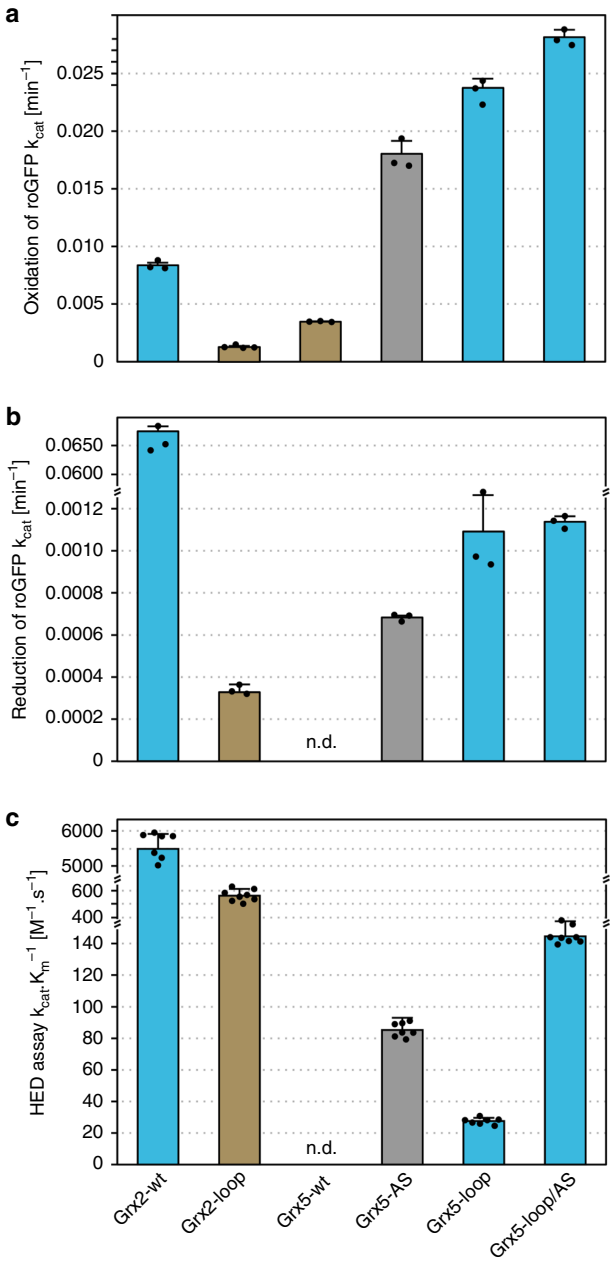

Fig. 3 Comparison of the catalytic activities of the wild-type and engineered Grxs. a Catalytic activity (k_{cat}) of the Grxs in the oxidation of roGFP2. **b** catalytic activity (k_{cat}) of the Grxs in the reduction of roGFP2; k_{cat} here was defined as the specific initial rate of roGFP oxidation and reduction, respectively, at 1μmol l^{-1} substrate concentration. **c** Catalytic efficiency ($k_{cat}.K_m^{-1}$) of the Grxs in the HED assay. All data are shown as mean ± sd. The roGFP2 assays were all performed at four different Grx concentrations with three replicates each, the HED assay data represent the mean of $n = 7$–8. n.d. not detected. Blue bars represents the proteins with the CxxC/S-type loop, brown bars proteins with the CGFS-type loop, the gray bar Grx5 with the CSYC active site of Grx2. Source data are provided as a Source data file.

glutathionylated roGFP2 intermediate (summarized in Supplementary Fig. 3). Notably, this roGFP2-SG intermediate is spectroscopically indistinguishable from the reduced protein. The kinetics of fluorescence changes must therefore reflect the overall reaction. In the reaction of the Grx-catalyzed oxidation of the 2-Cys roGFP2 by GSSG no significant amounts of the roGFP2-SG intermediate could be detected. We feel thus confident to conclude that oxidation of roGFP2 through Grxs is facilitated in steps 1–2–3 (Eqs. 1–3); reaction (2) is rate limiting for the full oxidation of roGFP2 and the ratiometric change in fluorescence excitation.

Grx2 catalyzed the reaction at reasonable rates, comparable to those of the classical CxxC-type Arabidopsis thaliana GrxC1 that was used as a highly efficient positive control in all reactions (Table 1, Supplementary Figs. 4 and 5). Introduction of the alternative loop in the Grx2-loop mutant led to a loss of 75% of its activity in the oxidative reaction. This reaction was also the only one in which wild-type Grx5 (Grx5-wt) showed some activity, ~42% of the activity of Grx2. Exchange of the active site to those of Grx2 increased the activity to 214%. The introduction of the CxxC/S-type loop increased the activity further to 285%, the combined Grx5-loop/AS mutation to 337% (Fig. 3a, details in Supplementary Fig. 4). Clearly, the shortening of the loop alone was sufficient to turn Grx5 into a highly efficient catalyst of roGFP2 oxidation.

Reduction of oxidized roGFP2 takes place in reaction order 3–2–1 (Eqs. 1–3, see above). The extension of the loop in the Grx2-loop mutant decreased the rate to 0.5%. Grx5-wt is inactive in this reaction, exchange of the active site (Grx5-AS) yielded an activity of ~1.1% of Grx2-wt. The CxxC/S-type loop in the Grx5-loop mutant increased the rate to 1.7% compared to Grx2-wt with some additional additive effect of the active site swap (Table 1, Fig. 3b, Supplementary Fig. 5). The shortening of the loop in the Grx5-loop mutant allowed the protein to facilitate the reaction, albeit at relatively low rates. Introduction of the extended CGFS-type loop diminished the oxidoreductase function of Grx2 with roGFP2 as model substrate.

The standard assay for Grxs is the so called HED (hydoxyethyl disulfide) assay. HED is a disulfide between two β-mercapto ethanol (βME) molecules. This assay requires both oxidative (5) and reductive (6) half reactions:

$$\mathrm{HED} + \mathrm{GSH} \rightleftharpoons \beta\mathrm{ME} - \mathrm{SG} + \mathrm{GSH}(\text{non enzymatically}) \quad (4)$$

$$\beta\mathrm{ME} - \mathrm{SG} + \mathrm{Grx} - \mathrm{SH} \rightleftharpoons \beta\mathrm{ME} + \mathrm{Grx} - \mathrm{S} - \mathrm{SG} \quad (5)$$

$$\mathrm{Grx} - \mathrm{S} - \mathrm{SG} + \mathrm{GSH} \rightleftharpoons \mathrm{Grx} - \mathrm{SH} + \mathrm{GSSG} \quad (6)$$

The HED assay is numerically not exact, since [HED] in the assay does not correspond to the [βME] in a 1:1 stoichiometric manner[30]. The assay does however allow to compare apparent catalytic efficiencies. Grx2 with the extended CGFS-type loop lost 90% of the wild-type protein's catalytic efficiency (Table 1, Fig. 3c, Supplementary Fig. 6). No activity could be recorded for Grx5-wt in this assay. All engineered variants, however, displayed clear activity: Grx5-AS at 1.5% of Grx2-wt, Grx5-loop at 0.5% and the combined Grx5-loop/AS protein at 2.6% (Fig. 3c).

We hypothesized that this markedly increased activity in the oxidation of roGFP2 resulted from an increased reactivity of the protein with glutathione disulfide moieties yielding the Grx-S-SG mixed disulfide (reaction 1). Oxidation of reduced Grx5-wt with GSSG led to 0.53 ± 0.10 mixed disulfides per monomer in equilibrium, the reaction of Grx5-loop with GSSG to 0.91 ± 0.10 Grx-S-SG mixed disulfides (Supplementary Fig. 7).

The oxidation and reduction of roGFP2 requires the formation of an intermediate protein-glutahione mixed disulfide (see above). To analyze the ability of the Grxs to facilitate the reversible (de)-glutathionylation of other proteins as well, we have analyzed their ability to de-glutathionylate proteins in HeLa cell extracts, and purified BSA and Sirt1 (Supplementary Fig. 8). In all cases, the Grx5 double mutant Grx5-loop/AS de-glutathionylated the

proteins most efficiently, while—with the exception of Sirt1—both the Grx5-loop and Grx5-AS mutants were less efficient. Wild-type Grx5 showed low (HeLa extract and BSA) or no (Sirt1) activity.

Effect of the mutations on FeS cluster binding and stability. Our structural analysis revealed significant differences in the orientation of the GSH thiol in both Grx classes. This thiol is also one of the ligands for the Fe_2S_2 cluster bound to the dimeric holo-complex of the proteins (Fig. 1). All wild-type and mutant proteins were isolated as brownish FeS proteins from *E. coli*. To ensure similar FeS occupancy of all proteins, we reconstituted the Fe_2S_2 cluster in both wild-type and mutant Grx2 and Grx5, respectively. We have quantified the FeS content of the reconstituted proteins from molar absorptivity and by colorimetric methods. The results, summarized in Supplementary Table 2, demonstrate a similar FeS occupancy for all proteins at around 70%.

The UV/VIS spectra (Fig. 4a) demonstrate the ability of all proteins to form FeS cluster-bridged holo-complexes. The spectra show the typical absorption bands around 320 and 420 nm. Especially the latter band differs between the Grx classes. We determined the second major peak of holo-Grx2 at 428 nm (using the 1st and 2nd derivatives of the spectra), the peak of holo-Grx5 at 413 nm (dotted vertical lines in Fig. 4a). For the Grx2-loop mutant, this absorption band shifted down to 421 nm, for the Grx5-loop mutant, the band shifted up to 420 nm. Hence, the exchange of the loop structures changed the spectral properties of the holo-protein complexes towards that of the other class. The exchange of the active site in Grx5-AS mutant did not induce notable changes in the absorbance of the FeS cofactor compared to Grx5-wt.

We have also analyzed the stability of the Fe_2S_2 clusters under ambient conditions at 25 °C. Clusters decay fitted well with first order kinetics (see the integrated first order kinetics in Fig. 4b). The clusters in Grx2-wt (first order rate constant: $(1.1 \pm 0.2) \times 10^{-5}\ s^{-1}$) were more stable than the ones bound to Grx5-wt ($k = (4.1 \pm 0.6) \times 10^{-5}\ s^{-1}$). This is in accordance with Grx5's function as FeS transferase. The Grx5-AS mutation stabilized the FeS clusters already ($k = (1.6 \pm 0.3) \times 10^{-5}\ s^{-1}$); the loop and loop/As mutations in Grx5 stabilized the clusters to essentially the same rate constant as observed for Grx2: Grx5-loop $k = (9.4 \pm 1.7) \times 10^{-6}\ s^{-1}$, Grx5-loop/AS $k = (1.2 \pm 0.2) \times 10^{-5}\ s^{-1}$.

Function of the engineered mutants in FeS biogenesis in vivo. The Grx5-loop mutant gained oxidoreductase activity, the Grx2-loop mutant lost most of its oxidoreductase activity. What about the in vivo function of the CGFS-type Grxs, i.e. mitochondrial FeS biogenesis? To analyze the functionality of our engineered mutants in vivo, we turned to the zebrafish model. The expression of the endogenous zebrafish mitochondrial CGFS-type Grx5 was silenced using the morpholino technique (see ref. [14]). The loss of Grx5 decreased the survival of the fish embryos 24 h post fertilization (hpf) from 98% (1 in 52) in our untreated control fish embryos to 56% in the knock-down fish (Fig. 5a, b). Complementation with mRNA for the expression of human Grx5-wt, that is not targeted by the morpholino, rescued the survival rate to 82%. The expression of human Grx2-wt (52% survival) as well as the Grx5-loop mutant (43% survival) with gained oxidoreductase activity could not complement the functional loss of Grx5. The human Grx2-loop mutant, that lost most of its oxidoreductase activity, however, rescued the viability of the Grx5-silenced embryos to the same level as the human Grx5-wt protein (83% survival).

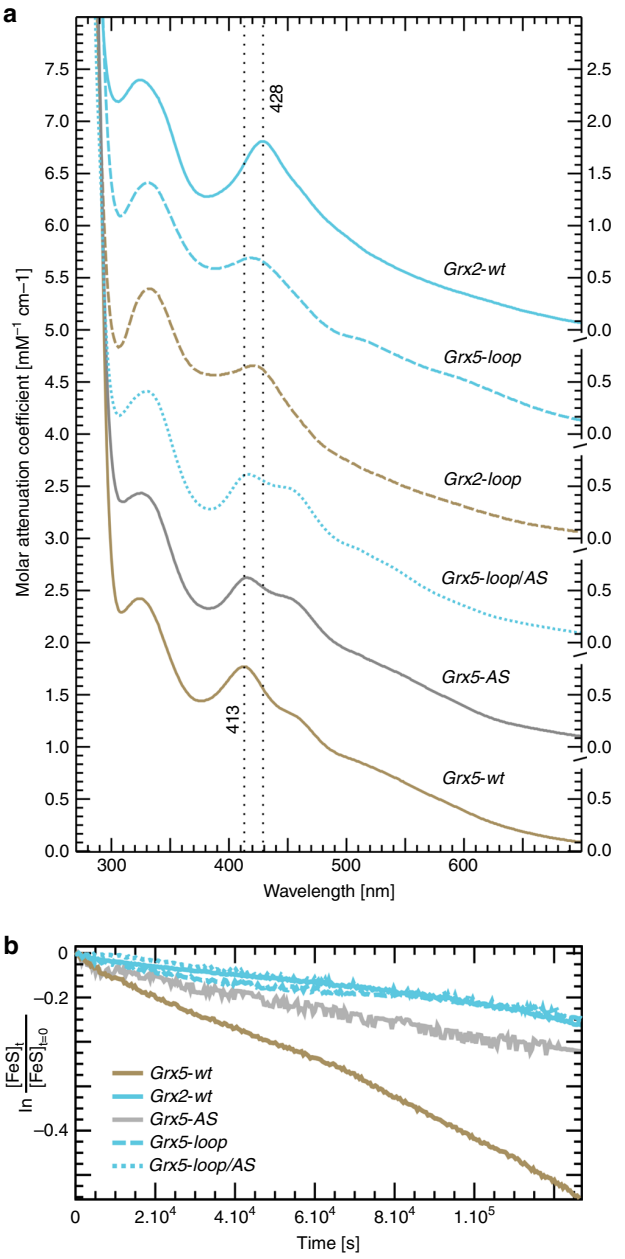

Fig. 4 FeS cluster binding of the wild-type and mutant Grx2 and Grx5. a Spectra of in vitro reconstituted holo-complexes as indicated. The upper spectra were all shifted 1 unit of $mM^{-1}\ cm^{-1}$ upwards for clarity. The dotted vertical lines indicate the calculated maximum of the absorption peak of wild-type Grx2 and Grx5, respectively. The spectra were normalized to the molar absorptivity of the proteins calculated from their primary structures using ProtParam. **b** Integrated first order kinetics of the decay of the FeS clusters of Grx2-wt, Grx5-wt, Grx5-AS, Grx5-loop, and Grx5-loop/AS under ambient conditions. The curves represent the mean of three independent experiments. Initial cluster concentrations ranged from 50 to 150 µmol l^{-1}. Rate constants were obtained from the slope of the curves following linear regression. $[FeS]_t$ is the cluster concentration at time point t, $[FeS]_{t=0}$ the initial cluster concentration. Blue curves represents the proteins with the CxxC/S-type loop, brown curves the proteins with the CGFS-type loop, the gray curve Grx5 with the CSYC active site of Grx2. Source data are provided as a Source Data file.

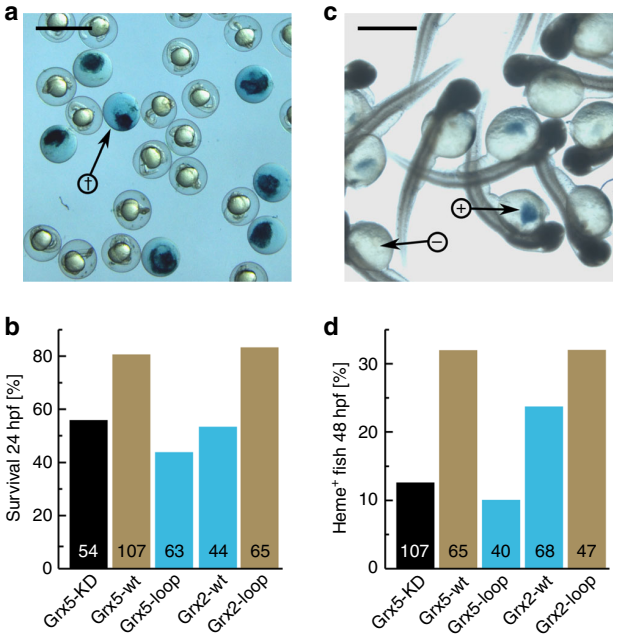

Fig. 5 Complementation of the loss of Grx5 in zebrafish by the engineered Grxs. a Example image and quantification **b** of dead (stained by methylen blue) and alive zebrafish embryos 24 h post fertilization (hpf). The arrow with cross in **a** points to a dead embryo. Heme-positive staining (**c**) and quantification (**d**) via diaminofluorene in zebrafish embryos 48 hpf. The arrows in **c** point to heme-positive (+) and negative (−) embryos. Zebrafish Grx5 was knocked-down by a specific morpholino (MO) and rescued with mRNA encoding human Grx5-wt, Grx5-loop, Grx2-wt, and Grx2-loop. All mRNAs contained the same standard mitochondrial target sequence. Percentage of survived embryos 24 hpf (**c**) and of heme positive embryos 48 hpf (**d**) was calculated. The bars for CGFS-type loop Grxs are depicted in brown, CxxC/S-type loop Grxs in blue. The numbers (*n*) of the analyzed (independently transfected) embryos were indicated within the bars. The scale bar in **a** measures 2 mm in length, the scale bar in **c** 0.5 mm. The black bar represents the controls, blue bars represents the proteins with the CxxC/S-type loop, brown bars proteins with the CGFS-type loop. Source data are provided as a Source data file.

The decreased survival of the Grx5-depleted embryos might be caused by a loss of FeS transfer to the various target proteins. One of these FeS proteins is ferrochelatase, the enzyme that catalyzes the final step in heme maturation[31]. As a result, only 13% of Grx5 knock-down fish could be stained positively for heme at 48 hpf (Fig. 5c, d), whereas 96% (69 of 72 embryos) of control fish were heme positive. Also this phenotype was partially rescued by mRNA encoding either human Grx5-wt or the Grx2-loop mutant (both resulted in 32% heme positive embryos), but not by the human Grx5-loop mutant (10%), and only to a lower extend by human Grx2-wt (24%). Together, these results confirm the gain of function in FeS cluster biosynthesis of the engineered loop mutant of Grx2.

Alternative conformations of the dimeric holo-complexes. The structures of the dimeric holo-complexes of Grx2 and Grx5 display profound differences (Fig. 6a, b). The different orientation of the GSH thiol (see also Fig. 2) causes different positions of the FeS clusters bound to the two classes of Grxs (Fig. 6a). This, in consequence, changes the relative orientation of the two protein subunits towards each other. Compared to the Grx2 holo-complex, the second Grx monomer in the Grx5 complex is rotated by ~90° (dotted arrow in Fig. 6b). We hypothesized that the CxxC/S- and CGFS-type loops predefine these different conformations.

Such differences can be assessed using CD spectroscopy. The ellipticity of the holo-complexes in the visible light, where the FeS cofactors absorb light (see Fig. 4a), is a result of the non-chiral cofactor complexed in between the chiral protein ligands. Hence, it also reflects the different orientations of the subunits towards each other. In fact, the spectra of wild-type Grx2 and Grx5 show some profound differences (Fig. 6c). Grx2-wt shows maxima at 305 and 447 nm, and a minimum at 368 nm. Grx5-wt displays maxima at 312, 362, and 456 nm, as well as minima at 346 and 408 nm. Our functional analysis of the proteins suggested that the Grx2-loop and the Grx5-loop mutants should form holo-complexes that reflect the conformations of the other Grx class. As depicted in Fig. 6c, the Grx5-loop mutant shows essentially the same features as Grx2-wt. In particular, it lost the Grx5-specific maximum at 362 nm and minimum at 408 nm. The Grx2-loop mutant displays features that better reflect the characteristics of the Grx5-wt protein than those of its Grx2-wt parent protein, it gained the Grx5-specific maximum in the region of 362 (shifted to 370) nm the minimum in the region of 408 nm (shifted to 420, Fig. 6c). The exchange of the active site in Grx5 resulted in CD properties that lay in between those of the two wild-type proteins.

Discussion

In general, CxxC/S-type Grxs function primarily in redox regulation and electron supply to metabolic enzymes, CGFS-type Grxs in FeS cluster biogenesis and iron trafficking[32,33]. The human CxxC/S-type Grx2 and the CGFS-type Grx5 can both form the dimeric or tetrameric holo-complex with the bridging Fe_2S_2 cluster that is ligated by the two N-terminal active site thiols and the thiols of two non-covalently bound GSH molecules[7,9,22]; both proteins are localized primarily in the matrix of mitochondria.

For Grx2, the Fe_2S_2 cluster was discussed to serve as redox sensor of the protein for its activation in response to various redox signals[5]. Disassembly of the holo-complex generates the apo-form of Grx2 that is enzymatically active in both the monothiol and dithiol reaction mechanisms and can be reduced by both GSH and thioredoxin reductase[12,34]. The protein protects from redox insults, e.g. induced by the anti-cancer drug doxorubicin[35–37], likely by catalyzing the reversible glutathionylation of membrane protein complexes inside mitochondria to regulate their function[38,39]. Moreover, the disassembly of the Grx2 Fe_2S_2 cluster by nitric oxide leads to the formation of dinitrosyl-diglutathionyl-iron complexes, and thus to the detoxification of nitric oxide and the protection of oligodendrocytes against inflammation-induced cell damage[40]. Grx5, on the other hand, is basically inactive as oxidoreductase. Instead, the protein has essential functions in the biogenesis of FeS proteins, a function that seems to be conserved in all eukaryotic cells[15–17,19,41–43]. At present, the most widely accepted function of the CGFS-type Grxs is to serve as transferases of their Fe_2S_2 clusters from the assembly machinery to target proteins[17,33]. Recent structural studies suggest that holo-Grx5 works as a metallo-chaperone preventing the Fe_2S_2 cluster to be released in solution and to form a transient, protein-protein intermediate with target proteins receiving the Fe_2S_2 cluster[44]. Based on these divergent functions, the consolidation of the CGFS-type and CxxC/S-type Grxs into one functional class as well as the classification of the CGFS-type Grxs as oxidoreductases may have to be revised.

The Grx5 mutant with the CxxC/S-type loop preceding the active site analyzed here (Grx5-loop) showed a clear increase in activity as reductant of the roGFP2 protein as well as in the HED assay (Table 1, Fig. 3). An even more pronounced increase in

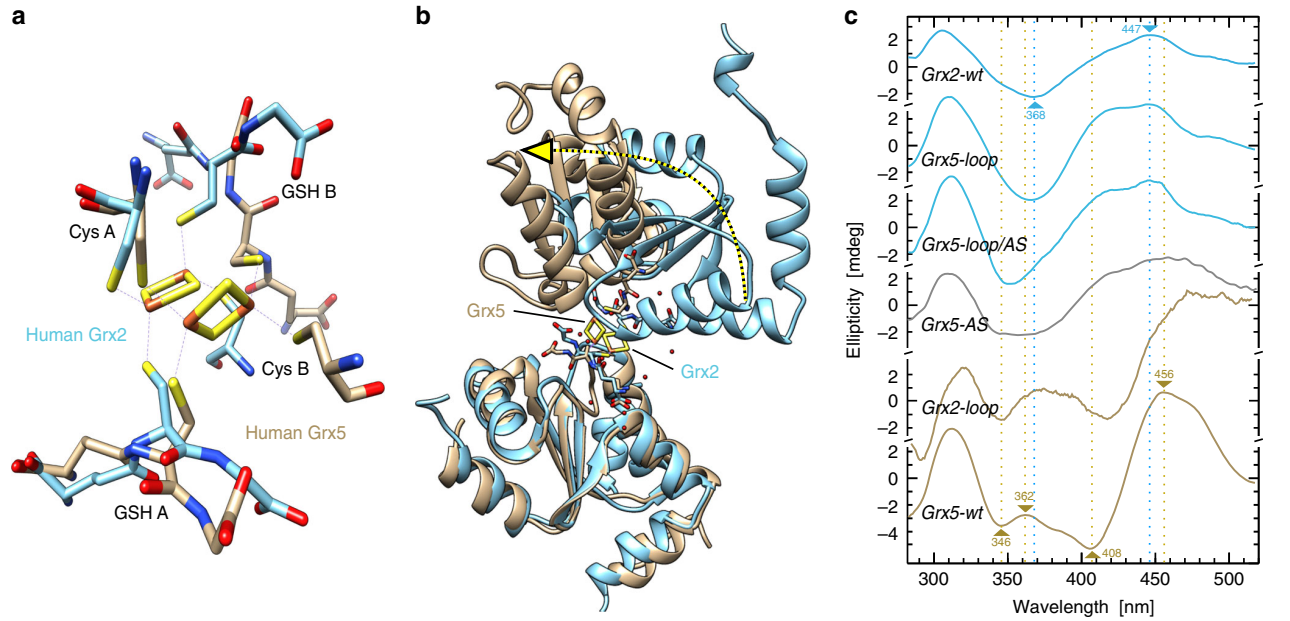

Fig. 6 The distinct loop structures determine the conformations of the holo-complexes. a, **b** Comparison of the dimeric holo-complexes of the CxxC/S-type Homo sapiens Grx2 (blue, PDB 2HT9) and the CGFS-type Homo sapiens Grx5 (brown, PDB 2WUL). The alternate positions of the Fe_2S_2 clusters are indicated (**a**) as well as the rotation of the second monomer induced by the shift and rotation of the FeS cluster (**b**, dotted arrow). The second dimer present in the 2WUL structure was omitted for clarity. **c** Circular dichroism spectra of the wild-type and engineered proteins as indicated. The concentration of the FeS holo-proteins was adjusted to 175 µM using the molar absorptivity of the FeS clusters for all CD spectra recorded. Blue curves represents the proteins with the CxxC/S-type loop, brown curves the proteins with the CGFS-type loop, the gray curve Grx5 with the CSYC active site of Grx2. Source data are provided as a Source Data file.

activity was demonstrated in the catalysis of the oxidation of the roGFP2 model substrate. In fact, here it exceeded the activity of the reference protein. Why is the oxidation reaction preferred? Both the reduction of roGFP2 as well as the HED assay require the reaction of the Grx-S-SG intermediate with a second molecule of GSH (reaction 1 reverse and reaction 6, see above), this second GSH binding site has only been established recently[10]. The additional exchange of the CGFS to the CSYC active site further increased the activity of the loop mutant. This was also true for the de-glutathionylation of the other proteins analyzed, the Grx5 double mutant was always the most efficient. Our results suggest that the Gly-Phe residues prefer a conformation that hinders the interaction with the second GSH molecule, likely by blocking or shifting the access to the mixed Grx-S-SG disulfide that has to be attacked in a 180° angle to form the tertiary intermediate required for the thiol-disulfide exchange reaction[28]. Likely, more features of the CGFS-type Grxs disfavor this second interaction, or— as suggested before—more features are required to fully facilitate the activation of the second GSH molecule for the attack of the disulfide[10].

The importance of the strictly conserved lysyl residue for the function of both classes of Grxs has been addressed before. Yeast CxxC/S-type Grx8p, which has an alanyl residue at the strictly conserved lysyl position, exhibited very low activity in standard assays[45,46]. Furthermore, mutations of the conserved lysyl residue in the CGFS-type human Grx5 or *A. thaliana* GrxS15 decreased the activity of various FeS-proteins indicating their decreased functionality as FeS cluster transfer proteins[19,47].

Our study provides evidence that the CGFS-type Grxs evolved in a way that hampers if not prevents the formation of the Grx-S-SG mixed disulfide intermediate between the N-terminal active site thiol and glutathione and thus impairs activity as oxidoreductases. Considering their primary function as Fe_2S_2 cluster carrier proteins, this would be a logical evolution as the thiol-disulfide oxidoreductase activity competes with the formation of the FeS holo-complex. The decreased stability of the Fe_2S_2 cluster coordinated by Grx5 (Fig. 4b) is the second consequence of the direct interaction of the amino group of the lysyl residue in the CGFS-type Grx loop with the GSH thiol, as demonstrated by the Grx5-loop mutant (Fig. 4b), that forms a considerable more stable holo-complex. The lower stability of the holo-complex may be seen as a prerequisite for a thermodynamically more favorable cluster transfer, as suggested, for instance, for *E. coli* CGFS-type Grx4 before[23]. The third consequence of the CGFS-type loop is a shift and rotation in the location of the Fe_2S_2 cluster in the holo-complex due to the rotation of the GSH cysteinyl side chain (see Figs. 1d, 2a, b, and 6a, b). This shift profoundly affects the orientation of the two monomers in the holo-complex towards each other (Fig. 6a). As discussed elsewhere, this may be a prerequisite for an efficient transfer of the Fe_2S_2 cluster[44]. Our CD spectroscopy results confirm the re-orientation of the two monomers in the engineered mutants towards the wild-type of the converse proteins. Our in vivo results in the zebrafish (Fig. 5) confirm the gain of FeS cluster transfer function in the Grx2-loop mutant, even though our rescue efficiency was relatively low compared to the one published before. Wingert et al.[14] had already pointed out the decrease in rescue efficiency with Grxs from different species. In addition, we changed the mitochondrial transit sequence of all proteins to one from *Neurospora crassa*, to exclude effects caused by different mitochondrial translocation efficiencies. It is likely that this further decreased rescue efficiency. The differences demonstrated using nearly 800 individual fish, however, support our conclusion that the loop is the major determinant discriminating between oxidoreductase activity and FeS transferase activity.

We suggest a refined model of Grx actions (summarized in Supplementary Fig. 9). As described earlier, all Grxs exhibit a similar binding site for the first GSH residue that is composed of

four conserved motifs, see[10,24]. This binding site allows the formation of the mixed disulfide Grx-S-SG intermediate that is a prerequisite for oxidoreductase activity. It does, however, also allow the non-covalent binding of GSH, a prerequisite for FeS cluster ligation. The major determinant of cluster ligation is the absence of a prolyl residue in the second position of the CxxC/S active site[7]. The extended loop preceding the active site, as well as the presence of a glycyl residue in position 2 of the active site in CGFS-type Grxs distinct two modes of GSH binding to this first binding site. One with the GSH thiol pointing towards the N-terminal active site Cys, in redox active Grxs, the second with the thiol orientation shifted away from the active site, in FeS transferring Grxs. The second GSH interaction site is required for the reduction of the Grx-S-SG intermediate by a second GSH molecule. The attack on the mixed disulfide requires access to the bond in a 180° angle to form the required tertiary intermediate[28]. The CGFS active site appears to partially block this access, however, our data also suggest that more features are required to fully facilitate this reaction.

In a recent study, Liedgens et al.[48] also addressed the structural differences between the two main classes of glutaredoxins with focus on the mechanistic understanding of the oxidoreductase functions of Grxs. Using *S. cerevisiae* Grx7, a CxxS-Type Grx, as model protein, the authors identified several key residues and quantified their contribution to the interactions with both the first and second molecule of GSH[48] (also see Supplementary Fig. 9). Together, these studies provide a mechanistic explanation for both the lack of redox activity of the CGFS-type Grxs as well as their higher propensity for Fe_2S_2 cluster transfer by affecting both the stability of the holo-complex as well as their interaction with target proteins. A small shift of only 0.2 nm in the position of the ε-amino group of a strictly conserved lysyl residue at the beginning of distinct loops separates the two Grx classes. These different conformations affect the position and reactivity of the GSH cysteinyl thiol, the orientation of the ligated Fe_2S_2 cluster, and the orientation of the monomers in the dimeric holo-complex. While the primary effect may seem small, the ripple effects profoundly control the functions of the proteins.

Methods

Materials. Chemicals and enzymes were purchased at analytical grade or better from Sigma-Aldrich (St. Louis, MO, USA). GSNO was synthesized as described by Hart et al.[49].

Structural analysis. Structures were acquired from the RSCB PDB Protein Data Bank [http://www.rcsb.org], ligands and water molecules were removed using Pymol. The most representative structure of NMR ensembles was identified using UCSF Chimera[50]. All pre-oriented protein structures were used to further compute the electrostatic potential and the iso-surfaces of the electrostatic potential. PQR files were generated using pdb2pqr[51] applying the amber force-field. VMD (visual molecular dynamics)[52] and APBS (Adaptive Poisson-Boltzmann Solver)[53] were used to compute the electrostatic potential in an aqueous solution containing 150 mM mobile ions at a temperature of 298 K.

Molecular dynamics simulations. For Grx2, PDB 2FLS was used for both simulations of the apo-protein and GSH complex. For Grx5, 2MMZ was used for the apo protein and 2WUL for the GHS-bound complex. All structures were prepared for MD simulations using UCSF Chimera[50] including the removal of all water molecules, non-complexed ions, and crystallization additives; adding any missing loops and residues via MODELLER[54] and using Dunbrack rotamer library[55]. Side chains with alternate location were fixed by selecting the highest-occupancy conformers. Preparation of the GSH complexes included parametrization of γ-glutamate residue using ACPYPE[56], with GAFF force field[57] and AM1-BCC[58] partial atomic charges assigned. All simulations were performed using Gromacs 2016.3[59]. The protein was parameterized using the AMBER99SB-ILDN force field, with the TIP3P water model[60]. Box distance was set to 1 nm and periodic boundary conditions were applied. The box was solvated and Na^+ and Cl^- ions were added at 0.1 M concentration to maintain unit neutrality. The solvated systems were energy minimized and equilibrated. The minimization ran using steepest descent for 1000 cycles followed by the conjugate gradient. Energy step size was set to 0.001 nm and the maximum number of steps was set to 50,000. The minimization was stopped when the maximum force fell below 1000 kJ/mol/nm using the Verlet cut-off scheme. Treatment of long-range electrostatic interactions was set to Particle Mesh-Ewald (PME)[61], and the short-range electrostatic and van der Waals cut-off set to 1.0 nm. Following the energy minimization, heating to 300 K was performed for 20 ps with a time step of 2 fs and position restraints applied to the backbone in a NVT ensemble. The constraint algorithm used was LINCS, which was applied to all bonds and angles in the protein[62]. The cut-off for non-bonded short-range interaction was set to 1.0 nm with the Verlet cut-off scheme. The temperature coupling was set between the protein and the non-protein entities by using a Berendsen thermostat, with a time constant of 0.1 ps and the temperature set to reach 300 K with the pressure coupling off. Pressure equilibration was run at 300 K with a Parrinello-Rahman barostat on and set to 1 bar[63] in a NPT ensemble. The equilibration trajectories were set to 5 ns (discarded from the analysis), and the production MD simulations were performed for 100 ns. Each simulation was run in triplicates. Analysis of the trajectories was performed using GROMACS tools, including root-mean-square deviation (RMSD) to assess overall stability, per-residue root-mean-square fluctuation (RMSF) to assess the local flexibility, and all the distributions of interatomic distances and angles.

Cloning of expression constructs. The Homo sapiens Grx2 (Grx2c) expression construct was described in[64,65], the Arabidopsis thaliana GrxC1 construct in[10]. Homo sapiens Grx5 was amplified from human cDNA by PCR using DyNAzyme EXT DNA polymerase (Thermo Scientific, Waltham MA, USA) and ligated into the pGEMT plasmid (Promega, Madison WI, USA). Primers were designed to insert restriction sites for NdeI (forward 5′-CACACACATATGGGCTCGGGC GCGGGC-3′) and BglII (reverse 5′-CACACAAGATCTTCACTTGGAGTCTTG GTCTTTCTTTTCATCTAAAAGG-3′). The insert was ligated into the expression vector pET15b (Merck, Darmstadt, Germany). Mutations of the amino acid sequence and amplification of the plasmids were performed by rolling circle PCR. We generated the mutants using the indicated primers and the reversible complementary counterparts if not stated otherwise. Grx5-loop: (5′-GGACAAGGT GGTGGTCTTCCTCAAGCCCCAGTGCGGCTTCAGCAACG-3′). For Grx2-loop: 5′-GGGACGCCGGAGCAGACATCCTGTTCTTACTGTACAATGG-3′ as forward and 5′-CTGCTCCGGCGTCCCTTTTGAGAAAATCACCACACAAT TATCAGAAATTG-3′ as reverse primer. The CGFS active site in Grx5 was replaced for CSYC using 5′-CAGCCCCAGTGCAGCTACTGCAACGCCGTG-3′ for the wild-type (Grx5-AS) and 5′-CAAGCCCCAGTGCAGCTACTGCAAC GCCGTG-3′ for the Grx5-loop mutant (Grx5-loop/AS). All constructs and mutations were verified by sequencing (Microsynth Seqlab, Göttingen, Germany).

Recombinant expression and purification. Homo sapiens Grx2, Grx5, their mutants, E. coli IscS, roGFP2, D. rerio Sirt1, and AtGrxC1 were expressed as His-tagged proteins and purified via immobilized metal affinity chromatography[7,10,66]. SDS-PAGE was performed using pre-casted TGX stain-free gels (4–20%, BioRad, Hercules CA, USA) and imaged according to the manufacturers' instructions. Protein concentration was determined at 280 nm ($\varepsilon_{Grx5} = 11{,}585$ and $\varepsilon_{Grx2} = 7{,}450$ M^{-1} cm^{-1}).

Differential scanning fluorimetry (thermofluor assay). The thermal stability of wild-type and mutant proteins were assayed using the thermofluor assay[67]. In brief, 10 µM protein, re-buffered in PBS were mixed with SYPRO Orange (1:100 diluted, Sigma-Aldrich) and heated in a CFX96 Real Time System from BioRad in 0.5 K increments from 20 to 95 °C in one hour. The increase in fluorescence due to binding of the dye to hydrophobic regions exposed during denaturation was recorded using the instrument's "FRET"-settings. The curves represent the average of seven replicates.

Kinetics of the reduction and oxidation of roGFP2 by Grxs. Interaction of Grxs with roGFP2 was analyzed in vitro by ratiometric time-course measurements on a fluorescence plate reader[68] (Clariostar; BMG Labtech, Offenburg, Germany) with excitation at 390 ± 10 and 480 ± 10 nm and detection of emitted light at 520 nm with a bandwidth of 10 nm. In all, 0.1 M potassium phosphate buffer pH 7.8 containing 1 µM roGFP2 and the respective Grx. Ratiometric time-course measurements were carried out with initially oxidized or reduced roGFP2, respectively. For the latter, the protein was reduced with 10 mM DTT for at least 20 min. The remaining DTT was removed by desalting spin columns (Zeba Spin Desalting Columns, Thermo Scientific). For interaction analysis with oxidized roGFP2, GSH (in 0.1 M potassium phosphate buffer, pH 7.0) was included to a final concentration of 2 mM. When working with reduced roGFP2, a highly negative redox potential of the glutathione buffer was maintained by addition of 10 U glutathione reductase and 100 µM NADPH. For oxidation of roGFP2, 40 µM GSSG were included in the wells. H_2O_2 and DTT were used at a final concentration of 10 mM to preset roGFP2 to the fully oxidized and fully reduced state, respectively, and determine maximum and minimum fluorescence ratios of roGFP2 as reference values. A basal background fluorescence of buffer or buffer containing 100 µM NADPH was subtracted from fluorescence reads for all samples. The k_{cat} calculated was defined as the specific initial rate of roGFP2 oxidation and reduction, respectively, at 1µmol·l^{-1} substrate concentration.

HED assay. The hydroxyethyl disulfide (HED) assay[34] was performed in a 96-well plate format. The final reaction mixtures of 200 µl contained 100 mM potassium phosphate buffer (pH 7.8), 200 µM NADPH, 1 mM GSH, 3×10^{-3} g l^{-1} glutathione reductase from yeast (G3664, Merck, Darmstadt, Germany), and variable concentrations of HED (0–1 mM). The concentration of the Grxs was optimized for all proteins individually and lay between 0.5 and 62.5 µg ml^{-1}. The assay was run for 20 min. The linear range of the decrease in absorption was determined for each reaction individually.

Analysis of protein de-glutathionylation. De-glutathionylation using single substrates follows a protocol published in ref. [66]. 30 µM of BSA (Sigma) or recombinant D. rerio Sirt1 were reduced with 10 mM DTT, desalted (Zeba spin, Thermo Fisher), glutathionylated with 150 µM Di-Eosin-GSSG (kind gift of Arne Holmgren), and desalted again. 10 µM substrate were incubated for 15 min at 37 °C with 1 mM GSH and ±50 µM pre-reduced Grx mutants. After SDS-PAGE, fluorescent GSH was visualized by UV-light and proteins were stained with Coomassie. For the de-glutathionylation of whole lysates, 40 µg HeLa cell extract was incubated with 5 mM GSSG. After desalting (PD10, GE Healthcare), cell extracts were incubated with 1 mM GSH and ±60 µM Grx mutants for five minutes. Proteins were separated by SDS-PAGE, glutathionylated proteins were visualized with anti-GSH antibodies (#ab19534, abcam, dilution 1:1000) after Western blotting.

Determination of free thiols. Proteins were reduced (50 mM DTT, 30 min), re-buffered in TE buffer (100 mM Tris/HCl and 2 mM EDTA) using NAP-5 columns (GE Healthcare) and incubated with 10 mM GSSG before alkylation with 10 mM NEM for 20 min each. Next, free thiols were assayed (see below) yielding the values for the oxidized and alkylated samples. Part of the samples were re-reduced (50 mM DTT, 30 min) and re-buffered again in TE to remove the excess of DTT. Next, the samples were incubated with 1 mM DNTB and 1% SDS in TE buffer for 15 min. Absorbance was measured at a wavelength of 412 nm using a 96-well plate reader (Tecan Infinite M200). The amount of free thiols was calculated using the molar absorption coefficient of $\varepsilon = 14{,}150\ M^{-1}\ cm^{-1}$ and normalized to the amount of protein in the sample.

Reconstitution and stability of FeS-clusters. Approximately 100 µM of the recombinant redoxins were incubated at RT under argon atmosphere in sodium phosphate buffer pH 8.0, including 200 mM NaCl, 5 mM DTT, 1 mM GSH, 200 µM $Fe(NH_4)_2$ $(SO_4)_2$ 250 µM cysteine, 10 µM pyridoxal phosphate, 1 µM *E. coli* IscS. After 2 h, the proteins were desalted using Zeba Spin columns and UV/Vis-spectra were recorded. Kinetics of FeS-cluster disassembly were followed at 420 nm at 25 °C. UV/Vis-spectra and kinetics were recorded by an UV-1800 spectrometer (Shimadzu Kyoto, Japan). FeS clusters were quantified as outlined below. All experiments were repeated independently at least three times. Initial cluster concentrations ranged from 80 to 250 µmol l^{-1}. Rate constants were obtained from the slope of the integrated first order kinetics: $\ln([FeS]_t \cdot [FeS]_{t=0}^{-1}) = k \cdot t$, where $[FeS]_t$ is the cluster concentration at time point t, $[FeS]_{t=0}$ the initial cluster concentration, k the first order rate constant and t the time in seconds.

Determination of iron content. The FeS content per Grx dimer was calculated from UV-vis spectra using the molar absorptivity of the cluster in 100% dimeric Grx2 at 430 nm as determined in ref. [69] ($\varepsilon_{430} = 3260\ M^{-1}\ cm^{-1}$). Protein bound iron was quantified according to ref. [70]. In brief, 200 µM of in vitro freshly reconstituted proteins were mixed with 0.5-fold volumes of 0.6 M HCl and 0.142 M $KMnO_4$ and incubated for 2 h at 60 °C. Next, the solution was incubated for 30 min at room temperature with 0.1-fold of the original sample volume of 6.5 mM ferrozine, 13.1 mM neocuproine 6, 2 M ascorbic acid, and 5 M ammonium acetate. The iron-ferrozine complex was quantified photometrically at 562 nm.

Zebrafish. Zebrafish (AB/TL wild-type line, ZFIN ID: ZDB-GENO-960809-7; ZDB-GENO-990623-2) were kept in standard conditions (14 h light and 10 h dark, 28 °C, pH 7.2, 500 µS). Eggs were, in accordance with national law, obtained by natural spawning. The morpholino targeting Grx5 (5-′CTGTCGACCTAAAAA CGCTATTCAT-3′, ZFIN ID: ZDB-MRPHLNO-051203-1)[14] was synthesized by Gene Tools and diluted in water to a concentration of 3 mM. Human wild-type and mutant Grx2 and five cDNAs were modified with the mitochondrial transit sequence of *Neurospora crassa* subunit 9 of the F1F0 ATPase (aa 1–69) and then cloned into the pGEM-T-Easy Vector (Promega) 3′ of the T7 promotor. Capped mRNA was generated with the mMessage/mMachine Kit (Ambion) and subsequently polyadenylated with the Poly(A) Tailing Kit (Invitrogen). Survival rate was determined after injection of 1.77 nl of a 1/8 dilution of the Grx5 morpholino and of 60 pg capped polyadenylated mRNA into embryos at the one cell stage. Dead embryos were visualized by accumulation of methylen blue present in the tank water at a concentration of 2 mg/l and counted 24 hpf. Heme staining was performed after injection of 1.77 nl of a 1/10 dilution of the morpholino together with 120 pg mRNA 48 hpf. Non-injected embryos served as controls. For dechorionation, embryos were incubated for 15 min with 0.5 mg/ml Pronase (Sigma). Staining with 2,7-Diaminofluorene (Sigma) was performed as described previously[21]. All zebrafish experiments were performed in accordance with the German and European animal welfare legislation. According to the EU Directive 2010/63/EU on the protection of animals used for scientific purposes, early life-stages of zebrafish are not protected as animals until the stage of being capable of independent feeding, i.e. 5 days post fertilization.

CD spectroscopy. CD spectra were recorded in 300 mM NaCl, 50 mM sodium phosphate, 1 M sucrose, pH 8 with the FeS holo-proteins at 175 µM concentration in a Jasco J-810 spectropolarimeter. The concentrations of the holo proteins were determined based on the molar absorptivity of the FeS-holo proteins at 430 nm ($\varepsilon_{430} = 3260\ M^{-1}\ cm^{-1}$)[69]. Buffer-only spectra were subtracted. A standard sensitivity of 100 mdeg was used with a data pitch of 1 nm, a scanning speed of 50 nm/min, and a band width of 1 nm. Three spectra were accumulated for each sample.

Software. All numerical calculations (spectra, kinetics) were performed and visualized using grace [https://plasma-gate.weizmann.ac.il/Grace/]. Blot pictures were normalized using ImageLab 5.1 (Biorad) and Gimp [https://www.gimp.org/]. Densiometric analyses were performed using ImageLab and ImageJ [https://imagej.net]. Structures were depicted using UCSF Chimera[49]. Picture panels and reaction schemes were generated using Inkscape [https://inkscape.org/].

Reporting summary. Further information on research design is available in the Nature Research Reporting Summary linked to this article.

Data availability

The data that support this study are available by the corresponding author upon reasonable request. Most of the data that support the findings of this study are available within the paper and its supplementary material. Source data are provided with this paper.

Received: 30 October 2019; Accepted: 18 June 2020;
Published online: 10 July 2020

References

1. Wilson, L. G., Asahi, T. & Bandurski, R. S. Yeast sulfate-reducing system. I. Reduction of sulfate to sulfite. *J. Biol. Chem.* **236**, 1822–1829 (1961).
2. Holmgren, A. Hydrogen donor system for Escherichia coli ribonucleoside-diphosphate reductase dependent upon glutathione. *Proc. Natl Acad. Sci. USA* **73**, 2275–9 (1976).
3. Russel, M., Model, P. & Holmgren, A. Thioredoxin or glutaredoxin in Escherichia coli is essential for sulfate reduction but not for deoxyribonucleotide synthesis. *J. Bacteriol.* **172**, 1923–1929 (1990).
4. Gravina, S. A. & Mieyal, J. J. Thioltransferase is a specific glutathionyl mixed disulfide oxidoreductase. *Biochemistry* **32**, 3368–3376 (1993).
5. Lillig, C. H. et al. Characterization of human glutaredoxin 2 as iron-sulfur protein: a possible role as redox sensor. *Proc. Natl Acad. Sci. USA* **102**, 8168–8173 (2005).
6. Feng, Y. et al. Structural insight into poplar glutaredoxin C1 with a bridging iron-sulfur cluster at the active site. *Biochemistry* **45**, 7998–8008 (2006).
7. Berndt, C. et al. How does iron sulfur cluster coordination regulate the activity of human glutaredoxin 2? *Antioxid. Redox Signal.* **9**, 151–157 (2007).
8. Rouhier, N. et al. Functional, structural, and spectroscopic characterization of a glutathione-ligated [2Fe-2S] cluster in poplar glutaredoxin C1. *Proc. Natl. Acad. Sci. USA.* **104**, 7379–7384 (2007).
9. Johansson, C., Kavanagh, K. L., Gileadi, O. & Oppermann, U. Reversible sequestration of active site cysteines in a 2Fe-2S-bridged dimer provides a mechanism for glutaredoxin 2 regulation in human mitochondria. *J. Biol. Chem.* **282**, 3077–82 (2007).
10. Begas, P., Liedgens, L., Moseler, A., Meyer, A. J. & Deponte, M. Glutaredoxin catalysis requires two distinct glutathione interaction sites. *Nat. Commun.* **8**, 14835 (2017).
11. Lillig, C. H. & Berndt, C. Glutaredoxins in thiol/disulfide exchange. *Antioxid. Redox Signal.* **18**, 1654–1665 (2013).
12. Zahedi Avval, F. & Holmgren, A. Molecular mechanisms of thioredoxin and glutaredoxin as hydrogen donors for Mammalian s phase ribonucleotide reductase. *J. Biol. Chem.* **284**, 8233–8240 (2009).
13. Meyer, A. J. & Dick, T. P. Fluorescent protein-based redox probes. *Antioxid. Redox Signal.* **13**, 621–650 (2010).
14. Wingert, R. A. et al. Deficiency of glutaredoxin 5 reveals Fe-S clusters are required for vertebrate haem synthesis. *Nature* **436**, 1035–1039 (2005).
15. Rodríguez-Manzaneque, M. T., Tamarit, J., Bellí, G., Ros, J. & Herrero, E. Grx5 is a mitochondrial glutaredoxin required for the activity of iron/sulfur enzymes. *Mol. Biol. Cell* **13**, 1109–21 (2002).

16. Mühlenhoff, U., Gerber, J., Richhardt, N. & Lill, R. Components involved in assembly and dislocation of iron-sulfur clusters on the scaffold protein Isu1p. *EMBO J.* **22**, 4815–25 (2003).
17. Bandyopadhyay, S. et al. Chloroplast monothiol glutaredoxins as scaffold proteins for the assembly and delivery of [2Fe-2S] clusters. *EMBO J.* **27**, 1122–1133 (2008) .
18. Jbel, M., Mercier, A. & Labbé, S. Grx4 monothiol glutaredoxin is required for iron limitation-dependent inhibition of Fep1. *Eukaryot. Cell* https://doi.org/10.1128/EC.00015-11 (2011).
19. Moseler, A. et al. The mitochondrial monothiol glutaredoxin S15 is essential for iron-sulfur protein maturation in Arabidopsis thaliana. *Proc. Natl Acad. Sci. USA* **112**, 13735–13740 (2015).
20. Mühlenhoff, U. et al. Cytosolic monothiol glutaredoxins function in intracellular iron sensing and trafficking via their bound iron-sulfur cluster. *Cell Metab.* **12**, 373–385 (2010).
21. Haunhorst, P. et al. Crucial function of vertebrate glutaredoxin 3 (PICOT) in iron homeostasis and hemoglobin maturation. *Mol. Biol. Cell* **24**, 1895–1903 (2013).
22. Johansson, C. et al. The crystal structure of human GLRX5: iron-sulfur cluster co-ordination, tetrameric assembly and monomer activity. *Biochem. J.* **433**, 303–311 (2011).
23. Iwema, T. et al. Structural basis for delivery of the intact $[Fe_2S_2]$ cluster by monothiol glutaredoxin. *Biochemistry* **48**, 6041–6043 (2009).
24. Berndt, C. & Lillig, C. H. Glutathione, glutaredoxins, and iron. *Antioxid. Redox Signal.* **27**, 1235–1251 (2017).
25. Herrero, E. & de la Torre-Ruiz, M. A. Monothiol glutaredoxins: a common domain for multiple functions. *Cell. Mol. Life Sci.* **64**, 1518–30 (2007).
26. Berndt, C., Schwenn, J.-D. & Lillig, C. H. The specificity of thioredoxins and glutaredoxins is determined by electrostatic and geometric complementarity. *Chem. Sci.* **6**, 7049–7058 (2015).
27. Martin, J. L. Thioredoxin–a fold for all reasons. *Struct. Lond. Engl. 1993* **3**, 245–50 (1995).
28. Deponte, M. & Lillig, C. H. Enzymatic control of cysteinyl thiol switches in proteins. *Biol. Chem.* **396**, 401–413 (2015).
29. Meyer, A. J. et al. Redox-sensitive GFP in Arabidopsis thaliana is a quantitative biosensor for the redox potential of the cellular glutathione redox buffer. *Plant J.* **52**, 973–986 (2007).
30. Szajewski, R. P. & Whitesides, G. M. Rate Constants and equilibrium constants for thiol-disulfide interchange reactions involving oxidized gluthathione. *J. Am. Chem. Soc.* **102**, 2011–2026 (1980).
31. Lange, H., Mühlenhoff, U., Denzel, M., Kispal, G. & Lill, R. The heme synthesis defect of mutants impaired in mitochondrial iron-sulfur protein biogenesis is caused by reversible inhibition of ferrochelatase. *J. Biol. Chem.* **279**, 29101–29108 (2004).
32. Lillig, C. H., Berndt, C. & Holmgren, A. Glutaredoxin systems. *Biochim. Biophys. Acta* **1780**, 1304–1317 (2008).
33. Rouhier, N., Couturier, J., Johnson, M. K. & Jacquot, J.-P. Glutaredoxins: roles in iron homeostasis. *Trends Biochem. Sci.* **35**, 43–52 (2010).
34. Johansson, C., Lillig, C. H. & Holmgren, A. Human mitochondrial glutaredoxin reduces s-glutathionylated proteins with high affinity accepting electrons from either glutathione or thioredoxin reductase. *J. Biol. Chem.* **279**, 7537–7543 (2004).
35. Lillig, C. H., Lonn, M. E., Enoksson, M., Fernandes, A. P. & Holmgren, A. Short interfering RNA-mediated silencing of glutaredoxin 2 increases the sensitivity of HeLa cells toward doxorubicin and phenylarsine oxide. *Proc. Natl Acad. Sci. USA* **101**, 13227–13232 (2004).
36. Enoksson, M. et al. Overexpression of glutaredoxin 2 attenuates apoptosis by preventing cytochrome c release. *Biochem. Biophys. Res. Commun.* **327**, 774–779 (2005).
37. Diotte, N. M., Xiong, Y., Gao, J., Chua, B. H. L. & Ho, Y.-S. Attenuation of doxorubicin-induced cardiac injury by mitochondrial glutaredoxin 2. *Biochim. Biophys. Acta* **1793**, 427–38 (2009).
38. Taylor, E. R. et al. Reversible glutathionylation of complex I increases mitochondrial superoxide formation. *J. Biol. Chem.* **278**, 19603–10 (2003).
39. Hurd, T. R. et al. Glutathionylation of mitochondrial proteins. *Antioxid. Redox Signal.* **7**, 999–1010 (2005).
40. Lepka, K. et al. Iron-sulfur glutaredoxin 2 protects oligodendrocytes against damage induced by nitric oxide release from activated microglia. *Glia* **65**, 1521–1534 (2017).
41. Picciocchi, A., Saguez, C., Boussac, A., Cassier-Chauvat, C. & Chauvat, F. CGFS-type monothiol glutaredoxins from the cyanobacterium Synechocystis PCC6803 and other evolutionary distant model organisms possess a glutathione-ligated [2Fe-2S] cluster. *Biochemistry.* **46**, 15018–15026 (2007).
42. Camaschella, C. et al. The human counterpart of zebrafish shiraz shows sideroblastic-like microcytic anemia and iron overload. *Blood* **110**, 1353–8 (2007).
43. Ye, H. et al. Glutaredoxin 5 deficiency causes sideroblastic anemia by specifically impairing heme biosynthesis and depleting cytosolic iron in human erythroblasts. *J. Clin. Invest.* **120**, 1749–1761 (2010).
44. Banci, L. et al. [2Fe-2S] cluster transfer in iron-sulfur protein biogenesis. *Proc. Natl. Acad. Sci. USA.* **111**, 6203–6208 (2014).
45. Eckers, E., Bien, M., Stroobant, V., Herrmann, J. M. & Deponte, M. Biochemical characterization of dithiol glutaredoxin 8 from Saccharomyces cerevisiae: the catalytic redox mechanism redux. *Biochemistry* **48**, 1410–1423 (2009).
46. Tang, Y. et al. Structure-guided activity enhancement and catalytic mechanism of yeast grx8. *Biochemistry* **53**, 2185–2196 (2014).
47. Liu, G. et al. Functional analysis of GLRX5 mutants reveals distinct functionalities of GLRX5 protein. *J. Cell. Biochem.* **117**, 207–217 (2016).
48. Liedgens, L. et al. Quantitative assessment of the determinant structural differences between redox-active and inactive glutaredoxins. *Nat. Commun.* **11**, 1725 (2020).
49. Hart, T. W. Some observations concerning the S-nitroso and S-phenylsulphonyl derivatives of L-cysteine and glutathione. *Tetrahedron Lett.* **26**, 2013–2016 (1985).
50. Pettersen, E. F. et al. UCSF Chimera–a visualization system for exploratory research and analysis. *J. Comput. Chem.* **25**, 1605–1612 (2004).
51. Dolinsky, T. J. et al. PDB2PQR: expanding and upgrading automated preparation of biomolecular structures for molecular simulations. *Nucleic Acids Res.* **35**, W522–525 (2007).
52. Humphrey, W., Dalke, A. & Schulten, K. VMD: visual molecular dynamics. *J. Mol. Graph.* **14**, 33–38 (1996). 27–28.
53. Baker, N. A., Sept, D., Joseph, S., Holst, M. J. & McCammon, J. A. Electrostatics of nanosystems: application to microtubules and the ribosome. *Proc. Natl Acad. Sci. USA* **98**, 10037–10041 (2001).
54. Webb, B. & Sali, A. Protein structure modeling with MODELLER. *Methods Mol. Biol.* **1137**, 1–15 (2014).
55. Huang, C. C., Meng, E. C., Morris, J. H., Pettersen, E. F. & Ferrin, T. E. Enhancing UCSF Chimera through web services. *Nucleic Acids Res.* **42**, W478–484 (2014).
56. Sousa da Silva, A. W. & Vranken, W. F. ACPYPE—AnteChamber PYthon Parser interfacE. *BMC Res. Notes* **5**, 367 (2012).
57. Wang, J., Wolf, R. M., Caldwell, J. W., Kollman, P. A. & Case, D. A. Development and testing of a general amber force field. *J. Comput. Chem.* **25**, 1157–1174 (2004).
58. Jakalian, A., Jack, D. B. & Bayly, C. I. Fast, efficient generation of high-quality atomic charges. AM1-BCC model: II. Parameterization and validation. *J. Comput. Chem.* **23**, 1623–1641 (2002).
59. Van Der Spoel, D. et al. GROMACS: fast, flexible, and free. *J. Comput. Chem.* **26**, 1701–1718 (2005).
60. Lindorff-Larsen, K. et al. Improved side-chain torsion potentials for the Amber ff99SB protein force field. *Proteins* **78**, 1950–1958 (2010).
61. Darden, T., York, D. & Pedersen, L. Particle mesh Ewald: An N·log(N) method for Ewald sums in large systems. *J. Chem. Phys.* **98**, 10089–10092 (1993).
62. Hess, B., Bekker, H., Berendsen, H. & Fraaije, J. LINCS: a linear constraint solver for molecular simulations. *J. Comput. Chem.* **18**, 12 (1998).
63. Parrinello, M. & Rahman, A. Polymorphic transitions in single crystals: a new molecular dynamics method. *J. Appl. Phys.* **52**, 7182–7190 (1981).
64. Lundberg, M. et al. Cloning and expression of a novel human glutaredoxin (Grx2) with mitochondrial and nuclear isoforms. *J. Biol. Chem.* **276**, 26269–75 (2001).
65. Lönn, M. E. et al. Expression pattern of human glutaredoxin 2 isoforms: identification and characterization of two testis/cancer cell-specific isoforms. *Antioxid. Redox Signal.* **10**, 547–558 (2008).
66. Bräutigam, L. et al. Glutaredoxin regulates vascular development by reversible glutathionylation of sirtuin 1. *Proc. Natl Acad. Sci. USA* **110**, 20057–20062 (2013).
67. Ericsson, U. B., Hallberg, B. M., Detitta, G. T., Dekker, N. & Nordlund, P. Thermofluor-based high-throughput stability optimization of proteins for structural studies. *Anal. Biochem.* **357**, 289–298 (2006).
68. Aller, I., Rouhier, N. & Meyer, A. J. Development of roGFP2-derived redox probes for measurement of the glutathione redox potential in the cytosol of severely glutathione-deficient rml1 seedlings. *Front. Plant Sci.* **4**, 506 (2013).
69. Lillig, C. H. et al. Characterization of human glutaredoxin 2 as iron-sulfur protein: a possible role as redox sensor. *Proc. Natl Acad. Sci. USA* **102**, 8168–8173 (2005).
70. Fish, W. W. Rapid colorimetric micromethod for the quantitation of complexed iron in biological samples. *Methods Enzymol.* **158**, 357–364 (1988).

Acknowledgements

We wish to express their gratitude to Prof. Andreas Reichert (HHU Düsseldorf) for the plasmid pVTU-mtALP harboring the mitochondrial transit sequence of *Neurospora*

crassa subunit 9 of the F1F0 ATPase (amino acids 1–69), and to the Zebrafish Core Facility (Medical Faculty University Bonn). We are also grateful to Thomas Ruppert (ZMBH Heidelberg) and Evelyn Sollner for support with mass spectroscopy and analysis of single-Cys roGFP mutants. This work was supported by grants from the Deutsche Forschungsgemeinschaft (to A.J.M.: ME 1567/9-1, ME 1567/9-2, ME 1567/13-1; to CB: BE 3259/5-1, BE 3259/5-2, BE 3259/6-1; to CHL: LI 984/3-1, LI 984/3-2, LI 984/4-1, GRK1947-A1; to T.P.D.: DI 731/3-2).

Author contributions

D.T., A.D.E., M.G., A.M., M.F.H., T.T.L., L.P., B.O., and U.M. performed and analyzed the experiments. T.P.D. provided essential reagents and constructs. J.V.dS. and A.K.B. performed the molecular dynamics simulations and analyzed the data. A.J.M., C.B., and C.H.L. conceptualized the study and analyzed the data. CB and CHL wrote the paper.

Competing interests

The authors declare no competing interests.

Additional information

Supplementary information is available for this paper at https://doi.org/10.1038/s41467-020-17323-0.

Correspondence and requests for materials should be addressed to C.H.L.

Peer review information *Nature Communications* thanks Caryn Outten, and the other, anonymous, reviewer(s) for their contribution to the peer review of this work. Peer reviewer reports are available.

Reprints and permission information is available at http://www.nature.com/reprints

Publisher's note Springer Nature remains neutral with regard to jurisdictional claims in published maps and institutional affiliations.

3a.3 | Supplementary information I contributed

Supplementary Fig. 3

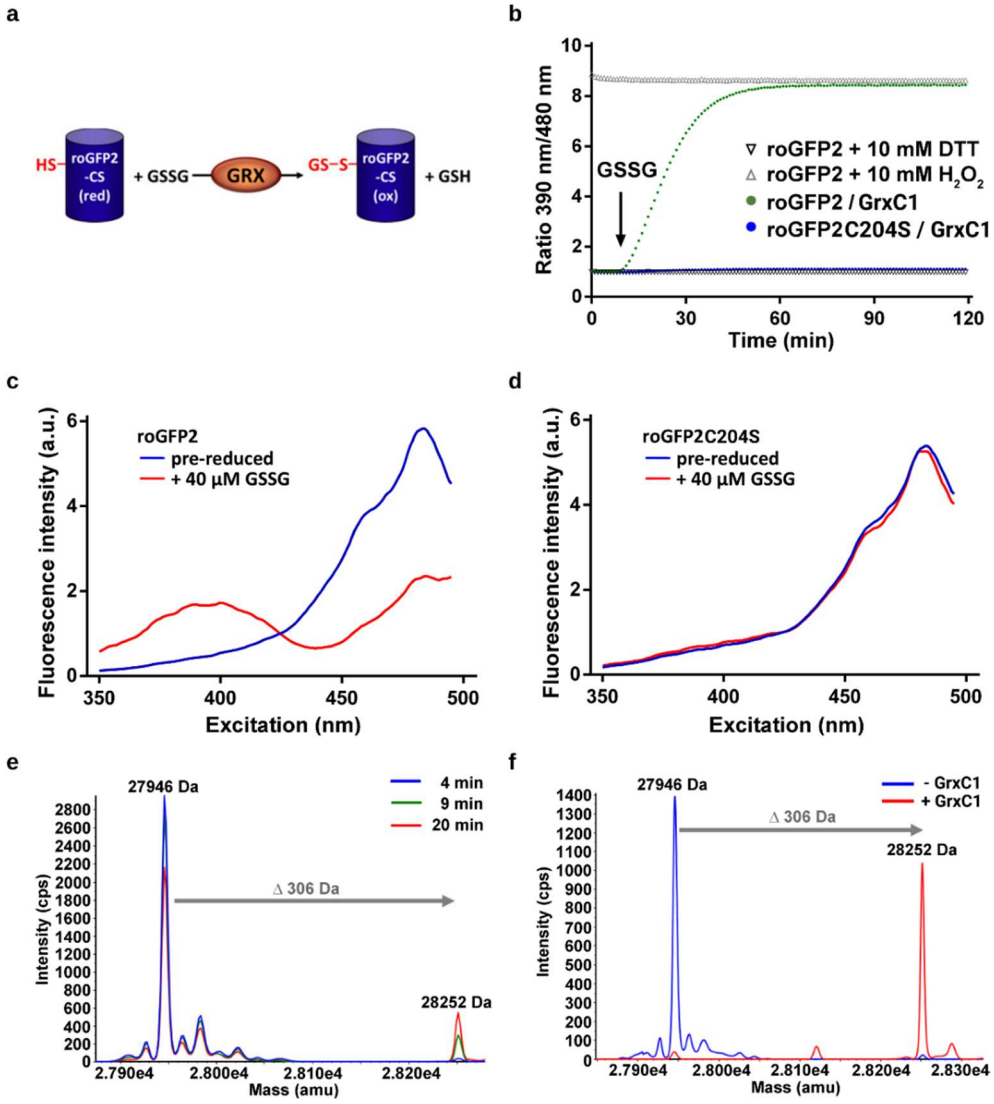

Supplementary Figure 3 – Mechanism of oxidation of the roGFP2 sensor. The roGFP2 sensor is oxidized via a glutathionylated intermediate (b, e-f), however, the ratiometric change of excitation properties only occurs after formation of the intra-molecular disulfide (c-d). Trapping of glutathionylated intermediates of glutaredoxin-mediated roGFP2 oxidation. (**a**) Glutaredoxin-mediated glutathionylation of single-cysteine roGFP2-C204S (roGFP2CS). (**b**) Time course for the Grx-mediated oxidation of roGFP2 and roGFP2-C204S triggered by addition of 40 µM GSSG (arrow). All data were normalized to the fluorescence ratios of DTT-treated proteins. (**c,d**) Excitation spectra of roGFP2 (**c**) and roGFP2-C204S (**d**) before and after oxidation by 40 µM GSSG in the presence of GrxC1. All proteins were pre-reduced by DTT, which was removed on a desalting column prior to the measurement. Spectra were collected with emission of 520 ± 5 nm (**e,f**) Identification of glutathionylated roGFP-C204S by ESI-Q-TOF analysis. Samples were injected either at different times after incubation of 5 µM roGFP2-C204S with 2 mM GSSG at pH 7.0 in the absence (**e**) or in the presence (**f**) of 5 µM Grx for 20 min. Molecular masses were determined with a precision of ±2 Da.

Supplementary Fig. 6

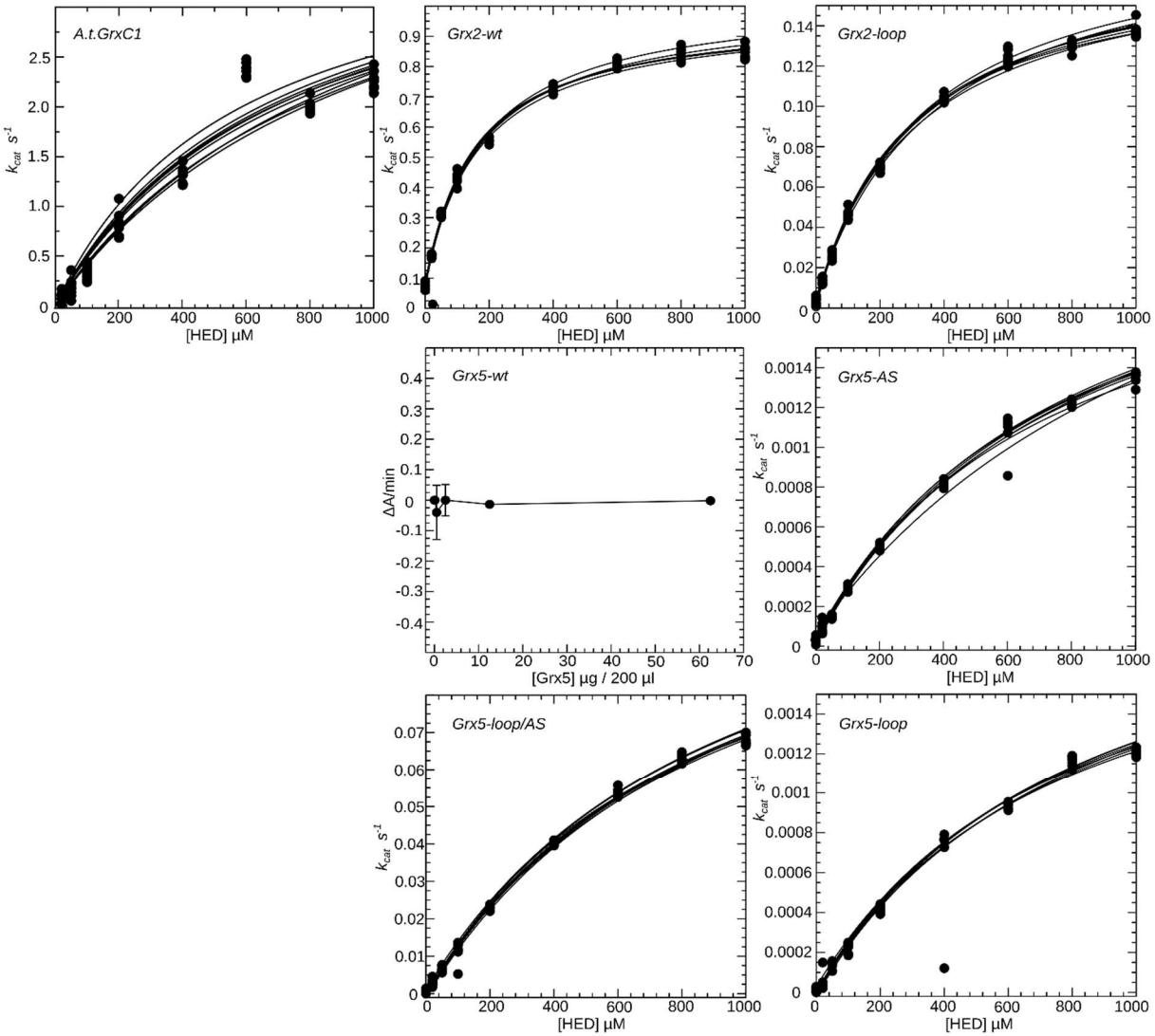

Supplementary Figure 6 - Kinetic analysis of the CGFS-type and CxxC/S-type Grxs in the HED assay. Michaelis-Menten plots of the HED concentration versus the catalytic activity. The curves represent the non-linear curve fitting to the original data (depicted as points) against the Michealis-Menten equation, n=7-8. Grx5-wt did not exhibit any activity in this assay as shown in the [enzyme] versus Δabsorbance-per-minute plot (mean ± sd, 8 biological replicates).

3b | Recombinant glutaredoxin S15 exhibits a limited oxidoreductase activity

Glutaredoxins (GRXs) cover several roles in different subcellular compartments, exhibiting diverse abilities depending on whether they belong to class I or class II (see Chapter 3a). The plant-specific class III GRXs is largely uncharacterised but recent studies report that the CC-type GRXs are *in vitro* inactive as GSH-dependent oxidoreductase (see Chapter 1.4) (Mrozek *et al.*, 2023).

Unlike in other eukaryotic cells, mitochondria in plants exclusively contain a single class II GRX, known as glutaredoxin S15 (GRXS15) (Moseler *et al.*, 2015; Ströher *et al.*, 2016). Thus, plant mitochondria lack class I GRXs (Schlößer *et al.*, 2023). Previous research reported that GRXS15 serves as essential Fe–S cluster transferase (Moseler *et al.*, 2015). However, whether GRXS15 can also act as oxidoreductases and substitute the functions of class I GRXs remains unclear.

In this chapter, we therefore investigated *in vitro* the putative oxidoreductase activity of Arabidopsis GRXS15 and three mutated versions. Specifically, we tested recombinant proteins lacking the mitochondrial targeting peptide (Supplementary Fig. 3b.1 and Appendix 1) for their oxidoreductase activity towards roGFP2 as a substrate (See Chapter 1.6). For the assay, we purified the roGFP2 sensor and the dithiol class I Arabidopsis GRXC1, which serves as positive control. Furthermore, we investigated the disulfide bond-mediated dimerization of GRXS15 by SDS-PAGE.

3b.1 | Results

3b.1.1 | Pre-reduction of GRXS15 increases its oxidation activity

Monothiol class II GRXs, including GRXS15, have been reported to have no *in vitro* reduction activity and generally a slow oxidation activity (Moseler *et al.*, 2015; Trnka *et al.*, 2020). Previous studies also examined the functional characteristics of the lysine mutant GRXS15 K83A, showing that this mutated version displayed enhanced oxidation activity but still no reduction activity (Moseler, 2017). Here, we tested the activity of both wild-type GRXS15 protein and its K83A variant towards roGFP2 and confirmed that GRXS15 K83A is about 2.5-fold more efficient in oxidising the pre-reduced sensor after addition of glutathione disulfide (GSSG), compared to the wild-type protein, although still at slower rate compared to GRXC1 (Fig. 3b.1). Our results also confirmed that, while GRXC1 could directly reduce roGFP2 after addition of GSH, both GRXS15 variants were completely lacking the reducing ability (Supplementary Fig. 3b.2).

Originally, we reasoned that the mutation of lysine 83 would negatively influence the binding of the glutathione molecule and therefore indirectly diminish the coordination of the [2Fe–2S] cluster. This may render the cysteines of the GRX more available for interaction with roGFP2, which may cause a more pronounced oxidoreductase activity (Moseler *et al.*, 2015). In order to test whether fully reduced cysteinyl residues are more prone to react with roGFP2 or with glutathione, we pre-reduced wild-type GRXS15 and the K83A mutant with DTT. We then desalted the enzymes to remove the reagent excess and tested the oxidoreductase ability of the enzymes following changes of roGFP2 fluorescence. To our surprise, we observed a massive enhancement in the ability of both pre-reduced GRXs to oxidise roGFP2. Wild-type GRXS15 and K83A variant displayed about 4-fold and 3-fold higher efficiency in oxidising the pre-reduced roGFP2, respectively (Fig. 3b.1).

Even more unexpectedly, both pre-reduced GRXs similarly displayed a minimal reduction ability. However, this activity was exceptionally slow to be considered negligible when compared with the activity of GRXC1. In fact, 3 µM of GRXS15 (3-fold the amount of GRXC1 in the same assay) was not able to reduce even 10 % of roGFP2 during a 3-hour reaction time (Supplementary Fig. 3b.2).

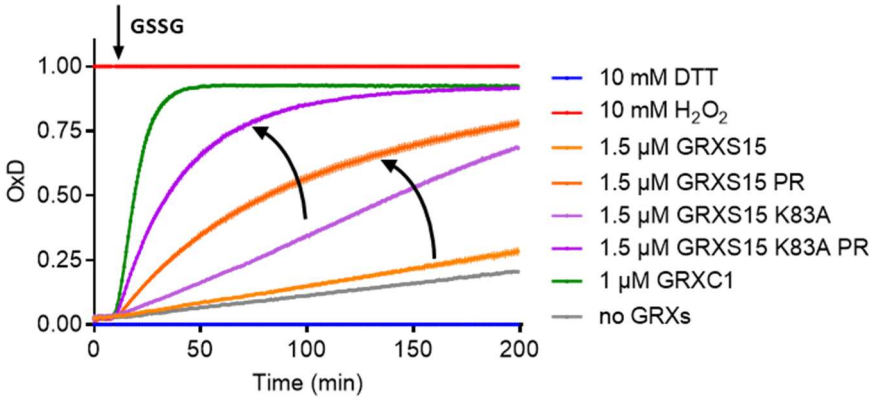

Fig. 3b.1 | Pre-reduction of GRXS15 accelerates the oxidation of roGFP2. 1 µM of pre-reduced roGFP2 was oxidised in the presence of 1.5 µM GRXS15 and its mutant version K83A. The enzymes were tested as purified without any further treatments and, alternatively, after pre-reduction (PR) with 10 mM DTT for 100 minutes on ice and subsequent desalting. The reaction was initiated by freshly prepared glutathione disulfide (GSSG), automatically injected 10 minutes after start of the measurement to a final concentration of 40 µM. 1 µM GRXC1 was used as a positive control and 1 µM of roGFP2 without any GRXs was used as negative control. Furthermore, 1 µM of roGFP2 either fully oxidised by 10 mM H_2O_2 or fully reduced by 10 mM DTT were used to define maximum oxidation and reduction of roGFP2. Filter-based excitation at 390 and 480 nm and detection of emitted light at 520 nm were followed over time in a plate reader. Data show the degree of oxidation of roGFP2 (OxD) as means ± SD (n = 3). The arrows indicate the acceleration of roGFP2 oxidation achieved with pre-reduced GRXS15 or GRXS15 K83A, respectively.

3b.1.2 | GRXS15 forms homodimers via intermolecular disulfide bonds

Having seen the pronounced change in oxidoreductase activity, we reasoned that the pre-reduction treatment could affect the intermolecular dimerization of the protein. Hence, we examined the oligomerization via SDS-PAGE of non-treated and pre-reduced proteins. Surprisingly, we found that after purification of recombinant proteins, both the wild-type and the K83A variant spontaneously formed homodimers, in a non-reducing environment. These homodimers were efficiently reduced by treatment with DTT. Moreover, we observed the spontaneous re-formation of homodimers when DTT is removed via desalting in a similar way for both proteins (Fig. 3b.2).

GRXS15 contains only one cysteine residue, in position 91, in the typical class II-type "CGFS" active site. To confirm that this residue is responsible for the disulfide bond-mediated dimerization, we purified the GRXS15 C91S mutant and showed that besides the complete loss of oxidoreductase activity (Supplementary Fig. 3b.3), it was also unable to form any dimer (Fig. 3b.2).

In addition, we tested old and freshly purified proteins, to verify whether the long storage could influence the dimerization of GRXS15. Furthermore, we also tested whether trans-4,5-dihydroxy-1,2-dithiane (DTTox) could enhance the formation of homodimers. However, we found that neither the age of the proteins nor the treatment with DTTox had any effect on the homodimerization (Supplementary Fig. 3b.4).

Our results suggest that the oxidoreductase activity of GRXS15 *in vitro* may be affected by the intermolecular disulfide-mediated homodimerization. However, since also the K83A can spontaneously form dimers (Fig. 3b.2), the homodimerization, may not be the main reason for the slow oxidation activity of the wild-type GRXS15.

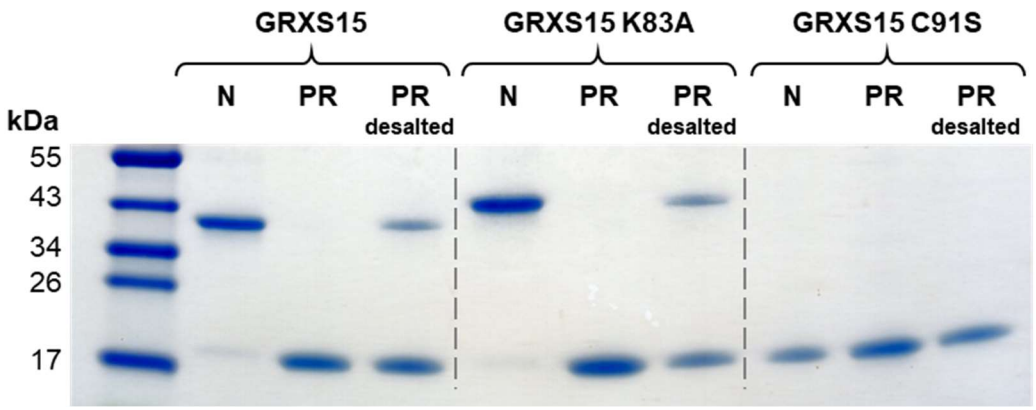

Fig. 3b.2 | GRXS15 forms homodimers via intermolecular disulfide bond. 3 µg of different protein variants were either not treated (**N**) or pre-reduced with 10 mM DTT for 100 minutes on ice (**PR**). Part of the pre-reduced samples was desalted using Zeba™ Spin columns to remove the DTT (**PR desalted**). After the treatments, the proteins were immediately prepared for SDS-PAGE gel electrophoresis, with the addition of non-reducing loading buffer. The

samples were boiled at 95 °C for 10 minutes and loaded on precast gel (Mini-PROTEAN TGX 12 %; Bio-Rad). After the run, the gel was stained with PageBlue™.

3b.1.3 | Generation of GRXS15 without class II-type loop

As shown in Chapter 3a (Trnka *et al.*, 2020), the main discriminant to distinguish class I and class II GRXs is the absence or presence of 5 amino acids between the conserved lysyl residue and the active site. This difference is not only highly conserved in all GRXs in Arabidopsis (Fig 3b.3) but also across different species and different kingdoms (Supplementary Fig. 3b.5).

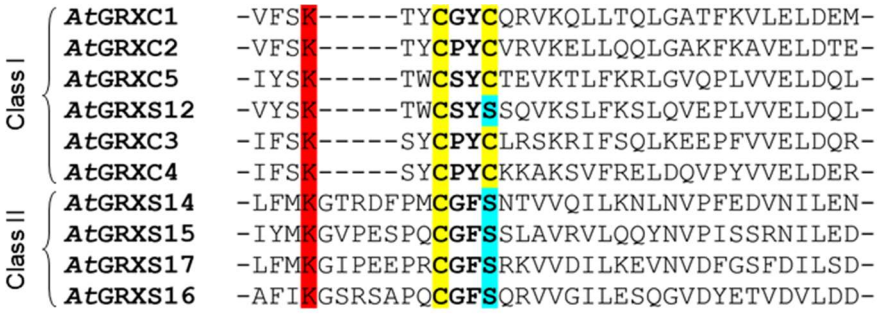

Fig. 3b.3 | Sequence analysis of Arabidopsis glutaredoxins. Primary sequence comparison of the class I and class II GRXs in Arabidopsis, around the active site. The alignment was generated by local multiple-sequence alignment (Clustal Omega, https://www.ebi.ac.uk/Tools/msa/clustalo/). The conserved lysyl residue is highlighted in red while in yellow the critical cysteine and in cyan the serine in the catalytic site. The class-specific string of 5 amino acids ("loop") clearly separates the two classes.

The positive charge of the lysyl residue electrostatically interacts with the coordinated glutathione molecule. The five amino acids form a loop structure, which determines the relative orientation of the lysyl residue consequently ruling the orientation of the GSH thiol (see Chapter 3a, Trnka *et al.* (2020)).

Since Arabidopsis GRXS15 possesses a type-II loop, we wanted to study whether this structure was essential for the activity of the protein and whether we could change its oxidoreductase activities. We thus cloned a modified version of GRXS15 lacking the five amino acids between the lysine 83 and the proline 89 (G84, V85, P86, E87, S88) and purified the truncated protein denominated GRXS15-loop (Fig. 3b.4 and Supplementary Fig. 3b.1).

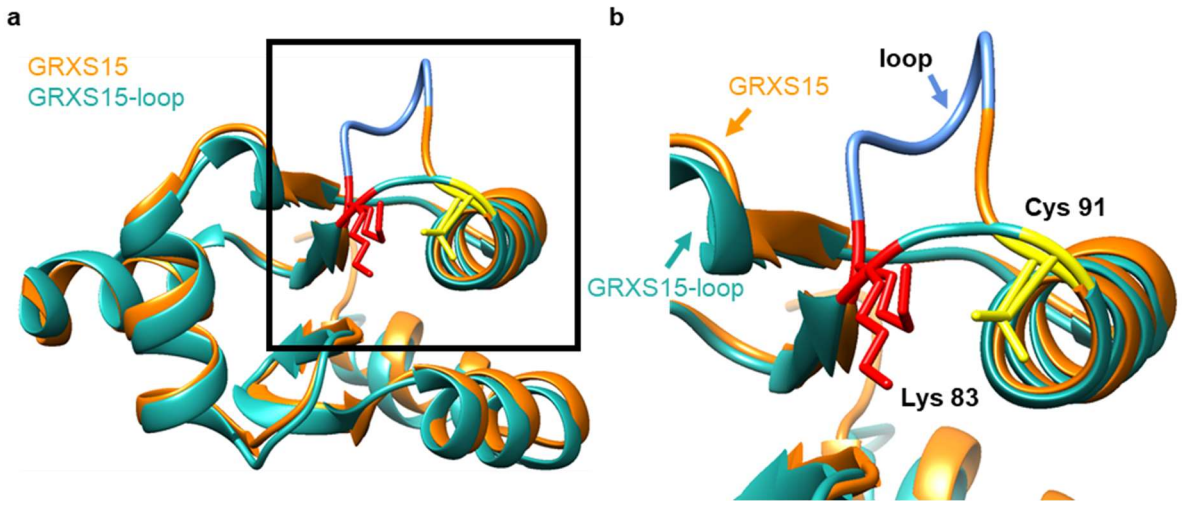

Fig. 3b.4 | Comparison of the 3D structures of GRXS15 with and without "loop". a Super-positioning of the structures of the GRXS15 model (orange) and the mutated version without the "loop" GRXS15-loop (cyan). The coordination of glutathione and and Fe–S cluster is not shown. Both structures are models generated by the *Phyre2* web portal (Kelley *et al.*, 2016). **b** Detail of the "loop" area (in blue) where the residues lysine 83 and cysteine 91 are highlighted (red and yellow, respectively).

3b.1.4 | GRXS15-loop is faster to oxidise but still unable to reduce roGFP2

After purification of the recombinant protein, we tested the oxidoreductase abilities of GRXS15-loop using the roGFP2 interaction assay. We found that the protein without the type-II loop exhibited an exceptionally enhanced oxidation activity, demonstrating over 16-times faster oxidation of roGFP2 compared to wild-type GRXS15 (Fig. 3b.5). Consistent with the previous results, pre-reduction of the proteins enhanced the speed of the oxidation reaction about 4-fold compared to wild-type GRXS15. The pre-reduced GRXS15-loop showed a faster oxidation but the difference with the non-treated protein was too small. Less concentrated amounts of enzyme should be used to have a correct estimation of the velocity enhancement (Fig. 3b.5).

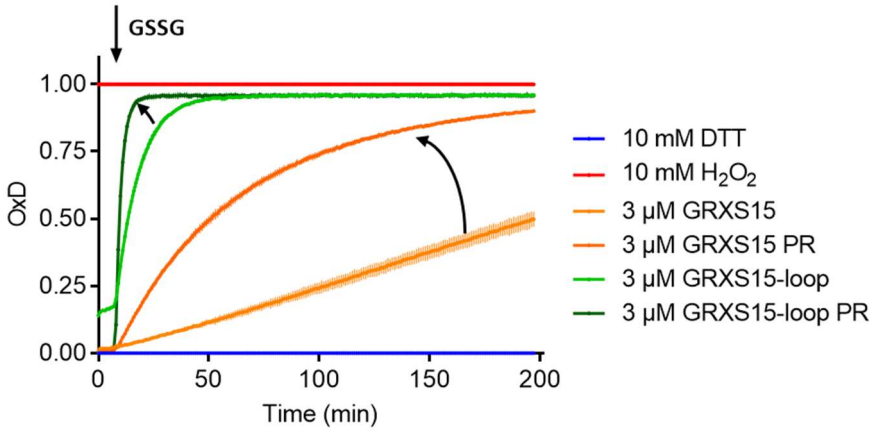

Fig. 3b.5 | GRXS15-loop is efficiently oxidising roGFP2. 1 µM of pre-reduced roGFP2 was oxidised in the presence of 3 µM GRXS15 and its mutant version lacking the loop (deleted the five amino acids between the lysine 83 and the proline 89). The enzymes were tested as purified without any further treatments and, alternatively, after

pre-reduction (PR) with 10 mM DTT for 100 minutes on ice and subsequent desalting. The reaction was initiated by freshly prepared glutathione disulfide (GSSG), automatically injected 10 minutes after start of the measurement to a final concentration of 40 µM. Furthermore, 1 µM of roGFP2 either oxidised by 10 mM H_2O_2 or fully reduced by 10 mM DTT were used to define maximum oxidation and reduction of roGFP2. Filter-based excitation at 390 and 480 nm and detection of emitted light at 520 nm were followed over time in a plate reader. Data show the degree of oxidation of roGFP2 (OxD) as means ± SD (n = 3). The arrows indicate the acceleration of roGFP2 oxidation achieved with pre-reduced GRXS15 or GRXS15-loop, respectively.

Surprisingly, the GRXS15-loop variant did not gain any reductase activity. In fact, neither wild-type GRXS15 nor GRXS15-loop exhibit any ability to reduce roGFP2 (Fig. 3b.6). These results were unexpected, considering previous findings that replacing the type-II loop with type-I loop allowed the human class II glutaredoxin 5 (*Hs*Grx5) to acquire the ability of reduction (Chapter 3a, Trnka *et al.* (2020)). Nevertheless, we found that pre-reduced proteins displayed a reductase activity, although very slowly. Notably, both wild-type GRXS15 and GRXS15-loop showed identical behaviour and velocity (Fig. 3b.6).

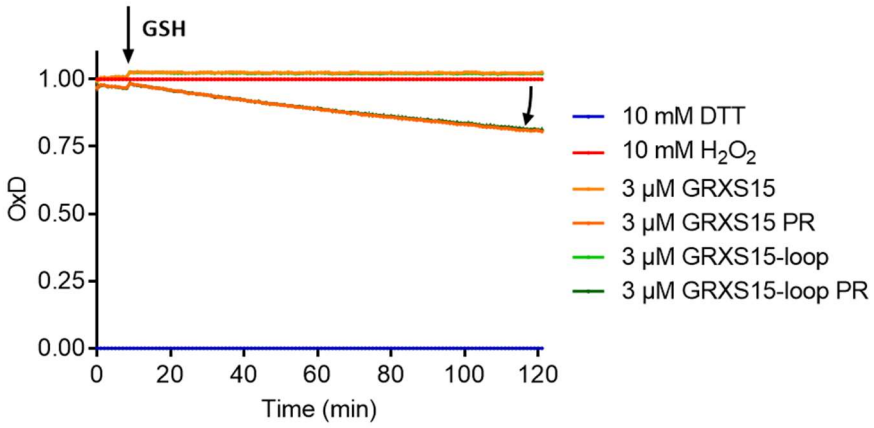

Fig. 3b.6 | GRXS15-loop has no reductase activity. 1 µM of roGFP2 was negligibly reduced in the presence of 3 µM GRXS15 and its mutant version lacking the loop (deleted the five amino acids between the lysine 83 and the proline 89). The enzymes were tested as purified without any further treatments and, alternatively, after pre-reduction (PR) with 10 mM DTT for 100 minutes on ice and subsequent desalting. The reaction is initiated by freshly prepared reduced glutathione (GSH), automatically injected 10 minutes after start of the measurement to a final concentration of 2 mM. A highly negative redox state of the glutathione buffer was maintained by addition of yeast glutathione reductase (GR) and NADPH to a final concentration of 1 U and 100 µM, respectively. Furthermore, 1 µM of roGFP2 either oxidised by 10 mM H_2O_2 or fully reduced by 10 mM DTT were used to define maximum oxidation and reduction of roGFP2. Filter-based excitation at 390 and 480 nm and detection of emitted light at 520 nm were followed over time in a plate reader. Data show the degree of oxidation of roGFP2 (OxD) as means ± SD (*n* = 3). The arrows indicate the acceleration of roGFP2 reduction achieved with pre-reduced GRXS15 or GRXS15-loop, respectively.

3b.1.5 | GRXS15-loop forms homodimers via intermolecular disulfide bonds

As already shown, GRXS15 can spontaneously form homodimers. We investigated whether GRXS15 lacking its type-II loop had this characteristic, by analysing freshly purified proteins treated with or without DTT via SDS-PAGE. We found that GRXS15-loop can self-homodimerize, comparably to wild-type GRXS15. Similarly, DTT treatment can dissolve the dimeric structure and, after removing the excess of DTT by desalting, there was a spontaneous re-dimerization (Fig. 3b.7).

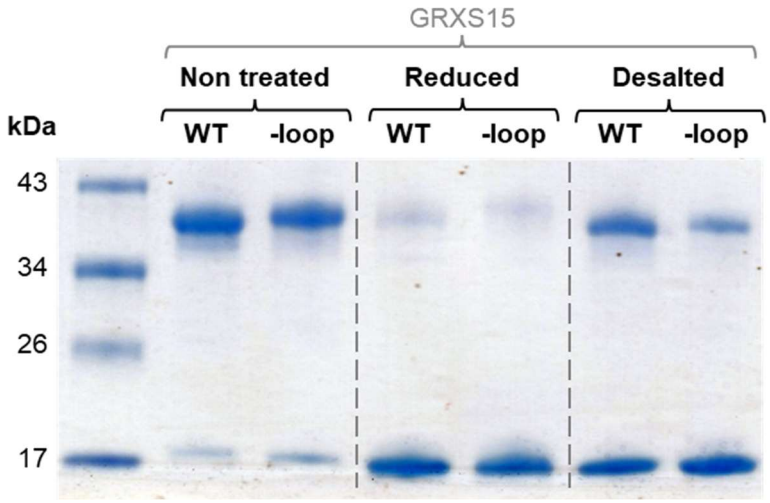

Fig. 3b.7 | GRXS15-loop self-homodimerize. 3 µg of both GRXS15 (WT) and GRXS15-loop (-loop) were either not treated or pre-reduced with 40 mM DTT for 100 minutes on ice (**Reduced**). Part of the pre-reduced samples was desalted using Zeba™ Spin columns to remove the DTT (**Desalted**). After the treatments, the proteins were immediately prepared for SDS-PAGE gel electrophoresis, with addition of non-reducing loading buffer. The samples were boiled at 95 °C for 10 minutes and loaded on precast gel (Mini-PROTEAN TGX 12 %; Bio-Rad). After the run, the gel was stained with PageBlue™.

3b.1.6 | GRXS15-loop can spontaneously oxidise roGFP2

Our previous results revealed that GRXS15-loop, without any pre-reduction, was already able to partially oxidise roGFP2 even before the injection of GSSG (Fig. 3b.5). This phenomenon led us to hypothesize a direct interaction between GRXS15-loop and the sensor, occurring in the absence of additional oxidising agents. To investigate this further, we incubated pre-reduced and desalted roGFP2 with freshly purified GRXS15-loop without any reductive treatments and monitored the redox state of the sensor over time in the plate reader. We observed a slow but gradual spontaneous oxidation of roGFP2, with oxidation of 38 % of the sensor occurring after 24 hours (Fig. 3b.8). Surprisingly, in the presence of GRXS15-loop, the oxidation of roGFP2 was significantly enhanced, resulting in more than 90 % of the sensor being oxidised after 24 hours (Fig. 3b.8).

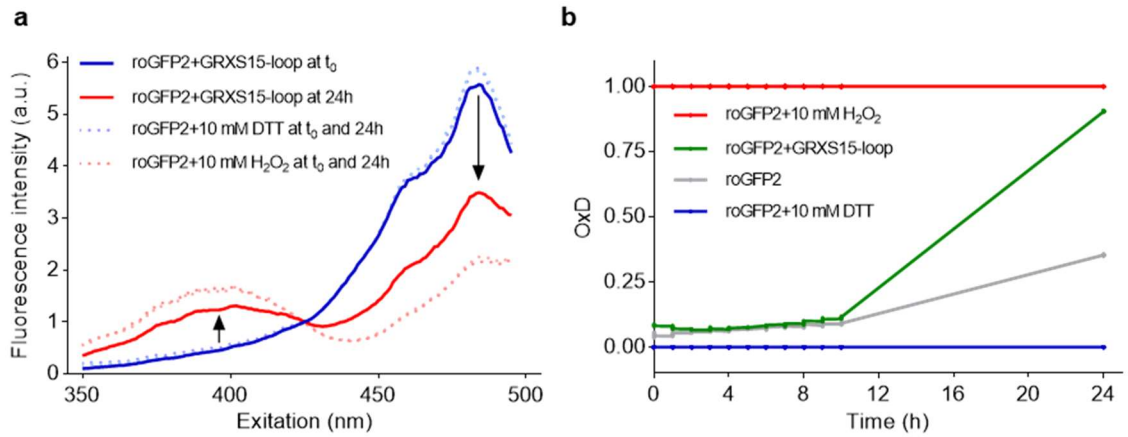

Fig. 3b.8 | roGFP2 is spontaneously oxidised by GRXS15-loop without addition of GSSG. 10 µM of roGFP2 was pre-reduced with 10 mM DTT for 100 minutes on ice and subsequently desalted. The sensor was incubated with 10 µM GRXS15-loop as purified without any further treatments in the same buffer for the roGFP2 interaction assay (100 mM K_2HPO_4/KH_2PO_4 buffer, pH 8.0, 0.1 mM EDTA) but without addition of glutathione disulfide (GSSG). Furthermore, 1 µM of roGFP2 either oxidised by 10 mM H_2O_2 or fully reduced by 10 mM DTT were used to define maximum oxidation and reduction of roGFP2. **a** Excitation spectra of roGFP2 with fluorescence intensity collected with emission of 520 ± 5 nm, data shows as means ± SD (*n* = 3) normalized to the fluorescence ratios of DTT-treated proteins. **b** Time course of oxidation of roGFP2 followed over time in a plate reader with filter-based excitation at 390 and 480 nm and detection of emitted light at 520 ± 5 nm, data shows degree of oxidation of roGFP2 (OxD) as means ± SD (*n* = 3).

3b.2 | Discussion

Our work provided important insights into the *in vitro* function of GRXS15 as a putative oxidoreductase. We confirmed that GRXS15 possess a slow oxidation activity and that it lacks reduction activity (Fig. 3b.1 and Supplementary Fig. 3b.2). However, we demonstrated that after pre-reduction with DTT, its oxidation capabilities increase and that the protein gains a limited reduction ability, although this is still very slow (Fig. 3b.1 and Supplementary Fig. 3b.2). This initial finding aligns with our recent study on GRXs (Chapter 3a, Trnka *et al.* (2020)) where we showed inactivity of class II *Hs*Grx5 in two types of reduction assays. Moreover, our observations that pre-reduced GRXS15 can reduce roGFP2, introduce a new aspect which was unknown before. Due to the slow reductase activity, however, the physiological relevance has to be questioned.

Nevertheless, it is essential to consider the artificial nature of the roGFP2 interaction assay. While the pH is maintained at 8 to simulate the mitochondrial matrix, the inclusion of 0.1 mM EDTA or the absence of the potentially oxidative environment existing in mitochondria can possibly hinder the oxidoreductase activity of GRXS15. It was also recently demonstrated that Arabidopsis mitochondrial thioredoxins TRXo1 and TRXo2 are able to reduce oxidised forms of GRXS15 such as dimers or glutathionylated forms *in vitro* (Christ *et al*., 2022). This observation may be attributed to the potentially oxidative environment within mitochondria, where GRXS15 could experience transient oxidation, possibly slowing down Fe–S cluster transfer activity. Reduction of these transiently oxidised forms would restore the capacity of GRXS15 to bind and transfer Fe–S clusters. The roGFP2 assay could be exploited to test whether the addition of TRXs in the reaction buffer could contribute to enhancing the reductase activity of GRXS15 *in vitro*.

Another important aspect to consider is that GRXS15 can homodimerized. Previous research demonstrated the pKa of the sole cysteine of GRXS15 is rather acidic, suggesting that at mitochondrial pH 8, the cysteinyl 91 residue predominantly exists in the thiolate form rather than in the thiol one (Christ *et al*., 2022). As our results showed GRXS15 spontaneously forms homodimers through its single cysteine residue 91 *in vitro* (Fig. 3b.2), this may suggest that, in mitochondrial physiological conditions, the protein may remain stable in its dimeric form. Nevertheless, besides the putative oxidoreductase activity of GRXS15, it is not explained how such dimer could efficiently coordinate [2Fe–2S] clusters *in vivo*. A possible hypothesis could be that GRXS15 is stable as homodimer, while it is separated in monomers after the interaction with the chaperon complex and the cluster uptake (see Chapter 2, Fig. 2.1). To test this hypothesis *in vivo,* a potential strategy could be to generate a mutated version of GRXS15, efficient in the coordination of [2Fe–2S] clusters but unable to form dimers. It would then be possible to test whether such mutated GRXS15 could complement null mutants Arabidopsis

lines (see Chapter 4, Moseler *et al.* (2021)). To further test the hypothesis *in vivo*, bimolecular fluorescence complementation could be used, similar to what was proposed for *Hs*Grx2 in Hoff *et al.* (2009). In this case, two different chimeric proteins composed of GRXS15 fused with two different fluorescent protein fragments are co-expressed *in planta*. When two GRXS15 monomers form a homodimer, the sensor is irreversibly reassembled and a specific fluorescence signal can be detected. In addition, since the complementation of the fluorescent protein is irreversible, it could be also possible to understand whether the GRXS15 dimers strictly need to be dissociated after the [2Fe–2S] cluster is released by GRXS15 to ISCA (see Chapter 2, Fig. 2.1). Alternatively, also exploiting FRET would give information about the association/dissociation of GRXS15 homodimers. In this instance, distinct fluorescence signals would be detected when GRXS15 is in monomeric or dimeric form. Measuring the fluorescence signals, it should be possible to understand whether GRXS15 stably self-dimerises via intermolecular disulfide bonds after having released the cluster.

Among the class I and class II GRXs of Arabidopsis, S15 is the sole one with a single cysteine located in the conserved catalytic motif "CGFS" (Appendix 1.3). Also, when compared to its mitochondrial homologs human *Hs*Grx5 and yeast *Sc*Grx5, Arabidopsis GRXS15 is unique in having only one cysteine (Supplementary Fig. 3b.6). To some extent, this is generally applicable for other plant mitochondrial GRXs. In fact, except for the poplar *Pt*GRXS15 and the microalgal *Cr*GRX5, all the mitochondrial GRXs of the classic photosynthetic model organisms (Arabidopsis, maize, barley, rice, moss, cyanobacteria) possess a single cysteine. In contrast, all mitochondrial class II GRXs from other classic model systems (yeast, worms, Drosophila, Zebrafish, mouse, human) have more than one cysteine (Supplementary Fig. 3b.5).

Previous studies have already reported the importance of an additional semi-conserved cysteine in the C-terminal region of monothiol GRXs for the oxidoreductase ability of the protein (Tamarit *et al.*, 2003; Fernandes *et al.*, 2005; Zaffagnini *et al.*, 2008; Gao *et al.*, 2010; Zannini *et al.*, 2019). A mechanism has been proposed where the cysteine in the “CGFS” active site of *At*GRXS16 forms an intramolecular disulfide bond with the C-terminal cysteine, facilitating the reduction of the protein after de-glutathionylation of a substrate, mimicking the dithiol GRXs (Zannini *et al.*, 2019). Similar observations have been made for bacterial *Ec*Grx4 (Fernandes *et al.*, 2005), yeast *Sc*Grx5 (Tamarit *et al.*, 2003) and green microalga *Cr*GRX3, *Cr*GRX5 and *Cr*GRX6 (Zaffagnini *et al.*, 2008; Gao *et al.*, 2010). However, *C. reinhardtii Cr*GRX6 does not possess any C-terminal cysteine and thus the dimerization may be due to the cysteine in the active site. Interestingly, *Cr*GRX6 is localized in the chloroplast where two other GRXs are present but none of them belong to class I (Lemaire *et al.*, 2004; Rouhier *et al.*, 2004). Yet, all these GRXs – except *Cr*GRX6 – contain the semi-conserved cysteine in the C-terminal region. Regarding the dimerization, besides monothiol GRXs, also poplar glutaredoxins *Pp*GRXC1

and *Pp*GRXC2 were reported to form intermolecular disulfide homodimers. However, these proteins both belong to class I, containing the common “CxxC” motif, and their dimerization involved the semi-conserved C-terminal cysteines rather than the cysteines in the active site (Couturier *et al.*, 2013).

Furthermore, the two mutated proteins GRXS15 K83A and GRXS15-loop exhibited the property of homodimerization comparably to wild-type GRXS15 (Fig. 3b.2 and Fig. 3b.7). Despite this characteristic, their ability to oxidise roGFP2 was significantly increased compared to the wild-type protein (Fig. 3b.1 and Fig 3b.5) suggesting that the dimerization through cysteine 91 is not the major impediment for the oxidation reaction but rather an intrinsic feature of the protein. Hence, the loop can be excluded as a determinant for the dimer formation. Notably, the human *Hs*Grx5 showed the capacity to form homodimers, although in a less pronounced manner compared to GRXS15. However, the *Hs*Grx5-loop displays an even lower ability to form dimers, compared to wild-type *Hs*Grx5 (Trnka *et al.*, 2020).

These last observations together with our results suggest that the presence of the C-terminal cysteine plays a key role in preventing protein homodimerization and may be essential for class II GRXs oxidoreductase abilities. It would be interesting to generate a new *grxs15* mutant, substituting the serine 145 with a cysteine. By adding a C-terminal cysteine, we hypothesize that GRXS15 S145C could gain an oxidoreductase activity similar to GRXS16, possibly mimicking the dithiol GRXs catalytic mechanism, as suggested in Zannini *et al.* (2019). In addition, *in vitro* experiments, such as SDS-PAGE, could be performed to understand whether the addition of the cysteine in GRXS15 S145C could prevent homodimerization. Thus, the expression of GRXS15 S145C in Arabidopsis could give important information on whether the dimerization of GRXS15 influences the efficiency of Fe–S cluster transfer in mitochondria.

Overall, the reason why most photosynthetic model organisms exclusively possess a single GRX within the mitochondria, and why these GRXs possess only a single cysteine remains unknown. Future work has to be determined whether in plants monothiol GRXs can fulfil the functions typically associated with class I GRXs in mitochondria or if other proteins of the TRX fold family can replace the missing class I GRX.

Based on the observations and evidence discussed above, we reasoned on the oxidoreductase catalytic mechanisms mediated by GRXS15 *in vitro*, proposing the following two models for the oxidation reaction:

a) According to the classical oxidation reaction scheme for the dithiol GRXs (Chapter 1, Fig. 1.7), GRXS15 undergoes glutathionylation (on its catalytic cysteine residue) by GSSG before interacting with roGFP2. This allows the GRX to transfer the glutathione residue to reduced

roGFP2, which subsequently spontaneously gets oxidized, releasing a molecule of GSH. This hypothesis is supported by the observation that single-cysteine variants of roGFP2 can be glutathionylated by GRXs (see Chapter 3a, Trnka *et al.* (2020)). It is not possible that GRXS15 homodimers are being glutathionylated by GSSG. Therefore, to facilitate glutathionylation, GRXS15 dimers need to be resolved into monomers. The K83A as well as the GRXS15-loop variants may be more prone to reduction and monomerization, which would expose the C91 for glutathionylation (Fig. 3b.9a).

b) The current data, however, may also be explained with an alternative reaction scheme. In this scenario, initially, GRXS15 coordinates a molecule of GSSG, subsequently the cysteine in the active site is glutathionylated. The protein then forms a complex through disulfide bridge with the reduced roGFP2, facilitated by an electron donated by the glutathione group. The sensor is then fully oxidised while GRXS15 ends up reduced.

Notably, in this novel scheme, the cysteine residue of GRXS15 does not directly transfer the GSH group to roGFP2. Instead, GSSG serves as an electron acceptor for the formation of an intermolecular disulfide bridge between GRXS15 and the sensor. Similar to the first hypothesis, GRXS15 variants K83A and GRXS15-loop may be more likely to dissociate the dimeric structure into monomers, allowing C91 to interact with the reduced roGFP2 (Fig. 3b.9b).

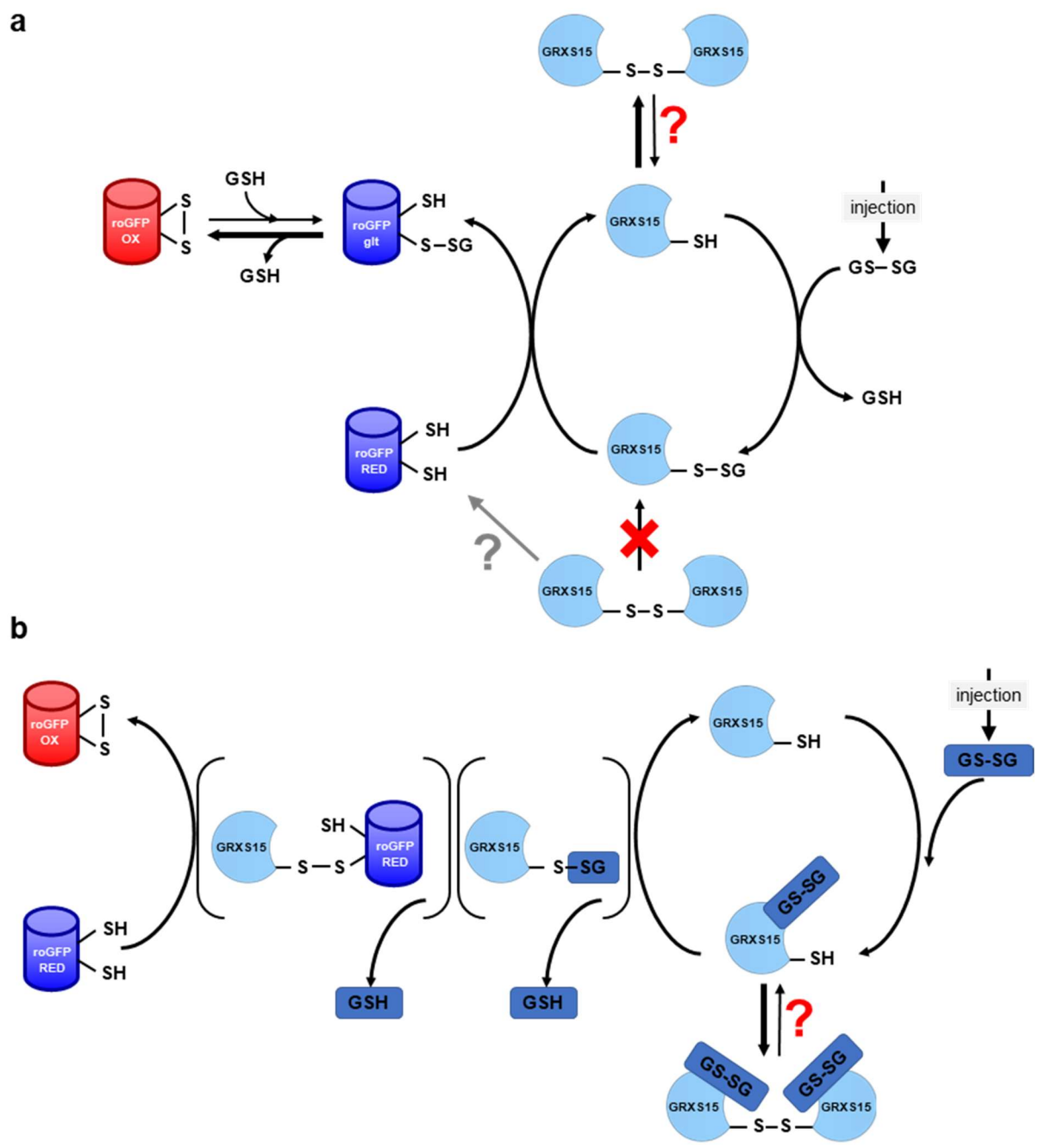

Fig. 3b.9 | Working models for the oxidation of roGFP2 mediated by GRXS15. a Following the classical reaction scheme for roGFP2 oxidation assay, after injection of glutathione disulfide (GSSG), the monothiol glutaredoxin S15 (GRXS15) undergoes glutathionylation. The glutathione group is then transferred to reduced roGFP2, which spontaneously substitutes the glutathione residue by forming an internal disulfide. It is assumed that GRXS15 in dimeric form cannot interact with either oxidised glutathione or reduced roGFP2. **b** Alternative reaction model, where GSSG is initially coordinated by GRXS15, thus serves to glutathionylate the cysteine in the active site of GRXS15. Hence, GRXS15 forms a complex with reduced roGFP2 through an intermolecular disulfide bond, leading to its oxidation.

The observation that GRXS15-loop can oxidise the sensor without the involvement of oxidising power derived from GSSG (Fig. 3b.8) supports the hypothesis that GRXS15 can interact with

roGFP2 via a disulfide bridge (Fig. 3b.10). This finding suggests not only the need to revise the reaction model but also considering the potential relevance of the intermolecular-disulfide-homodimer *in vivo* for oxidising protein substrates. However, since this phenomenon was observed specifically for the modified GRXS15-loop, further investigations are necessary to determine whether it is generally applicable to other class II GRXs or whether it is a distinct characteristic of monothiol class I GRXs (Zannini *et al.*, 2019; Zimmermann *et al.*, 2020). For instance, it would be necessary to test whether the variant *Hs*Grx5-loop used in Trnka *et al.* (2020) can oxidise roGFP2 without addition of GSSG. Furthermore, using the single-cysteine roGFP2 C204S to trap the intermediate GRXS15-roGFP2, we could visualise the heterodimer via SDS-PAGE, similarly to what was done by Trnka *et al.* (2020).

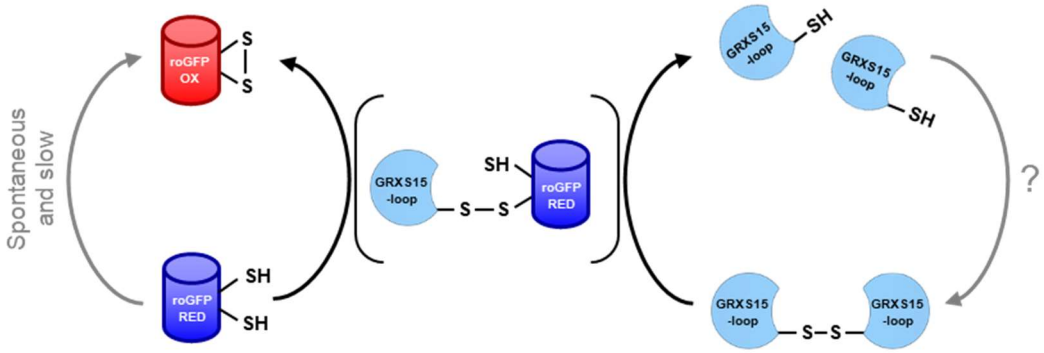

Fig. 3b.10 | Proposed model for the interaction between roGFP2 and GRXS15-loop. GRXS15-loop dimers interact with reduced roGFP2 forming a complex through an intermolecular disulfide bond, leading to oxidation of the sensor and reduction of the glutaredoxin. After the results of the SDS-PAGE analysis (Fig. 3b.7), GRXS15-loop is assumed to be mainly in dimeric form. It is also not excluded that both roGFP2 and monomeric GRXS15-loop can spontaneously be oxidised by *e.g.*, molecular oxygen present in the buffer.

The absence of a reductase activity *in vitro* for GRXS15 remains an unsolved question. The classical reaction scheme assumes that GSH spontaneously attacks roGFP2 and GRX facilitates its de-glutathionylation with subsequent reduction of the sensor (see Chapter 1, Fig. 1.7). However, for the reduction of roGFP2 mediated by GRXS15 (and generally all class II GRXs), cysteine 91 may be incapable of de-glutathionylating a substrate, *e.g.*, roGFP2 (Fig. 3b.11a). It is also possible that dimeric GRXS15 is reduced by GSH, as shown by Christ *et al.* (2022). In this case, only one of the two monomers would be directly available to interact with roGFP2, while the second monomer would be glutathionylated and would need to be de-glutathionylated through interaction with a second GSH molecule, resulting in the release of one molecule of GSSG (Fig. 3b.11a). However, this reaction is demonstrated to be extremely slow (Fig. 3b.1) and the efficiency of de-glutathionylation by GSH in the case of class II GRXs is still a subject of debate.

The minor reductase activity observed with pre-reduced enzymes (Fig. 3b.6 and Supplementary Fig. 3b.2) could be attributed to the availability of cysteine thiolate in the GRXS15 catalytic site. A second hypothesis is that GRXS15 initially attacks roGFP2. Previous studies have proposed the potential interaction between a monothiol class I GRXs and a protein target through an intermolecular disulfide bond, with GSH playing a role in resolving the heterodimers (Zannini *et al.*, 2019; Zimmermann *et al.*, 2020). However, in this scenario, roGFP2 would already change the properties in its excitation spectrum upon interaction with GRX, indicating a "reduced" state before the addition of GSH (Fig. 3b.11b). Contrary to our findings, it does not appear to be the case, since GRXC1 does not initiate the reduction of roGFP2 before the addition of GSH (Supplementary Fig. 3b.2). This mechanism is also not applicable to GRXS15, as both the wild-type protein and its K83A variant were unable to reduce the sensor in any cases.

An alternative hypothesis considers a revised reaction model. Similar to the second hypothesis for the oxidation reaction (Fig. 3b.9b), GRXS15 may coordinate a molecule of GSH, which triggers the reaction without involving the cysteine in the catalytic site. GRXS15 facilitates then the glutathionylation of roGFP2 using the coordinated GSH (Fig. 3b.11c). In this case, the class II GRXs generally may lack the ability to form this intermediate due to the position of the lysine 83 before the class II-type loop and its influence on the cysteine in the catalytic site.

It remains unclear why the truncated form of GRXS15, lacking its class II-type loop, is unable to reduce and does not become active like a monothiol class I GRX, as observed in Chapter 3a (Trnka *et al.*, 2020) for human *Hs*Grx5. This discrepancy emphasizes again the putative significant differences between the mitochondrial GRXs from plants and other class II GRXs in different organisms. It would be interesting to test whether the substitution of the serine in the “CGFS” motif with a second cysteine in combination with the modified class II-type loop would enhance the reductase activity of GRXS15.

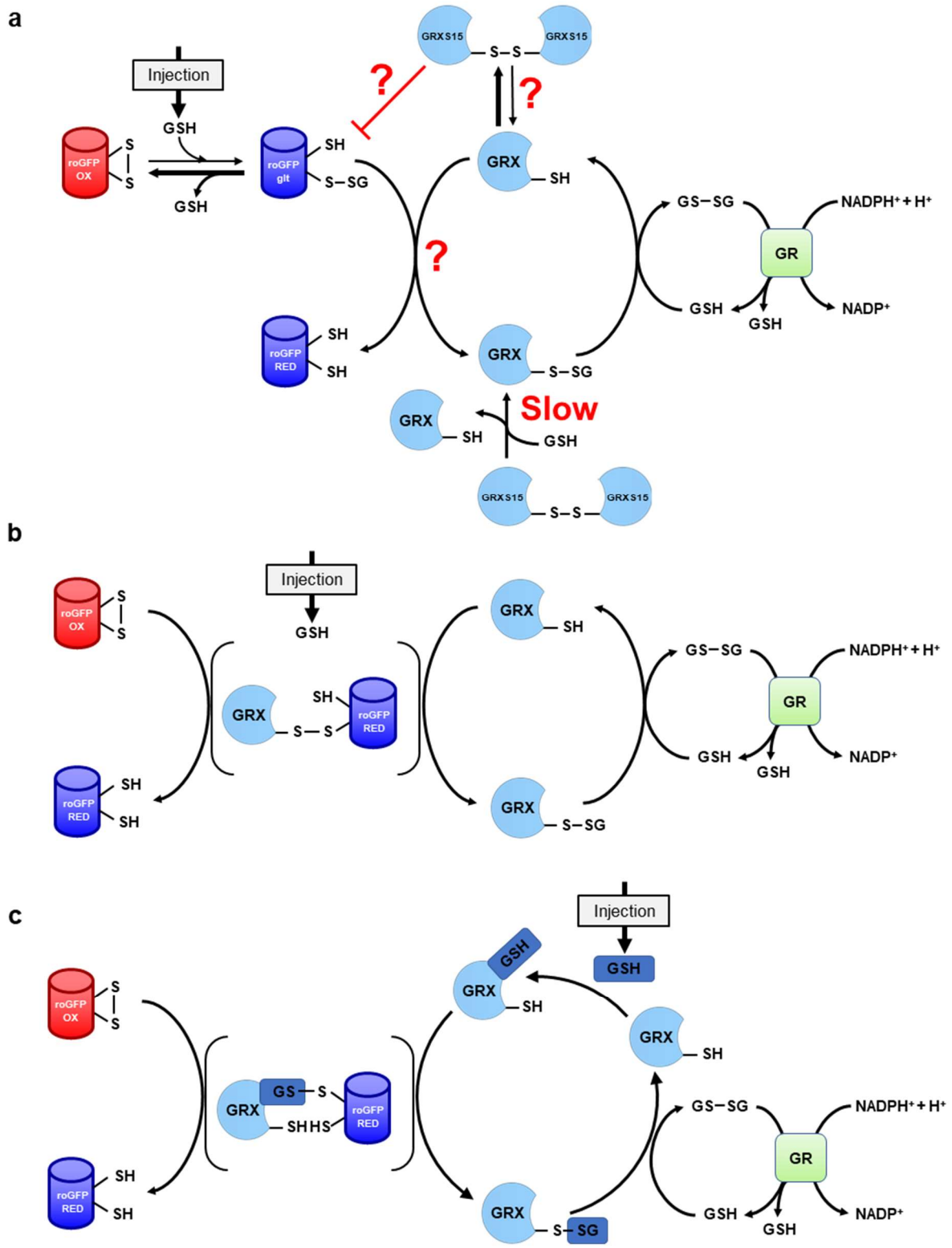

Fig. 3b.11 | Working models for the reduction of roGFP2 mediated by monothiol GRXs. a Following the classical model for roGFP2 reduction assay, glutathione (GSH) attacks first the roGFP2 disulfide, resulting glutathionylated. The reverse reaction is faster, but the glutathionylated roGFP2 can be trapped by the glutaredoxin (GRX), which attacks the glutathione sulfur atom leading to reduction of roGFP2. Finally, GRX undergoes de-glutathionylation by another GSH molecule, regenerating reduced GRX and releasing a glutathione disulfide (GSSG) molecule. Glutathione reductase (GR) maintains the highly negative redox state of the glutathione buffer, using NADPH as electron donor. In this model, GRXs that form intermolecular disulfide homodimers (*e.g.*, GRXS15) cannot interact with the glutathionylated roGFP2 but can be slowly reduced by GSH. **b** Firstly, GRX initiates the

reaction by attacking the disulfide of roGFP2 forming an intermolecular disulfide bond complex with the sensor. Subsequently, GSH resolves the disulfide, leading to reduced roGFP2 and glutathionylated GRX. A second molecule of GSH reduces and regenerates the glutathionylated GRX, releasing GSSG. **c** Alternative reaction model, where GSH is coordinated by GRX, without involving the cysteine in the GRX active site. GRX would then activate GSH to attack the roGFP2 disulfide forming a reaction intermediate with the sensor. GRX would then de-glutathionylate roGFP2 leading to its reduction and proceeding by the mechanism already described in (**a**) and (**b**).

3b.3 | Methods

3b.3.1 | Plasmid constructs

The plasmids for heterologous expression of the recombinant proteins were already available in the laboratory and previously generated using Gateway® cloning (Thermo). The gene for Arabidopsis GRXS15 (AT3G15660), the variants GRXS15 K83A, C91S and GRXS15-loop were encoded (without the mitochondrial targeting peptide) on the expression vector pETG10a, the gene for Arabidopsis GRXC1 (AT3G62950) on pET16b, the sensor roGFP2 on pET30b (Meyer *et al.*, 2007). All genes contain a sequence coding His6-tag at N-terminal, for purification via affinity chromatography (see Appendix 1.1 and 1.2 for complete sequences).

3b.3.2 | Generation of GRXS15-loop with site-directed mutagenesis

The plasmid pETG10a encoding GRXS15 was used as a template for removing 5 amino acids between the lysine 83 and the proline 89. The choice to remove these aa was based on the analysis of the sequences between class I and class II GRXs and considering the findings described in Chapter 3a (Trnka *et al.*, 2020). The modification was done exploiting the Q5® Site-Directed Mutagenesis kit (New England BioLabs) following the manufacturer's instruction, using the Q5SDM_S15-loop_F forward primer 5'-CCTCAGTGTGGGTTTAGC-3' and the Q5SDM_S15-loop_R reverse primer 3'-TTTCATGTAGATCATAACAGGATTATC-5'. After transformation into chemically competent *E. coli* DH5α and subsequent plasmid isolation, the mutation was confirmed by sequencing (Eurofins Genomics).

3b.3.3 | Bacteria method

All *E. coli* strains were grown in LB medium at a temperature of 37 °C (1 % (w/v) tryptone, 0.5 % (w/v) yeast extract, and 1 % (w/v) NaCl, pH 7). For solid plates, the media was supplemented with 1 % (w/v) agar before autoclaving. Antibiotics were sterile-filtered and added after autoclaving. To prepare an overnight culture, a single colony was inoculated in 5 mL of LB medium.

Chemically competent *E. coli* DH5α strain was transformed by heat shock. An aliquot of cells (100 µL) was combined with 1 µL of the respective plasmid. The mixture was incubated at 42 °C for 30 seconds. Subsequently, 500 µL of pre-warmed (37 °C) LB medium was added, and the transformed bacteria were incubated for 30 minutes at 37 °C. Finally, the culture was plated on LB agar plates containing the appropriate antibiotics and incubated overnight at 37 °C.

For plasmid extraction from *E. coli* DH5α, bacteria were inoculated in 5 mL of LB medium supplemented with the appropriate antibiotics and incubated overnight in a shaking incubator at 37 °C. Plasmid DNA isolation was performed using the NucleoSpin® Plasmid kit (Macherey-Nagel) following the manufacturer's protocol. The extracted DNA was eluted in 50 µL of dH_2O and quantified using the NanoDrop 2000 spectrophotometer.

3b.3.4 | Protein methods

Recombinant GRXS15, GRXS15 K83A and GRXS15-loop proteins were expressed in *E. coli* Lemo21(DE3), GRXS15 C91S protein was expressed in *E. coli* BL21(DE3), GRXC1 and roGFP2 proteins were expressed in *E. coli* Origami (DE3) and purified using affinity chromatography with an N-terminal His6-tag.

Bacteria were initially inoculated in 5 mL of LB medium including selective antibiotics and incubated overnight in a shaking incubator at 37 °C. The preculture was then used to inoculate 500 mL of LB medium and kept growing until reaching an OD_{600} of approximately 0.8. Protein expression was induced by adding IPTG (isopropyl-β-D-thiogalactopyranosid) to a final concentration of 0.5 mM.

After 18-24 h at 20 °C, the cultures were harvested by centrifugation at 8,000 *g* for 10 minutes at 4 °C and then resuspended in binding buffer (20 mM sodium phosphate buffer pH 7.4, 500 mM NaCl, 20 mM imidazole) supplemented with 0.5 mM PMSF (phenylmethylsulfonyl fluoride), cOmplete™ proteinase inhibitor cocktail (Roche) and 0.1 mg/ml DNAse I (Roche). The resuspended cells were incubated with 1 mg/mL lysozyme from chicken egg white (Sigma-Aldrich) in ice for 30 minutes. Following sonication, the cell debris was removed by centrifugation at 40,000 *g* for 20 minutes at 4 °C and the supernatant was filtered through a 0.45 µm sterile filter. The soluble proteins were loaded onto a 1 mL Ni^{2+} loaded HisTrap™ HP affinity column (GE Healthcare) by cycling over the column for at least 30 minutes with a constant flow rate of 1 mL/min using a peristaltic pump.

The loaded column was mounted on an ÄKTA Prime Plus chromatography system (GE Healthcare) and proteins were eluted with an imidazole gradient from 20 mM to 500 mM imidazole (in 20 mM PBS pH 7.4, 0.5 M NaCl) with a rate of 48 mM/min. According to the elution chromatogram, fractions with high protein content were collected and purity was analysed via SDS-PAGE (Supplementary Fig. 3b.1). Fractions with high purity of recombinant protein were buffer exchanged (30 mM TRIS-HCl, pH 8) using PD-10 desalting columns Sephadex™ G-25 M (Cytiva) and the eluted proteins were pooled and concentrated using size exclusion Vivaspin® Turbo 4, MWCO 10 kDa centrifugal concentrators (Sartorius) following the manufacturer's protocols.

Protein content was determined using the Bradford assay (Bradford, 1976) with bovine serum albumin (BSA) as the standard. For the measurements, 10 µL of the protein solution was mixed with 260 µL of Roti-Quant® reagent (ROTH) in flat base transparent 96-well plates (Sarstedt), followed by incubation for 5 minutes at room temperature. The optical density at OD_{595} of the samples was measured using a CLARIOstar® plate reader (BMG). Standard and protein samples were measured in triplicates for accuracy.

Proteins were separated with SDS-PAGE electrophoresis. Samples were boiled at 95 °C for 5 minutes in Laemmli sample buffer (2 % (w/v) SDS, 50 mM Tris-HCl pH 6.8, 0.002 % (w/v) bromophenol blue, 10 % (v/v) glycerol) as described by Laemmli (1970). For reducing the samples, 5 % (v/v) β-mercaptoethanol was added to the buffer. The protein samples were loaded onto a precast polyacrylamide gel (4-20 % Mini-PROTEAN® TGX™ Stain-Free, Bio-Rad) and the prestained PageRuler™ protein ladder (Thermo) was included as a molecular mass standard. Following electrophoresis, the gels were exposed to UV in INTAS ECL Chemostar imager (Intas) for visualization and documentation of proteins. Subsequently, the proteins were stained overnight using the PageBlue™ protein staining solution (Thermo) followed by destaining in water for several hours until the gel background was clear of dye.

3b.3.5 | roGFP2 interaction assay

The assay was performed using a fluorescence CLARIOstar® plate reader (BMG) with filter-based excitation at 390 ± 5 nm and 480 ± 5 nm, and detection of emitted light at 520 nm ± 5 nm. The time courses of the reactions were followed over time for at least 200 minutes.

For the reduction assay, 1 µM roGFP2 was mixed with GRX at a final concentration of 1 to 3 µM in reaction buffer (100 mM K_2HPO_4/KH_2PO_4 buffer, pH 8.0, 0.1 mM EDTA). The negative redox state of the glutathione buffer was maintained by the addition of 1 U of glutathione reductase from *S. cerevisiae* (Sigma-Aldrich) and NADPH at a final concentration of 100 µM. The reaction mix was loaded in triplicate into a flat base transparent 96-well plate (Sarstedt) and the reaction was initiated by freshly prepared GSH automatically injected after 10 minutes from the beginning of the measurement at a final concentration of 2 mM.

For oxidation assay, 50 µM of roGFP2 was incubated with DTT at a final concentration of 10 mM for 30 minutes and desalted using 7K MWCO Zeba™ Spin desalting columns (Thermo). At a final concentration of 1 µM, the pre-reduced sensor is then mixed with GRX at a final concentration of 1 to 3 µM in the reaction buffer. To initiate the reaction, GSSG at a final concentration of 40 µM was automatically injected into the wells after 10 minutes from the beginning of the measurement.

GRXs were pre-reduced using the same method as described for roGFP2. Maximum and minimum fluorescence ratios of roGFP2 were determined using fully oxidised and fully reduced sensor, obtained by pre-incubation with H_2O_2 or DTT, respectively, at a final concentration of 10 mM for at least 30 minutes. Basal background fluorescence was subtracted from all samples. Data analysis was performed in Excel (Microsoft) and plotted with GraphPad Prism 6.0 (www.graphpad.com) as average of technical triplicates ± sd. Normalization of fluorescence ratios and conversion of ratio data to the degree of oxidation for roGFP2 was performed as described in Meyer *et al.*, (2007).

For the incubation of roGFP2 with GRXS15-loop without the addition of GSSG, 10 µM roGFP2 was pre-reduced using DTT following the same method as the roGFP2 oxidation assay. The pre-reduced roGFP2 was kept on ice for 100 minutes and subsequently desalted. The sensor was incubated with 10 µM GRXS15-loop in the same buffer for the roGFP2 interaction assay (100 mM K_2HPO_4/KH_2PO_4 buffer, pH 8.0, 0.1 mM EDTA). Maximum oxidation and reduction states of roGFP2 were determined as described in the roGFP2 assay. The experiment was performed in triplicates with a 100 µL volume in a 96-well plate using a plate reader. The excitation spectra of roGFP2 were measured with fluorescence intensity collected with an emission of 520 ± 5 nm and the obtained data were normalized to the fluorescence ratios of DTT-treated proteins.

3b.3.6 | Phylogenetic analysis and protein modelling

Protein sequences of Arabidopsis GRXs and representative species were retrieved from NCBI Standard Protein Blast using Arabidopsis GRXC1 and Arabidopsis GRXS15 (UniProt identifier Q8L8T2 and Q8LBK6) as query sequences for class I and class II GRXs, respectively. After manual curation, sequences were aligned with Clustal Omega using default ClustalW parameters (https://www.ebi.ac.uk/Tools/msa/clustalo/). For the comparison of the 3D structures of GRXS15 and GRXS15-loop, the protein models were generated by the Phyre2 web portal (Kelley *et al.*, 2016). The models were visualized and super-positioned using UCSF Chimera (Pettersen *et al.*, 2004).

3b.4 | Supplementary

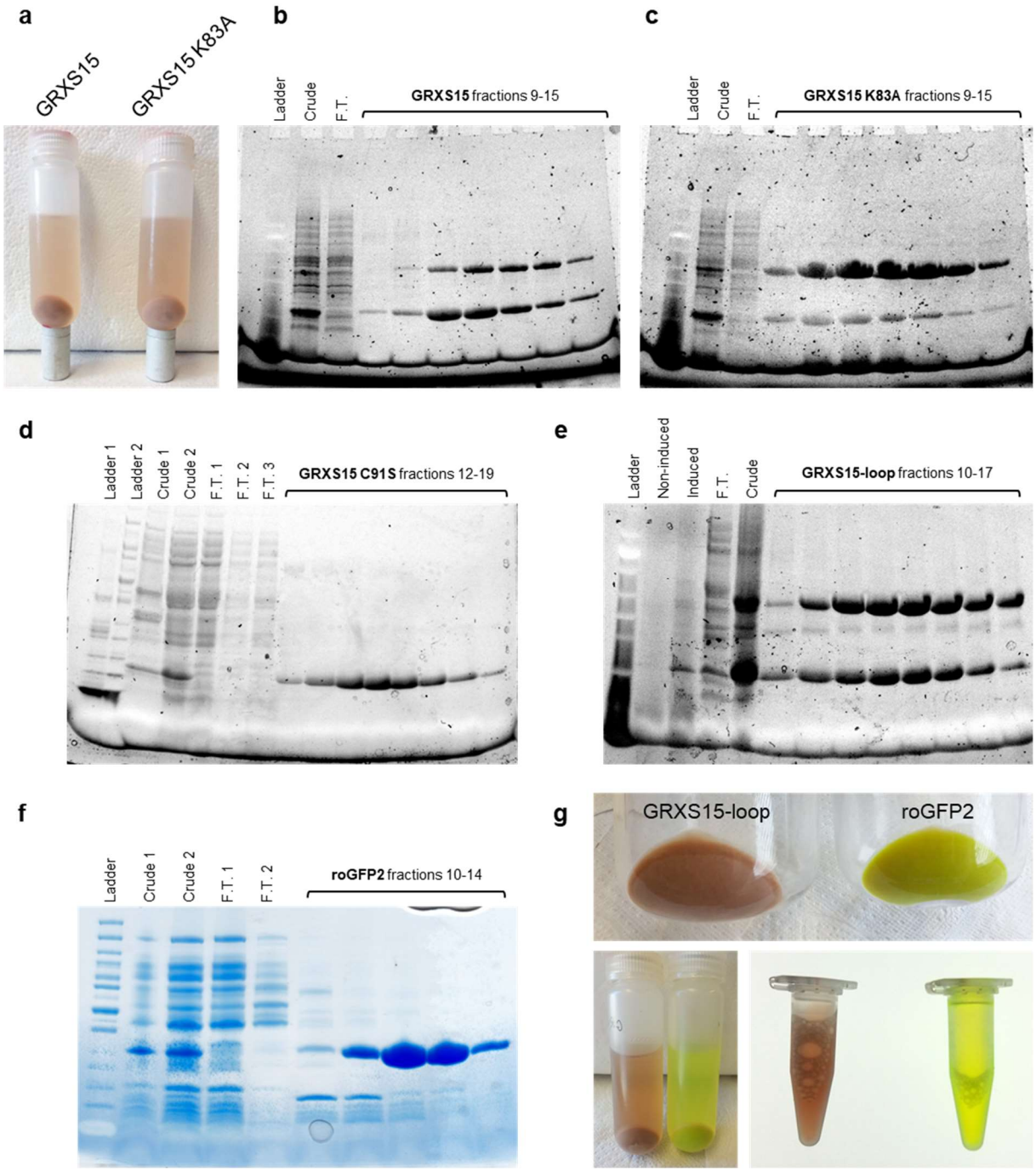

Supplementary Fig. 3b.1 | Histidine-tagged recombinant proteins purification by immobilized metal ion affinity chromatography. a Raw extract of GRXS15 and GRXS15 K83A mutant, with the bacterial pellet. Both crudes appear brownish because of the iron–sulfur cluster. **b-f** Protein SDS-PAGE gels of samples from the protein purification steps. The raw extract (**crude**) is the lysate of bacteria overexpressing the protein of interest after sonication and filtration (0.2 µm), in all the gels the overexpression of the protein of interest is visible. The flow through (**F.T.**) is the raw extract collected after the run into histidine trap column, the proteins of interest are clearly no longer visible, indicating that they are trapped in the column. The **fractions** are collected during the gradient elution in HPLC. In (**e**) a sample of non-induced and induced (with IPTG) bacterial cells collected during the bacterial culture were loaded on the gel. 10 µL of material was loaded in each well, all the samples were treated with non-reducing loading buffer and boiled at 95 °C for 5 minutes before loading. In (**b-e)** are shown the UV light image of

the gels, before the staining, exploiting the technology of the Stain-Free precast gels (Bio-Rad). In (**f**), the gel was stained with PageBlue™. **g** In order from top left to bottom right: the bacterial pellets of *E. coli* cells harvested after induction for overexpression of GRXS15-loop and roGFP2, the raw extract after the bacterial lysis, the two proteins purified and concentrated.

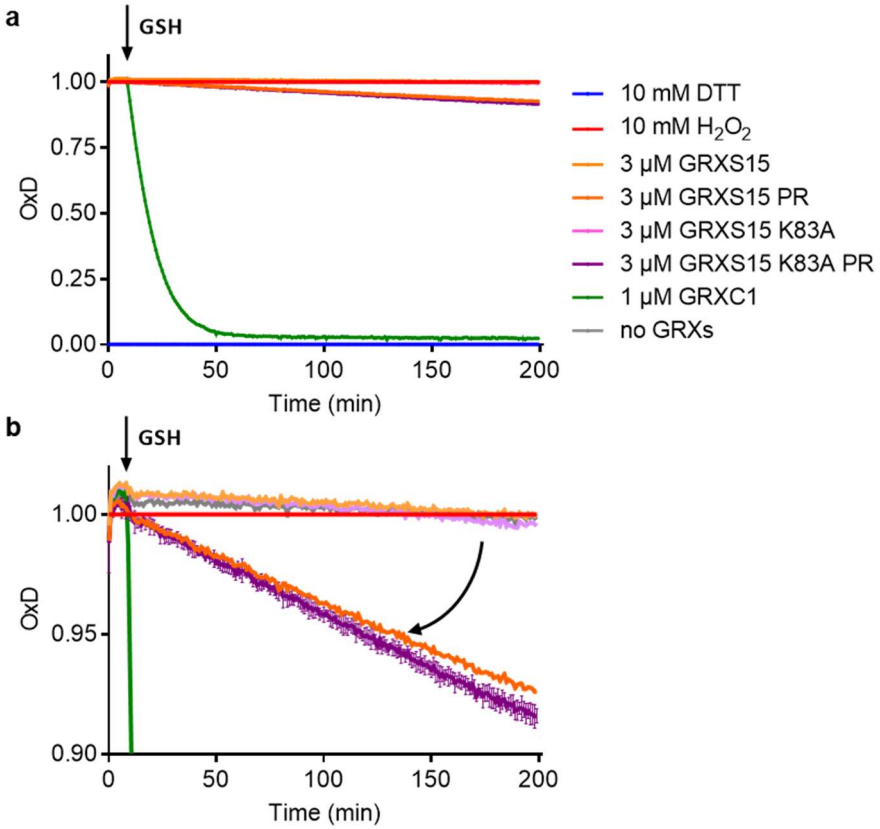

Supplementary Fig. 3b.2 | Pre-reduced GRXS15 shows negligible reductase activity. a 1 µM of roGFP2 was negligibly reduced by 1.5 µM GRXS15 and its mutant versions K83A. The enzymes were tested in their native form, as purified and pre-reduced (PR) with 10 mM DTT for 100 minutes and desalted. The reaction is initiated by freshly prepared reduced glutathione (GSH), automatically injected after 10 minutes from the start of the measurement at a final concentration of 2 mM. A highly negative redox state of the glutathione buffer was maintained by addition of yeast glutathione reductase (GR) and NADPH at a final concentration of 1 U and 100 µM, respectively. 1 µM GRXC1 was used as a positive control and 1 µM of roGFP2 without any GRXs was used as negative control. Furthermore, 1 µM of roGFP2 fully oxidised by H_2O_2 or fully reduced by DTT at a final concentration of 10 mM were used to define maximum oxidation and reduction of roGFP2. Filter-based excitation at 390 and 480 nm and detection of emitted light at 520 nm were followed over time in plate reader. Data shows the degree of oxidation of roGFP2 (OxD) as means ± SD (n = 3). **b** Expansion of the assay shown in (**a**), the arrow points from the assays performed with untreated to pre-reduced enzymes, highlighting the differences in the velocity of the reaction.

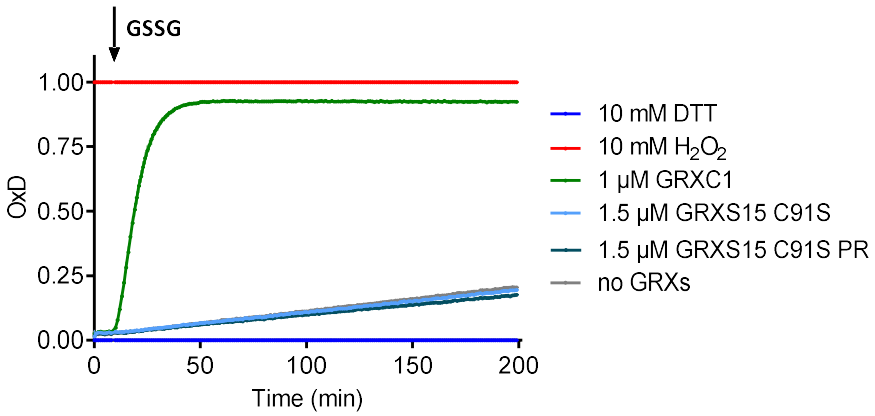

Supplementary Fig. 3b.3 | GRXS15 C91S has no oxidoreductase activity. 1.5 µM of GRXS15 C91S was tested for oxidation of 1 µM of pre-reduced roGFP2. The enzyme was tested in its native form, and pre-reduced (PR) with 10 mM DTT for 100 minutes and desalted. The reactions were triggered by freshly prepared glutathione disulfide (GSSG) automatically injected after 10 minutes at a final concentration of 40 µM. 1 µM GRXC1 was used as a positive control and 1 µM of roGFP2 without any GRXs was used as negative control. Furthermore, 1 µM of roGFP2 fully oxidised by H_2O_2 or fully reduced by DTT at a final concentration of 10 mM were used to define maximum oxidation and reduction of roGFP2. Filter-based excitation at 390 and 480 nm and detection of emitted light at 520 nm were followed over time in plate reader. Data shows the degree of oxidation of roGFP2 (OxD) as means ± SD (*n* = 3).

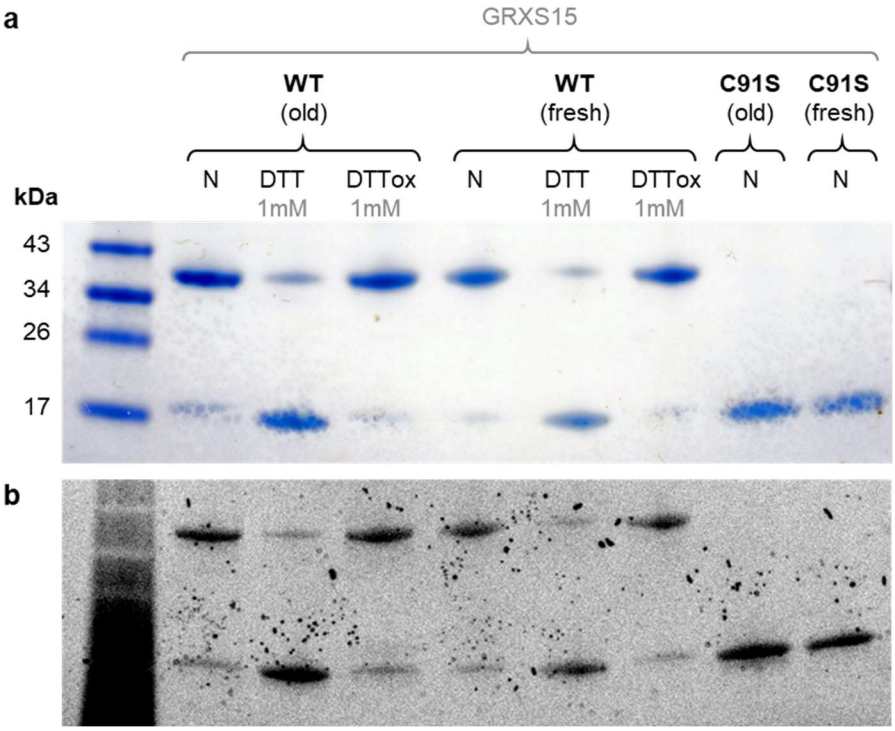

Supplementary Fig. 3b.4 | Old and fresh proteins show similar dimer formation. a 5 µg of each protein was either not treated (**N**), reduced with 1 mM DTT (**Red**) and oxidised with 1 mM trans-4,5-Dihydroxy-1,2-dithiane (**DTTox**) overnight on ice. The samples had different ages, from 2 years after purification, stored at -20 °C (old) and just purified (fresh). After addition of non-reducing loading buffer, the samples were boiled at 95 °C for 10 minutes and immediately loaded in precast gel (Mini-PROTEAN TGX Stain-Free 12 %; Bio-Rad). After the run, the gel was stained with PageBlue™. **b** UV light image was taken before the staining.

	Species	Protein name	Alignment around active site	Alignment around C-terminal	Total cys
Class I	*Arabidopsis thaliana*	*At*GRXC1	... VVVFSRTY-----CGYCQRVKQ ...	... VFIKGNHIGGCDRVM ...	3
	Zea mays	*Zm*GRX1	... LVVFSRTS-----CPFCVRVKQ ...	... VFINGKHIGGCDDTM ...	3
	Hordeum vulgare	*Hv*GRXC6	... VVVFSRSY-----CPFCVQVKK ...	... VFINGKHIGGCDDTL ...	3
	Oryza sativa Japonica	*Os*GRXC1	... VVIFSMSS-----CCMCHTVTR ...	... VFIGGRLVGSTDKVM ...	4
	Populus trichocarpa	*Pt*GRXC1	... VVVFSRTY-----CGYCNRVKQ ...	... VFIGGKNIGGCDTVV ...	3
	Physcomitrella patens	*Pp*GRXC1	... VVVYSRTY-----CPYCMRVKK ...	... VFVGGKLVGGVDAVM ...	3
	Synechocystis PCC 6803	*Sy*GRXA	... IEIYTWST-----CPFCMRALA ...	... IFIDDQHIGGCDDIY ...	4
	Chlamydomonas reinhardtii	*Cr*GRX1	... VVVYSRTH-----CPYCMKAKS ...	... VFINGKFLGGGDDTA ...	2
	Escherichia coli	*Ec*GRX3	... VEIYTRET-----CPYCHRAKA ...	... IFIDAQHIGGCDDLY ...	3
	Saccharomyces cerevisiae	*Sc*GRX1	... IFVASRTY-----CPYCHAALN ...	... IYINGKHIGGNDDLQ ...	2
	Caenorhabditis elegans	*Ce*GRX1	... VVVFSRSY-----CPYCHKARA ...	... VFINGKFFGGGDDTA ...	3
	Drosophila melanogaster	*Dm*GRX1	... VVIFSRSY-----CPYCSMAKE ...	... CFIDGKFVGGGTDVK ...	3
	Danio rerio	*Dr*GRX2	... VVIFSRTT-----CPYCKMAKG ...	... VFINGQCIGGGSDTK ...	8
	Mus musculus	*Mm*GRX2	... VVIFSRTS-----CSYCSMAKK ...	... IFVNGRFIGGARTLT ...	5
	Homo sapiens	*Hs*GRX2	... VVIFSRTS-----CSYCTMAKK ...	... IFVNGTFIGGATDTH ...	4
Class II	*Arabidopsis thaliana*	*At*GRXS15	... VMIYMRGVPESPQCGFSSLAVR ...	... IFIKGEFIGGSDIIL ...	1
	Zea mays	*Zm*GRXS15	... VVIYMRGYPDAPRCGFSALAVK ...	... IFIKGEFVGGSDIIL ...	1
	Hordeum vulgare	*Hv*GRXS4	... VIIYMRGHPQAPRCGFSALAVK ...	... IFINGEFVGGSDIIL ...	1
	Oryza sativa Japonica	*Os*GRXS4	... VLIYMRGYPDAPRCGFSALAVR ...	... IFIKGEFVGGSDIIL ...	1
	Populus trichocarpa	*Pt*GRXS15	... IVIYMRGYPDLPQCGFSALAVR ...	... IFIKGEFIGGSDIIM ...	2
	Physcomitrella patens	*Pp*GRXS15	... VMVFMRGVPQAPQCGFSAMVVR ...	... VYVNGEFVGGSDILI ...	1
	Synechocystis PCC 6803	*Sy*GRX4	... VMVFMRGTKLMPQCGFSNNVVQ ...	... VYVNGEFVGGSDIMI ...	1
	Chlamydomonas reinhardtii	*Cr*GRX5	... SIAKDRGTPDSPQCGFSRMACV ...	... VFVNGEFIGGCDILM ...	3
	Escherichia coli	*Ec*GRX4	... ILLYMRGSPKLPSCGFSAQAVQ ...	... LWVDGELVGGCDIVI ...	3
	Saccharomyces cerevisiae	*Sc*GRX5	... VVLFMRGTPEFPKCGFSRATIG ...	... LYVNKEFIGGCDVIT ...	2
	Caenorhabditis elegans	*Ce*GRX5	... VVVFMRGTQQEPACGFSRNVKL ...	... VYVKGEFVGGCDILI ...	2
	Drosophila melanogaster	*Dm*GRX5	... VVVFMRGNPQAPRCGFSNAVVQ ...	... VFINGEFVGGCDILL ...	2
	Danio rerio	*Dr*GRX5	... VVVFMRGTPAQPMCGFSNAVVQ ...	... VFFNGEFVGGCDILL ...	3
	Mus musculus	*Mm*GRX5	... VVVFLRGTPEQPQCGFSNAVVQ ...	... VYLNGEFVGGCDILL ...	2
	Homo sapiens	*Hs*GRX5	... VVVFLRGTPEQPQCGFSNAVVQ ...	... VYLNGEFVGGCDILL ...	2

Supplementary Fig. 3b.5 | Sequences alignment of GRXs from different species and different kingdoms. Representative glutaredoxins homologues of Arabidopsis GRXC1 (cytosolic class I) and homologues of Arabidopsis GRXS15 (mitochondrial class II) were retrieved from NCBI Standard Protein Blast. The alignment was generated by local multiple alignments of the amino acid sequences (Clustal Omega with ClustalW parameters; https://www.ebi.ac.uk/Tools/msa/clustalo/). The grey line separates the class I and class II GRXs. The count of cysteine residues does not include the mitochondrial targeting peptide.

```
AtGRXS15        MAASLSSRLIKGIANLKAVRSSRLTSASVYQNGMMRFSSTVPSDSDTHDDFKPTQKVP--  58
HsGrx5          -------------------MSGSL---GRAAAALLRWGRGAGG----GGLWGPGVRAAGS  34
ScGrx5          -------MF---LPKFNPIRSFSP---ILRAKTLLRYQNRM-------------------  28

AtGRXS15        PDSTDSLKDIVENDVKDNPVMIYMKGVPESPQCGFSSLAVRVLQQYNVP---ISSRNILE  115
HsGrx5          GAGGGGSAEQLDALVKKDKVVVFLKGTPEQPQCGFSNAVVQILRLHGVR--DYAAYNVLD  92
ScGrx5          -YLSTEIRKAIEDAIESAPVVLFMKGTPEFPKCGFSRATIGLLGNQGVDPAKFAAYNVLE  87

AtGRXS15        DQELKNAVKSFSHWPTFPQIFIKGEFIGGSDIILNMHKEGELEQKLKDVSGNQD------  169
HsGrx5          DPELRQGIKDYSNWPTIPQVYLNGEFVGGCDILLQMHQNGDLVEELKKLGIHSTLL-DEK  151
ScGrx5          DPELREGIKEFSEWPTIPQLYVNKEFIGGCDVITSMARSGELADLLEEAQALVPEEEEET  147

AtGRXS15        ------      169
HsGrx5          KDQDSK      157
ScGrx5          KDR---      150
```

Supplementary Fig. 3b.6 | Sequences alignment of the mitochondrial class II glutaredoxins from Arabidopsis, human and yeast. Primary structure comparison of the mitochondrial class II *At*GRXS15 from Arabidopsis (*Arabidopsis thaliana*), *Hs*Grx5 from human (*Homo sapiens*) and *Sc*Grx5 from yeast (*Saccharomyces cerevisiae*). The alignment was generated by local multiple-sequence alignment (Clustal Omega, https://www.ebi.ac.uk/Tools/msa/clustalo/). The cysteines as well as the active site “CGFS” are highlighted in yellow while the conserved lysyl residue before the active site is highlighted in red.

4 | Consequences of GRXS15 decrease activity

This chapter presents the research paper published in *Plant Physiology* in 2021:

"The function of glutaredoxin GRXS15 is required for lipoyl-dependent dehydrogenases in mitochondria"

Anna Moseler, Inga Kruse, Andrew E. Maclean, ***Luca Pedroletti****, Marina Franceschetti, Stephan Wagner, Regina Wehler, Katrin Fischer-Schrader, Gernot Poschet, Markus Wirtz, Peter Dörmann, Tatjana M. Hildebrandt, Rüdiger Hell, Markus Schwarzländer, Janneke Balk and Andreas J. Meyer. (2021)*

Plant Physiology, 186: 1507–1525; doi.org/10.1093/plphys/kiab172.

The complete supplementary data are available under "Supplemental data" on the website: *https://academic.oup.com/plphys/article/186/3/1507/6226523#304831117.*

4.1 | Summary and personal contribution

Iron-sulfur (Fe–S) clusters play essential roles in various biological processes across all forms of life and their assembly and distribution to Fe–S-dependent proteins need to be finely regulated. The monothiol glutaredoxin S15 (GRXS15) localized in plant mitochondria can bind a [2Fe–2S] cluster and transfer this to other proteins, as demonstrated *in vitro* (Azam *et al.*, 2020). However, the precise role of the protein *in planta* is only partially understood. In this research paper, we unravelled the link between GRXS15 and the four lipoyl-dependent dehydrogenases in Arabidopsis mitochondria.

Since *grxs15* null mutants are embryo lethal, we used lines that overexpress the mutated variant GRXS15 K83A, which is compromised in Fe–S cluster coordination (more details in the previous Chapters 3s and Chapter 3b) in a *grxs*15 null mutant background and the knockdown line *amiR* (*GRXS15*^{amiR}; Ströher *et al.* (2016)). These GRXS15-compromised mutants, collectively referred to as *grxs15* mutants, showed a dwarf phenotype. To investigate whether the lack of growth could be due to defects in Fe–S cluster biosynthesis, we systematically analysed several mitochondrial metabolic pathways dependent on Fe–S enzymes.

Biotin synthase (BIO2) requires [2Fe–2S] and [4Fe–4S] clusters to function and it is unknown how the enzyme receives these clusters (Fig. 8 in Moseler *et al.* (2021); for more details see Chapter 2, Pedroletti et *al.* (2023a)). We found that neither the abundance of biotin-dependent methylcrotonyl-CoA carboxylase (MCCase) nor the fatty acid synthesis, reliant on mitochondrial biotin which is exported from mitochondria, were changed in *grxs15* mutants.

Consistently, supplementing of the growth media with biotin was unable to rescue the growth retardation of *grxs15* mutants. This strongly suggested that their dwarf phenotype is not primarily caused by defects in biotin synthesis.

Cofactor of nitrate reductase and xanthine dehydrogenase 2 (CNX2) requires [4Fe–4S] clusters to synthesise a precursor of the molybdenum cofactor (Moco) in the mitochondrial matrix. However, we found no striking defects of Moco-dependent enzymes nitrate reductase (NR), xanthine dehydrogenase (XDH) and aldehyde oxidase (AO) in *grxs15* mutants, suggesting that Moco-dependent nitrogen metabolism was not limiting upon impaired GRXS15 function.

Enzyme complexes of the mitochondrial electron transport chain (mETC) contain a total of 12 Fe–S clusters (Fig. 8 in Moseler *et al.* (2021); for more details see Chapter 2). Although *grxs15* plants showed decreased root respiration, we found no differences between wild type and the *grxs15* mutants when we measured respiration in isolated mitochondria and analysed the activity and abundance of the respective complexes and the capacity of the alternative oxidases (AOXs). Since wild type and *grxs15* mutants also showed similar cytosolic ATP levels, we argued that the mETC was not the major system affected by GRXS15 impairment.

Mitochondrial aconitases (ACOs) require [4Fe–4S] clusters for their activity (Fig. 8 in Moseler *et al.* (2021)). Contrary to previous work, we found no differences in ACOs activity in *grxs15* mutants, suggesting that ACOs defects were not the main cause of the *grxs15* dwarfism.

Furthermore, we analysed the *grxs15 K83A* mutant for signs of oxidative stress resulting from improper Fe–S cluster transfer by the mutant protein. We found no differences in neither reactive oxygen species (ROS) levels nor in H_2O_2 concentration nor in the glutathione redox potential between the *grxs15* and wild-type plants.

To investigate potential other metabolic defects in *grxs15* plants, we metabolically profiled *grxs15 K83A* mutants and found that most quantified organic acids were elevated compared to wild type. Pyruvate showed the most significant change, with a more than four-fold increase compared to the wild type. 2-oxoglutarate (2-OG) also slightly increased in the mutant lines. Both metabolites are degraded by the protein complexes pyruvate dehydrogenase complex (PDC) and oxoglutarate dehydrogenase complex (OGDC), respectively, and both require a lipoyl cofactor to operate. Since lipoylation defects were previously associated with knockdown lines of GRXS15 (Ströher *et al.*, 2016), we measured PDC activity in isolated mitochondria and found it to be reduced in mitochondria isolated from *grxs15 K83A* plants.

The lipoyl cofactor is essential for two other mitochondrial protein complexes, glycine decarboxylase complex (GDC) and branched-chain α-keto acids dehydrogenase complex (BCKDC). We found that lipoylation of GDC was reduced in the *grxs15* mutants and that keto

acids derived from branched-chain amino acid degradation massively accumulated in *grxs15 K83A* mutants, indicating decreased activity of BCKDC.

Taken together, our results showed that while most Fe–S cluster-dependent processes are unaffected in *grxs15* mutants, there is an accumulation of all the metabolites directly linked to the four mitochondrial lipoyl-dependent enzymes. Thus, we hypothesised that the impaired Fe–S cluster supply in *grxs15* mutants specifically affects lipoyl synthase (LIP1) which relies on Fe–S cluster for the biosynthesis of the lipoyl cofactor, directly affecting the lipoyl-dependent dehydrogenase complexes (Fig. 8 in Moseler *et al.,* (2021)).

My personal contribution to this study was to phenotype and analyse all the *grxs15* mutants in one single dataset, including the knockdown mutant *grxs15-1* (Moseler *et al.*, 2015; Ströher *et al.*, 2016) (more detail in Chapter 5, Pedroletti *et al.* (2023b)). Particularly, I have grown the *grxs15-1*, *amiR*, *K83A #3* and *#4* mutants next to wild type on vertical ½ MS agar plates to phenotype young seedlings and analyse the root length. I also phenotyped older plants on soil. The obtained results are shown in Supplemental Figure S1, which is attached after the manuscript, in Section 5.3.

I conducted preliminary experiments to investigate the potential role of GRXS15 in drought tolerance and the influence of various substrates on the growth of plants with compromised GRXS15 activity. The obtained results were not part of this research paper but are reported in Appendix 2.

Overall, this research represents a significant stride towards understanding the role *in vivo* role of GRXS15 and, more broadly, shedding light on the Fe–S cluster distribution in the mitochondrion. The important insights achieved by this study served as the cornerstone for the hypothesis that we further explored in the next Chapter 5 (Pedroletti *et al.*, 2023b).

4.2 | Manuscript

Attached on the following pages is the manuscript published in *Plant Physiology (doi.org/10.1093/plphys/kiab172).*

doi:10.1093/plphys/kiab172 PLANT PHYSIOLOGY 2021: 186: 1507–1525

Plant Physiology®

Research Article

The function of glutaredoxin GRXS15 is required for lipoyl-dependent dehydrogenases in mitochondria

Anna Moseler ,[1,2] Inga Kruse ,[3,4,§] Andrew E. Maclean,[3,4,#] Luca Pedroletti ,[1] Marina Franceschetti ,[3] Stephan Wagner ,[1] Regina Wehler,[5] Katrin Fischer-Schrader ,[6] Gernot Poschet,[7] Markus Wirtz ,[7] Peter Dörmann ,[5] Tatjana M. Hildebrandt ,[8] Rüdiger Hell ,[7] Markus Schwarzländer,[9] Janneke Balk [3,4] and Andreas J. Meyer [1,10,*,†]

1 Institute of Crop Science and Resource Conservation (INRES)—Chemical Signalling, University of Bonn, 53113 Bonn, Germany
2 Université de Lorraine, INRAE, IAM, Nancy 54000, France
3 Department of Biological Chemistry, John Innes Centre, Norwich NR4 7UH, UK
4 School of Biological Sciences, University of East Anglia, Norwich NR4 7TJ, UK
5 Institute of Molecular Physiology and Biotechnology of Plants (IMBIO), University of Bonn, 53115 Bonn, Germany
6 Department of Chemistry, Institute for Biochemistry, University of Cologne, 50674 Cologne, Germany
7 Centre for Organismal Studies, University of Heidelberg, 69120 Heidelberg, Germany
8 Institute of Plant Genetics, Leibniz University Hannover, 30167 Hannover, Germany
9 Institute of Plant Biology and Biotechnology (IBBP)—Plant Energy Biology, University of Münster, 48143 Münster, Germany
10 Bioeconomy Science Center, c/o Forschungszentrum Jülich, 52425 Jülich, Germany

*Author for communication: andreas.meyer@uni-bonn.de
†Senior author.
§ Present address: Strathclyde Institute of Pharmacy and Biomedical Sciences, University of Strathclyde, Glasgow G1 1XQ, UK.
#Present address: Wellcome Trust Centre for Integrative Parasitology, University of Glasgow, Glasgow G12 8TA, UK.

A.M. and A.J.M. conceived the research with specific input from M.S. and J.B.; A.M. A.J.M., and J.B. designed the experiments and interpreted the data. I.K., A.E.M., M.F., S.W., R.W., K.F.S., G.P., M.W., T.M.H., and L.P. contributed experimental data, structural information and analyzed the data. A.M. and A.J.M. wrote the manuscript with support from M.S., T.H., M.W. R.H., P.D., and J.B.; A.J.M. agrees to serve as the author responsible for contact and ensures communication.
The author responsible for distribution of materials integral to the findings presented in this article in accordance with the policy described in the Instructions for Authors (https://academic.oup.com/plphys/pages/general-instructions) is: Andreas J. Meyer (andreas.meyer@uni-bonn.de).

Abstract

Iron–sulfur (Fe–S) clusters are ubiquitous cofactors in all life and are used in a wide array of diverse biological processes, including electron transfer chains and several metabolic pathways. Biosynthesis machineries for Fe–S clusters exist in plastids, the cytosol, and mitochondria. A single monothiol glutaredoxin (GRX) is involved in Fe–S cluster assembly in mitochondria of yeast and mammals. In plants, the role of the mitochondrial homolog GRXS15 has only partially been characterized. Arabidopsis (*Arabidopsis thaliana*) *grxs15* null mutants are not viable, but mutants complemented with the variant *GRXS15 K83A* develop with a dwarf phenotype similar to the knockdown line *GRXS15*^{amiR}. In an in-depth metabolic analysis of the variant and knockdown *GRXS15* lines, we show that most Fe–S cluster-dependent processes are not affected, including biotin biosynthesis, molybdenum cofactor biosynthesis, the electron transport chain, and aconitase in the tricarboxylic acid (TCA) cycle. Instead, we observed an increase in most TCA cycle intermediates and amino acids, especially pyruvate, glycine, and branched-chain amino acids (BCAAs). Additionally, we found an accumulation of branched-chain α-keto acids (BCKAs), the first degradation products resulting from transamination of BCAAs. In wild-type plants, pyruvate, glycine, and BCKAs are all metabolized through decarboxylation by mitochondrial lipoyl cofactor (LC)-dependent dehydrogenase complexes. These enzyme complexes are very abundant, comprising a major sink for LC. Because biosynthesis of LC

Received March 16, 2021. Accepted April 02, 2021. Advance access publication April 15, 2021

depends on continuous Fe–S cluster supply to lipoyl synthase, this could explain why LC-dependent processes are most sensitive to restricted Fe–S supply in *grxs15* mutants.

Introduction

Since the early days of biological evolution, iron–sulfur (Fe–S) clusters have been employed as catalytic co-factors for electron transfer reactions and are nowadays present in a plethora of essential proteins (Pain and Dancis, 2016). Because Fe–S clusters are inherently unstable they do not exist in free form but always need to be chaperoned before reaching their final destination apoproteins. Among the proteins thought to be involved in Fe–S cluster transfer is a specific subtype of glutaredoxins (GRXs) capable of coordinating [2Fe–2S] clusters as a protein dimer (Banci et al., 2014; Couturier et al., 2015; Lill and Freibert, 2020).

GRXs are ubiquitous proteins, which form a large family with several subfamilies in plants (Rouhier et al., 2008; Meyer et al., 2009). Although their canonical function is glutathione-dependent redox catalysis, dissection of the function of subclasses and individual family members reveals an unexpectedly diverse picture (Deponte, 2013; Liedgens et al., 2020; Trnka et al., 2020). Class II GRXs share a CGFS amino acid motif in the active site and are proposed to serve as carrier proteins for Fe–S cluster between the assembly machinery and receiving apoproteins. A second proposed function is the repair of oxidation-sensitive Fe–S clusters (Couturier et al., 2015). In Arabidopsis (*Arabidopsis thaliana*), Fe–S cluster assembly machineries are present in the cytosol, plastids, and mitochondria, and at least one monothiol GRX is located in each of these compartments: GRXS15 in mitochondria; GRXS14 and GRXS16 in plastids; and GRXS17 in the cytosol (Cheng et al., 2006; Bandyopadhyay et al., 2008; Knuesting et al., 2015; Moseler et al., 2015). While plants deficient in plastidic GRXS14 did not display any growth phenotype under nonstress conditions, genetic stacking of a *grxs14* null mutant and knockdown of *GRXS16* caused pronounced growth retardation (Rey et al., 2017). Exposure of *grxs14* and the double mutant to prolonged darkness led to accelerated chlorophyll loss compared to wild-type (WT) and decreased abundance of proteins involved in the maturation of Fe–S proteins. Mutants lacking the cytosolic GRXS17 were sensitive to high temperature and long-day photoperiod (Cheng et al., 2011; Knuesting et al., 2015; Martins et al., 2020). However, the activities of cytosolic Fe–S proteins, like aconitase (ACO) or aldehyde oxidase (AO), were not substantially altered in *grxs17* null mutants (Knuesting et al., 2015; Iñigo et al., 2016).

The mitochondrial GRXS15 is indispensable as indicated by embryonic lethality of null mutants (Moseler et al., 2015). Partial complementation with a mutated *GRXS15 K83A* variant, which is weakened in its ability to coordinate an [2Fe–2S] cluster in vitro, results in a dwarf phenotype (Moseler et al., 2015). A similar dwarf phenotype has also been reported for a *GRXS15* knockdown line (Ströher et al., 2016). Expression of *GRXS15* in the yeast (*Saccharomyces cerevisiae*) *grx5* mutant can partially rescue the impaired growth and ACO activity (Moseler et al., 2015), suggesting a conserved function in Fe–S cluster assembly. Grx5 in yeast and its homolog in vertebrates are thought to have a general role in the early steps of Fe–S cluster transfer leading to pleiotropic effects due to the simultaneous impairment of several central mitochondrial processes (Lill and Freibert, 2020). In vitro data showed that Arabidopsis GRXS15 was able to interact with the scaffold proteins iron-sulfur cluster assembly (ISCA)1a/2 and to deliver [2Fe–2S] cluster resulting in the generation of [4Fe–4S] cluster on the ISCA complex (Azam et al., 2020). Mitochondria contain at least 26 Fe–S proteins that are involved in different processes, including electron transport [complexes I–III in the respiratory electron transport chain (ETC)] and the tricarboxylic acid (TCA) cycle [ACO and succinate dehydrogenase (SDH)]. A general role of GRXS15 in the early steps of Fe–S cluster transfer would therefore predict pleiotropic effects of diminished GRXS15 activity, due to the simultaneous impairment of several central mitochondrial processes. The number of potential defective sites is even further amplified if the synthesis of enzyme cofactors and the function of several cofactor-dependent enzymes, in turn, is compromised. Indeed, pathways for biosynthesis of the molybdenum cofactor (Moco) and lipoyl cofactor (LC) involve the mitochondrial [4Fe–4S] proteins GTP-3′,8-cyclase (CNX2; cofactor of nitrate reductase [NR] and xanthine dehydrogenase [XDH] 2) and lipoyl synthase (LIP1; Yasuno and Wada, 2002; Schwarz and Mendel, 2006). It should be noted that Δ*grx5* mutants in yeast also have a defect in iron signaling and accumulate toxic levels of iron as a consequence (Rodríguez-Manzaneque et al., 2002), for which there is so far no evidence in Arabidopsis *grxs15* mutants.

A study of two different *GRXS15* knockdown mutants in Arabidopsis by Ströher et al. (2016) found normal activities of ACO (one [4Fe-4S] cluster) and complex I (one [2Fe-2S]cluster and seven [4Fe-4S] clusters) but a pronounced decrease in LC-dependent proteins. Diminished presence of the LC itself and decreased abundance of mitochondrial LIP1 (mLIP1) led to the conclusion that GRXS15 plays a putative role in transfer of Fe–S clusters for mitochondrial LC synthesis (Ströher et al., 2016). In the mitochondrial matrix, four enzyme complexes depend on lipoamide as a prosthetic group: the pyruvate dehydrogenase complex (PDC), the 2-oxoglutarate (2-OG) dehydrogenase complex (OGDC), the glycine decarboxylase complex (GDC), and the branched-chain α-keto acid (BCKA) dehydrogenase complex (BCKDC; Taylor et al., 2004; Solmonson and DeBerardinis,

2018). The PDC acts as the entry point of acetyl-CoA into the TCA cycle, while OGDC acts within the TCA cycle to convert 2-OG to succinyl-CoA. The GDC catalyzing the oxidative decarboxylation of glycine is essential for photorespiration (Douce et al., 2001), but also for C1 metabolism (Mouillon et al., 1999). BCKDC is involved in the catabolism of the three branched-chain amino acids (BCAAs) leucine (Leu), valine (Val), and isoleucine (Ile), and their corresponding BCKAs (Araújo et al., 2010; Gu et al., 2010; Peng et al., 2015). Whether all these LC-dependent enzymes are affected similarly in *grxs15* mutants and whether other pathways containing Fe–S enzymes are diminished and thus constitute bottlenecks that severely restrict metabolic fluxes is yet unknown because the respective mutants have not been metabolically characterized.

Here, we aimed to identify the most severe metabolic bottlenecks caused by severely restricted capacity of GRXS15 mutants in Fe–S transfer. We consider several candidate Fe–S proteins involved in essential mitochondrial processes starting with biotin biosynthesis, followed by Moco biosynthesis, capacity of the mitochondrial ETC (mETC), TCA cycle flow, and closing with the biosynthesis of LC. We assess how these Fe–S-related processes are affected in *grxs15-3* null mutants complemented with *GRXS15 K83A* and in $GRXS15^{amiR}$ knockdown mutants trying to pin down the cause of the phenotype and by that the functional significance of GRXS15. By direct comparison of partially complemented null mutants and knockdown mutants, we resolve previous contradictions about the role of GRXS15 in the maturation of Fe–S containing enzymes.

Results

GRXS15 K83A causes retardation in growth

To complete embryogenesis, GRXS15 is essential in plants. To bypass embryo lethality, Arabidopsis *grxs15* null mutants were complemented with the *GRXS15 K83A* variant and these complemented plants are able to grow, but have small rosette leaves (Moseler et al., 2015). Based on this observation, we aimed to further analyze the growth phenotype and compare it with published records of *grxs15* knockdown mutants. The dwarf phenotype of the *GRXS15 K83A* complementation lines #1 to #5 becomes apparent at the early seedling stage (Figure 1, A and B). Analysis of root length in five randomly selected lines consistently also showed a concomitant reduction of primary root length compared to WT (Figure 1B). Although only minor differences in seedling size could be observed, line #3 was the best growing complementation line, and line #4 the weakest (Figure 1C; Moseler *et al.*, 2015). This effect was stable and consistent over several generations. The phenotype is similar to $GRXS15^{amiR}$ knockdown lines reported by (Ströher et al. 2016; Supplemental Figure S1). The insertion line *grxs15-1* carrying a T-DNA in an intron within the 5′-UTR (Moseler et al. 2015), which had been reported to display a short root phenotype (Ströher et al., 2016) cannot be clearly distinguished from the WT in our hands, neither at seedling stage nor at rosette stage (Supplemental Figure S1). This allele was excluded from further analysis. To test whether the reduced growth of *GRXS15 K83A*-complemented null mutants was true growth retardation or caused by delayed germination, the two lines #3 and #4 were scored for the timing of radical emergence. The absence of any difference between WT and the two mutants suggests that the growth phenotype reflects a genuine growth retardation (Figure 1C).

Biotin-mediated metabolism is not impaired when GRXS15 function is diminished

Following our earlier observation that GRXS15 can coordinate a [2Fe–2S] cluster (Moseler et al., 2015), similar to the homologs in yeast and mammals (Uzarska et al., 2013; Banci et al., 2014), we embarked on testing a number of pathways of Fe–S-dependent metabolism that may be affected in the mutant. One putative target protein of GRXS15 is mitochondrial biotin synthase (BIO2, At2g43360) since it relies on supply of a [2Fe–2S] and a [4Fe–4S] cluster. BIO2 catalyzes the final step in biotin biosynthesis, which acts as an essential cofactor in several carboxylases in energy metabolism. Destruction of the [2Fe–2S] cluster for sulfur supply to biotin with each catalytic cycle and subsequent turnover increases the demand of the BIO2 protein for [2Fe–2S] clusters (Ugulava et al., 2001). *bio2* null mutants were previously described as embryo-defective, arrested mostly at globular or heart stage of embryo development (Patton et al., 1998; Meinke, 2019). Because lack of biotin typically causes degradation of the respective apoproteins (Solbiati et al., 2002), we tested for the abundance of biotin-dependent methylcrotonoyl-CoA carboxylase (MCCase), which is involved in Leu degradation in mitochondria. None of the five analyzed *grxs15* complementation lines showed a decrease in protein abundance of the biotinylated MCCase subunit A (MCCA; Figure 2A). Biotin is also exported to the cytosol and the chloroplasts, where it is required for synthesis and elongation of fatty acids by hetero and homomeric acetyl-CoA carboxylase (ACCase). Total fatty acids in seeds amounted to 7.6 ± 0.8 nmol $seed^{-1}$ in line #4 and 7.6 ± 1.0 nmol $seed^{-1}$ in the WT and no difference in relative abundance of specific fatty acids in seeds was observed (Figure 2C). In 8-d-old seedlings, the amount of total fatty acids did not differ in line #4 10.3 ± 0.4 nmol (mg FW)$^{-1}$ compared to 8.8 ± 1.0 nmol (mg FW)$^{-1}$ in WT, but a 23% increase in α-linolenic acid (18:3) was observed (Figure 2B).

bio2 mutants can be rescued by the addition of biotin to both arrested embryos cultured in vitro and to mutant plants grown on soil (Schneider et al., 1989; Patton et al., 1998; Pommerrenig et al., 2013). External supply of biotin or its precursor desthiobiotin to a $GRXS15^{amiR}$ knockdown mutant and the complemented line #4 in both cases improved growth slightly but did not rescue the growth defects of either of the lines (Figure 2D). It should be noted though that also the WT grew better with the supply of biotin or desthiobiotin. These results suggest that growth retardation of

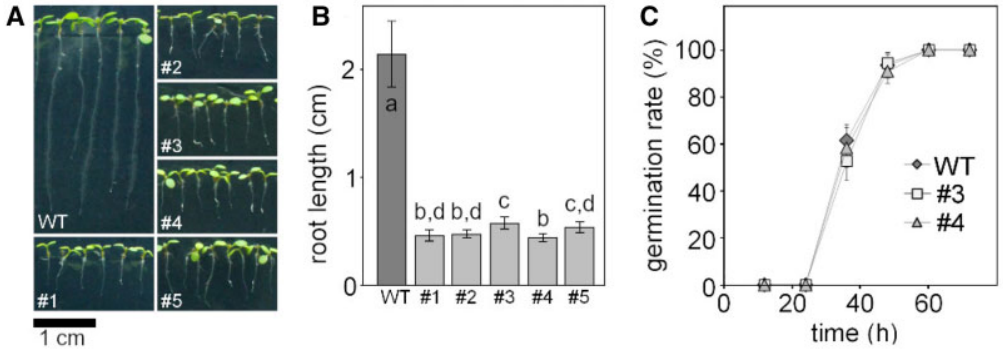

Figure 1 Complementation of the Arabidopsis *grxs15-3* mutant with *UBQ10*$_{pro}$*:GRXS15 K83A*. A, 8-d-old WT seedlings compared with *GRXS15 K83A* mutants grown on vertical agar plates under long-day conditions. B, Primary root length of 8-d-old *GRXS15 K83A* mutants compared to WT ($n = 35$; means ± SD). Different letters indicate significant differences between the different lines; $P \leq 0.05$; (one-way analysis of variance (ANOVA) with post hoc Holm–Sidak analyses). C, Germination rate of *GRXS15 K83A* lines #3 and #4 compared to WT. All seeds were initially stratified at 4°C in the dark for 1 d ($n = 6$ with 20–25 seeds each; means ± SD). Germination was assessed with the emergence of the radicle. No statistically significant differences were found using Student's *t* test analysis ($P > 0.05$).

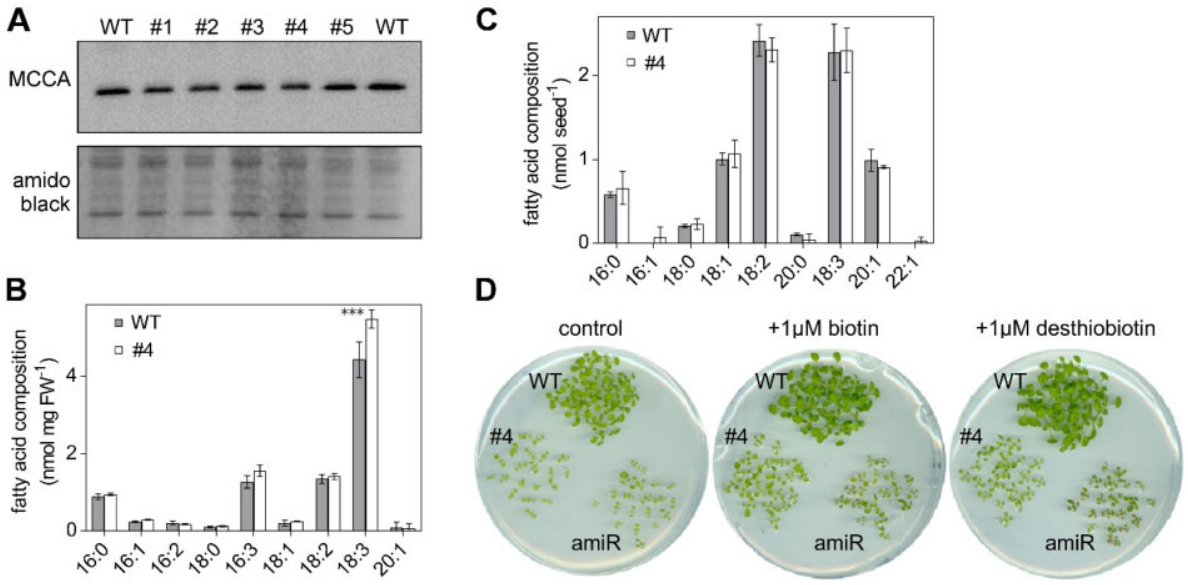

Figure 2 *GRXS15 K83A* mutation has no impact on the biotin pathway in Arabidopsis seedlings. A, Immunoblot analysis of biotinylated MCCA in mitochondria (mito) of *GRXS15 K83A* mutants compared with WT. In the upper, biotinylated MCCA was detected by streptavidin HRP in isolated mito from 2-week-old seedlings (9 µg protein was loaded per lane). In the lower, amido black staining of the membrane is shown as a control for protein loading. B and C, Fatty acids quantified by gas chromatography of 8-d-old seedlings (B) and seeds (C) of *GRXS15 K83A* line #4 compared to WT ($n = 3–4$; means ± SD). The statistical analysis (two-way ANOVA with post hoc Holm–Sidak comparisons for WT versus *grxs15*) indicated no significant ($P \leq 0.05$) change except for 18:3 (***$P < 0.001$). D, *GRXS15 K83A* line #4, the knockdown line *GRXS15*^{amiR} (amiR), and WT plants were grown on horizontal plates with 1/2 MS agar without sucrose. The medium contained either no biotin (control), 1 µM biotin or 1 µM desthiobiotin.

grxs15 mutants is not primarily caused by defects in biotin synthesis.

Moco-dependent nitrogen metabolism is not limiting upon impaired GRXS15 function

The Moco precursor cyclic pyranopterin monophosphate (cPMP) is synthesized in the mitochondrial matrix by the CNX2 (At2g31955) and the cPMP synthase CNX3 (At1g01290) and is exported to the cytosol for subsequent biosynthesis steps (Bittner, 2014; Kruse et al., 2018). Because CNX2 contains two [4Fe–4S] clusters, we hypothesized that Moco biosynthesis and hence Moco-dependent biochemical pathways may be affected by defects in mitochondrial Fe–S transfer. The most abundant Moco-dependent enzymes include NR, AO, XDH, and sulfite oxidase. Arabidopsis generally prefers nitrate as nitrogen source (Sarasketa et al., 2014), but mutants deficient in Moco biosynthesis can be rescued by providing ammonium as a nitrogen source to bypass NR

(Wang et al., 2004; Kruse et al., 2018), revealing NR as the main recipient of Moco. While the preference for nitrate (KNO_3) over ammonium ($(NH_4)_2SO_4$) could be confirmed in WT plants, we found that the growth retardation of *GRXS15 K83A* roots is more pronounced on nitrate than on ammonium as sole nitrogen source (Figure 3A). Similar results were obtained when seedlings were grown on NH_4Cl instead of $(NH_4)_2SO_4$ to control for possible impacts of the respective counter anions on the growth behavior (Supplemental Figure S2A).

The pronounced growth retardation on nitrate could be indicative of severe NR deficiency similar to *nia1 nia2* mutants lacking functional NR (Wilkinson and Crawford, 1993). A similar NR deficiency has been described for mutant alleles of the ABC transporter ATM3 that is involved in Moco biosynthesis (Bernard et al., 2009; Teschner et al., 2010; Kruse et al., 2018). *atm3-1* mutants display a severe growth phenotype and are chlorotic (Figure 3B). While *GRXS15 K83A* mutants are also smaller than WT, they are not chlorotic and thus do not phenocopy *atm3-1* (Figure 3, A and B). Despite NR activity being diminished to 50% of WT, root growth of *atm3-1* was still better on nitrate than on ammonium (Figure 3, A and C). NR activity was not altered in the *GRXS15 K83A* mutants #3 and #4 (Figure 3C). Despite the unaffected NR activity, both *grxs15* mutants contained significantly less nitrate than WT seedlings (Figure 3D). Nitrite and other inorganic anions like chloride, sulfate, or phosphate were not altered between the mutant lines and WT (Supplemental Figure S2B). All other tested Moco-dependent enzymes such as AO or XDH showed no decrease in activity in the *grxs15* mutants compared to WT (Figure 3, E and F). Taken together, these results suggest that NR activity in *GRXS15 K83A* mutants is sufficient to use nitrate as the sole nitrogen source and does not explain the growth inhibition on nitrate.

Impaired GRXS15 function leads to decreased root respiration

The mETC contains three enzyme complexes with a total of 12 Fe–S cofactors: complex I with two [2Fe–2S] and six [4Fe–4S] clusters, complex II with one [2Fe–2S], one [3Fe–4S], and one [4Fe–4S] cluster, and complex III with one

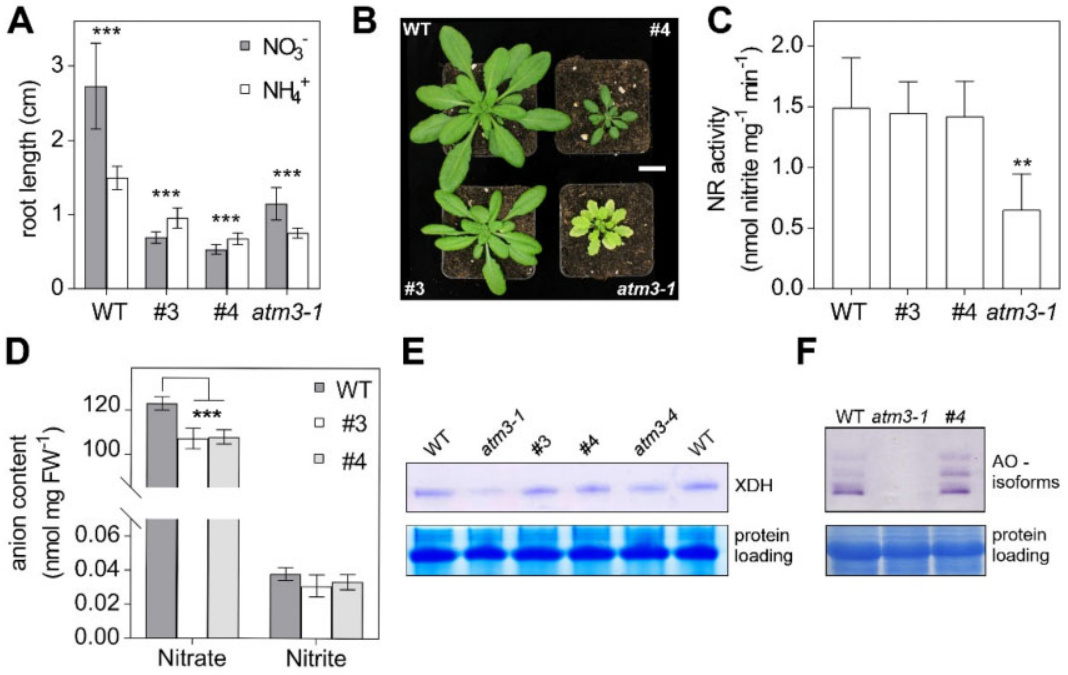

Figure 3 Growth of Arabidopsis *GRXS15 K83A* mutants is affected by the nitrogen source. A, Primary root length of *GRXS15 K83A* lines #3 and #4 as well as *atm3-1* seedlings compared to WT grown on vertical agar plates containing 5 mM KNO_3 or 2.5 mM $(NH_4)_2SO_4$ as N-source for 8 d under long-day conditions ($n = 30$; means ± SD). Student's *t* test analysis showed significant differences between the growth on the different inorganic N-sources in all lines ***$P < 0.001$. B, Representative 4-week-old plants of WT, *GRXS15 K83A* lines #3 and #4, and *atm3-1* all grown on soil under long-day conditions. Scale bar = 2 cm. C, NR activity in WT, lines #3 and #4 as well as in *atm3-1*. Activity was analyzed in 4-week-old plants grown on soil by measuring the presence of nitrite via the Griess reaction ($n = 4$; means ± SD, one-way ANOVA with post hoc Holm–Sidak comparisons for WT versus mutant lines **$P \leq 0.01$). D, Nitrate and nitrite content of 8-d-old WT and *GRXS15 K83A* lines #3 and #4 seedlings grown on agar plates ($n = 4$; means ± SEM). The statistical analysis (two-way ANOVA with post hoc Holm–Sidak comparisons for WT versus *grxs15*) indicated a significant change in the nitrate content; ***$P \leq 0.001$. E, In-gel activity of XDH in WT, *atm3-1*, and *GRXS15 K83A* mutants. Equal amounts of protein (35 µg) extracted from 8-d-old seedlings were separated on nondenaturing PA gel and stained for XDH activity using hypoxanthine as substrate. As a control of protein-loading, the gel was subsequently stained with Coomassie. F, In-gel activities of AO in WT and *atm3-1* as well as *grxs15* mutants. Equal amounts of protein were separated by nondenaturing PAGE and stained for AO activity using synthetic aldehydes (1-naphthaldehyde and indole-3-carboxaldehyde) as substrates. For control of protein loading, the gel was subsequently stained with Coomassie.

[2Fe–2S] cluster (Couturier et al., 2015; Meyer et al., 2019). Thus, we measured the respiration of detached roots and dissected the capacity of complexes I and II-linked electron flow. Indeed, roots of line #3 displayed a decreased respiration rate of 1.31 ± 0.35 nmol oxygen (O_2) min^{-1} (mg DW)$^{-1}$ compared with the WT rate of 2.92 ± 0.62 nmol O_2 min^{-1} (mg DW)$^{-1}$ (Figure 4A). This is similar to root tips of *GRXS15*^{amiR} knockdown plants, which were reported to consume less O_2 than WT plants (Ströher et al., 2016). Addition of the cytochrome *c* oxidase inhibitor KCN decreased the rate of both lines down to similar values. The remaining rates are accounted for by the presence of alternative oxidases (AOXs), since they could be inhibited by propylgallate (pGal). Interestingly, the AOX capacity appeared unchanged in line #3, even though AOX is highly inducible by mitochondrial dysfunction. Next, we investigated if the decreased root respiration is due to defects in the respiratory machinery or due to restricted metabolite turnover, or both. First, we compared the abundance of respiratory complexes in isolated mitochondria from *GRXS15 K83A* line #4, *GRXS15*^{amiR} by Blue Native–PAGE. None of the respiratory complexes including the Fe–S cluster containing complexes I–III was decreased in abundance in either mutant (Figure 4B). Additionally, we purified mitochondria from whole seedlings of the *GRXS15 K83A* line #3 and supplemented them with succinate or pyruvate/malate, respectively, as respiratory substrates. Succinate provides electrons to the ubiquinone pool of the mETC via complex II, while pyruvate/malate feeding predominantly provides NADH mainly generated by malate dehydrogenase, NAD-malic enzyme, and PDC. In addition, NADPH is also generated mainly due to the promiscuous specificity of mitochondrial

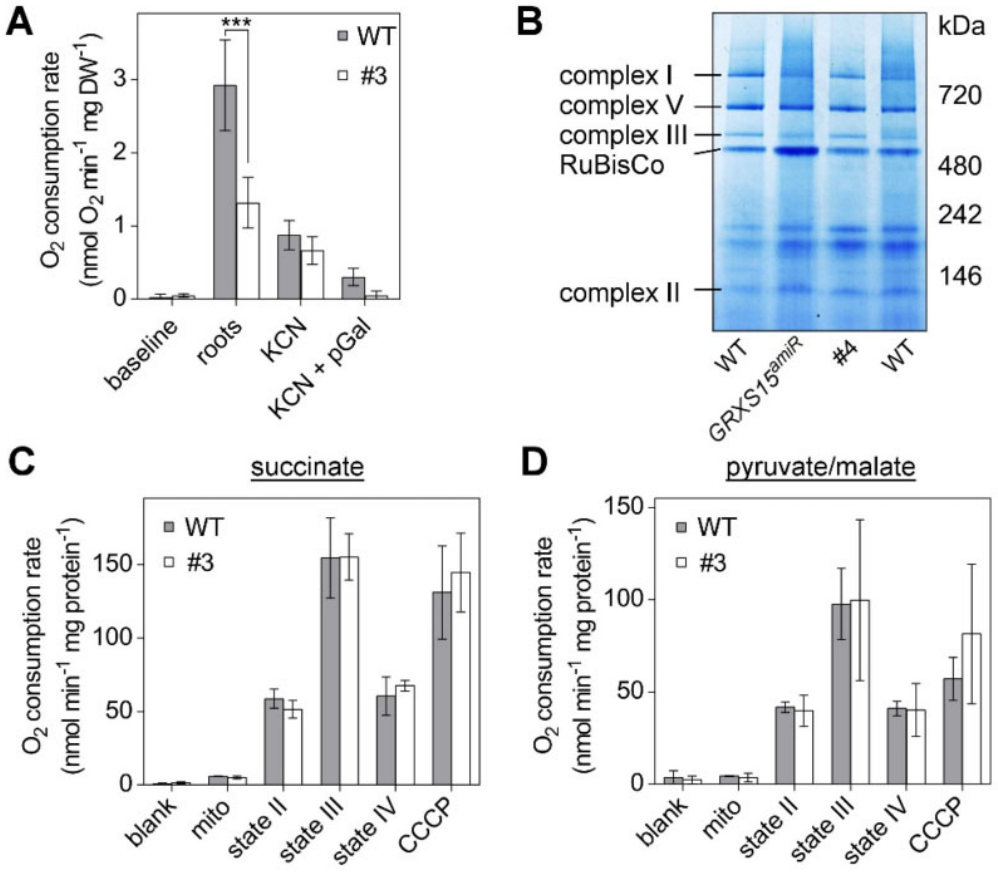

Figure 4 Respiration in complemented Arabidopsis *grxs15* mutants. A, Root respiration rate of *GRXS15 K83A* line #3 (4.5-week old) and the respective WT grown to similar size (2-week old) after addition of the cytochrome c oxidase inhibitor KCN (4 mM) alone or together with the AOX inhibitor pGal (0.2 mM; $n = 4$; means $\pm$ SD). The statistical analysis (two-way ANOVA with post hoc Holm–Sidak comparisons for WT versus *grxs15* mutant) indicated a significant difference in the respiration of mito from WT and *GRXS15 K83A* line #3; ***$P \leq 0.001$. B, Respiratory complexes I, II, III, and V separated by Blue Native–PAGE and visualized with Coomassie staining in WT, *GRXS15 K83A* line #4, and *GRXS15*^{amiR}. Mito were purified from 4-week-old plants. C and D, O_2 consumption rates for purified mito from WT *and GRXS15 K83A* line #3 energized with succinate (left) or pyruvate/malate (right). O_2 consumption was measured before (blank) and after addition of mito. State II respiration was initiated by the addition of the respective substrate (State II; succinate (10 mM succinate, 0.25 mM ATP) or pyruvate/malate (10 mM pyruvate, 10 mM malate, 0.3 mM NAD, and 0.1 mM thiamine pyrophosphate). State III respiration was initiated by the addition of 50 μM ADP. State IV represents the respiration after ADP consumption and CCCP shows the respiration after addition of the protonophore carbonyl cyanide m-CCCP (10 μM), which uncouples electron transport from ATP synthesis. All results are based on three independent preparations of mito and are shown as means $\pm$ SEM.

malate dehydrogenase, NAD-malic enzyme, which also accepts $NADP^+$ as electron acceptor, and most prominently by NADP-isocitrate dehydrogenase (IDH; Møller and Rasmusson, 1998; Møller et al., 2020). In addition to oxidation by complex I, NADH is also oxidized by NDA-type alternative dehydrogenases (Elhafez et al., 2006). NADPH is oxidized by NDC-type alternative dehydrogenase, NADPH-dependent thioredoxin reductases A and B, and glutathione reductase 2 (Reichheld et al., 2005; Rasmusson et al., 2008; Marty et al., 2019). No differences in the respiration of isolated mitochondria were found with supply of succinate or pyruvate/malate (Figure 4, C and D), suggesting that the differences in respiration observed in whole roots cannot be accounted for by decreased capacities of the Fe–S cluster-containing complexes. In summary, similar total respiratory activities of WT and mutants further indicate that the in vivo difference in respiration rate is not due to a defect at the level of the mETC, but rather upstream or downstream.

The capacity for electron flow in isolated mitochondria does not allow conclusions about the actual mETC activity in planta. Hence, we tested whether the decreased respiration rate may result in a change of the ATP status of the cells. For analyses of the $MgATP^{2-}$ level WT plants as well as the *grxs15* mutants #3 and #4 were transformed with the $MgATP^{2-}$ biosensor ATeam1.03-nD/nA (De Col et al., 2017) targeted to the cytosol. As cytosolic ATP is predominantly provided by the mitochondria (Igamberdiev et al., 2001; Voon et al., 2018), any disturbance in the mitochondrial ATP synthesis will also affect the ATP level in the cytosol. Similar to the report by De Col et al. (2017) higher Venus/cyan fluorescent protein (CFP) fluorescence ratios indicating more efficient Förster resonance energy transfer between the sensor subunits and hence higher $MgATP^{2-}$ levels were found in cotyledons compared to roots (Supplemental Figure S3). However, no differences in the Venus/CFP emission ratio could be observed between WT and *GRXS15 K83A* mutants indicating similar cytosolic ATP levels (Supplemental Figure S3). It should be noted though that the energy charge of the adenylate pool cannot be deduced from these results as it would require also analysis of AMP and ADP.

Previously, we reported a 60% decrease in ACO activity in *GRXS15 K83A* mutants while the total amount of ACO protein remained unchanged (Moseler et al., 2015). A decrease in ACO activity could at last partially explain the decreased respiration rate, but a decrease in ACO activity was not seen by Ströher et al. (2016). To clarify the situation, we measured the activity of ACO, a [4Fe–4S] enzyme, in the *GRXS15 K83A* and $GRXS15^{amiR}$ mutants grown side by side under the same conditions. We found no significant difference as a result of depleted or mutated GRXS15 protein in total leaf extracts (Figure 5A). Additionally, the abundance of ACO protein was the same (Figure 5B).

Furthermore, the mitochondrial ACO activity in purified mitochondria was analyzed in both *grxs15* mutant lines. Here, we found a slight decrease in ACO activity (normalized for citrate synthase) and no obvious difference in protein abundance (Supplemental Figure S4, A and B). However, we discovered that ACO is prone to partial inhibition in leaf extracts of the *grxs15* mutants, which likely caused the initially reported decrease (Supplemental Figure S4, C and D). The mutant-specific inhibition is not seen in isolated mitochondria; therefore, we argue that the decreased activity is due to the accumulation of a metabolite in the tissue that is removed in the course of the mitochondrial isolation.

Diminished GRXS15 activity does not lead to any major signs of oxidative stress

Yeast Δ*grx5* mutant, as well as a Arabidopsis *grxs14* null mutant, are sensitive to oxidative stress and at least for the Δ*grx5*, it was shown that specific proteins are oxidized in this mutant (Rodríguez-Manzaneque et al., 1999; Cheng et al., 2006). Therefore, we analyzed the *GRXS15 K83A* mutant for any signs of oxidative stress that may result from iron-mediated reactive oxygen species (ROS) formation as a possible consequence of an improper Fe–S cluster transfer by the GRXS15 K83A protein variant. However, staining of leaves with 3, 3-diaminobenzidine (DAB) for H_2O_2 and nitro blue tetrazolium (NBT) for superoxide revealed no differences between WT and *grxs15* mutants (Supplemental Figure S5). Since histological stains only provide a crude indication of major changes in ROS dynamics, but are not sufficiently sensitive to resolve localized intracellular changes in oxidant load, we next analyzed mitochondria-specific changes in H_2O_2 concentration or the glutathione redox potential (E_{GSH}). The genetically encoded sensors roGFP2-Orp1 (Nietzel et al., 2019) and roGFP2-hGrx1 (Albrecht et al., 2014) were expressed in the mitochondrial matrix of both WT and mutant plants. Both sensors were highly reduced under control conditions and neither roGFP2-Orp1 nor roGFP2-hGrx1 revealed any significant differences between WT and *GRXS15 K83A* mutants in mitochondria of cotyledons and root tips (Supplemental Figure S5, B and C). Both roGFP2-sensor variants remained highly reduced in all lines as indicated by similar fluorescence ratios that resembled those after incubation with dithiothreitol (DTT) for full sensor reduction. This indicates no major oxidative challenge in the mitochondrial matrix. Both sensors were responsive to oxidative challenge as indicated by a pronounced ratio change upon H_2O_2 addition.

Diminished GRXS15 activity leads to accumulation of TCA cycle intermediates

To investigate any other metabolic defects in the *GRXS15 K83A* mutant, we measured the concentrations of several organic acids in the *GRXS15 K83A* mutants. We found most of the analyzed organic acids in the complemented *grxs15* mutants #3 and #4 to be increased. Pyruvate showed the most pronounced change, increasing by more than four-fold from 31.5 ± 2.4 pmol $(mg\ FW)^{-1}$ in the WT to 131.76 ± 3.8 and 153.97 ± 16.5 pmol $(mg\ FW)^{-1}$ in lines #3 and #4 (Figure 6). The accumulation of citrate and isocitrate was

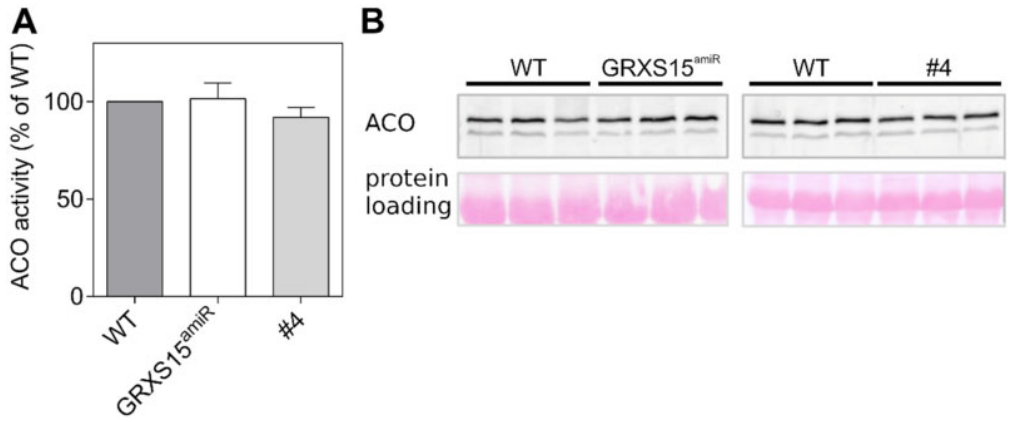

Figure 5 ACO activities in leaf extracts of *grxs15* mutants. A, ACO activity of *GRXS15*^{amiR} and *GRXS15 K83A* line #4 compared to the respective WTs in leaf extracts from 3-week-old seedlings, measured by spectrophotometry in a coupled assay. $n = 3$; means ± SD. WT ACO activity was 35.3 ± 2.2 mU/mg protein for *GRXS15*^{amiR} and 50.6 ± 5.1 mU/mg for the parental line of *GRXS15 K83A* lines, while the activity for the mutants was 35 ± 2.4 and 46.6 ± 2.1 mU/mg, respectively. B, Protein blot analysis of ACO in total leaf extracts from individual plants under denaturing conditions (all three ACO isozymes have the same electrophoretic mobility). Twenty micrograms of total protein extract was loaded. Total protein staining on the membrane after transfer with Ponceau S served as a loading control.

significant in line #4, but not in line #3. 2-OG and malate showed minor increases in line #3 and pronounced increases in line #4. This trend did not reach statistical significance, however. A similarly concerted accumulation of TCA cycle intermediates was previously observed in antisense lines of the mitochondrial manganese superoxide dismutase 1 (MSD1; Morgan et al., 2008). Those lines showed impaired mitochondrial ACO activity to <50%, suggesting that the compromised ACO activity is sufficient as an explanation for the rearrangements in the pools of TCA cycle intermediates. However, pyruvate content was not determined in the *MSD1* antisense lines and the increased pyruvate content found in *GRXS15 K83A* lines cannot be straightforwardly linked to ACO activity.

Alterations in pyruvate and glycine metabolism are associated with impairment of LC-dependent enzymes under diminished GRXS15 activity

The pronounced pyruvate accumulation may be caused by a backlog of metabolites due to a lower TCA flux or by a diminished activity of PDC, which catalyzes the decarboxylation of pyruvate to acetyl-CoA (Yu et al., 2012). The E2 subunit of this multi-enzyme complex uses an LC, the synthesis of which was shown to be compromised in *GRXS15*^{amiR} mutants (Ströher et al., 2016). In plant mitochondria, the lipoyl moiety is an essential cofactor of four protein complexes: PDC, OGDC, BCKDC, and GDC (Taylor et al., 2004). Ströher et al. (2016) showed decreased lipoylation of PDC E2-2 and E2-3 but no effects on E2-1. On the other hand, a pronounced decrease was observed in all GDC H protein isoforms, and differences in the degree of lipoylation were explained by different modes of lipoylation. To get insight into the metabolic effects of diminished GRXS15 activity, we tested for protein lipoylation in the weakest complementation line #4 and directly compared the results to lipoylation in *GRXS15*^{amiR} and WT. GRXS15 was barely detectable in *GRXS15*^{amiR} while in line #4 the mutated GRXS15 K83A had been shown earlier to be present at even higher amounts than the endogenous protein in WT plants (Moseler et al., 2015; Ströher et al., 2016). Immunodetection of the lipoyl group with specific antibodies to the cofactor indicated that the amount of lipoate bound to the H subunit isoforms of GDC was decreased in the *GRXS15 K83A* mutant to a similar extent as in *GRXS15*^{amiR} (Figure 7A). In contrast, the H protein levels were largely unchanged in all tested lines. Effective lipoylation could be restricted by the activity or the abundance of mLIP1. An activity assay for mLIP1 in plant extracts has not been developed. Using antibodies raised against recombinant mLIP1, there was no difference in the protein levels between line #4, *GRXS15*^{amiR}, and WT controls (Figure 7A). However, this does not exclude an enzymatic defect in mLIP1.

To further test whether the accumulation of pyruvate was due to a less active PDC, we measured the activity of the PDC in isolated mitochondria. Interestingly, there was a 22% reduction in PDC activity for the *GRXS15 K83A* mutant. While the WT had a PDC activity of 92.7 ± 6.5 nmol NADH mg^{-1} min^{-1} the *GRXS15 K83A* line #3 had significantly lower activity of only 72.40 ± 6.2 nmol NADH mg^{-1} min^{-1} (Figure 7B).

The pronounced increase of pyruvate and several TCA intermediates (Figure 6) may have further effects on downstream metabolites. Given that intermediates of glycolysis and the TCA cycle are hubs for synthesis of amino acids and because mutants defective in PDC subunit E2 show an increase in the pools of nearly all amino acids (Yu et al., 2012), we profiled the abundance of amino acids. Most amino acids were increased in the mutants compared to WT seedlings, with more pronounced increases in line #4 compared to line #3 (Figure 7C; Supplemental Table S1). Particularly, high increases in amino acid abundance of > 200% were observed for glycine and serine derived from 3-

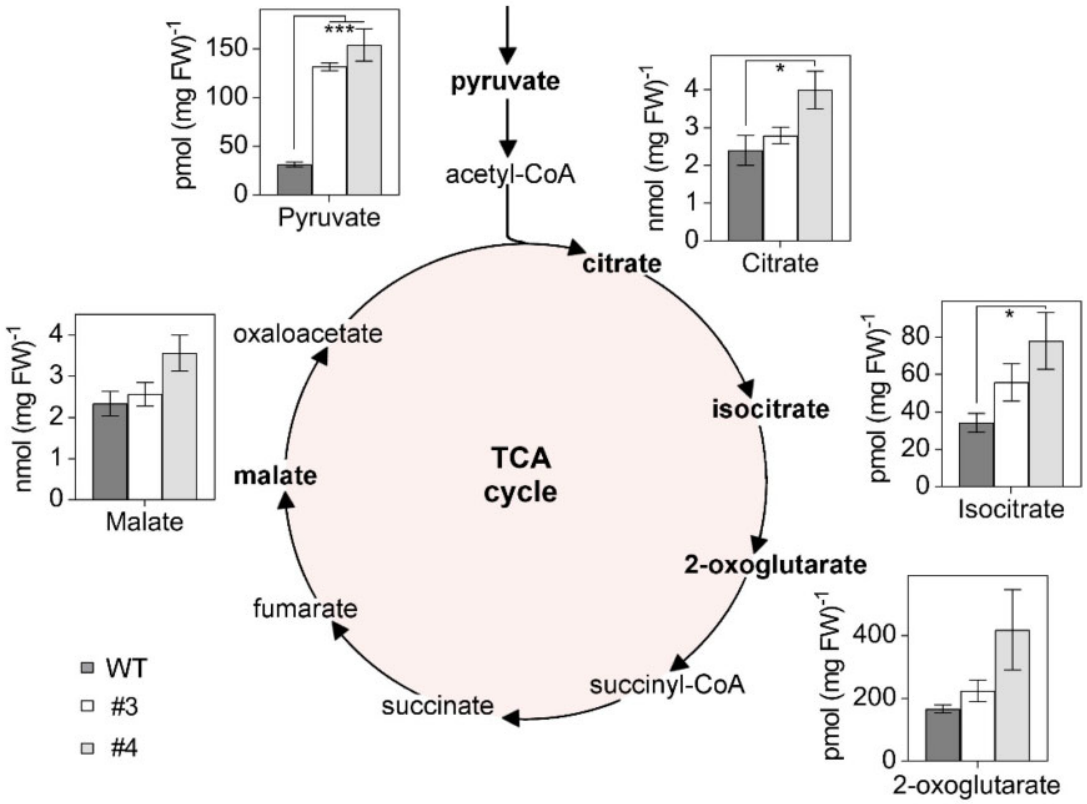

Figure 6 Organic acids of the TCA cycle accumulate in Arabidopsis *GRXS15 K83A* mutants. Organic acids were analyzed in 8-d-old seedlings of WT compared to *GRXS15 K83A* lines #3 and #4 ($n = 4–5$; means ± SEM). The statistical analysis (one-way ANOVA with post hoc Holm–Sidak comparisons for WT vs. mutant lines) indicated significant changes; *$P \leq 0.05$; ***$P \leq 0.001$.

phosphoglycerate (3PG), for alanine, Leu, and Val all derived from pyruvate, and for Ile (Figure 7C; Supplemental Table S1). The Gly/Ser ratio, indicative of photorespiratory effects, did not show any pronounced change and varied only between 0.33 ± 0.04 for the WT, 0.4 ± 0.1 for line #3, and 0.37 ± 0.12 for line #4.

BCAA metabolism is strongly impaired in response to diminished GRXS15 activity and LC availability

Leu, Val, and Ile are classified as BCAAs, which share a common degradation pathway that is localized in the mitochondrion. Because the BCAA catabolism pathway involves LC-dependent BCKDC, the increase in the pools of all three BCAAs may not exclusively result from increased availability of their parent compounds, but also from restricted BCAA degradation capacity. To test this hypothesis, we measured the content of the respective keto acids resulting from deamination of the BCAAs by BCAA transaminase (BCAT; Supplemental Figure S6A). The keto acids α-ketoisocaproic acid (KIC), α-keto-β-methylvaleric acid (KMV), and α-ketoisovaleric acid (KIV) derived from the BCAAs accumulated massively in both *GRXS15 K83A* mutants (Figure 7D). Here, KIC accumulated in the *GRXS15 K83A* mutants up to 15-fold, resulting in values of 3.5 ± 0.11 pmol (mg FW)$^{-1}$ in line #3 and 3.8 ± 0.6 pmol (mg FW)$^{-1}$ in line #4 compared to 0.25 ± 0.032 pmol (mg FW)$^{-1}$ in the WT. KIV and KMV increased six- to sevenfold in the *GRXS15 K83A* mutants. These pronounced changes support the hypothesis of decreased BCKDC activity creating a bottleneck in keto acid catabolism (Supplemental Figure S6A). The higher accumulation of KIC can be accounted for by the preference of BCKDC for the Val derivative (Taylor et al., 2004) resulting in KIV to be metabolized faster and to accumulate less strongly. Despite the presumed bottleneck in catabolism of BCAAs, the *grxs15* mutants did not show enhanced Leu sensitivity (Supplemental Figure S6B). Similarly, *ivdh* mutants deficient in isovaleryl-CoA dehydrogenase did not display an increased sensitivity to external supply of Leu compared to WT. To exclude that the accumulation of keto acids is just due to an increased abundance of the respective BCAAs, we measured the BCAAs and their deaminated keto acids in the mutant *root meristemless1* (*rml1*; Cheng et al., 1995; Vernoux et al., 2000). *rml1* is severely compromised in glutathione biosynthesis, and is characterized by only residual amounts of glutathione, accumulation of cysteine, and largely inhibited growth (Vernoux et al., 2000). We found a significant increase in all three BCAAs in *rml1* compared to the WT but no accumulation of the respective keto acids (Supplemental Figure S7). Hence, the accumulation of BCAAs alone cannot account for an increase of KIV, KIV, and KMV.

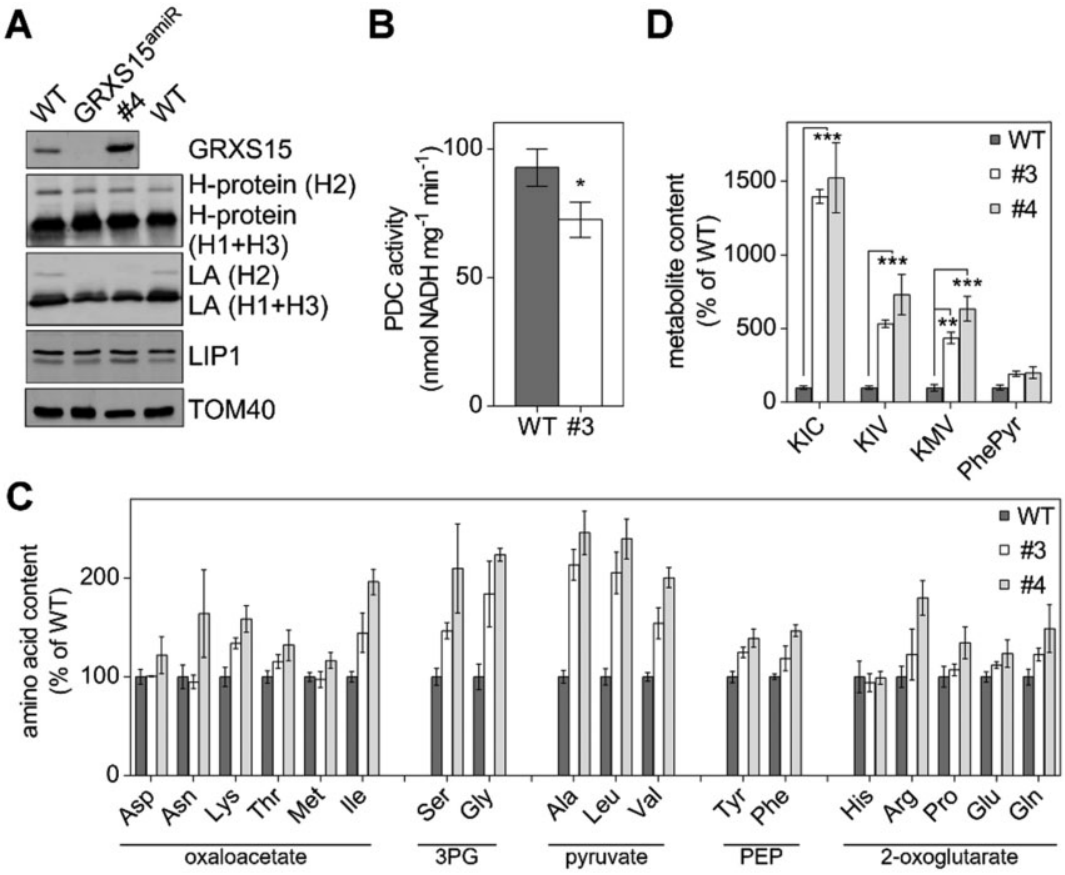

Figure 7 LC-dependent enzymes are affected in Arabidopsis *GRXS15 K83A* mutants. A, Immunoblot analysis using antibodies against GRXS15, glycine dehydrogenase H-protein (H1-3), LC (LA), mLIP1 as well as TOM40 for a loading control. Fifteen micrograms of isolated mitochondrial protein were loaded per lane. B, PDC activity in isolated mito. Reduction of NAD^+ was measured in extracts of mito isolated from 14-d-old WT seedlings and the *GRXS15 K83A* line #3 ($n = 5$; means ± SEM). The statistical analysis (one-way ANOVA with post hoc Holm–Sidak comparisons for WT versus *grxs15* mutant) indicated a significant change; *$P = 0.025$). C, Relative abundance of amino acids in 8-d-old seedlings of WT compared to *GRXS15 K83A* lines #3 and #4. WT was set to 100% ($n = 4–5$, means ± SEM). Absolute values and statistical analysis are provided in Supplemental Table S1. Amino acids were categorized after their respective common precursor. PEP: phosphoenolpyruvate. D, Analysis of the breakdown products of Leu, Ile, and Val—KIC, KIV, and KMV—and phenylpyruvate (PhePyr) in seedlings of WT compared to *GRXS15 K83A* lines #3 and #4. WT was set to 100% ($n = 4–5$; means ± SEM). Absolute values are provided in Supplemental Table S1. The statistical analysis (two-way ANOVA with post hoc Holm–Sidak comparisons for WT versus *grxs15* mutant) indicated significant changes; **$P \leq 0.01$; ***$P \leq 0.001$.

Discussion

GRXS15 function limits growth

Null mutants of mitochondrial GRXS15 are embryo-defective but can be partially complemented with a mutated GRXS15 protein compromised in its ability to coordinate a [2Fe–2S] cluster (Moseler et al., 2015). The bottleneck in Fe–S coordination results in a dwarf phenotype similar to the phenotype of severe knockdown mutants generated through expression of artificial microRNAs (Supplemental Figure S1; Ströher et al., 2016) but how exactly the modification of either activity or abundance of GRXS15 impacts on plant growth and development remained unclear. Less severe knockdown mutants resulting from a T-DNA insertion in the 5′-UTR of *GRXS15* limited the abundance of GRXS15 to ~20% of WT levels, but did not show a macroscopic phenotype beyond early seedling stage under nonstress conditions (Ströher et al., 2016). The growth phenotype of more severe *grxs15* mutants is most apparent in very short roots, which may be linked to the fact that *GRXS15* is strongly expressed in roots, particularly in the maturation and meristematic zone (Belin et al., 2015). The primary function of GRXS15 is assumed to be a role in mitochondrial Fe–S cluster transfer (Moseler et al., 2015; Ströher et al., 2016). Recently, an interaction of GRXS15 with ISCA scaffold proteins and a transfer of a [2Fe–2S] cluster from GRXS15 to the ISCA complex was shown in vitro (Azam et al., 2020). This implies that a compromised GRXS15 function potentially may have implications for Fe–S-dependent pathways, including biosynthesis of biotin and Moco, the mETC, and the TCA cycle. While biotin feeding experiments clearly excluded biotin biosynthesis as the limiting factor, the picture was less clear for Moco, which is an essential cofactor for several cytosolic enzymes (Schwarz and Mendel, 2006). Nitrate assimilation, which is dependent on Moco-containing NR, initially showed the

expected nitrate sensitivity. Measurements of extractable NR activity, however, showed no defects. Because, similarly XDH and AOs did not show changes in their activities between mutants and the WT, deficiencies in Moco supply can be excluded as a putative metabolic bottleneck in *GRXS15 K83A* mutants. Nitrate sensitivity in *grxs15* mutants leaves us with the conundrum of a different link between mitochondrial functions of GRXS15 and nutrient assimilation, which deserves further investigation in the future.

GRXS15 does not affect energy balance and ROS levels

Diminished growth coincides with decreased root respiration rates in both, severe *GRXS15*^{amiR} knockdown mutants (Ströher et al., 2016) and the weak complementation line #3 investigated in this work (Figure 4A). Because the mETC contains 12 Fe–S proteins involved in electron transport (Couturier et al., 2015; Meyer et al., 2019), restricted supply of Fe–S clusters would be expected to affect electron flow along the mETC. In humans (*Homo sapiens*), it was observed that a patient deficient in mitochondrial GLRX5 suffers from decreased abundance and hence activity of complex I (Ye et al., 2010). In yeast, Δ*grx5* mutants displayed a decreased complex II activity, albeit an unaffected protein abundance in this complex (Rodríguez-Manzaneque et al., 2002). In contrast, we found no changes in abundance of any mETC complexes in severe *grxs15* mutants of Arabidopsis (Figure 4B). Consistently, feeding of mitochondria isolated from *GRXS15 K83A* mutants with succinate revealed that SDH, which contains three different Fe–S clusters (Figueroa et al., 2001), does not constitute a bottleneck in mitochondrial metabolism of *grxs15* mutants. Generally, the respiratory capacity is not affected in the mutants compared to WT, which indicates that supply of Fe–S clusters to components of the mETC is not compromised in *grxs15* mutants. The lower respiratory rate in *GRXS15 K83A* mutants also does not lead to changes in ATP levels. This, however, may also partially be due to decreased consumption of ATP with restricted growth and also the activity of adenylate kinase that contributes to formation of ATP (and AMP) from ADP to buffer the ATP level (De Col et al., 2017). Our overall conclusion to this point is that reduced respiration is likely due to restricted substrate supply rather than assembly of complexes in the mETC and their supply with Fe–S clusters. Restricted supply of reducing equivalents may result from a slowdown of the TCA cycle and also from severely compromised contributions of the electron-transfer flavoprotein (ETF)/ETF:ubiquinone oxidoreductase (ETF/ETFQO) to ubiquinone reduction (Supplemental Figure S6). Electrons that enter the mETC via ETF/ETFQO originate from IVDH-mediated oxidation of acyl-CoAs as products of BCKDC. The ETF/ETFQO pathway has been shown to contribute significant amounts of electrons in stress situations (Ishizaki et al., 2005; Pires et al., 2016). The concomitant increase in BCKAs and particularly BCAAs may contribute to the dwarf phenotype as disruption in BCAA homeostasis has been shown to lead to pleiotropic effects including growth retardation (Cao et al., 2019).

GRXS15 affects enzymes and metabolites in the TCA cycle

GRXS15 was detected as part of higher-order protein assemblies in a mitochondrial complexome analysis (Senkler et al., 2017). A particularly strong interaction between GRXS15 and mitochondrial IDH1 was observed in yeast two-hybrid screens with IDH1 as bait and this interaction was subsequently confirmed by bimolecular fluorescence assays (Zhang et al., 2018). Consistent with a suspected role of GRXS15 in IDH1 function, the isocitrate content was decreased significantly in a *grxs15* knockdown mutant, while the relative flux through the TCA cycle increased (Zhang et al., 2018). IDH1 has recently been reported to contain several redox-active thiols that can change their redox state depending on substrate availability for the TCA (Nietzel et al., 2020). The IDH1–GRXS15 interaction thus could point at a possible function of GRXS15 as a thiol-switch operator for regulatory thiols. This is unlikely though, because GRXS15 does not show any reductive activity and only weak oxidative activity (Moseler et al., 2015; Begas et al., 2017). The increase in all analyzed metabolites of the TCA cycle is rather consistent with metabolite patterns found in knockdown mutants of mitochondrial MnSOD, in which increased levels of organic acids correlated with a decrease in ACO activity (Morgan et al., 2008). ACO contains a [4Fe–4S] cluster and has frequently been used as an enzymatic marker for defects in Fe–S cluster assembly and transfer in yeast and human cells (Rodríguez-Manzaneque et al., 2002; Bandyopadhyay et al., 2008; Liu et al., 2016). It came as a surprise that ACO was reported to be unaffected in mitochondria of Arabidopsis *grxs15* mutants, both in abundance and activity (Ströher et al., 2016). Consistent with this report, we also found no change in abundance or activity of total ACOs and only a minor change in mitochondrial ACO activity (Figure 5). Thus, the unchanged ACO activity in *GRXS15 K83A* mutants does not explain the most pronounced increase in pyruvate, which accumulates up to five-fold and thus supersedes the accumulation of all other TCA cycle intermediates at least by a factor of two. A knockdown of mitochondrial and cytosolic ACO activities in wild tomato led to a reduction in 2-OG levels but an increase in citrate and isocitrate by 40%–50%. A similar change in these organic acids of the TCA cycle was found in an SDH mutant (Carrari et al., 2003; Huang et al., 2013). The pattern of organic acids in *GRXS15 K83A* mutants is thus clearly different from other TCA cycle mutants.

GRXS15 has a function in protein lipoylation

PDC and OGDC do not contain an Fe–S cluster but rather belong to a class of four dehydrogenase complexes that all involve lipoylated subunits. Decreased lipoylation of GDC-H proteins and reduced PDC activity is fully consistent with previous observations on *GRXS15*^{amiR} mutants by Ströher et al. (2016). Additionally, the lack of changes in abundance

of 2-OG found for *GRXS15 K83A* mutants in this work is consistent with the absence of detectable changes in lipoylation of OGDC-E2 reported by Ströher et al. Similar to the Arabidopsis mutants, humans carrying mutations in mitochondrial GLRX5 are also deficient in lipoylation of mitochondrial proteins (Baker et al., 2014). A deficiency in lipoylation in Arabidopsis *grxs15* mutants is further supported by increased amounts of pyruvate as well as several other organic acids and amino acids derived from pyruvate and 2-OG (Figures 6 and 7C). Similar increases in pyruvate, as well as the accumulation of most amino acids, were also shown for Arabidopsis plants with a mutated PDC-E2 subunit resulting in 30% PDC activity (Yu et al., 2012). A much more pronounced increase of alanine in *PDC-E2* mutants than in *GRXS15 K83A* mutants may be attributed to a higher severity of the metabolic bottleneck if PDC activity is down to 30%. Of all metabolites analyzed in this study, the 4- to 15-fold increases of BCKAs in *GRXS15 K83A* mutants were the most pronounced relative changes compared to the WT. The findings that these increases were stronger in more severe mutants, point at BCKDC as a critical bottleneck. The keto acids, KIC, KIV, and KMV are products of transamination of the BCAAs Leu, Ile, and Val (Hildebrandt et al., 2015). Further degradation of the keto acids in *GRXS15 K83A* mutants is limited because BCKDC relies on efficient lipoylation of the E2 subunit. Indeed, selective accumulation of BCAAs, but not of the respective keto acids, in the *rml1* mutant supports the notion that the increase in BCKAs in GRXS15 K83A is likely due to metabolic restriction in further degradation of the keto acids.

In summary, decreased activity of the mitochondrial GRXS15 appears to selectively restrict protein lipoylation. Lipoylation of mitochondrial proteins is mediated through coordinated action of lipoate-protein ligase, octanoyltransferase, and mLIP1 (Ewald et al., 2014). mLIP1 contains two [4Fe–4S] clusters, which link the function of this enzyme to the Fe–S cluster transfer machinery (Balk and Schaedler, 2014). At a first glance, a selective defect in only one out of about 26 mitochondrial [4Fe–4S] proteins (Przybyla-Toscano et al., 2021) may seem surprising and poses the question for an explanation. Either mLIP1 has a specific requirement for GRXS15 in the assembly of its Fe–S cofactors, or mLIP1 is more sensitive than other Fe–S enzymes to restricted Fe–S cluster supply. However, none of these hypotheses are as yet supported by available experimental data. A third possible explanation is based on established protein abundance. Recently, Fuchs et al. (2020) reported quantitative data for the abundance of proteins in single mitochondria (Figure 8). mLIP1 was estimated to be present with only 85 copies in a single mitochondrion compared to 4,200 copies of ACO2 and 9,900 copies of ACO3 (Figure 8; Fuchs et al., 2020). In the absence of any other evidence, we have to assume that all apoproteins have a similar likelihood of receiving a [4Fe–4S] cluster based on random interactions of transfer proteins with apoproteins. In case of a compromised Fe–S supply, there will be an equal decrease of supply to all recipients but, in relative terms, mLIP1 with 85 copies might be stronger compromised than other recipients with higher copy numbers. This hypothesis needs to be tested in future work.

At this point an alternative mechanistic explanation for the selective effect of GRXS15 deficiency on protein lipoylation appears most plausible. The radical *S*-adenosylmethionine enzyme mLIP1 contains two [4Fe–4S] clusters one of which is required as a substrate, that is, as sulfur donor to octanoyl-residues (Figure 8; McCarthy and Booker, 2017). Continuous destruction of Fe–S clusters during lipoylation may thus render LC-dependent enzymes indirectly sensitive to defects in Fe–S supply. With the need for one [4Fe–4S] cluster to be replaced after each catalytic cycle and thus, having a higher turnover rate, the bottleneck is bound to become even more severe than in enzymes that use their Fe–S clusters only for electron transfer reactions. The notion that supply of LC is close to demand, has been observed in a study overexpressing H-protein, which negatively affected lipoate supply to E2 subunits of PDC and OGDC in the roots (López-Calcagno et al., 2019).

Conclusion

We show that compromising the ability of GRXS15 to coordinate [2Fe–2S] clusters results in severe defects only in enzymes relying on LC. These results are in agreement with findings by Ströher et al. (2016) who reported diminished lipoylation of proteins in $GRXS15^{amiR}$ lines and hypothesized that diminished respiration and the short root mutant phenotype could be a consequence of the incomplete LC loading of important TCA cycle enzymes. Here we expand and specify the picture, by systematically probing for metabolic bottlenecks in mitochondrial pathways that rely on supply with Fe–S clusters. While changes in several metabolites were found, the primary defects can be assigned to the mitochondrial dehydrogenase complexes, all of which contain a lipoylated subunit. Those results emphasize the importance of mLIP1 as an important sink for Fe–S clusters, which becomes manifest if GRXS15-mediated Fe–S cluster transfer is restricted. The fact that most other Fe–S-dependent pathways are not seriously affected by deficiencies in *GRXS15 K83A* complementation lines may be explained by the effective relative abundance of different proteins in mitochondria. We propose that an increased demand for Fe–S as sulfur donor combined with the very low abundance of mLIP1 leads to the manifestation of a potentially lethal bottleneck.

Material and methods

Plant material and methods

Previously described Arabidopsis (*A. thaliana*) complementation lines *grxs15-3* $UBQ10_{pro}$*:GRXS15 K83A* (Moseler et al., 2015) and the knockdown line $GRXS15^{amiR}$ (Ströher et al., 2016), as well as *atm3-1* and *atm3-4* (Teschner et al., 2010) were used in this study. Arabidopsis ecotype Col-0 ([L.] Heyn.) segregated from the T-DNA line *grxs15-3*) was used as WT. Unless stated differently, surface-sterilized seeds were

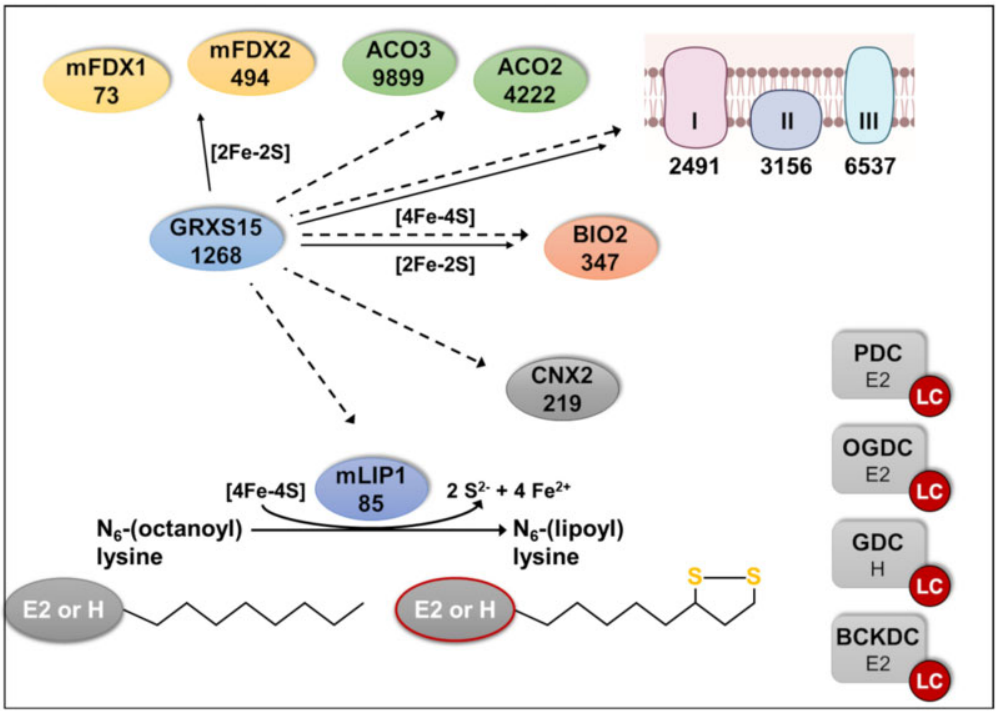

Figure 8 Lipoylation of mitochondrial proteins depends on GRXS15. Distribution of Fe–S clusters in Arabidopsis mitochondria to Fe–S proteins and lipoylation of proteins via mLIP1. Putative transfer of Fe–S clusters is indicated by solid arrows for [2Fe–2S] and dashed arrows for [4Fe–4S]. Intermediate complexes of Fe–S transfer and assembly of [4Fe–4S] clusters are not shown. mFDX1/2: mitochondrial ferredoxin 1/2; ACO2/3: aconitase 2/3; BIO2: biotin synthase 2; I, II, and III represent complexes I (2 [2Fe–2S], 6 [4Fe–4S]), II (1 [2Fe–2S], 1 [3Fe–4S], 1 [4Fe–4S]), and III (1 [2Fe–2S]) of the mETC; E2 and H are the lipoylated subunits of the four dehydrogenase complexes PDC, GDC, OGDC, and BCKDC. Numbers indicate the estimated copy number of the respective proteins or protein complexes (copy number of Fe–S coordinating subunits in the mETC are listed in Supplemental Table S2) according to Fuchs et al. (2020) which is based on mito from a heterotrophic Arabidopsis cell culture.

grown on vertical plates containing nutrient medium (Meyer and Fricker, 2000) with 0.1% (w/v) sucrose solidified with 0.8% (w/v) agar under long-day conditions with a diurnal cycle of 16-h light at 22°C and 8-h dark at 18°C. The light intensity was 75 µE m^{-2} s^{-1} and 50% air humidity.

Germination rate was scored by observing radical emergence in seeds plated on vertical culture plates using a stereomicroscope (M165 FC; Leica, Wetzlar, Germany). Root growth was documented photographically on vertical culture plates containing 0.8% (w/v) phytagel and 0.1% (w/v) sucrose. Five and 8 d after stratification, root length was documented and measured using Adobe Illustrator CS5.1.

Influence of the nitrogen source on root length was analyzed on plates containing 5 mM KNO_3 or 2.5 mM $(NH_4)_2SO_4$, 2.5 mM KH_2PO_4, 2 mM $MgSO_4$, 2 mM $CaCl_2$, 50 µM Fe-EDTA, 70 µM H_3BO_4, 14 µM $MnCl_2$, 0.5 µM $CuSO_4$, 1 µM $ZnSO_4$, 0.2 µM $NaMoO_4$, 10 µM NaCl, 0.01 µM $CoCl_2$, 0.8% (w/v) phytagel, and 0.1% (w/v) sucrose, pH 5.8. To check for possible effects of counter anions, $(NH_4)_2SO_4$ was replaced by NH_4Cl and grown otherwise exactly under the same conditions.

Blue Native–PAGE

Mitochondrial samples were solubilized in 1% (w/v) *n*-dodecyl β-D-maltoside and subjected to Blue Native–PAGE as described previously (Meyer et al., 2011; Kühn et al., 2015).

Isolation of mitochondria

Arabidopsis mitochondria were purified from 2- or 4-week-old seedlings as described before (Sweetlove et al., 2007) with slight modifications. All steps were performed on ice or at 4°C. Seedlings were homogenized using mortar and pestle and the homogenate was filtered (Miracloth; Merck Millipore, Burlington, MA, USA) before cellular debris was pelleted by centrifugation for 5 min at 1,200 *g*. The supernatant was centrifuged for 20 min at 18,000 *g*, and the pellet of crude mitochondria was gently resuspended in wash buffer (0.3 M sucrose, 0.1% (w/v) BSA and 10 mM TES, pH 7.5) and centrifuged for 5 min at 1,200 *g*. The supernatant was transferred into a new tube and centrifuged for 20 min at 18,000 *g*. The pellet was gently resuspended in final wash buffer (0.3 M sucrose, 10 mM TES, pH 7.5), loaded directly on a 0–6% (v/v) Percoll gradient and centrifuged for 40 min at 40,000 *g*. Mitochondria were transferred into a new tube and washed 3 times with final wash buffer (0.3 M sucrose, 10 mM TES pH 7.5).

Respiration assays

O_2 consumption of intact Arabidopsis roots and isolated mitochondria was measured in Oxytherm Clark-type electrodes (Hansatech, Norfolk, UK; www.hansatech-instruments.com) as described before (Wagner et al., 2015). Whole roots from seedlings vertically grown on agar plates were cut below the hypocotyl-root junction and assayed in a volume of 1.2 mL

containing 5 mM KCl, 10 mM MES, and 10 mM $CaCl_2$, pH 5.8, and after addition of 4 mM KCN and 0.2 mM pGal.

O_2 consumption of isolated mitochondria was measured in a volume of 1 mL containing 0.3 M mannitol, 10 mM TES-KOH pH 7.5, 5 mM KH_2PO_4, 10 mM NaCl, 2 mM $MgSO_4$, and 0.1% (w/v) bovine serum albumin. O_2 consumption rate was measured before (blank) addition of mitochondria and after addition of mitochondria or respective substrate; State II; succinate (10 mM succinate, 0.25 mM ATP) or pyruvate/malate (10 mM pyruvate, 10 mM malate, 0.3 mM NAD and 0.1 mM thiamine pyrophosphate), State III; ADP (50 μM ADP). Additionally, O_2 consumption rate was analyzed after ADP consumption (State IV) and after addition of 10 μM carbonyl cyanide m-chlorophenylhydrazone (CCCP).

Histological detection of ROS

For detection of increased H_2O_2 production, leaves were stained with DAB (Thordal-Christensen et al., 1997). Leaves were vacuum-infiltrated in a solution containing 0.1 mg mL^{-1} DAB, 50 mM potassium phosphate buffer pH 7.6 and 0.1% (v/v) Silwet L-77. After infiltration, the leaves were incubated for 20–24 h in the dark and destained by lactic acid:glycerol:EtOH (1:1:3) for 30 min at 70°C.

For histochemical staining of superoxide, NBT was used (Hoffmann et al., 2013). Leaves were vacuum-infiltrated in a solution containing 0.1 mg mL^{-1} NBT, 50 mM potassium phosphate buffer pH 7.6 and 0.1% (v/v) Silwet L-77. After infiltration, the leaves were incubated for 30 min in the dark and destained by lactic acid:glycerol:EtOH (1:1:3) for 30 min at 70°C.

Determination of metabolite levels via HPLC

Aliquots (45–55 mg) of freshly ground plant tissue were used for absolute quantification of amino acid, α-keto acid, and organic acid content each.

Free amino acids and α-keto acids were extracted with 0.5 mL ice-cold 0.1 M HCl in an ultrasonic ice bath for 10 min. Cell debris and insoluble material were removed by centrifugation for 10 min at 25,000 *g*. For the determination of α-keto acids, 150 μL of the resulting supernatant were mixed with an equal volume of 25 mM o-phenylendiamine solution and derivatized by incubation at 50°C for 30 min. After centrifugation for 10 min, the derivatized keto acids were separated by reversed phase chromatography on an Acquity HSS T3 column (100 mm × 2.1 mm, 1.7 μm; Waters, Milford, USA) connected to an Acquity H-class UPLC system. Prior separation, the column was heated to 40°C and equilibrated with five column volumes of solvent A (0.1% [v/v] formic acid in 10% [v/v] acetonitrile) at a flow rate of 0.55 mL min^{-1}. Separation of keto acid derivatives was achieved by increasing the concentration of solvent B (acetonitrile) in solvent A (2 min 2% (v/v) B, 5 min 18% (v/v) B, 5.2 min 22% (v/v) B, 9 min 40% (v/v) B, 9.1 min 80% (v/v) B and hold for 2 min, and return to 2% (v/v) B in 2 min). The separated derivatives were detected by fluorescence (Acquity FLR detector, Waters, excitation: 350 nm, emission: 410 nm) and quantified using ultrapure standards (Sigma, St Louis MO, USA). Data acquisition and processing were performed with the Empower3 software suite (Waters). Derivatization and separation of amino acids were performed as described by Yang et al. (2015).

Total organic acids were extracted with 0.5 mL ultra-pure water for 20 min at 95°C. Organic acids were separated using an IonPac AS11-HC (2 mm; Thermo Scientific, Waltham, MA, USA) column connected to an ICS-5000 system (Thermo Scientific) and quantified by conductivity detection after cation suppression (ASRS-300 2 mm, suppressor current 95–120 mA). Prior separation, the column was heated to 30°C and equilibrated with five column volumes of solvent A (ultra-pure water) at a flow rate of 0.38 mL min^{-1}. Separation of anions and organic acids was achieved by increasing the concentration of solvent B (100 mM NaOH) in buffer A (8 min 4% (v/v) B, 18 min 18% (v/v) B, 25 min 19% (v/v) B, 43 min 30% (v/v) B, 53 min 62% (v/v) B, 53.1 min 80% (v/v) B for 6 min, and return to 4% (v/v) B in 11 min). Soluble sugars were separated on a CarboPac PA1 column (Thermo Scientific) connected to the ICS-5000 system and quantified by pulsed amperometric detection . Column temperature was kept constant at 25°C and equilibrated with five column volumes of solvent A (ultra-pure water) at a flow rate of 1 mL min^{-1}. Baseline separation of carbohydrates was achieved by increasing the concentration of solvent B (300 mM NaOH) in solvent A (from 0 to 25 min 7.4% (v/v) B, followed by a gradient to 100% (v/v) B within 12 min, hold for 8 min at 100% (v/v) B, return to 7.4% (v/v) B and equilibration of the column for 12 min). Data acquisition and quantification were performed with Chromeleon 7 (Thermo Scientific).

AO and XDH assay

AO and XDH assays were performed similar as described previously by Koshiba et al. (1996) and Hesberg et al. (2004). For determination of AO and XDH activities, Arabidopsis seedlings were homogenized in extraction buffer (0.1 M potassium phosphate buffer pH 7.5, 2.5 mM EDTA and 5 mM DTT) and centrifuged for 10 min at 16,000 *g* and 4°C. Enzyme activities of AO and XDH in the resulting supernatant were detected after native PAGE by activity staining. Activity of AO was developed in a reaction mixture containing 0.1 M potassium phosphate buffer pH 7.5, 1 mM 1-naphthaldehyde, 1 mM indole-3-carboxaldehyde, 0.1 mM phenazine methosulfate (PMS), and 0.4 mM 3-(4,5-dimethylthiazol-2-yl)-2,5-diphenyltetrazolium bromide (MTT). Activity of XDH was analyzed with a staining solution of 1 mM hypoxanthine, 1 mM MTT, and 0.1 mM PMS in 250 mM Tris–HCl, pH 8.5.

NR assay

NR assay was performed as described previously (Scheible et al., 1997) with slight modifications. Leaves were homogenized in extraction buffer (50 mM 3-(N-morpholino)propanesulfonic acid (MOPS), pH 7.0, 50 mM KCl, 5 mM Mg acetate, 1 mM $CaCl_2$, 2 mM Na-citrate, and 1 mM DTT) and centrifuged for 10 min at 20,000 *g* and 4°C. NR activity was

measured in a reaction mixture containing 50 mM MOPS, pH 7.0, 50 mM KCl, 5 mM Mg acetate, 1 mM $CaCl_2$, 10 mM KNO_3, and 0.4 mM NADH. At consecutive time points, 150 µL aliquots were removed from the mixture and the reaction was stopped by adding 54 mM zinc acetate and 37.5 µM PMS. Thereafter, 0.475% (v/v) sulfanilamide in 1 N HCl and 0.005% (v/v) *N*-(1-naphthyl)-ethylenediamine was added. Samples were allowed to stand for 15 min at RT in the dark and the absorbance of the produced azo-dye was measured at 540 nm.

ACO assay

ACO activity in cell extracts and purified mitochondria was assayed by coupling this activity to IDH and measuring the formation of NADPH. Leaf tissue was homogenized in 1.5 volumes of 50 mM Tris–HCl pH 8, 50 mM KCl, 0.2% (v/v) Triton X-100, 2 mM sodium citrate and 1 mM dithiothreitol, followed by centrifugation at 13,000*g* for 10 min at 4°C to remove cell debris. Each sample was processed immediately before activity measurement, except where stated, to avoid inactivation by O_2. The reaction (1 mL) contained 100–150 µg of leaf protein extract or 15–20 µg mitochondrial protein in 0.1 M Tris–HCl pH 8, 1.5 mM $MgCl_2$, 0.1% (v/v) Triton X-100, 1 mM $NADP^+$ and 0.36 U IDH. After 20–30 s of equilibration, the reaction was started by adding 0.15 mM cis-aconitic acid. The formation of NADPH was followed over time by measuring the increase in absorbance at 340 nm in a JASCO V-550 spectrophotometer.

PDC assay

To estimate the activity of PDC, mitochondria were isolated as described previously and reduction of NAD^+ was measured at 340 nm in a reaction mixture containing ~10 µg mitochondria in 100 mM MOPS pH 7.4, 1 mM $CaCl_2$, 1 mM $MgCl_2$, 4 mM cysteine, 0.45 mM thiamine pyrophosphate, 0.18 mM Coenzyme A, 3 mM NAD^+ and 0.1% (v/v) Triton X-100. The reaction was started with 7.5 mM pyruvate.

Fatty acid methyl ester measurement

The analysis of fatty acids was performed by quantification of their respective fatty acid methyl esters (FAMEs) via gas chromatography coupled with a flame ionization detector as described before (Browse et al., 1986). One milliliter 1 N HCl in methanol was added to five seeds or ~50 mg homogenized seedlings as well as 5 µg pentadecanoic acid as internal standard. Samples were incubated at 80°C for 2 h (seeds) or 30 min (seedlings). After cooling down, 1 mL 0.9% (w/v) NaCl and 1 mL hexane were added. Samples were mixed vigorously and centrifuged with 1,000 *g* for 3 min. The hexane phase was transferred to a GC vial. FAMEs were quantified using pentadecanoic acid as internal standard.

Western blotting

For protein blot analysis, total cell extract or purified organelles were heated for 5 min and separated on standard sodium dodecyl sulfate-PAGE. Proteins were transferred to a membrane (BioTrace PVDF Transfer Membrane; Pall Corporation, Port Washington, NY, USA) and labeled with antibodies (Streptavidin HRP: ab7403; Abcam, Cambridge, UK; lipoic acid: ab58724, ACO): see Bernard et al. (2009). Antibodies against GRXS15 and mLIP1 were kindly provided by Nicolas Rouhier and Jonathan Przybyla-Toscano (Nancy) and the H protein antibody a kind gift of Olivier Keech (Umea). The TOM40 antibody was a kind gift of Jim Whelan (Melbourne). Immunolabeling was detected by chemiluminescence by using secondary horseradish peroxidase-conjugated antibodies and Pierce ECL Western Blotting Substrate.

Fluorescence microscopy

Fluorescent plants were selected using a stereomicroscope (Leica M165 FC) equipped with a GFP filter.

A confocal laser scanning microscope (Zeiss LSM 780, attached to an Axio Observer.Z1; Carl Zeiss Microscopy) equipped with a solid state 405 nm laser and an Argon laser for excitation at 458 nm and 488 nm, and a ×40 (C-Apochromat, 1.20 numerical aperture, water immersion) or ×63 lens (Plan-Apochromat, 1.40 numerical aperture, oil immersion) was used for confocal imaging. For ratiometric analyses of mitochondrially localized roGFP2-hGrx1 (Albrecht et al., 2014) or roGFP2-Orp1 (Nietzel et al., 2019), lines with similar expression levels in WT and mutants were selected. For both sensors, roGFP2 was excited at 405 and 488 nm. For both excitation wavelengths, roGFP2 fluorescence was collected with a bandpass filter of 505–530 nm.

The cytosolic ATeam 1.03-nD/nA was excited at 458 nm and emission of CFP (mseCFP) and Venus (cp173-mVenus) was collected at 499–544 nm and 579–615 nm, respectively. Background signal was subtracted before ratiometric analysis.

For all emissions, intensities from four scans were averaged. Ratiometric analysis was performed using a custom-written MATLAB script (Fricker, 2016) using x,y noise filtering and fluorescence background subtraction.

Statistical analysis

Statistics and error bars were applied for independent experiments with at least three biological replicates using the program GraphPad Prism version 6.

Accession numbers

GRXS15 (At3g15660), BIO2 (At2g43360), MCCA (At1g03090), ATM3 (At5g58270), CNX2 (At2g31955), CNX3 (At1g01290), NR1 (At1g77760), NR2 (At1g37130), AAO1 (At5g20960), AAO2 (At3g43600), AAO3 (At2g27150), XDH1 (At4g34890) XDH2 (At4g34900), ACO1 (At4g35830), ACO2 (At4g26970), ACO3 (At2g05710), mLIP1 (At2g20860), IVDH (At3g45300), and BCAT (At5g65780).

Supplemental data

The following materials are available in the online version of this article.

Supplemental Figure S1. Arabidopsis mutants affected in GRXS15 function develop a dwarf phenotype.

Supplemental Figure S2. Moco enzymes and anions are not affected in Arabidopsis *GRXS15 K83A* mutants.

Supplemental Figure S3. In vivo monitoring of ATP levels in the cytosol of Arabidopsis *GRXS15 K83A* mutants.

Supplemental Figure S4. Activity and stability of ACO in mitochondria and leaf extracts.

Supplemental Figure S5. Analysis of the oxidation state of the Arabidopsis *grxs15* mutants.

Supplemental Figure S6. Catabolism of BCAAs in Arabidopsis seedlings.

Supplemental Figure S7. BCAAs and their respective keto acids in the *rml1* mutant.

Supplemental Table S1. Content of amino acids and keto acids of Arabidopsis WT and *GRXS15 K83A* lines #3 and #4.

Supplemental Table S2. Fe–S cluster containing subunits of complexes of the mETC with the estimated copy numbers in mitochondria isolated from heterotrophic Arabidopsis cell culture.

Acknowledgments

We would like to thank Elke Ströher and Harvey Millar for providing the knockdown line *GRXS15*^{amiR} as well as Nicolas Rouhier, Johnathan Przybyla-Toscano, Olivier Keech, and Jim Whelan for providing antibodies. We thank Philippe Fuchs, Stefanie Müller-Schüssele, and Nicolas Rouhier for helpful discussion and critical reading of the manuscript.

Funding

This work was supported by grants of the German Research Foundation (Deutsche Forschungsgemeinschaft) through the priority program SPP1710 'Dynamics of thiol-based redox switches in cellular physiology' (ME1567/9-1/2, SCHW1719/7-1, HE1848/16-1), the Emmy Noether program (SCHW1719/1-1), an individual grant (ME1567/12-1), and through the Research Training Group 2064 "Water use efficiency and drought stress responses: From Arabidopsis to Barley," I.K. was funded by the Doctoral Training Program of the Biotechnology and Biological Sciences Research Council (BBSRC); A.E.M. was funded by a PhD studentship from the John Innes Foundation; M. F. and J.B. are funded by BBSRC grant awards BB/P012523/1 and BB/P012574/1. A.M. is recipient of a Feodor Lynen Research Fellowship from the Alexander von Humboldt Foundation.

Conflict of interest statement: None declared.

References

Albrecht SC, Sobotta MC, Bausewein D, Aller I, Hell R, Dick TP, Meyer AJ (2014) Redesign of genetically encoded biosensors for monitoring mitochondrial redox status in a broad range of model eukaryotes. J Biomol Screen **19**: 379–386

Araújo WL, Ishizaki K, Nunes-Nesi A, Larson TR, Tohge T, Krahnert I, Witt S, Obata T, Schauer N, Graham IA, et al. (2010) Identification of the 2-hydroxyglutarate and isovaleryl-CoA dehydrogenases as alternative electron donors linking lysine catabolism to the electron transport chain of Arabidopsis mitochondria. Plant Cell **22**: 1549–1563

Azam T, Przybyla-Toscano J, Vignols F, Couturier J, Rouhier N, Johnson MK (2020) The Arabidopsis mitochondrial glutaredoxin GRXS15 provides [2Fe-2S] clusters for ISCA-mediated [4Fe-4S] cluster maturation. Int J Mol Sci **21**: 9237

Baker PR, Friederich MW, Swanson MA, Shaikh T, Bhattacharya K, Scharer GH, Aicher J, Creadon-Swindell G, Geiger E, MacLean KN, et al. (2014) Variant non ketotic hyperglycinemia is caused by mutations in LIAS, BOLA3 and the novel gene GLRX5. Brain **137**: 366–379

Balk J, Schaedler TA (2014) Iron cofactor assembly in plants. Annu Rev Plant Biol **65**: 125–153

Banci L, Brancaccio D, Ciofi-Baffoni S, Del Conte R, Gadepalli R, Mikolajczyk M, Neri S, Piccioli M, Winkelmann J (2014) [2Fe-2S] cluster transfer in iron–sulfur protein biogenesis. Proc Natl Acad Sci **111**: 6203–6208

Bandyopadhyay S, Gama F, Molina-Navarro MM, Gualberto JM, Claxton R, Naik SG, Huynh BH, Herrero E, Jacquot JP, Johnson MK, et al. (2008) Chloroplast monothiol glutaredoxins as scaffold proteins for the assembly and delivery of [2Fe–2S] clusters. EMBO J **27**: 1122–1133

Begas P, Liedgens L, Moseler A, Meyer AJ, Deponte M (2017) Glutaredoxin catalysis requires two distinct glutathione interaction sites. Nat Commun **8**: 14835

Belin C, Bashandy T, Cela J, Delmore-Hinoux V, Riondet C, Reichheld JP (2015) A comprehensive study of thiol reduction gene expression under stress conditions in *Arabidopsis thaliana*. Plant Cell Environ **38**: 299–314

Bernard DG, Cheng Y, Zhao Y, Balk J (2009) An allelic mutant series of ATM3 reveals its key role in the biogenesis of cytosolic iron-sulfur proteins in Arabidopsis. Plant Physiol **151**: 590–602

Bittner F (2014) Molybdenum metabolism in plants and crosstalk to iron. Front Plant Sci **5**: 28

Browse J, McCourt PJ, Somerville CR (1986) Fatty acid composition of leaf lipids determined after combined digestion and fatty acid methyl ester formation from fresh tissue. Anal Biochem **152**: 141–145

Cao P, Kim SJ, Xing A, Schenck CA, Liu L, Jiang N, Wang J, Last RL, Brandizzi F (2019) Homeostasis of branched-chain amino acids is critical for the activity of TOR signaling in Arabidopsis. Elife **8**: e50747

Carrari F, Nunes-Nesi A, Gibon Y, Lytovchenko A, Loureiro ME, Fernie AR (2003) Reduced expression of aconitase results in an enhanced rate of photosynthesis and marked shifts in carbon partitioning in illuminated leaves of wild species tomato. Plant Physiol **133**: 1322–1335

Cheng JC, Seeley KA, Sung ZR (1995) RML1 and RML2, Arabidopsis genes required for cell proliferation at the root tip. Plant Physiol **107**: 365–376

Cheng NH, Liu JZ, Brock A, Nelson RS, Hirschi KD (2006) AtGRXcp, an Arabidopsis chloroplastic glutaredoxin, is critical for protection against protein oxidative damage. J Biol Chem **281**: 26280–26288

Cheng NH, Liu JZ, Liu X, Wu Q, Thompson SM, Lin J, Chang J, Whitham SA, Park S, Cohen JD, et al. (2011) Arabidopsis monothiol glutaredoxin, AtGRXS17, is critical for temperature-dependent postembryonic growth and development via modulating auxin response. J Biol Chem **286**: 20398–20406

De Col V, Fuchs P, Nietzel T, Elsässer M, Voon CP, Candeo A, Seeliger I, Fricker MD, Grefen C, Møller IM, Bassi A, et al. (2017) ATP sensing in living plant cells reveals tissue gradients and stress dynamics of energy physiology. Elife **6**: e26770

Couturier J, Przybyla-Toscano J, Roret T, Didierjean C, Rouhier N (2015) The roles of glutaredoxins ligating Fe–S clusters: sensing, transfer or repair functions? Biochim Biophys Acta Mol Cell Res **1853**: 1513–1527

Deponte M (2013) Glutathione catalysis and the reaction mechanisms of glutathione-dependent enzymes. Biochim Biophys Acta Gen Subj **1830**: 3217–3266

Douce R, Bourguignon J, Neuburger M, Rébeillé F (2001) The glycine decarboxylase system: a fascinating complex. Trends Plant Sci **6**: 167–176

Elhafez D, Murcha MW, Clifton R, Soole KL, Day DA, Whelan J (2006) Characterization of mitochondrial alternative NAD(P)H dehydrogenases in Arabidopsis: intraorganelle location and expression. Plant Cell Physiol **47**: 43–54

Ewald R, Hoffmann C, Florian A, Neuhaus E, Fernie AR, Bauwe H (2014) Lipoate-protein ligase and octanoyltransferase are essential for protein lipoylation in mitochondria of Arabidopsis. Plant Physiol **165**: 978–990

Figueroa P, León G, Elorza A, Holuigue L, Jordana X (2001) Three different genes encode the iron-sulfur subunit of succinate dehydrogenase in *Arabidopsis thaliana*. Plant Mol Biol **46**: 241–250

Fricker MD (2016) Quantitative redox imaging software. Antioxid Redox Signal **24**: 752–762

Fuchs P, Rugen N, Carrie V, Elsässer M, Finkemeier I, Giese J, Hildebrandt TM, Kühn K, Maurino VG, Ruberti C, et al. (2020) Single organelle function and organization as estimated from Arabidopsis mitochondrial proteomics. Plant J **101**: 420–441

Gu L, Jones AD, Last RL (2010) Broad connections in the Arabidopsis seed metabolic network revealed by metabolite profiling of an amino acid catabolism mutant. Plant J **61**: 579–590

Hesberg C, Hänsch R, Mendel RR, Bittner F (2004) Tandem orientation of duplicated xanthine dehydrogenase genes from *Arabidopsis thaliana*: differential gene expression and enzyme activities. J Biol Chem **279**: 13547–13554

Hildebrandt TM, Nunes Nesi A, Araújo WL, Braun HP (2015) Amino acid catabolism in plants. Mol Plant **8**: 1563–1579

Hoffmann C, Plocharski B, Haferkamp I, Leroch M, Ewald R, Bauwe H, Riemer J, Herrmann JM, Neuhaus HE (2013) From endoplasmic reticulum to mitochondria: absence of the Arabidopsis ATP antiporter Endoplasmic Reticulum Adenylate Transporter1 perturbs photorespiration. Plant Cell **25**: 2647–2660

Huang S, Taylor NL, Ströher E, Fenske R, Millar AH (2013) Succinate dehydrogenase assembly factor 2 is needed for assembly and activity of mitochondrial complex II and for normal root elongation in Arabidopsis. Plant J **73**: 429–441

Igamberdiev AU, Bykova NV, Lea PJ, Gardeström P (2001) The role of photorespiration in redox and energy balance of photosynthetic plant cells: a study with a barley mutant deficient in glycine decarboxylase. Physiol Plant **111**: 427–438

Iñigo, S Durand, AN Ritter, A Le Gall, S Termathe, M Klassen, R Tohge, T De Coninck, B Van Leene, JDe Clercq R, et al. (2016) Glutaredoxin GRXS17 associates with the cytosolic iron-sulfur cluster assembly pathway. Plant Physiol **172**: 858–873

Ishizaki K, Larson TR, Schauer N, Fernie AR, Graham IA, Leaver CJ (2005) The critical role of Arabidopsis electron-transfer flavoprotein: ubiquinone oxidoreductase during dark-induced starvation. Plant Cell **17**: 2587–2600

Knuesting J, Riondet C, Maria C, Kruse I, Bécuwe N, König N, Berndt C, Tourrette S, Guilleminot-Montoya J, Herrero E, et al. (2015) Arabidopsis glutaredoxin S17 and its partner, the nuclear factor Y subunit C11/negative cofactor 2α, contribute to maintenance of the shoot apical meristem under long-day photoperiod. Plant Physiol **167**: 1643–1658

Koshiba T, Saito E, Ono N, Yamamoto N, Sato M (1996) Purification and properties of flavin- and molybdenum-containing aldehyde oxidase from coleoptiles of maize. Plant Physiol **110**: 781–789

Kruse I, Maclean AE, Hill L, Balk J (2018) Genetic dissection of cyclic pyranopterin monophosphate biosynthesis in plant mitochondria. Biochem J **475**: 495–509

Kühn K, Obata T, Feher K, Bock R, Fernie AR, Meyer EH (2015) Complete mitochondrial complex I deficiency induces an up-regulation of respiratory fluxes that is abolished by traces of functional complex I. Plant Physiol **168**: 1537–1549

Liedgens L, Zimmermann J, Wäschenbach L, Geissel F, Laporte H, Gohlke H, Morgan B, Deponte M (2020) Quantitative assessment of the determinant structural differences between redox-active and inactive glutaredoxins. Nat Commun **11**: 1725

Lill R, Freibert SA (2020) Mechanisms of mitochondrial iron-sulfur protein biogenesis. Annu Rev Biochem **89**: 1

Liu G, Wang Y, Anderson GJ, Camaschella C, Chang Y, Nie G (2016) Functional analysis of GLRX5 mutants reveals distinct functionalities of GLRX5 protein. J Cell Biochem **117**: 207–217

López-Calcagno PE, Fisk S, Brown KL, Bull SE, South PF, Raines CA (2019) Overexpressing the H-protein of the glycine cleavage system increases biomass yield in glasshouse and field-grown transgenic tobacco plants. Plant Biotechnol J **17**: 141–151

Martins L, Knuesting J, Bariat L, Dard A, Freibert SA, Marchand CH, Young D, Thuy Dung NH, Voth W, Debures A, et al. (2020) Redox modification of the iron-sulfur glutaredoxin GRXS17 activates holdase activity and protects plants from heat stress. Plant Physiol **184**: 676–692

Marty L, Bausewein D, Müller C, Bangash SAK, Moseler A, Schwarzländer M, Müller-Schüssele SJ, Zechmann B, Riondet C, Balk J, et al. (2019) Arabidopsis glutathione reductase 2 is indispensable in plastids, while mitochondrial glutathione is safeguarded by additional reduction and transport systems. New Phytol **224**: 1569–1584

McCarthy EL, Booker SJ (2017) Destruction and reformation of an iron-sulfur cluster during catalysis by lipoyl synthase. Science **358**: 373–377

Meinke DW (2019) Genome-wide identification of EMBRYO-DEFECTIVE (EMB) genes required for growth and development in Arabidopsis. New Phytol **226**: 306–325

Meyer AJ, Fricker MD (2000) Direct measurement of glutathione in epidermal cells of intact Arabidopsis roots by two-photon laser scanning microscopy. J Microsc **198**: 174–181

Meyer EH, Solheim C, Tanz SK, Bonnard G, Millar AH (2011) Insights into the composition and assembly of the membrane arm of plant complex I through analysis of subcomplexes in Arabidopsis mutant lines. J Biol Chem **286**: 26081–26092

Meyer EH, Welchen E, Carrie C (2019) Assembly of the complexes of the oxidative phosphorylation system in land plant mitochondria. Annu Rev Plant Biol **70**: 23–50

Meyer Y, Buchanan BB, Vignols F, Reichheld JP (2009) Thioredoxins and glutaredoxins: unifying elements in redox biology. Annu Rev Genet **43**: 335–367

Møller IM, Igamberdiev AU, Bykova NV, Finkemeier I, Rasmusson AG, Schwarzländer M (2020) Matrix redox physiology governs the regulation of plant mitochondrial metabolism through posttranslational protein modifications. Plant Cell **32**: 573–594

Møller IM, Rasmusson AG (1998) The role of NADP in the mitochondrial matrix. Trends Plant Sci **3**: 21–27

Morgan MJ, Lehmann M, Schwarzländer M, Baxter CJ, Sienkiewicz-Porzucek A, Williams TCR, Schauer N, Fernie AR, Fricker MD, Ratcliffe RG, et al. (2008) Decrease in manganese superoxide dismutase leads to reduced root growth and affects tricarboxylic acid cycle flux and mitochondrial redox homeostasis. Plant Physiol **147**: 101–114

Moseler A, Aller I, Wagner S, Nietzel T, Przybyla-Toscano J, Mühlenhoff U, Lill R, Berndt C, Rouhier N, Schwarzländer M, et al. (2015) The mitochondrial monothiol glutaredoxin S15 is essential for iron-sulfur protein maturation in *Arabidopsis thaliana*. Proc Natl Acad Sci USA **112**: 13735–13740

Mouillon JM, Aubert S, Bourguignon J, Gout E, Douce R, Rébeillé F (1999) Glycine and serine catabolism in non-photosynthetic higher plant cells: their role in C1 metabolism. Plant J **20**: 197–205

Nietzel T, Mostertz J, Ruberti C, Née G, Fuchs P, Wagner S, Moseler A, Müller-Schüssele SJ, Benamar, A et al. (2020) Redox-mediated kick-start of mitochondrial energy metabolism

drives resource-efficient seed germination. Proc Natl Acad Sci USA **117**: 741–751

Nietzel T, Elsässer M, Ruberti C, Steinbeck J, Ugalde JM, Fuchs P, Wagner S, Ostermann L, Moseler A, Lemke P, Fricker MD, et al. (2019) The fluorescent protein sensor roGFP2-Orp1 monitors in vivo H2O2 and thiol redox integration and elucidates intracellular H2O2 dynamics during elicitor-induced oxidative burst in Arabidopsis. New Phytol **221**: 1649–1664

Pain D, Dancis A (2016) Roles of Fe–S proteins: from cofactor synthesis to iron homeostasis to protein synthesis. Curr Opin Genet Dev **38**: 45–51

Patton DA, Schetter AL, Franzmann LH, Nelson K, Ward ER, Meinke DW (1998) An embryo-defective mutant of Arabidopsis disrupted in the final step of biotin synthesis. Plant Physiol **116**: 935–946

Peng C, Uygun S, Shiu SH, Last RL (2015) The impact of the branched-chain ketoacid dehydrogenase complex on amino acid homeostasis in Arabidopsis. Plant Physiol **169**: 1807–1820

Pires MV, Pereira Júnior AA, Medeiros DB, Daloso DM, Pham PA, Barros KA, Engqvist MKM, Florian A, Krahnert I, Maurino VG, et al. (2016) The influence of alternative pathways of respiration that utilize branched-chain amino acids following water shortage in Arabidopsis. Plant Cell Environ **39**: 1304–1319

Pommerrenig B, Popko J, Heilmann M, Schulmeister S, Dietel K, Schmitt B, Stadler R, Feussner I, Sauer N (2013) SUCROSE TRANSPORTER 5 supplies Arabidopsis embryos with biotin and affects triacylglycerol accumulation. Plant J **73**: 392–404

Przybyla-Toscano J, Boussardon C, Law SR, Rouhier N, Keech O (2021) Gene atlas of iron-containing proteins in *Arabidopsis thaliana*. Plant J **106**: 258-274

Rasmusson AG, Geisler DA, Møller IM (2008) The multiplicity of dehydrogenases in the electron transport chain of plant mitochondria. Mitochondrion **8**: 47–60

Reichheld JP, Meyer E, Khafif M, Bonnard G, Meyer Y (2005) AtNTRB is the major mitochondrial thioredoxin reductase in *Arabidopsis thaliana*. FEBS Lett **579**: 337–342

Rey P, Becuwe N, Tourrette S, Rouhier N (2017) Involvement of Arabidopsis glutaredoxin S14 in the maintenance of chlorophyll content. Plant Cell Environ **40**: 2319–2332

Rodríguez-Manzaneque MT, Ros J, Cabiscol E, Sorribas A, Herrero E (1999) Grx5 glutaredoxin plays a central role in protection against protein oxidative damage in *Saccharomyces cerevisiae*. Mol Cell Biol **19**: 8180–8190

Rodríguez-Manzaneque MT, Tamarit J, Bellí G, Ros J, Herrero E (2002) Grx5 is a mitochondrial glutaredoxin required for the activity of iron/sulfur enzymes. Mol Biol Cell **13**: 1109–1121

Rouhier N, Lemaire SD, Jacquot JP (2008) The role of glutathione in photosynthetic organisms: emerging functions for glutaredoxins and glutathionylation. Annu Rev Plant Biol **59**: 143–166

Sarasketa A, González-Moro MB, González-Murua C, Marino D (2014) Exploring ammonium tolerance in a large panel of *Arabidopsis thaliana* natural accessions. J Exp Bot **65**: 6023–6033

Scheible WR, Lauerer M, Schulze ED, Caboche M, Stitt M (1997) Accumulation of nitrate in the shoot acts as a signal to regulate shoot-root allocation in tobacco. Plant J **11**: 671–691

Schneider T, Dinkins R, Robinson K, Shellhammer J, Meinke DW (1989) An embryo-lethal mutant of *Arabidopsis thaliana* is a biotin auxotroph. Dev Biol **131**: 161–167

Schwarz G, Mendel RR (2006) Molybdenum cofactor biosynthesis and molybdenum enzymes. Annu Rev Plant Biol **57**: 623–647

Senkler J, Senkler M, Eubel H, Hildebrandt T, Lengwenus C, Schertl P, Schwarzländer M, Wagner S, Wittig I, Braun HP (2017) The mitochondrial complexome of *Arabidopsis thaliana*. Plant J **89**: 1079–1092

Solbiati J, Chapman-Smith A, Cronan JE (2002) Stabilization of the biotinoyl domain of Escherichia coli acetyl-CoA carboxylase by interactions between the attached biotin and the protruding "thumb" structure. J Biol Chem **277**: 21604–21609

Solmonson A, DeBerardinis RJ (2018) Lipoic acid metabolism and mitochondrial redox regulation. J Biol Chem **293**: 7522–7530

Ströher E, Grassl J, Carrie C, Fenske R, Whelan J, Millar AH (2016) Glutaredoxin S15 is involved in Fe-S cluster transfer in mitochondria influencing lipoic acid-dependent enzymes, plant growth, and arsenic tolerance in Arabidopsis. Plant Physiol **170**: 1284–1299

Sweetlove LJ, Taylor NL, Leaver CJ (2007) Isolation of intact, functional mitochondria from the model plant *Arabidopsis thaliana*. In D Leister and JM Herrmann, eds, Mitochondria: Practical Protocols, Humana Press, Totowa, NJ, pp 125–136

Taylor NL, Heazlewood JL, Day DA, Millar AH (2004) Lipoic acid--dependent oxidative catabolism of α-keto acids in mitochondria provides evidence for branched-chain amino acid catabolism in Arabidopsis. Plant Physiol **134**: 838–848

Teschner J, Lachmann N, Schulze J, Geisler M, Selbach K, Santamaria-Araujo J, Balk J, Mendel RR, Bittner F (2010) A novel role for Arabidopsis mitochondrial ABC transporter ATM3 in molybdenum cofactor biosynthesis. Plant Cell **22**: 468–480

Thordal-Christensen H, Zhang Z, Wei Y, Collinge DB (1997) Subcellular localization of H2O2 in plants. H2O2 accumulation in papillae and hypersensitive response during the barley—powdery mildew interaction. Plant J **11**: 1187–1194

Trnka D, Engelke AD, Gellert M, Moseler A, Hossain MF, Lindenberg TT, Pedroletti L, Odermatt B, de Souza JV, Bronowska AK, Dick TP, et al. (2020) Molecular basis for the distinct functions of redox-active and FeS-transfering glutaredoxins. Nat Commun **11**: 3445

Ugulava NB, Sacanell CJ, Jarrett JT (2001) Spectroscopic changes during a single turnover of biotin synthase: destruction of a [2Fe-2S] cluster accompanies sulfur insertion. Biochemistry **40**: 8352–8358

Uzarska MA, Dutkiewicz R, Freibert SA, Lill R, Mühlenhoff U (2013) The mitochondrial Hsp70 chaperone Ssq1 facilitates Fe/S cluster transfer from Isu1 to Grx5 by complex formation. Mol Biol Cell **24**: 1830–1841

Vernoux T, Wilson RC, Seeley KA, Reichheld JP, Muroy S, Brown S, Maughan SC, Cobbett CS, Van Montagu M, Inzé D, et al. (2000) The ROOT MERISTEMLESS1/CADMIUM SENSITIVE2 gene defines a glutathione-dependent pathway involved in initiation and maintenance of cell division during postembryonic root development. Plant Cell **12**: 97–110

Voon CP, Guan X, Sun Y, Sahu A, Chan MN, Gardeström P, Wagner S, Fuchs P, Nietzel T, Versaw WK, et al. (2018) ATP compartmentation in plastids and cytosol of *Arabidopsis thaliana* revealed by fluorescent protein sensing. Proc Natl Acad Sci USA **115**: 10778–10787

Wagner S, Behera S, De Bortoli S, Logan DC, Fuchs P, Carraretto L, Teardo E, Cendron L, Nietzel T, Füßl M, et al. (2015) The EF-hand Ca2+ binding protein MICU choreographs mitochondrial Ca2+ dynamics in Arabidopsis. Plant Cell **27**: 3190–3212

Wang R, Tischner R, Gutiérrez RA, Hoffman M, Xing X, Chen M, Coruzzi G, Crawford NM (2004) Genomic analysis of the nitrate response using a nitrate reductase-null mutant of Arabidopsis. Plant Physiol **136**: 2512–2522

Wilkinson JQ, Crawford NM (1993) Identification and characterization of a chlorate-resistant mutant of *Arabidopsis thaliana* with mutations in both nitrate reductase structural genes NIA1 and NIA2. Mol Gen Genet **239**: 289–297

Yang Y, M. Pollard, A., Höfler, C., Poschet, G., Wirtz, M., Hell, R., Sourjik, V. (2015) Relation between chemotaxis and consumption of amino acids in bacteria. Mol Microbiol **96**: 1272–1282

Yasuno R, Wada H (2002) The biosynthetic pathway for lipoic acid is present in plastids and mitochondria in *Arabidopsis thaliana*. FEBS Lett **517**: 110–114

Ye H, Jeong SY, Ghosh MC, Kovtunovych G, Silvestri L, Ortillo D, Uchida N, Tisdale J, Camaschella C, Rouault TA (2010) Glutaredoxin 5 deficiency causes sideroblastic anemia

by specifically impairing heme biosynthesis and depleting cytosolic iron in human erythroblasts. J Clin Invest **120**: 1749–1761

Yu H, Du X, Zhang F, Zhang F, Hu Y, Liu S, Jiang X, Wang G, Liu D (2012) A mutation in the E2 subunit of the mitochondrial pyruvate dehydrogenase complex in Arabidopsis reduces plant organ size and enhances the accumulation of amino acids and intermediate products of the TCA Cycle. Planta **236**: 387–399

Zhang Y, Swart C, Alseekh S, Scossa F, Jiang L, Obata T, Graf A, Fernie AR (2018) The extra-pathway interactome of the TCA cycle: expected and unexpected metabolic interactions. Plant Physiol **177**: 966–979

4.3 | Supplementary information I contributed

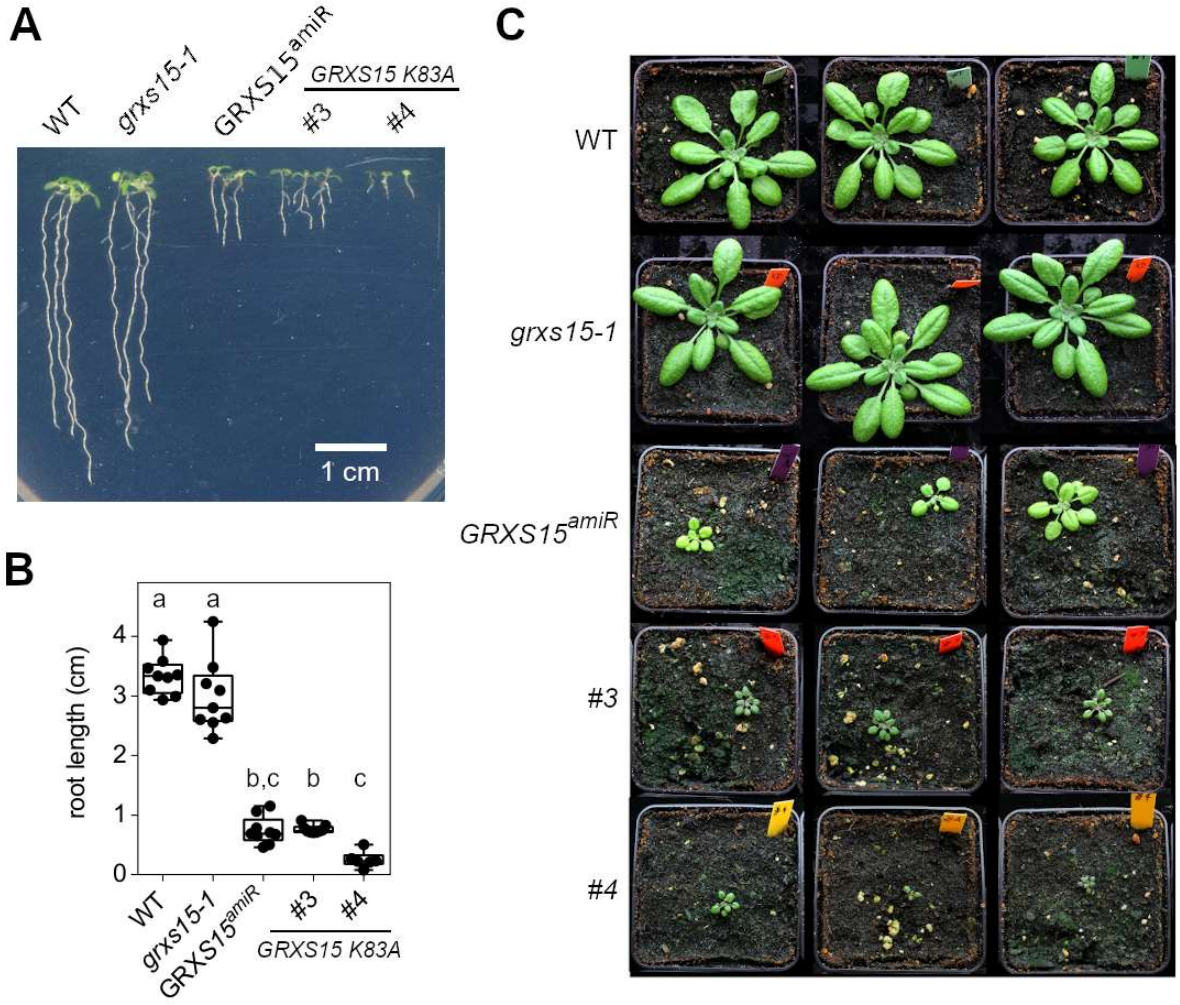

Supplemental Figure S1. Arabidopsis mutants affected in GRXS15 function develop a dwarf phenotype.

A, B: Growth of different *grxs15* mutants (*grxs15-1*, GRXS15^{amiR}, *GRXS15 K83A* lines *#3* and *#4*) and Wild type (WT) seedlings on vertical plates with 0.8% agar under long-day conditions. Seedlings were documented and quantitatively analyzed for their root length 10 days after germination. (n = 6-9; the box plot shows the median as center line with the box for the first to the third quartile and whiskers indicating min and max values, points represent individual values of the whole data set). Different letters indicate significant differences between the different lines; $P \leq 0.05$; (one-way ANOVA).

C: Phenotypes of soil-grown plants after five weeks under long-day conditions (16 h light, 19°C, 8 h dark, 17°C; 50% rh).

5 | Janus-faced LIP1 causes acute mitochondrial sulfide intoxication

This chapter presents the unpublished research paper:

"Altered iron-sulfur cluster transfer in Arabidopsis mitochondria reveals lipoyl synthase as a Janus-faced enzyme that generates toxic sulfide"

***Luca Pedroletti**, Anna Moseler, Stefan Timm, Gernot Poschet, Maria Homagk, Jeremy X. L. The, Stephan Wagner, Markus Wirtz, Rüdiger Hell and Andreas J. Meyer.*

The manuscript has been submitted to *The Plant Cell* and, at the time of the writing of this thesis, is under review. The manuscript is available in bioRxiv (open access) on:

bioRxiv; doi: https://doi.org/10.1101/2023.08.30.555573.

The complete supplemental material is provided with the attached manuscript, in Section 5.2.

5.1 | Summary and personal contribution

Iron–sulfur (Fe–S) clusters are fundamental cofactors of many mitochondrial proteins. Their distribution among the respective target proteins, as well as the consequences of alteration in their fluxes, are still not fully understood.

In this research paper, we investigated why compromised Fe–S cluster transfer via glutaredoxin S15 (GRXS15) mainly impacts lipoyl synthase (LIP1). We showed that LIP1 activity and abundance must be tightly controlled because directly connected to sulfide release. In addition, we found that in Arabidopsis mitochondrial cysteine biosynthesis plays a key role in the fixation of excessive sulfide in mitochondria.

Mitochondrial Fe–S cluster assembly occurs in two steps: the formation of [2Fe–2S] clusters and its subsequent assembly into [4Fe–4S] clusters (see Chapter 2, Pedroletti et al. (2023a)). In plants, GRXS15 plays a role in connecting the two assembly machineries by transferring [2Fe–2S] clusters. As shown in Chapter 4 (Moseler *et al.*, 2021), decreased cluster transfer activity through interference with GRXS15 leads to specific defects associated with lipoyl-(LA) dependent enzymes.

Here, we hypothesised that genetically engineered bottleneck in cluster supply particularly affects LIP1 due to its low abundance compared to other mitochondrial [4Fe–4S] proteins and its continuous consumption of [4Fe–4S] clusters for LA biosynthesis (Lanz and Booker, 2015; McCarthy and Booker, 2017; Fuchs *et al.*, 2020).

One of the four mitochondrial LA-dependent enzymes is the glycine dehydrogenase complex (GDC), a key enzyme involved in photorespiration (Douce *et al.*, 2001; Bauwe, 2023). We thus hypothesised that diminished capacity of GRXS15 for Fe–S cluster transfer caused a photorespiratory phenotype. Hence, we grew two *grxs15* knockdown lines (*grxs15-1* and *amiR*) and two complemented lines that overexpress the mutated variant GRXS15 K83A (*K83A #3* and *K83A #4*) (see Chapter 4, Moseler *et al.* (2021)) under high atmospheric CO_2 to suppress photorespiration. With this approach, we found partial suppression of the dwarf phenotype of the most severely affected *grxs15 K83A* complementation lines and provoking the re-adjustment of the metabolite profile by overcoming the low GDC activity.

To test if the Fe–S cluster supply bottleneck indeed primarily affects LIP1 due to its low abundance, we genetically removed a highly abundant [4Fe–4S]-containing protein, aconitase 3 (ACO3), from *grxs15* plants by crossing the mutants with an Arabidopsis *aco3* knockout line. We hypothesised that this would allow for redistribution of clusters between the remaining Fe–S-dependent proteins increasing the number of [4Fe–4S] clusters available for LIP1. The loss of ACO3 partially suppressed the dwarf phenotypes of the mutants and almost completely reverted the characteristic metabolite profiles of *grxs15* mutants to a wild-type metabolite signature. Particularly, the accumulation of metabolites associated with LA-dependent enzymes decreased to *aco3* levels in the double mutants, suggesting that loss of ACO3 enabled the redirection of [4Fe–4S] clusters to LIP1, resulting in sufficient cluster supply and thus the reestablishment of lipoylation activity in the *grxs15* mutants.

With a different strategy, we redirected Fe–S clusters to LIP1 by increasing its copy number. For this, we overexpressed LIP1 in *grxs15* mutants showing that it completely suppresses the dwarfism of *grxs15 K83A*. Concomitantly, the metabolite analysis of the lines overexpressing LIP1 uncovered a decrease of pyruvate, 2-oxoglutarate and the three branched chain keto-acids, which were typically accumulated in *grxs15* mutants.

However, contrary to expectations, overexpressing LIP1 had a deleterious effect in the wild type and *grxs15* knockdown mutants with substantial residual GRXS15 activity, resulting in reduced growth with curly leaves, delayed development and accumulation of several metabolites, especially cysteine. In addition, we observed that the severity of the phenotype was dependent on the zygosity of LIP1 overexpression, with homozygous plants being the most severely affected.

Lipoyl synthase is widely conserved in pro- and eukaryotes and has been shown to require two [4Fe–4S] clusters for its catalytic activity: a reducing cluster and an additional auxiliary cluster from which sulfur atoms are extracted during catalysis (McCarthy and Booker, 2017). The question of whether the auxiliary cluster is recycled or degraded during each catalytic cycle remains a subject of ongoing debate (see Chapter 1.8). We hypothesized that the reason

for the LIP1-induced toxicity is due to its increased [4Fe–4S] clusters consumption, resulting in more sulfide release, which is particularly toxic in the mitochondrial matrix since it can inhibit the cytochrome *c* oxidase (COX) (Nicholls *et al.*, 2013). We demonstrated via immunoblotting and respiration measurements that LIP1 overexpression increases alternative oxidases (AOXs) expression and activity, as a compensatory mechanism to cope with the inhibition of COX. Our results also show the reduced deleterious effects in the *grxs15 K83A* mutants compared to wild-type and knockdown lines, which correlated with the suppression of their dwarfism and the general beneficial effect of LIP1 overexpression in these lines.

Finally, we studied the mechanisms for detoxification of sulfide. In plants, sulfide can be utilized in the mitochondrial matrix to synthesise cysteine through activity of the *O*-acetylserine (thiol) lyase C (OAS-TL C) (Heeg *et al.*, 2008). To investigate whether increasing the mitochondrial sulfide detoxification capacity can revert the effects of excess sulfide released by overexpression of LIP1, we simultaneously overexpressed OAS-TL C and LIP1 in wild-type plants. The results show that the dwarf phenotype caused by LIP1 overexpression was partially suppressed. Furthermore, the respiration of wild-type plants overexpressing both LIP1 and OAS-TL C became more sensitive to COX inhibition, suggesting that the toxicity of sulfide originating from LIP1 was partially rescued by overexpression of OAS-TL C.

Taken together, our data confirmed the central role of GRXS15 for the availability of Fe–S cluster in mitochondria. We showed that a bottleneck in cluster transfer in *grxs15* mutants primarily affects the activity of LIP1, which is the first enzyme that experiences a shortage of Fe–S cluster if the upstream delivery system is impaired, likely due to its low abundance and inability to effectively compete for a limited pool of Fe–S clusters.

My personal contribution to this study includes the design and performance of most of the experiments, the data analysis and bibliographic research. I further largely contributed to writing the manuscript draft and assembled all the figures.

Specifically, I generated the crosses and found homozygote lines of the double mutant *amiR aco3* and the triple mutants *K83A #3 aco3* and *#4 aco3* (Fig. 2 and Supplementary Fig. 4). I phenotyped the seedlings on plates and mature plants on soil, analysed the root length, the rosette leaf area and the inflorescence height (Fig. 2 and Supplementary Fig. 5).

Furthermore, I cloned the sequence coding for *LIP1* in the vectors for the overexpression, transformed the wild type and the four *grxs15* mutants via floral dip, found homozygote lines and verified with confocal microscopy the mitochondrial co-localization (Fig. 3 and Supplementary Fig. 7). I phenotyped seedlings on plates, older plants on soil and single leaves. I analysed the root length, rosette leaf area, fresh weight, floral induction and inflorescence development (Fig. 3, Fig. 4 and Supplementary Fig. 8-12, 17 and 18) and also transformed

wild-type plants and WT+LIP1 with the construct for overexpression of OAS-TL C via floral dip and isolated homozygous lines. I phenotyped mature plants on soil and analysed the rosette area (Fig. 5).

Moreover, I analysed and plotted all the metabolic data for the high CO_2 experiment (Fig. 1 and Supplementary Fig. 2 and 16). I prepared the material for the metabolomics analysis of the line crossed with *aco3* (Fig. 2 and Supplementary Fig. 6) and the line overexpressing LIP1 (Fig. 3 and Supplementary Fig. 15), analysed and plotted the results.

I supervised and analysed all the qRT-PCRs (Fig. 4 and Supplementary Fig. 1, 3 and 8), performed and analysed all the western blots (Fig. 3, Fig .4 and Supplementary Fig. 1, 13, 14 and 20), organized and analysed the respiration measurements (Fig. 4, Fig. 5 and Supplementary Fig. 19).

Overall, our research refines the model for the mitochondrial iron–sulfur cluster trafficking and provides a deeper understanding of the *in vivo* activity of LIP1. Our genetic framework can be further used to improve our understanding of plant mitochondrial Fe–S cluster biology.

5.2 | Manuscript

Attached on the following pages are the manuscript and supplemental material published in bioRxiv (*doi: https://doi.org/10.1101/2023.08.30.555573*).

Altered iron-sulfur cluster transfer in Arabidopsis mitochondria reveals lipoyl synthase as a Janus-faced enzyme that generates toxic sulfide

Luca Pedroletti[1], Anna Moseler[1], Stefan Timm[2], Gernot Poschet[3], Maria Homagk[1], Jeremy X. L. The[1], Stephan Wagner[1], Markus Wirtz[3], Rüdiger Hell[3], Andreas J. Meyer[1,*]

[1]University of Bonn, INRES - Chemical Signalling, Bonn, Germany
[2]University of Rostock, Plant Physiology Department, Rostock, Germany
[3]Heidelberg University, Centre for Organismal Studies, Heidelberg, Germany

*__Correspondence__: andreas.meyer@uni-bonn.de

Short title: LIP1 releases sulfide from Fe–S clusters

Abstract

Iron–sulfur (Fe–S) cluster are vital cofactors in all domains of life. Mitochondrial Fe–S cluster assembly occurs in two major steps to first build [2Fe–2S] clusters and subsequently assemble these into [4Fe–4S] clusters. The two assembly machineries are interconnected by glutaredoxin S15 (GRXS15) that transfers [2Fe–2S] clusters to the second machinery. Diminished cluster transfer activity of GRXS15 in Arabidopsis mitochondria causes specific defects associated with lipoyl synthase (LIP1) activity. Conversely, overexpression of *LIP1* in wild-type plants causes the release of toxic amounts of sulfide that can be detoxified by increasing the capacity for sulfide fixation through overexpression of *O*-acetylserine-(thiol)-lyase. The release of sulfide by lipoyl synthase causes a disturbance of mitochondrial sulfide homeostasis resulting in distinct and readily observable macroscopic phenotypes. These phenotypes enable a direct readout of consequences resulting from defects in Fe–S cluster assembly or targeted modulation of Fe–S cluster flux in mitochondria.

Introduction

Multiple essential mitochondrial proteins depend on iron–sulfur (Fe–S) clusters as cofactors to enable electron transfer reactions or catalytic activities (Przybyla-Toscano *et al.*, 2020). Assembly of Fe–S clusters occurs in two major steps with the initial synthesis of [2Fe–2S] clusters by a first machinery followed by a subsequent assembly into [4Fe–4S] clusters by a second machinery (Balk and Schaedler, 2014; Pedroletti *et al.*, 2023). Glutaredoxin S15 (GRXS15) has been identified as an essential transfer chaperone for [2Fe–2S] clusters to the [4Fe–4S] cluster assembly machinery in *Arabidopsis thaliana* (Arabidopsis) (Moseler *et al.*, 2015; Azam *et al.*, 2020; Trnka *et al.*, 2020). Complementation of embryo-lethal null mutants with weak mutant alleles and severe knockdown of *GRXS15* both lead to dwarfism and defects in mitochondrial protein lipoylation (Moseler *et al.*, 2015; Ströher *et al.*, 2016; Moseler *et al.*, 2021). Similarly, mutants with severely diminished levels of the [4Fe–4S] cluster carriers NifU-like4 (NFU4) and NifU-like5 (NFU5) cause an impairment of mitochondrial glycine decarboxylase (GDC) activity, which also points at dysfunction of lipoyl synthase (LIP1) (Przybyla-Toscano *et al.*, 2022). While diminished LIP1 activity in *nfu* mutants may be explained with the specificity of NFUs for cluster transfer to LIP1 (Przybyla-Toscano *et al.*, 2022), it is less obvious why a bottleneck upstream of the [4Fe–4S] assembly machinery at GRXS15 should have similar specific metabolic consequences in protein lipoylation rather than broader effects at multiple mitochondrial Fe–S proteins.

Protein lipoylation in mitochondria occurs on subunits of four multiprotein complexes, including GDC, pyruvate dehydrogenase (PDC), 2-oxoglutarate dehydrogenase (OGDC), and branched-chain α-keto acid dehydrogenase (BCKDC) (Douce *et al.*, 2001; Solmonson and DeBerardinis, 2018). Defects in protein lipoylation consequently affect all four complexes and result in a characteristic alteration of metabolic signatures in the respective mutants (Fu *et al.*, 2020; Lill and Freibert, 2020; Moseler *et al.*, 2021; Przybyla-Toscano *et al.*, 2022). The highly conserved LIP1 belongs to the family of radical *S*-adenosylmethionine (SAM) enzymes, which all contain a [4Fe–4S] cluster and catalyse formation of a 5′-deoxyadenosyl radical to target largely inert substrates for hydrogen abstraction. LIP1 carries an additional ‘auxiliary’ [4Fe–4S] cluster that provides the two sulfur atoms required for synthesis of lipoic acid (LA) (McLaughlin *et al.*, 2016; McCarthy and Booker, 2017). In mitochondria of Arabidopsis suspension culture cells, LIP1 is very lowly abundant with only 85 copies per mitochondrion (Fuchs *et al.*, 2020). Nevertheless, it has been proposed that LIP1 may be a major sink for [4Fe–4S] clusters if one cluster is sacrificed in each catalytic cycle (Pedroletti *et al.*, 2023). The fate of the fragmentary cluster after abstraction of two sulfur atoms is unknown and it possibly falls apart, releasing ferrous iron and sulfide.

Free sulfide, which under alkaline conditions is predominantly present as hydrosulfide anion (HS^-), inhibits complex IV (cytochrome *c* oxidase, COX) of the mitochondrial electron transport chain (mETC) with IC_{50} values between 6.9 nM and 200 nM (Kabil and Banerjee, 2010; Birke *et al.*, 2012; Nicholls *et al.*, 2013; Domán *et al.*, 2023). To prevent inhibition of COX and a block in ATP synthesis, mitochondria require appropriate mechanisms for removal of sulfide. In fission yeast (*Schizosaccharomyces pombe*) and human mitochondria, sulfide is detoxified via sulfide quinone oxidoreductase (SQR), which channels electrons from sulfide directly into the mETC and transfers the resulting sulfane (S^0) sulfur to reduced glutathione (GSH) to generate *S*-sulfanylglutathione (Theissen *et al.*, 2003; Vitvitsky *et al.*, 2021; Zhang *et al.*, 2021). Plants do not have SQR but contain a mitochondrial cysteine synthase complex (CSC) consisting of serine acetyltransferase2;2 (SERAT2;2) and *O*-acetylserine (thiol) lyase C (OAS-TL C) to fix sulfide (Heeg *et al.*, 2008; Watanabe *et al.*, 2008). Because cysteine biosynthesis in plants is assumed to be largely confined to chloroplasts and cytosol rather than mitochondria (Krüger *et al.*, 2009; Takahashi *et al.*, 2011) and because OAS-TL C in mitochondria accounts for only 5 % of the total OAS-TL activity, the role for mitochondrial cysteine biosynthesis has remained enigmatic (Birke *et al.*, 2012).

Here, we investigated the distribution of [4Fe–4S] clusters between different apoproteins in plant mitochondria and the question why diminished transfer of [2Fe–2S] clusters by GRXS15 specifically results in deficient protein lipoylation. We hypothesized that LIP1, despite its very low abundance, is effectively a large sink for [4Fe–4S] clusters, because it sacrifices a cluster in each catalytic cycle. We further proposed that sulfide release from cluster disintegration creates the primary demand for cysteine biosynthesis in mitochondria. To test these hypotheses, we exploited different mutants affected in GRXS15-mediated [2Fe–2S] transfer, altered the [4Fe–4S] distribution by modifying the abundance of different apoproteins, and investigated the respective metabolic effects. The model for sulfide release by LIP1 and the essential role of cysteine biosynthesis in the matrix was validated genetically and by physiological characterization of the engineered plants.

Results

Diminished capacity of GRXS15 for iron–sulfur cluster transfer causes a partial photorespiratory phenotype

To dissect the consequence of GRXS15 deficiencies, we first compiled a collection of *grxs15* mutants with different abundance and activity of GRXS15 that had been described earlier (Moseler *et al.*, 2015; Ströher *et al.*, 2016; Moseler *et al.*, 2021). The T-DNA insertion mutant *grxs15-1* and the artificial microRNA interference mutant *amiR* are knockdown lines with residual GRXS15 while *K83A #3* and *#4* are *grxs15* null mutants that were complemented with

a GRXS15 variant (K83A) compromised in its ability to coordinate the [2Fe–2S] cluster. Severity of the phenotype in *K83A #3* and *#4* inversely correlates with the expression levels of the complementation construct, which is highest in the least severe mutant *#3* (Moseler *et al.*, 2015). Generally, the complementation lines *K83A #3* and *#4* are more severely affected than the knockdown lines (Supplemental Figure S1).

In *amiR*, *K83A #3* and *#4*, compromised lipoylation of mitochondrial proteins results in accumulation of substrates of the four lipoyl-dependent dehydrogenase enzyme complexes, pyruvate, 2-oxoglutarate (2-OG), glycine and branched-chain α-keto acids (BCKAs) (Ströher *et al.*, 2016; Moseler *et al.*, 2021). Because glycine decarboxylation by GDC is an essential step in photorespiration (Douce *et al.*, 2001; Bauwe, 2023) (Figure 1A), we reasoned that the severe dwarf phenotype of *grxs15* mutants may be interpreted, at least to some extent, as a photorespiratory phenotype. To test this hypothesis, we initially grew the *grxs15* mutants under elevated CO_2 to suppress photorespiration.

Growth in 5,000 ppm CO_2 partially rescued the dwarf phenotype of the most severe *grxs15* mutants *K83A #3* and *#4* compared to plants grown in ambient CO_2 of 390 ppm (Figure 1, B-D). Diminished RubisCO-mediated oxygenation of ribulose-1,5-bisphophate in plants exposed to high CO_2 consistently led to a decrease in glycine levels. While this effect is already evident in wild type (WT) plants, it is far more pronounced in *grxs15* mutants, which all accumulate glycine 2 to 4-fold with respect to the WT under ambient conditions. High CO_2 levels caused glycine to drop to levels comparable to the glycine content in WT plants (Figure 1E). Although serine was also slightly increased in most mutant lines (Figure 1F), the increase in glycine was more pronounced and, thus, consistently led to an increase in the glycine-to-serine ratio, which serves as a measure of impaired GDC activity. Interestingly, a significant decrease in serine was observed in *K83A* mutants grown in high CO_2 (Figure 1F). This may suggest that especially in rosette leaves other pathways in different compartments contribute to serine biosynthesis (Ros *et al.*, 2014; Anoman *et al.*, 2019). *K83A* mutants also showed increased levels of the photorespiratory intermediates glyoxylate and glycerate in normal air, which was more pronounced in the most severe *K83A #4* mutant. At least in the *K83A* mutants high CO_2 caused a decrease of these metabolites (Supplemental Figure S2). The respective changes may at least in part explain the severe growth phenotypes. Pyruvate and 2-OG that had been found increased in young *K83A* seedlings (Moseler *et al.*, 2021) were barely altered in rosette leaves and not significantly affected by high CO_2 (Figure 1, G and H).

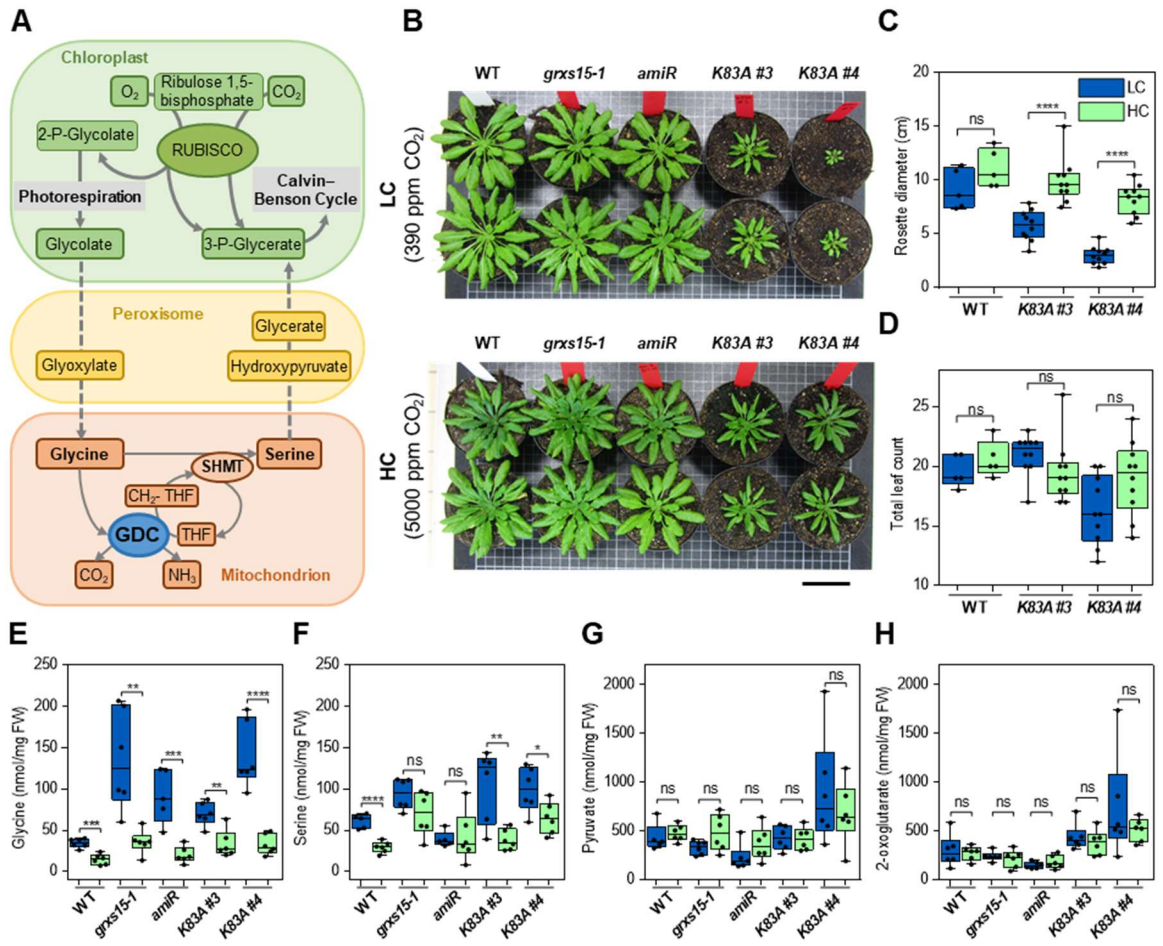

Figure 1 Suppression of the photorespiratory flux enables partial recovery of dwarf *grxs15* mutants. A, Schematic representation of the photorespiratory pathway highlighting the key role of glycine decarboxylase (GDC). For simplicity, the scheme does not indicate the correct stoichiometry. B, Phenotypes of two representative 8-week-old wild type (WT) and *grxs15* mutant plants grown in low CO_2 (LC, shown in blue) and high CO_2 (HC, shown in green), respectively, under a 12h/12h day/night regime. Scale bar: 5 cm. C, D, Rosette diameter and total leaf counts of WT and the *K83A* mutants grown in LC or HC (n = 5-10). E-H, Effect of atmospheric CO_2 on the abundance of glycine, serine, pyruvate and 2-oxoglutarate in leaves of 8-week-old WT and *grxs15* mutant plants (n = 5-6). All box plots show the median as centre line with the box for the first to the third quartile and whiskers indicating min and max values of the whole data set. Asterisks represent significant differences (*=$P \leq 0.1$, **= $P \leq 0.01$, ***= $P \leq 0.001$, ****= $P \leq 0.0001$, ns: not significant) calculated according to Student's *t*-test (α = 0.05). *P*-values: Supplemental Data Set 1.

Deletion of the highly abundant ACO3 suppresses the dwarf phenotype of mutants with diminished GRXS15 capacity

Lipoyl synthase, which catalyses the last step in the lipoylation pathway, is a low-abundant mitochondrial protein. Based on the low copy number of only 85 LIP1 proteins per mitochondrion versus more than 10,000 for the [4Fe–4S] cluster proteins aconitase 2 and 3 (ACO2 and ACO3) (Fuchs *et al.*, 2020), we reasoned that LIP1 may not be supplied with sufficient [4Fe–4S] clusters if a bottleneck occurs in the upstream supply chain. In *grxs15* mutants, expression of *ACO2* and *ACO3* were increased up to 2.7-fold and 4-fold, respectively,

while expression levels of *LIP1* did not change (Supplemental Figure S3). Even if changes in expression levels would only partially correlate with changes in protein abundance, it is likely that this transcriptional activation further shifts the ACO3/LIP1 abundance imbalance towards ACO3 in *grxs15* mutants. More ACO3 and the respective need for [4Fe–4S] would most likely render LIP1 even less competitive for receiving sufficient clusters to attain catalytic activity. This situation likely aggravates if the auxiliary [4Fe–4S] cluster gets sacrificed for supply of two sulfhydryl groups to an octanoyl residue in each catalytic cycle similar to the mechanism of the bacterial homologue of LIP1, LipA (McCarthy and Booker, 2017). Therefore, we hypothesized that alterations in demand for [4Fe–4S] clusters through modulation of apoprotein abundance may allow to redirect the flux of [4Fe–4S] clusters towards LIP1. Because *aco3* null mutants show only a mild growth impairment compared to WT plants (Figure 2, A and B), and because ACO3 is more abundant than ACO2 (Moeder *et al.*, 2007; Fuchs *et al.*, 2020), we selected the *aco3* mutant for crossing with different *grxs15* mutants (Supplemental Figure S4).

Interestingly, loss of *ACO3* in all cases partially suppressed the dwarf phenotypes of *amiR*, *K83A #3* and *#4*, especially at later developmental stages (Figure 2, A and B and Supplemental Figure S5). In both, *amiR* and *K83A #3,* loss of *ACO3* ultimately led to phenotypes similar to *aco3*. For the *amiR aco3* double mutant the root length was already 7.3-fold longer (*amiR aco3* 3.9 ± 0.07 cm versus *amiR* 0.53 ± 0.02 cm; Supplemental Figure 5, A and B) and the rosette of 4-week-old plants were twice as large as in the original *amiR* single mutant (*amiR aco3* 60.0 ± 3.8 cm^2 versus *amiR* 26.3 ± 3.5 cm^2; Figure 2, A and B). Ten days after germination, the cross of *K83A #3* and *aco3* (for simplicity hereafter called *#3 aco3*) showed only a tendency for increased root length compared to the *K83A #3* background, but after 17 days, the suppression of the short root phenotype was apparent (Supplemental Figure 5, A-C). When grown on soil for four weeks *#3 aco3* double mutant plants had an 18-fold larger rosette area than the original *K83A #3* mutant (*#3 aco3* 49.9 ± 8.8 cm^2 versus *K83A #3* 2.7 ± 1.1 cm^2; Figure 2, B and C). The growth-promoting effect of *ACO3* loss was also apparent in *#4 aco3*, although less pronounced than in *#3*, most likely because *#4* plants are generally more compromised than *#3* plants. While flower stalks of *K83A #3* and *#4* remained short compared to WT, inflorescence development in 8-week-old plants was at least partially rescued by the loss of *ACO3* (Supplemental Figure S5D).

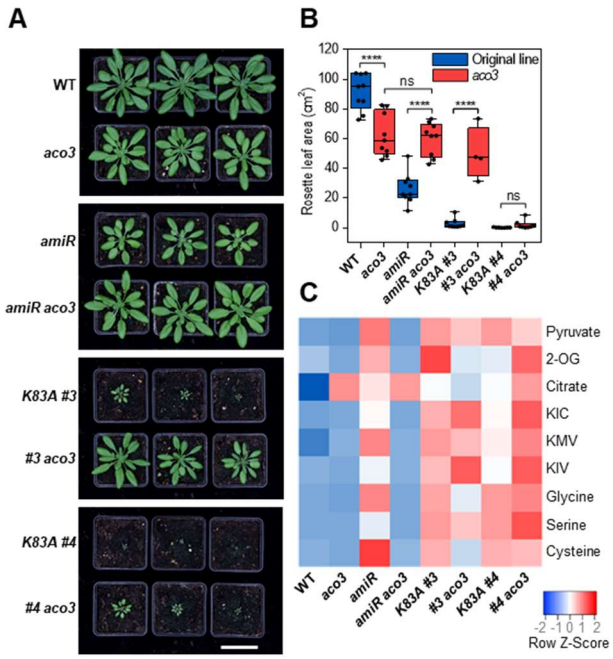

Figure 2 Loss of *ACO3* partially suppresses the dwarfism of *grxs15* mutants. A, 5-week-old plants grown on soil under long-day conditions. *aco3* and double homozygous crosses are compared with WT and the respective parental lines. Scale bar: 5 cm. B, Analysis of rosette leaf area of 4-week-old plants grown on soil (*n* = 4-9). The box plot shows the median as centre line with the box for the first to the third quartile and whiskers indicating min and max values of the whole data set. Asterisks represent significant differences (****= $P \leq 0.0001$, ns: not significant) calculated according to one-way ANOVA with Tukey's multiple comparisons test (α = 0.05). *P*-values: Supplemental Data Set 2. Data for WT and the different *grxs15* mutants are shown in blue, data for *aco3* and the respective crosses are shown in red. C, Heat map of key metabolites known to be associated with lipoyl cofactor-dependent enzymes. Metabolites were measured in 8-day-old seedlings (see Supplemental Figure S6 and Supplemental Data Set 2 for absolute values). Z-scores of the mean were calculated for each metabolite and are presented as a heat map. Decreased metabolites are depicted in blue and increased metabolites in red.

To further characterize the metabolic consequences of the combined decrease in GRXS15-based supply of [2Fe–2S] clusters and loss of *ACO3*, we analysed key metabolites that were all found to be increased in *grxs15* seedlings due to diminished LIP1 activity (Moseler *et al.*, 2021). Notably, accumulation of pyruvate, 2-OG, α-keto acids, and glycine in *amiR* was reverted to *aco3* levels in *amiR aco3* (Figure 2C and Supplemental Figure 6, A-G). Contrary to the expectation that GDC deficiency in *amiR* should cause a decrease in serine as a product of glycine decarboxylation, serine also increased when GRXS15 activity was diminished. Yet, the increased glycine-to-serine ratio consistently points at GDC deficiency, which normalized when *ACO3* was lost. This picture was less consistent in line *K83A #3 aco3*, which showed a decrease in glycine and 2-OG, but no change in pyruvate and the α-keto acids α-ketoisocaproic acid (KIC) and α-keto-β-methylvaleric acid (KMV). α-ketoisovaleric acid (KIV) was even further increased in *K83A #3 aco3*. *K83A #4 aco3* mutants showed an increase in all α-keto acids and 2-OG, but no pronounced change in pyruvate, glycine and serine. Compared to the WT, citrate was increased in *aco3* and all *grxs15* mutants but without any additive effect in double mutants

(Figure 2S and Supplemental Figure 6C). With multiple metabolic connections between different metabolites within one compartment or even across different compartments, it can be expected that a metabolic block in one specific enzyme may have rather pleiotropic consequences in several other metabolite pools. This is highlighted by an increase in cysteine in *grxs15* mutants, which trails the increase in the precursors glycine and serine, albeit at much lower concentrations (Figure 2C, Supplemental Figure S6, G-I). Loss of *ACO3* in *amiR* and *K83A #3* caused a decrease in cysteine. Only in the most severe mutant *K83A #4,* additional loss of *ACO3* did not bring down the levels of these three amino acids although the severe growth phenotype was already slightly suppressed (Figure 2, Supplemental Figure S6, G-I). Taken together, these results suggest that loss of the highly abundant [4Fe–4S] sink ACO3 enables redirection of [4Fe–4S] clusters to LIP1 to regain at least partial lipoylation activity in *grxs15* mutants indicated by readjustment of metabolite levels.

Overexpression of *LIP1* rescues severe *grxs15 K83A* mutants but is deleterious for the wild type and *grxs15* knockdown mutants

Having established experimental evidence for putative redirection of [4Fe–4S] clusters from ACO3 to LIP1 in *aco3* mutants, we next hypothesised that also overexpression of *LIP1* may render the respective sink more competitive over other apoproteins for a limited [4Fe–4S] pool. To test this hypothesis, we constructed overexpression vectors for *LIP1* driven by the CaMV 35S promoter (Figure 3A). To validate correct mitochondrial targeting, we added a C-terminal GFP (Figure 3, A and B; Supplemental Figure S7).

Consistent with our hypothesis, overexpression of *LIP1* largely suppressed dwarfism of *K83A #3* and *#4* in several independent lines. This effect was apparent at all developmental stages with significant increases in root length, rosette size, biomass and flower stalk height (Figure 3, C-E; Supplemental Figures S8-S10). In all independent lines, plants with the *K83A #4* background remained slightly smaller than *K83A #3*. Unexpectedly, however, *LIP1* overexpression had the opposite effect in the WT and the two knockdown mutants *grxs15-1* and *amiR*, where increased LIP1 abundance resulted in significantly reduced growth and delayed development. In these cases, the rosette area of 4-week-old plants was decreased by 70 % for the WT, 64 % in *grxs15-1* and 77 % in *amiR*, which was largely mirrored in the fresh weight of the respective rosettes (Figure 3, C-E). The rosette leaves in these plants showed a curly phenotype similar to other mutants with disturbed mitochondrial metabolism (Supplemental Figure S11; (Lee *et al.*, 2021)). Flower initiation in these mutants was delayed by one to two weeks and the inflorescences remained much shorter than in plants without overexpression of *LIP1* (Supplemental Figure S10C). Notably, parallel experiments in which

LIP1 was overexpressed without *GFP* led to similar results indicating that the GFP tag did not provoke any deleterious effect (Supplemental Figure S12).

To further substantiate either beneficial or deleterious effects of *LIP1* overexpression in different genetic backgrounds, we tested for LIP1 protein abundance with immunodetection in protein blots. Overexpression of *LIP1-GFP* in all lines caused high abundance of LIP1-GFP with the expected molecular mass of ~70 kDa (Figure 3F, Supplemental Figure S13A). In addition to the LIP1-GFP band, blots probed with α-LIP1 showed another band with an apparent molecular mass of ~45 kDa likely representing free LIP1, and a distinct band for free GFP when probed with α-GFP (Supplemental Figure S14). The absence of residual fluorescence in the cytosol (Supplemental Figure S7) strongly suggests that the cleavage of LIP1-GFP occurred during or after protein extraction. Although overexpression generally resulted in high abundance of LIP1, some differences in protein levels were apparent. Notably, the LIP1-GFP band at ~70 kDa was most intense for *amiR* and *K83A #4* but far less intense for *K83A #3*. The lipoylation pattern detected by probing the protein blots with an LA-specific antibody did not change for E2 subunits of PDC and OGDC. Contrary to our expectation, for H1 and H3 subunits of GDC, a slight decrease in lipoylation was found in WT and *grxs15-1* after *LIP1* expression. For H2 in these lines, the decrease was even more pronounced. However, an increased protein lipoylation was observed for the H2 subunit of GDC at least in *amiR* and *K83A #3* overexpressing *LIP1-GFP* (Figure 3F; Supplemental Figure S13). In mitochondria isolated from WT and *grxs15-1* overexpressing *LIP1-GFP*, this was not observed, but it should be noted that the amount of H2 was already diminished in these severely compromised dwarf mutants.

Overexpression of *LIP1* affected the metabolite signature with pronounced decreases of the key metabolites pyruvate, 2-OG and all three BCKAs that generally accumulated in *grxs15* seedlings (Figure 3G and Supplemental Figure S15). For glycine and serine, the picture was less uniform with glycine being increased in WT and *grxs15-1* seedlings overexpressing *LIP1*, but only minor or no changes in the more severe *grxs15* mutants, which all had increased glycine levels without additional LIP1 (Figure 3G and Supplemental Figure S15G). Serine was increased after *LIP1* overexpression in WT and all *grxs15* mutants. Interestingly, all lines except *K83A #4* overexpressing *LIP1* showed an increase in cysteine of 60-100 % compared to control plants (Supplemental Figure S15H). Accumulation of glycine and serine was also found in rosette leaves of soil-grown plants with diminished GRXS15 activity (Figure 1, E and F; Supplemental Figure S16). In these older plants, *LIP1* overexpression caused an increase in glycine and serine, which was largely abolished in high CO_2. This result suggests that photorespiration was the main source of the increase in glycine, serine and potentially cysteine rather than the overexpression of *LIP1* itself. Different from the positive effect of high CO_2 on the *K83A* mutants (Figure 1B), the same mutants rescued by *LIP1* overexpression did not

show further growth improvement as seen before but rather a decrease in biomass (Supplemental Figure S16A).

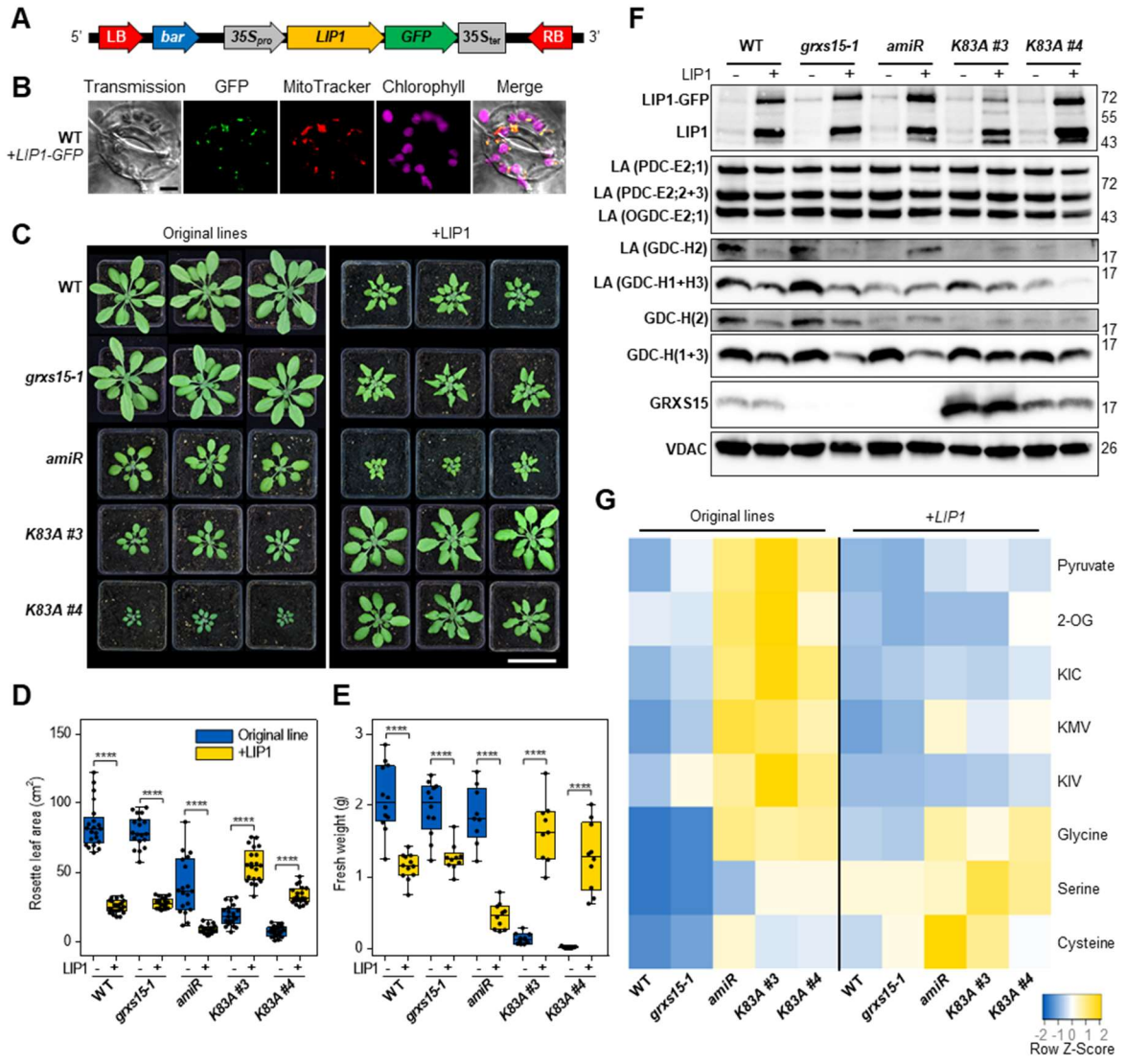

Figure 3 Overexpression of *LIP1* is deleterious for wild type plants and *grxs15* knock-down mutants but beneficial for the *K83A* mutants. A, Schematic representation of the construct used for overexpression of *LIP1*. The expressed protein has GFP fused at its C-terminus. B, Confocal microscopy images of guard cells from 7-day-old wild type seedlings stably expressing *LIP1-GFP*. Fluorescence images were collected with the following wavelength settings: GFP (λ_{ex} = 488 nm; λ_{em} = 520 nm), MitoTracker Orange (λ_{ex} = 543 nm; λ_{em} = 597 nm), chlorophyll autofluorescence (λ_{ex} = 633 nm; λ_{em} = 675 nm). The merge image shows the overlap of all four individual channels. Scale bar = 5 µm. C, 5-week-old plants grown on soil in long-day conditions. Subpanels on the left show the original lines, with their respective genetic background. Subpanels on the right show the same lines overexpressing *LIP1-GFP*. Scale bar: 5 cm. D, Rosette leaf area analysis of 4-week-old plants (n = 21). E, Shoot fresh weight of 7-week-old plants (n = 9-12). All box plots show the median as centre line with the box for the first to the third quartile and whiskers indicating min and max values of the whole data set. Asterisks represent significant differences (****= $P \leq 0.0001$) calculated according to one-way ANOVA with Tukey's multiple comparisons test (α = 0.05). *P*-values: Supplemental Data Set 3. Data for WT and the different *grxs15* mutants are shown in blue, data for the respective lines overexpressing *LIP1* are shown in yellow. F, Protein gel blot analysis with primary antibodies raised against LIP1, GRXS15, LA, GDC-H, and VDAC for loading control. Mitochondria were isolated from seedlings grown in hydroponic culture or from leaves of plants grown on soil and 15-20 µg protein loaded per lane. A blot with extended exposure for the detection of GRXS15 indicates some residual amounts of GRXS15 in *grxs15-1* and *amiR* (Supplemental Figure S1). G, Heat map of metabolites known to be substrates of LA-dependent enzymes or in case of serine and cysteine

are derivatives of glycine. Metabolites were extracted from 8-day-old seedlings (for absolute values see Supplemental Figure S15 and Supplemental Data Set 3). Z-scores of the mean were calculated for each metabolite and are presented as a heat map, with decreased metabolites coded in blue and increased metabolites depicted in yellow.

LIP1 causes a dose-dependent phenotypic response and induction of AOX

Next, we wondered why in addition to reduced GDC-H lipoylation overexpression of *LIP1* is deleterious for the WT and for plants with diminished abundance of wild type GRXS15, i.e. *grxs15-1* and *amiR*. While searching for plants with homozygous *LIP1* overexpression in the WT background it became apparent that severity of the phenotype depends on the zygosity with homozygous plants being most severely affected (Figure 4, A-C; Supplemental Figure S17). The zygosity-dependent negative gene dosage effect was also seen in the other *grxs15* mutants (Supplemental Figure S18).

Based on *in vitro* studies with bacterial LipA, it has been suggested that lipoylation activity sacrifices the auxiliary [4Fe–4S] cluster to provide sulfur atoms required for lipoic acid biosynthesis (McCarthy and Booker, 2017). We therefore hypothesised that increased LIP1 activity leads to consumption of more [4Fe–4S] clusters for abstraction of sulfur atoms and that the remains of these clusters fall apart with the inevitable release of sulfide. Inhibition of COX by sulfide would then lead to increased expression and activity of alternative oxidase (AOX) as an overflow valve for electrons in the mETC (Figure 4D; (Selinski *et al.*, 2018)). Consistent with this hypothesis, the COX inhibitor potassium cyanide (KCN) largely blocked respiration in wild type roots but far less in roots from WT overexpressing *LIP1* (Figure 4E). Conversely, *LIP1* overexpression in WT plants resulted in KCN-insensitivity but more pronounced inhibition of respiration when propyl gallate (pGal) as an inhibitor of AOX was applied (Figure 4E; Supplemental Figure S19). The basic respiration of WT plants overexpressing *LIP1* was consistently higher than the respiration of non-transformed plants (Supplemental Figure S19C). Interestingly, respiration of roots from *K83A #3* plants overexpressing *LIP1* decreased significantly in the presence of KCN. With this, the sensitivity of the mETC in *K83A #3* with LIP1 to respiratory inhibitors was more similar to the WT than to WT plus LIP1, which suggests that the *K83A* mutation generates a major bottleneck for Fe–S cluster supply (Figure 4E; Supplemental Figure S19).

Changes in electron flow after *LIP1* overexpression caused a pronounced increase in AOX protein levels in WT plants and the two knockdown mutants *grxs15-1* and *amiR* overexpressing *LIP1* (Figure 4F; Supplemental Figure S20). In the two *K83A* mutants that were largely (*#3*) or partially (*#4*) rescued by LIP1, AOX was still increased but far less abundant than in the two knockdown lines. The relative abundance of AOX in mature leaves of the two *K83A* mutants with higher levels in *#4* plants matches with the degree of growth retardation, which is also more severe in *#4* than in *#3* (Supplemental Figure S20A; Figure 3C).

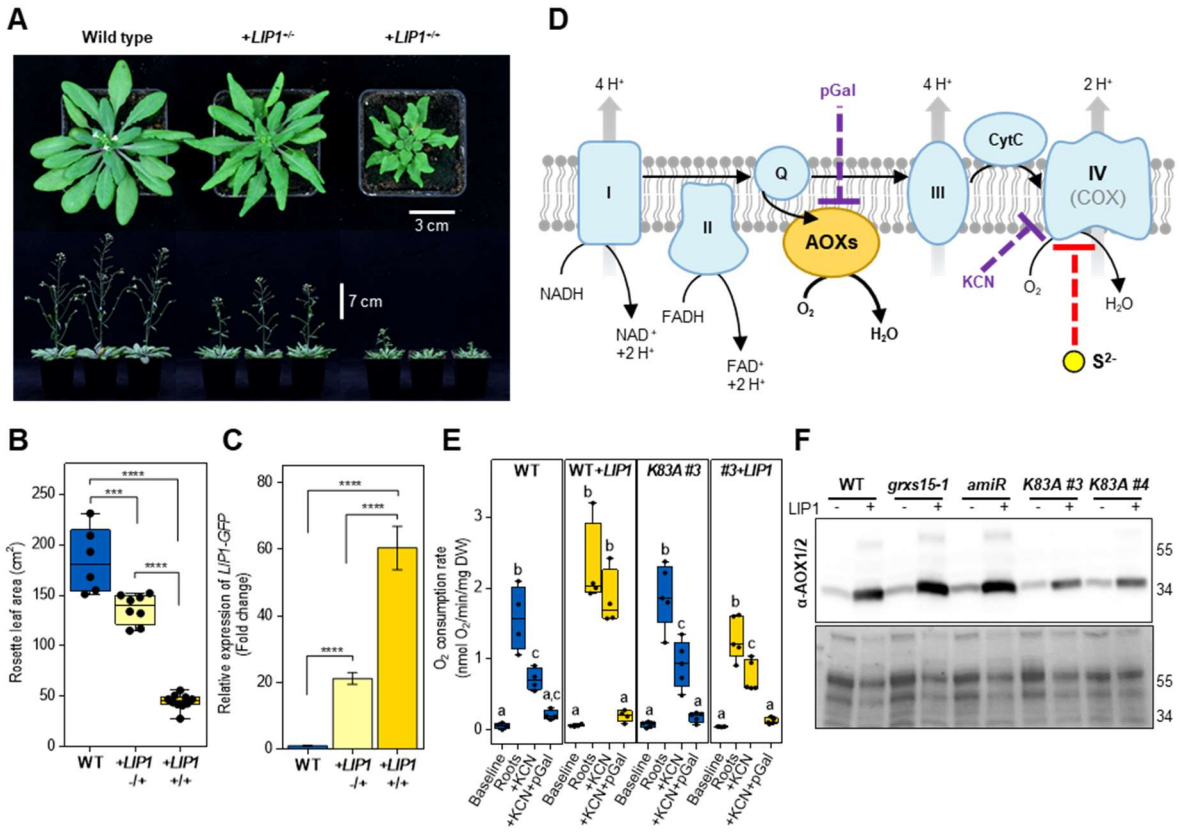

Figure 4 Excessive LIP1 activity causes inhibition of cytochrome *c* oxidase. A, Representative picture of 6- (top row) and 7-week-old (bottom row) wild type plants overexpressing *LIP1-GFP* in hemizygous (+/-) and homozygous (+/+) form. B, Analysis of rosette area of 4-week-old plants grown on soil in long-day conditions (*n* = 6-8). C, Relative expression level of *LIP1* determined by qRT-PCR. RNA was isolated from 8-day-old seedlings. The presented data are means ± SEM (*n* = 3). The box plot shows the median as centre line with the box for the first to the third quartile and whiskers indicating min and max values of the whole data set. Asterisks represent significant differences (***= $P \leq 0.001$, ****= $P \leq 0.0001$) according to one-way ANOVA with Tukey's multiple comparisons test (α = 0.05). *P*-values: Supplemental Data Set 4. Data for WT and the different *grxs15* mutants are shown in blue, data for the respective lines overexpressing *LIP1* are shown in yellow. D, Scheme of the mitochondrial electron transport chain where alternative oxidases (AOXs) (in yellow) act as terminal electron acceptors when the cytochrome *c* oxidase (COX) is inhibited by sulfide (S^{2-}) (dashed red line). Inhibition of COX by potassium cyanide (KCN) and AOX by propyl gallate (pGal) is indicated by dashed purple lines. E, Respiration of roots of 16-day-old seedlings grown on ½ MS vertical agar plates. After recording the basal root respiration without inhibitors (roots only), COX was first inhibited by addition of KCN at a final concentration of 4 mM. Subsequently, AOXs were inhibited by addition of pGal at a final concentration of 200 µM (*n* = 4-5). Different letters indicate significant differences between treatments calculated according to one-way ANOVA with Tukey's multiple comparisons test separately for each line (α = 0.05). *P*-values: Supplemental Data Set 4. F, Protein gel blot analysis with primary antibodies raised against AOXs (detects all isoforms: AOX1a-AOX1d and AOX2). Mitochondria were isolated from 16-day-old seedlings grown in hydroponic culture and 15 µg protein loaded per lane. The Amido Black stained membrane at the bottom serves as loading control.

Mitochondrial cysteine biosynthesis in Arabidopsis keeps sulfide released by LIP1 under control

To prevent poisoning of COX by sulfide, evolution exploited two mechanisms for conversion of sulfide to largely innocuous products. Animal cells and most fungi oxidise sulfide by the inner mitochondrial membrane protein SQR, while plants can use sulfide in the mitochondrial matrix for cysteine production by OAS-TL C (Theissen *et al.*, 2003; Birke *et al.*, 2012; Vitvitsky *et al.*, 2021). To assess whether the increased mitochondrial sulfide load in *LIP1* overexpression lines can be countered by increasing the endogenous mitochondrial scavenging capacity for sulfide, we additionally overexpressed *OAS-TL C* (Figure 5A). Consistent with the hypothesis that overexpressed *LIP1* releases toxic amounts of sulfide that exceed the endogenous detoxification capacity, we observed at least partial recovery of the dwarf phenotype observed in *LIP1* overexpressors with more than a 2-fold increment in rosette area (Figure 5, B and C). Moreover, the respiration of WT plants overexpressing both *LIP1* and *OAS-TL C* showed again increased sensitivity to KCN, indicating that the inhibition of COX by sulfide originating from *LIP1* was partially rescued by overexpression of *OAS-TL C* (Figure 5D). Overexpression of *OAS-TL C* itself did not exhibit any harmful effect on the WT (Figure 5, B and D).

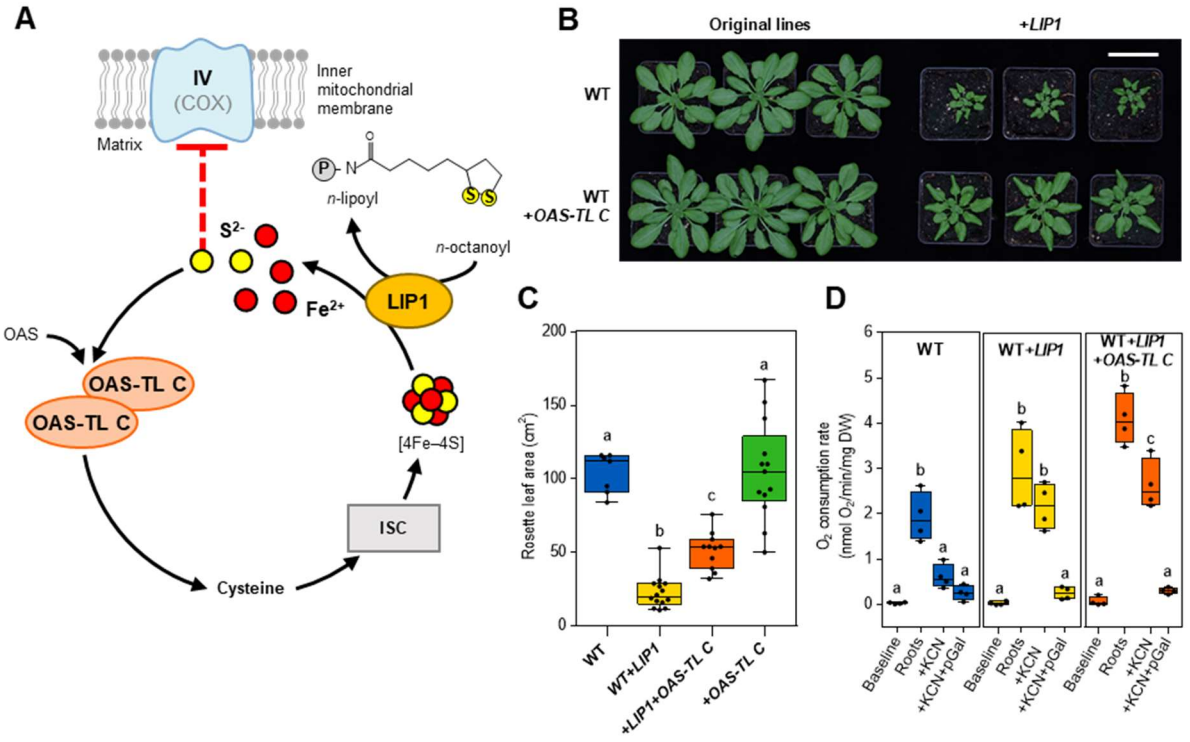

Figure 5 Overexpression of *OAS-TL C* suppresses sulfide toxicity resulting from *LIP1* overexpression. A, Hypothetic model for the lipoylation reaction with concomitant sulfide release and its subsequent refixation by OAS-TL C. Cysteine provides the mitochondrial iron–sulfur cluster (ISC) assembly machinery with the required sulfur. LIP1 sacrifices a [4Fe–4S] cluster and releases sulfide that needs to be detoxified to avoid poisoning of COX. B, Representative photos of 5-week-old plants grown on soil in long-day conditions. Plants overexpressing *LIP1-GFP* (right) are compared with their respective genetic background (left). Scale bar: 5 cm. C, Rosette area analysis of 4-week-old plants overexpressing

LIP1 or *LIP1* plus *OAS-TL C* compared with the WT (*n* = 7-14). D, Respiration of roots of 16-day-old seedlings grown on ½ MS vertical agar plates. After recording the basal root respiration without inhibitors ('Roots'), COX was first inhibited by addition of KCN at a final concentration of 4 mM. Subsequently, AOXs were inhibited by addition of pGal at a final concentration of 200 µM (*n* = 4). All box plots show the median as centre line with the box for the first to the third quartile and whiskers indicating min and max values of the whole data set. Different letters indicate significant differences between treatments calculated according to one-way ANOVA with Tukey's multiple comparisons test separately for each line (α = 0.05). *P*-values: Supplemental Data Set 5.

Discussion

Lipoylation is a rare, but yet essential posttranslational lysine modification that is evolutionarily conserved from bacteria to humans (Rowland *et al.*, 2018). Defects in lipoylation reactions thus cause severe metabolic disorders or even lethality in plants, yeast and mammals (Sulo and Martin, 1993; Yi and Maeda, 2005; Navarro-Sastre *et al.*, 2011; Tort *et al.*, 2013; Mayr *et al.*, 2014; Bauwe, 2023). In plants, deficiencies in Fe–S cluster supply become most apparent from defects in GDC and the concomitant increase in glycine and the glycine-to-serine ratio (Przybyla-Toscano *et al.*, 2022). This increase in glycine can be prevented if the metabolic demand on GDC is minimized by suppressing photorespiration in a high CO_2 atmosphere (Przybyla-Toscano *et al.*, 2022). The same physiological response occurs also in mutants with severe deficiencies in GRXS15-dependent [2Fe–2S] cluster transfer between the two Fe–S cluster assembly machineries (Figure 1; Figure 6). Without any external input, the lipoylation-deficient phenotype can also be suppressed by altering the distribution of [4Fe–4S] clusters between the highly abundant ACO3 and the very low abundant LIP1 (Figure 2; Figure 3C). Under normal growth conditions, loss of *ACO3* does not severely compromise the plant because mitochondria also contain ACO2 to serve in the TCA cycle (Hooks *et al.*, 2014). Losing ACO3 as an [4Fe–4S] apoprotein makes more clusters available for LIP1 and thus enables increased LIP1 activity even in severe *grxs15* mutants. As an orthogonal approach, also *LIP1* overexpression rescued the most severely compromised *grxs15* mutants carrying a K83A variant of GRXS15 (Figure 3C). All these results consistently show that LIP1 requires sufficient [4Fe–4S] cluster supply to attain full lipoylation activity. Previously, it was considered that GRXS15 might also be involved in repair of Fe–S clusters or have an oxidoreductase function (Couturier *et al.*, 2015; Zhang *et al.*, 2018). Our data, however, show that at least in severely compromised *grxs15* mutants, cluster supply rather than any other putative function of GRXS15 is the limiting factor for plant performance.

Wild-type plants and mutants less compromised in [2Fe–2S] cluster transfer, however, showed a very different response to *LIP1* overexpression (Figure 3C). The very low abundance of endogenous GRXS15 in *grxs15-1* and *amiR* plants caused a partial photorespiratory phenotype identified by increased glycine-to-serine ratios already. Apparently, however, the capacity for [2Fe–2S] cluster transfer is still sufficient to enable a minimum [4Fe–4S] cluster

supply to LIP1 to avoid accumulation of more toxic photorespiratory intermediates upstream of glycine (Timm *et al.*, 2008; Dellero *et al.*, 2016). Overexpression of *LIP1* in these mutants and in the WT allows for efficient redirection of more [4Fe–4S] clusters to LIP1, which became most apparent by the reversion of the photorespiratory metabolite signature in the *grxs15* knockdown mutants. Yet, increased *LIP1* levels in these plants surprisingly turned out to be deleterious. Dependence of this phenotype on LIP1 is also supported by a gene-dosage-dependent increase in severity in hemizygous and homozygous *LIP1* overexpressors. Apparently, increased abundance of LIP1 can attract more [4Fe–4S] clusters than what would normally be necessary to maintain physiological needs, which ultimately causes toxic side effects (Figure 6).

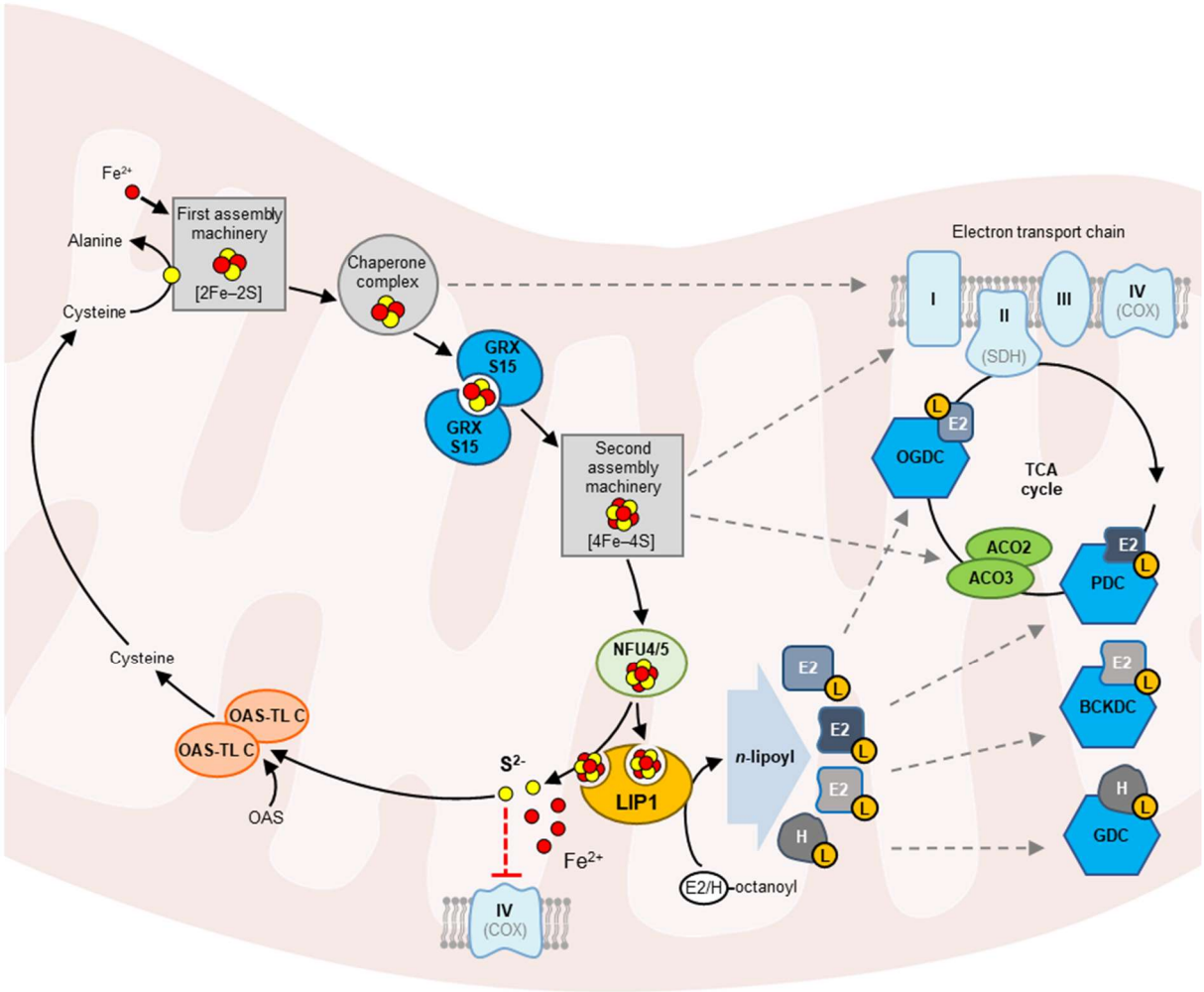

Figure 6 Working model of iron–sulfur cluster assembly and transfer machineries in plant mitochondria, with LIP1 as an Fe–S cluster consuming enzyme. On the top left, a simplification of the first assembly machinery, which utilises cysteine as sulfur source (yellow circles) and iron (red circles) to build [2Fe–2S] clusters, is depicted. After assembly, a chaperone complex acts as a hub for further direct or indirect delivery of [2Fe–2S] clusters to target proteins such subunits of complexes I, II and III in the mitochondrial electron transport chain (ETC) (dashed arrow) and to glutaredoxin S15 (GRXS15). GRXS15 is the key enzyme for transfer of [2Fe–2S] clusters from the first assembly machinery to the second, where [4Fe–4S] clusters are being built. These are then distributed to target proteins, such as ETC complexes, aconitases 2 and 3 (ACO2/3) and lipoyl synthase (LIP1). Delivery of [4Fe–4S] to LIP1 relies on the NifU-like proteins NFU4/5. LIP1 requires one [4Fe–4S] cluster for its catalytic activity and uses a second, auxiliary, cluster as sulfur source to synthesise the lipoyl cofactor, which is necessary

for the activity of four mitochondrial dehydrogenase complexes glycine decarboxylase (GDC), pyruvate dehydrogenase (PDC), 2-oxoglutarate dehydrogenase (OGDC), and branched-chain α-keto acid dehydrogenase (BCKDC). LIP1 transfers two sulfur atoms from the auxiliary cluster to the *n*-octanoyl residue on the dehydrogenase subunits E2 or H to convert these into *n*-lipoyl prosthetic groups (L). In the absence of any established repair mechanism, the remnants of the cluster are assumed to disintegrate and release sulfide. Similarly, entire auxiliary clusters may fall apart if they are not used immediately, *e.g.*, in case of substrate shortage for LIP1 or increased LIP1 abundance. To prevent poisoning of cytochrome *c* oxidase (COX, complex IV), the toxic sulfide is utilised by *O*-acetylserine-(thiol)-lyase C (OAS-TL C) to synthesise cysteine, which can be reused for a new round of Fe–S cluster assembly.

Based on *in vitro* experiments with recombinant LipA from *E. coli* and human LIAS (both homologs of Arabidopsis LIP1), it was reported that the enzymes in the presence of NFUs can potentially direct all four sulfide ions from the auxiliary cluster into the lipoyl product rather than releasing two of them into solution (McCarthy and Booker, 2017; Warui *et al.*, 2022). Yet, if only a single catalytic cycle is possible because NFU is missing, only two sulfur atoms are extracted from a [4Fe–4S] cluster while the residuals fall apart and release the remaining two sulfides. Detection of sulfide is a major challenge as all current techniques have severe disadvantages and limitations (Kolluru *et al.*, 2013). This applies even more when specific measurements of the sulfide pool in the mitochondrial matrix are to be conducted. Here, we thus indirectly deduce that overexpression of *LIP1* goes along with a pronounced increase in free sulfide. First, COX was strongly inhibited in *LIP1* overexpression plants. With an IC_{50} as low as 6.9 nM (Birke *et al.*, 2012) already a minor increase in sulfide would cause inhibition of COX (Figure 4). This inhibition, possibly in combination with reductive stress imposed by sulfide, triggers a retrograde signal leading to induction of AOX (Fuchs *et al.*, 2020). Increased AOX may compensate for loss of COX activity by offering an alternative route for transfer of electrons to molecular oxygen to avoid overreduction of the ubiquinone pool and concomitant production of reactive oxygen species in the mETC (Millar *et al.*, 2011; Selinski *et al.*, 2018). The predominant isoform AOX1a has been shown to be involved in dissipating thiol-mediated reductive stress (Fuchs *et al.*, 2022). Whether the sulfide released by LIP1 accumulates to sufficient levels for generation of reductive stress remains unknown at this stage. The increased respiration observed under these circumstances in detached Arabidopsis roots is likely an attempt of plants to provide sufficient energy in form of ATP even with a truncated mETC. Because this necessarily goes along with an increased carbon turnover, the block of respiration by sulfide has severe bioenergetic consequences and ultimately causes growth retardation (Birke *et al.*, 2012).

The second piece of evidence for release of sulfide by LIP1 in Arabidopsis results from suppression of the retarded phenotype by overexpressing *OAS-TL C* (Figure 5B). To prevent accumulation of sulfide in the matrix, plants contain local cysteine biosynthesis capacity in mitochondria (Haas *et al.*, 2008; Heeg *et al.*, 2008; Álvarez *et al.*, 2012b). Overexpression of

OAS-TL C suppresses the dwarf phenotype of WT plants overexpressing *LIP1*. Taken together, all these results support the conclusion that [4Fe–4S] clusters inserted in LIP1 collapse and release poisonous sulfide. Based on the finding that in the absence of NFU the auxiliary [4Fe–4S] cluster collapses after extraction of two sulfur atoms (McCarthy and Booker, 2017) one may speculate whether sulfide toxicity is a consequence of such cluster disintegration during catalysis.

Increased enzymatic activity of overexpressed *LIP1* in Arabidopsis would require the respective substrates for lipoylation. Lipoyl synthases use the octanoylated GDC subunit H2 as their primary substrate for synthesis of the lipoyl moiety, which is subsequently transferred to E2 subunits of the other dehydrogenase complexes (Schonauer *et al.*, 2009; Solmonson and DeBerardinis, 2018; Pietikäinen *et al.*, 2021; Bauwe, 2023). The overall lipoylation pattern on the respective proteins, however, was not massively altered in *LIP1* overexpression lines, especially in WT and GRXS15 knockdown lines. The need for a suitable substrate for the overexpressed LIP1 thus leaves a conundrum. One possibility for providing new substrates for lipoylation would be the presence of lipoamidase activities similar to the sirtuin lipoamidase activities found in mammals and *E. coli* (Mathias *et al.*, 2014; Rowland *et al.*, 2017). So far, however, no such activity has been reported for plants.

An alternative explanation for the acute toxic effects resulting from overexpression of lipoyl synthases may result from cluster instability. The [4Fe–4S] cluster of LipA is known to be sensitive to traces of oxygen and for losing iron and sulfide to yield a [2Fe–2S] cluster upon exposure to air (Ollagnier-de Choudens *et al.*, 2000). Especially in situations with limited substrate supply for the lipoylation reaction, it cannot be excluded that lipoyl synthases lose [4Fe–4S] clusters through oxidative decomposition. If the remaining [2Fe–2S] cluster also becomes unstable after its replacement by a new [4Fe–4S] cluster, this process would ultimately set free four sulfides and thus generate a severe sulfide load in the matrix. Oxidative decomposition of clusters from overexpressed *LIP1* suggests that this likely does happen from the endogenous protein as well, particularly when only limited substrate is available. Interestingly, Arabidopsis mutants deficient in mitochondrial acyl carrier proteins have a similar phenotype as *LIP1* overexpressors. While this is at least in parts caused by lipoylation deficiency (Fu *et al.*, 2020), it might be possible that such mutants also suffer from increased sulfide and inhibition of COX.

The pronounced sulfide release after overexpression of LIP1 in WT plants suggests that the mitochondrial Fe–S cluster assembly machineries have sufficient capacity to serve all available [4Fe–4S] apoproteins. The uncontrolled release of sulfide as a potentially toxic side product suggests that tight control of protein abundance might be the only means for risk management. This is consistent with low abundance of LIP1 in Arabidopsis suspension culture cells (Fuchs *et al.*, 2020) and the absence of any evidence for induction of *LIP1* under specific stress

situations. Low abundance of lipoyl synthases is also found in *Saccharomyces cerevisiae* (Ho *et al.*, 2018) and in human cells where LIAS is present with only 23,904 copies per cell, which represents just 0.007 % of all mitochondrial proteins (Morgenstern *et al.*, 2021). Uncontrolled potential release of sulfide by lipoyl synthases also provides a strong argument for maintaining sulfide detoxification systems in mitochondria of most eukaryotic lineages (Theissen *et al.*, 2003; Kabil and Banerjee, 2010; Birke *et al.*, 2012).

Irrespective of whether the released sulfide is a side product of the [4Fe–4S] cluster-sacrificing catalytic activity of lipoyl synthases or a result of uncontrollable oxidative decomposition, the experimental system with overexpression of lipoyl synthases associated with distinct and easily observable phenotypes offers an experimental framework to further study mitochondrial Fe–S assembly and cluster distribution. The increasing severity of phenotypes in mutants with compromised GRXS15-dependent [2Fe–2S] cluster transfer in combination with *LIP1* overexpression and the redirection of [4Fe–4S] clusters through sink modulation both highlight the applicability of the assay. Similarly, one can envisage that the tools can be used to further study mitochondrial sulfide production or detoxification.

Materials and methods

Plant material and growth conditions

The *Arabidopsis thaliana* ecotype Columbia-0 ([L.] Heynh.) was used as the main experimental organism. The T-DNA insertion line *grxs15-1* (SALK_112767) has been described earlier (Moseler *et al.*, 2015). Seeds of *aco3* (SALK_014661) (Moeder *et al.*, 2007) were obtained from NASC (Nottingham Arabidopsis Stock Centre, https://arabidopsis.info/). The knockdown line *amiR* (*GRXS15*^{amiR} (Ströher *et al.*, 2016)) was provided by Janneke Balk, John Innes Centre, University of East Anglia, UK. The complementation lines *K83A #3* and *K83A #4* (*grxs15-3 UBQ10*$_{pro}$*:GRXS15 K83A*) were described previously (Moseler *et al.*, 2015; Moseler *et al.*, 2021). The lines *amiR*, *K83A #3* and *#4* were crossed with *aco3* and the double homozygous F_3 generations were used throughout this study.

For phenotypic characterization of seedlings, seeds were surface-sterilized with 70 % (v/v) ethanol for 10 min followed by washing with sterile water and plated on half-strength Murashige and Skoog medium (½ MS, Duchefa Biochemie, Haarlem, NL) with addition of 0.1 % (w/v) sucrose, 0.05 % (w/v) MES (pH 5.8, KOH) and solidified with 0.8 % (w/v) agar. Seeds were stratified at 4 °C in the dark for 2-3 days. Plates were incubated vertically under long-day conditions (16 h light at 22 °C and 8 h dark at 18 °C) at a light intensity of ~100 µmol photons m^{-2} s^{-1} and 50 % air humidity. Ten days after germination, root growth was documented photographically and root length was measured using Fiji ImageJ (https://imagej.nih.gov/ij/). For documentation of seedling phenotypes, 17-day-old seedlings were transferred from plates to a black mat and photographed.

For hydroponic seedling culture, surface-sterilized seeds were gently sown on a layer of microagar floating in sterile glass pots filled with 50 mL liquid ½ MS medium with 1 % (w/v) sucrose, 0.04 % (w/v) MES (pH 5.8, KOH). Pots were closed with transparent plastic lids, placed at 4 °C in the dark for two days for seed stratification, and subsequently transferred onto rotary shakers and gently agitated in the growth cabinet under long-day conditions for 16 days.

To obtain larger plants, the seeds were placed onto a standard soil mixture (Floradur B-seed, Perlite Perligran 0-6 and quartz sand in a ratio of 10:1:1, respectively) and stratified for at least 2 days in the dark at 4 °C and high humidity. Subsequently, pots were transferred to the light under long-day conditions (16 h light at 21 °C and 8 h dark at 19 °C) with light intensity of 100-120 µmol photons m^{-2} s^{-1} and 50 % air humidity. The plants were grown in individual pots randomly distributed among greenhouse trays and documented photographically after four weeks for rosette area measurements using Leaf Lab, a custom-written MATLAB script) and after eight weeks for documentation of inflorescences. For determination of the fresh weight, whole rosettes of 7-week-old plants were cut at the base and directly weighted with an

analytical scale. To track the floral induction, the growth of plants was monitored three times a week for a visible floral bud. Similarly, the height of the main inflorescence was measured three times a week with a ruler, starting from the base on the rosette. To characterize rosette development and leaf phenotypes, 31-day-old rosettes were dissected and the leaves aligned according to their developmental age.

For experiments with altered CO_2 conditions, seeds were surface-sterilized with chloric acid and sown on a mixture of soil (Einheitserde; Einheitserdewerk Uetersen Werner Tantau GmbH und Co. KG, Uetersen, DE) and vermiculite (4:1). Pots were incubated at 4 °C for at least two days for stratification and transferred to a growth chamber with defined environmental conditions (SANYO) for eight weeks (principal growth stage 5.1) (Boyes *et al.*, 2001). Plants were grown either in high CO_2 (HC; 5,000 ppm CO_2) or in low CO_2 (LC, 390 ppm CO_2) for control. In both conditions, the photoperiod was 12/12 h day/night cycle with light intensity of ~100 µmol m^{-2} s^{-1} and ~70 % relative humidity. Plants were regularly watered and fertilized weekly (0.2 % Wuxal, Aglukon, Düsseldorf, DE).

For genotyping, a complete list of primers is provided in Supplemental Table S1.
To analyse the zygosity of plants expressing the K83A variant of GRXS15, plants were allowed to self-fertilize. Mature siliques were subsequently checked on a stereomicroscope (Leica M165 FC) for aborted seeds, which would be expected if the transgene was still segregating.

Generation of transgenic plants

For overexpression of *LIP1* the coding sequence was amplified from cDNA generated from WT plants with primers indicated in Supplemental Table S2 adding *att*B sites. The obtained fragment was purified and BP-recombined into the pDONR207 Gateway donor vector (Invitrogen Waltham, USA). Subsequently, the recombined pDONR207 vector was LR-recombined with a modified pSS01 destination vector (Brach *et al.*, 2009) containing 35S promoter and the gene coding *GFP* in frame with the C-terminus of the Gateway cassette. Alternatively, pDONR207_*LIP1* with a stop codon was LR-recombined with pB7WG2 (Karimi *et al.*, 2002), for overexpression of *LIP1* without *GFP*. After recombination, the expression clone was verified by colony PCR after transformation into *E. coli* DH5α. The vector pMDC32_*35S*$_{pro}$:*OAS-TL C* for overexpression of *OAS-TL C* was kindly provided by Cecilia Gotor (Álvarez *et al.*, 2012a).

Agrobacterium tumefaciens (AGL-1) were transformed by electroporation with the final constructs and used to transform plants by floral dipping (Clough and Bent, 1998). T_1 seeds from plants transformed with pSS01_*35S*$_{pro}$:*LIP1-GFP* and pB7WG2_*35S*$_{pro}$:*LIP1* were harvested and selected either with 240 mg/L glufosinate ammonium solution (Basta) or screened for fluorescence on a stereomicroscope (Leica M165 FC) equipped with a GFP filter (excitation: 470 ± 20 nm, emission: 525 ± 25 nm). T_1 plants transformed with

pMDC32_*35S$_{pro}$*:*OAS-TL C* were screened *in vitro* by 20 µg/mL hygromycin (Harrison *et al.*, 2006). The following generations of mutants were screened by herbicide resistance or fluorescence for segregation, growing mutants in agar plates or on soil. Only lines following a Mendelian segregation were kept (Supplemental Tables S3-S5). Three independent lines for each obtained mutant were selected and screened for the homogeneity of the effects induced by the insertions.

Subcellular localization of proteins

To verify mitochondrial targeting of LIP1, 7-day-old seedlings stably expressing *LIP1-GFP* were vacuum-infiltrated for 30 min with 200 nM MitoTracker Orange (Invitrogen). To test for colocalization seedlings were imaged on a confocal microscope (Zeiss LSM 780, connected to an Axio Observer.Z1 (Carl Zeiss Microscopy, Jena, DE). Imaging was performed with a C-Apochromat x40 (C-Apochromat 40x/1.2 W corr) water-immersion objective. Fluorescence was recorded with λ_{ex} = 488 nm and λ_{em} = 520 nm for GFP, λ_{ex} = 543 nm, λ_{em} = 597 nm for MitoTracker Orange and λ_{ex} = 633 nm, λ_{em} = 675 nm for chlorophyll autofluorescence. Data acquisition was performed using Zen 3.2 (blue edition) Zeiss software.

Isolation of intact mitochondria

High-pure intact mitochondria were isolated from 16-day-old seedlings grown in liquid culture following the protocol of Escobar *et al.* (2006) with slight modifications. About 10-20 g seedling material was ground with 2 g quartz sand in 300 mL extraction buffer (250 mM sucrose, 1.5 mM EDTA, 15 mM MOPS, 0.4 % (w/v) BSA, 0.6 % (w/v) PVP-40, 10 mM DTT, 100 mM ascorbic acid) and filtered through a layer of Miracloth (Merck Millipore) for two times. Cell debris was removed by centrifugation at 1,300 *g* for 5 min (Beckman Centrifuge Avanti® J-26-XP). Afterwards, the supernatant was centrifuged at 18,000 *g* for 20 min to obtain a pellet. The pellet was gently resuspended with a fine brush in 300 mL wash buffer (300 mM sucrose, 10 mM TES, 0,1 % (w/v) BSA). Both centrifugation steps were repeated a second time. Resuspended fractions (~2 mL) were loaded on PVP gradient (300 mM sucrose, 10 mM TES, 0.1 % (w/v) BSA, 32 % (v/v) Percoll, 0-6 % (w/v) PVP-40) and centrifuged at 40,000 *g* for 40 min with disengaged active-deceleration. Mitochondria fraction at the lower part of the gradient was recovered and washed twice in 60 mL final wash buffer (300 mM sucrose, 10 mM TES) reobtaining mitochondria pellet with centrifuged at 23,700 *g* for 15 min and resuspending it by carefully agitating the tube. The mitochondria pellet was finally resuspended in 500 µL final wash buffer.

Leaf mitochondria from older plants were isolated following the “Method A” described in Keech *et al.* (2005) (Keech *et al.*, 2005) for crude, well-coupled mitochondria. About 5 g of 7-week-old leaves from plants grown on soil in long-day conditions were used.

Protein blotting and immunodetection

After estimation of protein concentrations via Bradford (Roti-Quant) monitoring absorbance at 595 nm with a CLARIOstar microplate reader, 15 µg of pure isolated mitochondria were mixed with Laemmli buffer (2 % (w/v) SDS, 50 mM Tris-HCl pH 6.8, 0.002 % (w/v) bromophenol blue, 5 % (v/v) β-mercaptoethanol and 10 % (v/v) glycerol), sonicated for 2 min in ultrasonic bath (Bandelin Sonorex) and boiled at 95 °C for 5 min. The samples were electrophoresed on sodium dodecyl sulfate–polyacrylamide gel electrophoresis (SDS–PAGE) precast 4-20 % Mini-PROTEAN TGX gel (Bio-Rad) to separate the proteins.

For immunoblotting the separate protein were semi-dry blotted or wet-blotted on BioTrace PVDF Transfer Membrane (Pall Corporation). Blots were probed in TBS-T with 1:1,000 anti-LIP1 (G231072/63, (Moseler *et al.*, 2021)), 1:1,000 anti-LA (ab58724; Abcam), 1:5,000 anti-GDC-H (As05 074; Agrisera), 1:2,500 anti-GRXS15 (Moseler *et al.*, 2015), 1:5,000 anti-GFP (A-6455; Thermo) or 1:1,000 anti-AOX1/2 (AS04 054; Agrisera) antibodies conjugated to horseradish peroxidase (HRP). 1:20,000 Goat anti-rabbit poly-horseradish peroxidase secondary antibody (#31461; Thermo) was used for detection of chemiluminescence and developed using Pierce ECL Plus Western Blotting Solution (Thermo). Signals were detected on INTAS ECL ChemoStar imager. For the loading control, the PVDF membrane is stained with Amido black staining (0.1 % (w/v) amido black, 45% (v/v) ethanol, 10 % (v/v) acetic acid) or a dedicated gel was prepared and proteins were stained with PageBlue Protein Staining solution (Thermo).

Metabolite analysis

The determination of metabolites related to photorespiration was carried out by liquid chromatography coupled to tandem mass spectrometry (LC-MS/MS) analysis using the LCMS-8050 system (Shimadzu, Japan). For this purpose, we harvested leaf material (~25 mg) from fully expanded rosette leaves of plants at growth stage 5.1 (Boyes *et al.*, 2001) grown in high CO_2 (HC - 5000 ppm CO_2) or low CO_2 (LC – 390 ppm CO_2) at the end of the day (EoD, 11 h illumination). The material was immediately frozen in liquid nitrogen and stored at -80 °C until further analysis. Extraction of soluble primary intermediates was carried out using LC-MS grade chemicals according to (Arrivault *et al.*, 2009; Arrivault *et al.*, 2015) and the samples were analysed exactly as described in Reinholdt *et al.* (2019). The compounds were identified and quantified using multiple reaction monitoring (MRM) according to the values provided in the LC-MS/MS method package and the LabSolutions software package (Shimadzu, JP). Authentic standard substances (Merck, DE) at varying concentrations were used for calibration and peak areas normalized to signals of the internal standard ((morpholino)-ethanesulfonic acid (MES), 1 mg/mL). Data were interpreted using the Lab solution software package (Shimadzu, JP).

Regarding the other metabolites, 40-50 mg of 8-day-old seedlings growing on agar plates in long-day condition were collected at beginning of the day (BoD: 2 h after the light is on) and flash-frozen in liquid nitrogen before powdering with glass beads using a TissueLyser II (Qiagen).

Ion chromatography was performed for absolute quantification of anion content by extraction with 0.7 mL ultra-pure water for 45 min at 95 °C. Samples were centrifuged at 4 °C and 20,000 *g* for 15 min and 100 µL of the supernatant were transferred to a chromatography vial. After addition of 200 µL ultra-pure water (1:3 dilution), anions were separated using an IonPac AS11-HC (2 mm, Thermo Scientific) column connected to an ICS-5000 system (Thermo Scientific) and quantified by conductivity detection after cation suppression (ASRS-300 2 mm, suppressor current 23-78 mA). Prior to separation, the column was heated to 30 °C and equilibrated with five column volumes of solvent A (ultra-pure water) at a flow rate of 0.3 mL min^{-1}. Separation of anions was achieved by increasing the concentration of solvent B (100 mM NaOH) in buffer A linearly as follows: 0-8 min: 4 % B, 18-25 min: 4 %-18 % B, 25-43 min: 19 %-30 % B, 43-53 min: 30 %-62 % B, 53-53.1 min: 62 %-80 % B, 53.1-59 min: 80 % B, 59-59.1 min: 4 % B, and 59.1-70 min: 4 % B. Data acquisition and quantification were performed with Chromeleon 7 software (Thermo Scientific).

Free amino acids and thiols were extracted from 40-50 mg of seedlings with 0.4 mL of 0.1 M HCl in an ultrasonic ice-bath for 10 min. The resulting extracts were centrifuged twice for 10 min at 4 °C and 16,400 *g* to remove cell debris. Amino acids were derivatized with AccQ-Tag reagent (Waters) and determined as described in Weger *et al.* (2016). Total glutathione and cysteine were quantified by reducing disulfides with DTT followed by thiol derivatization with the fluorescent dye monobromobimane (Thiolyte, Calbiochem). Derivatization was performed as described in Wirtz *et al.* (2004). UPLC-FLR analysis was carried out using an Acquity H-class UPLC system. Separation was achieved with a binary gradient of buffer A (100 mM potassium acetate, pH 5.3) and solvent B (acetonitrile) with the following gradient: 0 min 2.3 % buffer B, 0.99 min 2.3 %, 1 min 70 %, 1.45 min 70 %, and re-equilibration to 2.3 % B in 1.05 min at a flow rate of 0.85 mL min^{-1}. The column (Acquity BEH Shield RP18 column, 50 mm x 2.1 mm, 1.7 µm, Waters) was maintained at 45 °C and sample temperature was kept constant at 14 °C. Monobromobimane conjugates were detected by fluorescence at 480 nm after excitation at 380 nm and quantified using ultrapure standards (Sigma).

For determination of intracellular BCKA content, the same acidic extracts were used. For derivatization with DMB (1,2-diamino-4,5-methylendioxybenzene), 30 µL extract were mixed with 30 µL DMB derivatization reagent (5 mM DMB, 20 mM sodium hydrosulfite, 1 M 2-mercaptoethanol, 1.2 M HCl) and incubated at 100 °C for 45 min. After 10 min centrifugation, the reaction was diluted with 240 µL 10 % acetonitrile. UPLC system, column and solvent were used as described above. Baseline separation of DMB derivates was achieved by increasing

the concentration of acetonitrile (B) in buffer A as follows: 2 min 2 % B, 4.5 min 15 % B, 10.5 min 38 % B, 10.6 min 90 % B, hold for 2 min and return to 2 % B in 3.5 min.

The separated derivates were detected by fluorescence (Acquity FLR detector, Waters, OPD: excitation: 350 nm, emission: 410 nm; DMB: excitation: 367 nm, emission: 446 nm) and quantified using ultrapure standards (Sigma). Data acquisition and processing were performed with the Empower3 software suite (Waters).

Oxygen consumption measurements

Respiration of roots of 16-day-old seedlings grown on ½ MS vertical agar plates in standard long-day condition was analysed using a Clark-type oxygen electrode (Oxygraph, Hansatech) as described in Wagner *et al.* (2015). Roots from 15-30 seedlings (about 100 mg fresh weight) were cut with a scalpel, rolled and plugged in the oxygraph chamber filled with 1.2 mL incubation medium (5 mM KCl, 10 mM MES, and 10 mM $CaCl_2$, pH 5.8). After recording the basal root respiration (5 min) oxygen consumption was followed in response to the sequential addition of the inhibitors 25 µL of KCN (potassium cyanide) at final concentration of 4 mM and 25 µL of pGal (propyl gallate) at final concentration of 200 µM. The measure was repeated switching the order of the inhibitors. The results were normalized on the dry weight of the roots (DW) and on the base respiration rate without inhibitors.

Gene expression analysis

8-day-old seedlings growing on agar plates in long-day condition were collected and flash-frozen in liquid nitrogen before powdering with metal beads using a TissueLyser II (Qiagen). Total RNA was isolated using the NucleoSpin® RNA Kit (Thermo) and cDNA was synthetized from 10 µg RNA using RevertAid First strand cDNA Synthesis Kit (Thermo) following the supplier instructions. qRT-PCR was performed with PerfeCTa SYBR Green FastMix (Quanta) in a 384-well plate using a CFX96 Real-Time PCR Detection System. The two reference genes *SAND* and *TIP41* were used for normalization. Three technical replicates for each of three independent biological replicates were performed for each experiment. The primers used are listed in Supplemental Table S6. PCR efficiency for each primer pair was assessed by conducting calibration dilution curves in dedicated run.

Statistical analyses and data plotting

Quantified data were plotted and statistically analysed with GraphPad Prism 6. All the box plots show the median (center line) that divides the first to the third quartile, min and max values are indicated by whiskers, points represent individual values of the whole data set. Outliers were automatically identified with ROUT Method (Q = 10 %) and not shown. Significant differences were calculated according to Student's *t*-test (two-tailed with 95 % confidence interval) or one-

way ANOVA with Tukey's multiple comparisons (with 95 % confidence interval). Asterisks represent significant differences (*=P ≤ 0.1, **= P ≤ 0.01, ***= P ≤ 0.001, ****= P ≤ 0.0001, ns: not significant).

Accession numbers

GRXS15 (AT3G15660), *ACO3* (AT2G05710), *ACO2* (AT4G26970), *LIP1* (AT2G20860), *OAS-TL C* (AT3G59760), *SERAT2;2* (AT3G13110), *H protein 1* (AT2G35370), *H protein 2* (AT2G35120), *H protein 3* (AT1G32470), *PDC-E2 1* (AT3G52200), *PDC-E2 2* (AT3G13930), *PDC-E2 3* (AT1G54220), *PDC-E2 4* (AT3G25860), *OGDC-E2 1* (AT5G55070), *SAND* (AT2G28390), *TIP41* (AT4G34270).

Funding

This project was funded by the Deutsche Forschungsgemeinschaft through grant ME1567/12-1 to A.J.M.. A.M. was supported by a fellowship from the Humboldt Foundation and is grateful to the University of Bonn for further funding. S.T. thanks Martin Hagemann (Rostock) for support and the University of Rostock for funding. The LC-MS/MS equipment at the University of Rostock was financed through the Hochschulbauförderungsgesetz program (GZ: INST 264/125-1 FUGG).

Acknowledgements

We thank Timon Könen, Lisa Zander and Juan Carlos Davila Frantzen for support in plant maintenance and basic phenotype characterization. We also thank Nicolas Rouhier and Jonathan Przybyla-Toscano for providing the LIP1 antibody.

References

Álvarez, C., García, I., Romero, L.C., and Gotor, C. (2012a). Mitochondrial sulfide detoxification requires a functional isoform O-Acetylserine(thiol)lyase C in *Arabidopsis thaliana*. Mol Plant. **5,** 1217-1226.

Álvarez, C., García, I., Moreno, I., Pérez-Pérez, M.E., Crespo, J.L., Romero, L.C., and Gotor, C. (2012b). Cysteine-generated sulfide in the cytosol negatively regulates autophagy and modulates the transcriptional profile in Arabidopsis. Plant Cell **24,** 4621-4634.

Anoman, A.D., Flores-Tornero, M., Benstein, R.M., Blau, S., Rosa-Téllez, S., Bräutigam, A., Fernie, A.R., Muñoz-Bertomeu, J., Schilasky, S., Meyer, A.J., Kopriva, S., Segura, J., Krueger, S., and Ros, R. (2019). Deficiency in the phosphorylated pathway of serine biosynthesis perturbs sulfur assimilation. Plant Physiol. **180,** 153-170.

Arrivault, S., Guenther, M., Ivakov, A., Feil, R., Vosloh, D., Van Dongen, J.T., Sulpice, R., and Stitt, M. (2009). Use of reverse-phase liquid chromatography, linked to tandem mass spectrometry, to profile the Calvin cycle and other metabolic intermediates in Arabidopsis rosettes at different carbon dioxide concentrations. Plant J. **59,** 826-839.

Arrivault, S., Guenther, M., Fry, S.C., Fuenfgeld, M.M.F.F., Veyel, D., Mettler-Altmann, T., Stitt, M., and Lunn, J.E. (2015). Synthesis and use of stable-isotope-labeled internal standards for quantification of phosphorylated metabolites by LC–MS/MS. Anal. Chem. **87,** 6896-6904.

Azam, T., Przybyla-Toscano, J., Vignols, F., Couturier, J., Rouhier, N., and Johnson, M.K. (2020). The Arabidopsis mitochondrial glutaredoxin GRXS15 provides [2Fe-2S] clusters for ISCA-mediated [4Fe-4S] cluster maturation. Int. J. Mol. Sci. **21,** 9237.

Balk, J., and Schaedler, T.A. (2014). Iron cofactor assembly in plants. Annual review of plant biology **65,** 125-153.

Bauwe, H. (2023). Photorespiration – Rubisco's repair crew. J. Plant Physiol. **280,** 153899.

Birke, H., Haas, F., De Kok, L., Balk, J., Wirtz, M., and Hell, R. (2012). Cysteine biosynthesis, in concert with a novel mechanism, contributes to sulfide detoxification in mitochondria of *Arabidopsis thaliana*. Biochem. J. **445,** 275-283.

Boyes, D.C., Zayed, A.M., Ascenzi, R., McCaskill, A.J., Hoffman, N.E., Davis, K.R., and Gorlach, J. (2001). Growth stage-based phenotypic analysis of Arabidopsis: a model for high throughput functional genomics in plants. Plant Cell **13,** 1499-1510.

Brach, T., Soyk, S., Müller, C., Hinz, G., Hell, R., Brandizzi, F., and Meyer, A.J. (2009). Non-invasive topology analysis of membrane proteins in the secretory pathway. Plant J. **57,** 534-541.

Clough, S.J., and Bent, A.F. (1998). Floral dip: a simplified method for Agrobacterium-mediated transformation of *Arabidopsis thaliana*. Plant J **16,** 735-743.

Couturier, J., Przybyla-Toscano, J., Roret, T., Didierjean, C., and Rouhier, N. (2015). The roles of glutaredoxins ligating Fe–S clusters: Sensing, transfer or repair functions? Biochim Biophys Acta Mol Cell Res. **1853,** 1513-1527.

Dellero, Y., Jossier, M., Schmitz, J., Maurino, V.G., and Hodges, M. (2016). Photorespiratory glycolate–glyoxylate metabolism. J. Exp. Bot. **67,** 3041-3052.

Domán, A., Dóka, É., Garai, D., Bogdándi, V., Balla, G., Balla, J., and Nagy, P. (2023). Interactions of reactive sulfur species with metalloproteins. Redox. Biol. **60,** 102617.

Douce, R., Bourguignon, J., Neuburger, M., and Rébeillé, F. (2001). The glycine decarboxylase system: a fascinating complex. Trends Plant Sci. **6,** 167-176.

Escobar, M.A., Geisler, D.A., and Rasmusson, A.G. (2006). Reorganization of the alternative pathways of the Arabidopsis respiratory chain by nitrogen supply: opposing effects of ammonium and nitrate. Plant J. **45,** 775-788.

Fu, X., Guan, X., Garlock, R., and Nikolau, B.J. (2020). Mitochondrial fatty acid synthase utilizes multiple acyl carrier protein isoforms. Plant Physiol. **183,** 547-557.

Fuchs, P., Bohle, F., Lichtenauer, S., Ugalde, J.M., Feitosa Araujo, E., Mansuroglu, B., Ruberti, C., Wagner, S., Müller-Schüssele, S.J., Meyer, A.J., and Schwarzländer, M. (2022). Reductive stress triggers ANAC017-mediated retrograde signaling to safeguard the endoplasmic reticulum by boosting mitochondrial respiratory capacity. Plant Cell **34,** 1375-1395.

Fuchs, P., Rugen, N., Carrie, C., Elsässer, M., Finkemeier, I., Giese, J., Hildebrandt, T.M., Kühn, K., Maurino, V.G., Ruberti, C., Schallenberg-Rüdinger, M., Steinbeck, J., Braun, H.-P., Eubel, H., Meyer, E.H., Müller-Schüssele, S.J., and Schwarzländer, M. (2020). Single organelle function and organization as estimated from Arabidopsis mitochondrial proteomics. Plant J. **101,** 420-441.

Haas, F.H., Heeg, C., Queiroz, R., Bauer, A., Wirtz, M., and Hell, R. (2008). Mitochondrial serine acetyltransferase functions as a pacemaker of cysteine synthesis in plant cells. Plant Physiol. **148,** 1055-1067.

Harrison, S.J., Mott, E.K., Parsley, K., Aspinall, S., Gray, J.C., and Cottage, A. (2006). A rapid and robust method of identifying transformed *Arabidopsis thaliana* seedlings following floral dip transformation. Plant Methods **2,** 19.

Heeg, C., Kruse, C., Jost, R., Gutensohn, M., Ruppert, T., Wirtz, M., and Hell, R. (2008). Analysis of the Arabidopsis *O*-acetylserine(thiol)lyase gene family demonstrates compartment-specific differences in the regulation of cysteine synthesis. Plant Cell **20,** 168-185.

Ho, B., Baryshnikova, A., and Brown, G.W. (2018). Unification of protein abundance datasets yields a quantitative *Saccharomyces cerevisiae* proteome. Cell Syst. **6,** 192-205.e193.

Hooks, M.A., Allwood, J.W., Harrison, J.K.D., Kopka, J., Erban, A., Goodacre, R., and Balk, J. (2014). Selective induction and subcellular distribution of ACONITASE 3 reveal the importance of cytosolic citrate metabolism during lipid mobilization in Arabidopsis. Biochem. J. **463,** 309-317.

Kabil, O., and Banerjee, R. (2010). Redox biochemistry of hydrogen sulfide. J. Biol. Chem. **285,** 21903-21907.

Karimi, M., Inze, D., and Depicker, A. (2002). GATEWAY vectors for Agrobacterium-mediated plant transformation. Trends Plant Sci. **7,** 193-195.

Keech, O., Dizengremel, P., and Gardeström, P. (2005). Preparation of leaf mitochondria from *Arabidopsis thaliana*. Physiol Plant. **124,** 403-409.

Kolluru, G.K., Shen, X., Bir, S.C., and Kevil, C.G. (2013). Hydrogen sulfide chemical biology: Pathophysiological roles and detection. Nitric Oxide **35,** 5-20.

Krüger, S., Niehl, A., Martin, M.C.L., Steinhauser, D., Donath, A., Hildebrandt, T., Romero, L.C., Hoefgen, R., Gotor, C., and Hesse, H. (2009). Analysis of cytosolic and plastidic serine acetyltransferase mutants and subcellular metabolite distributions suggests interplay of the cellular compartments for cysteine biosynthesis in *Arabidopsis*. Plant Cell Environ. **32,** 349-367.

Lee, C.P., Elsässer, M., Fuchs, P., Fenske, R., Schwarzländer, M., and Millar, A.H. (2021). The versatility of plant organic acid metabolism in leaves is underpinned by mitochondrial malate–citrate exchange. Plant Cell **33,** 3700-3720.

Lill, R., and Freibert, S.-A. (2020). Mechanisms of mitochondrial iron-sulfur protein biogenesis. Annu. Rev. Biochem. **89,** 471-499.

Mathias, R.A., Greco, Todd M., Oberstein, A., Budayeva, Hanna G., Chakrabarti, R., Rowland, Elizabeth A., Kang, Y., Shenk, T., and Cristea, Ileana M. (2014). Sirtuin 4 is a lipoamidase regulating pyruvate dehydrogenase complex activity. Cell **159,** 1615-1625.

Mayr, J.A., Feichtinger, R.G., Tort, F., Ribes, A., and Sperl, W. (2014). Lipoic acid biosynthesis defects. J. Inherit. Metab. Dis. **37,** 553-563.

McCarthy, E.L., and Booker, S.J. (2017). Destruction and reformation of an iron-sulfur cluster during catalysis by lipoyl synthase. Science **358,** 373-377.

McLaughlin, M.I., Lanz, N.D., Goldman, P.J., Lee, K.-H., Booker, S.J., and Drennan, C.L. (2016). Crystallographic snapshots of sulfur insertion by lipoyl synthase. Proceedings of the National Academy of Sciences of the United States of America **113,** 9446-9450.

Millar, A.H., Whelan, J., Soole, K., and Day, D.A. (2011). Organization and regulation of mitochondrial respiration in plants. Annual review of plant biology **62,** 79-104.

Moeder, W., del Pozo, O., Navarre, D.A., Martin, G.B., and Klessig, D.F. (2007). Aconitase plays a role in regulating resistance to oxidative stress and cell death in Arabidopsis and *Nicotiana benthamiana*. Plant Mol Biol **63,** 273-287.

Morgenstern, M., Peikert, C.D., Lübbert, P., Suppanz, I., Klemm, C., Alka, O., Steiert, C., Naumenko, N., Schendzielorz, A., Melchionda, L., Mühlhäuser, W.W.D., Knapp, B., Busch, J.D., Stiller, S.B., Dannenmaier, S., Lindau, C., Licheva, M., Eickhorst, C., Galbusera, R., Zerbes, R.M., Ryan, M.T., Kraft, C., Kozjak-Pavlovic, V., Drepper, F., Dennerlein, S., Oeljeklaus, S., Pfanner, N., Wiedemann, N., and Warscheid, B. (2021). Quantitative high-confidence human mitochondrial proteome and its dynamics in cellular context. Cell Metab. **33,** 2464-2483.e2418.

Moseler, A., Aller, I., Wagner, S., Nietzel, T., Przybyla-Toscano, J., Mühlenhoff, U., Lill, R., Berndt, C., Rouhier, N., Schwarzländer, M., and Meyer, A.J. (2015). The mitochondrial monothiol glutaredoxin S15 is essential for iron-sulfur protein maturation in *Arabidopsis thaliana*. Proc. Natl. Acad. Sci. U.S.A. **112,** 13735-13740.

Moseler, A., Kruse, I., Maclean, A.E., Pedroletti, L., Franceschetti, M., Wagner, S., Wehler, R., Fischer-Schrader, K., Poschet, G., Wirtz, M., Dörmann, P., Hildebrandt, T.M., Hell, R., Schwarzländer, M., Balk, J., and Meyer, A.J. (2021). The function of glutaredoxin GRXS15 is required for lipoyl-dependent dehydrogenases in mitochondria. Plant Physiol. **186,** 1507-1525.

Navarro-Sastre, A., Tort, F., Stehling, O., Uzarska, Marta A., Arranz, José A., del Toro, M., Labayru, M.T., Landa, J., Font, A., Garcia-Villoria, J., Merinero, B., Ugarte, M., Gutierrez-Solana, Luis G., Campistol, J., Garcia-Cazorla, A., Vaquerizo, J., Riudor, E., Briones, P., Elpeleg, O., Ribes, A., and Lill, R. (2011). A fatal mitochondrial disease is associated with defective NFU1 function in the maturation of a subset of mitochondrial Fe-S proteins. Am. J. Hum. Genet. **89,** 656-667.

Nicholls, P., Marshall, Doug C., Cooper, Chris E., and Wilson, Mike T. (2013). Sulfide inhibition of and metabolism by cytochrome c oxidase. Biochem. Soc. Trans. **41,** 1312-1316.

Ollagnier-de Choudens, S., Sanakis, Y., Hewitson, K.S., Roach, P., Baldwin, J.E., Münck, E., and Fontecave, M. (2000). Iron-sulfur center of biotin synthase and lipoate synthase. Biochemistry **39,** 4165-4173.

Pedroletti, L., Moseler, A., and Meyer, A.J. (2023). Assembly, transfer, and fate of mitochondrial iron–sulfur clusters. J. Exp. Bot. **74,** 3328-3344.

Pietikäinen, L.P., Rahman, M.T., Hiltunen, J.K., Dieckmann, C.L., and Kastaniotis, A.J. (2021). Genetic dissection of the mitochondrial lipoylation pathway in yeast. BMC Biology **19,** 14.

Przybyla-Toscano, J., Christ, L., Keech, O., and Rouhier, N. (2020). Iron–sulfur proteins in plant mitochondria: roles and maturation. Journal of Experimental Botany **72,** 2014-2044.

Przybyla-Toscano, J., Maclean, A.E., Franceschetti, M., Liebsch, D., Vignols, F., Keech, O., Rouhier, N., and Balk, J. (2022). Protein lipoylation in mitochondria requires Fe–S cluster assembly factors NFU4 and NFU5. Plant Physiol. **188,** 997-1013.

Reinholdt, O., Schwab, S., Zhang, Y., Reichheld, J.-P., Fernie, A.R., Hagemann, M., and Timm, S. (2019). Redox-regulation of photorespiration through mitochondrial thioredoxin o1. Plant Physiol. **181,** 442-457.

Ros, R., Muñoz-Bertomeu, J., and Krüger, S. (2014). Serine in plants: biosynthesis, metabolism, and functions. Trends Plant Sci. **19,** 564-569.

Rowland, E.A., Snowden, C.K., and Cristea, I.M. (2018). Protein lipoylation: an evolutionarily conserved metabolic regulator of health and disease. Curr Opin Chem Biol. **42,** 76-85.

Rowland, E.A., Greco, T.M., Snowden, C.K., McCabe, A.L., Silhavy, T.J., and Cristea, I.M. (2017). Sirtuin lipoamidase activity is conserved in bacteria as a regulator of metabolic enzyme complexes. mBio **8,** 10.1128/mbio.01096-01017.

Schonauer, M.S., Kastaniotis, A.J., Kursu, V.A.S., Hiltunen, J.K., and Dieckmann, C.L. (2009). Lipoic acid synthesis and attachment in yeast mitochondria. J. Biol. Chem. **284,** 23234-23242.

Selinski, J., Scheibe, R., Day, D.A., and Whelan, J. (2018). Alternative oxidase is positive for plant performance. Trends Plant Sci. **23,** 588-597.

Solmonson, A., and DeBerardinis, R.J. (2018). Lipoic acid metabolism and mitochondrial redox regulation. J. Biol. Chem. **293,** 7522-7530.

Ströher, E., Grassl, J., Carrie, C., Fenske, R., Whelan, J., and Millar, A.H. (2016). Glutaredoxin S15 is involved in Fe-S cluster transfer in mitochondria influencing lipoic acid-dependent enzymes, plant growth, and arsenic tolerance in Arabidopsis. Plant Physiol. **170,** 1284-1299.

Sulo, P., and Martin, N.C. (1993). Isolation and characterization of LIP5. A lipoate biosynthetic locus of *Saccharomyces cerevisiae*. J. Biol. Chem. **268,** 17634-17639.

Takahashi, H., Kopriva, S., Giordano, M., Saito, K., and Hell, R. (2011). Sulfur assimilation in photosynthetic organisms: molecular functions and regulations of transporters and assimilatory enzymes. Annual review of plant biology **62,** 157-184.

Theissen, U., Hoffmeister, M., Grieshaber, M., and Martin, W. (2003). Single eubacterial origin of eukaryotic sulfide:quinone oxidoreductase, a mitochondrial enzyme conserved from the early evolution of eukaryotes during anoxic and sulfidic times. Mol. Biol. Evol. **20,** 1564-1574.

Timm, S., Nunes-Nesi, A., Parnik, T., Morgenthal, K., Wienkoop, S., Keerberg, O., Weckwerth, W., Kleczkowski, L.A., Fernie, A.R., and Bauwe, H. (2008). A cytosolic pathway for the conversion of hydroxypyruvate to glycerate during photorespiration in Arabidopsis. Plant Cell **20,** 2848-2859.

Tort, F., Ferrer-Cortès, X., Thió, M., Navarro-Sastre, A., Matalonga, L., Quintana, E., Bujan, N., Arias, A., García-Villoria, J., Acquaviva, C., Vianey-Saban, C., Artuch, R., García-Cazorla, À.,

Briones, P., and Ribes, A. (2013). Mutations in the lipoyltransferase LIPT1 gene cause a fatal disease associated with a specific lipoylation defect of the 2-ketoacid dehydrogenase complexes. Hum. Mol. Genet. **23,** 1907-1915.

Trnka, D., Engelke, A.D., Gellert, M., Moseler, A., Hossain, M.F., Lindenberg, T.T., Pedroletti, L., Odermatt, B., de Souza, J.V., Bronowska, A.K., Dick, T.P., Mühlenhoff, U., Meyer, A.J., Berndt, C., and Lillig, C.H. (2020). Molecular basis for the distinct functions of redox-active and FeS-transfering glutaredoxins. Nat. Commun. **11,** 3445.

Vitvitsky, V., Kumar, R., Libiad, M., Maebius, A., Landry, A.P., and Banerjee, R. (2021). The mitochondrial NADH pool is involved in hydrogen sulfide signaling and stimulation of aerobic glycolysis. J. Biol. Chem. **296**.

Wagner, S., Behera, S., De Bortoli, S., Logan, D.C., Fuchs, P., Carraretto, L., Teardo, E., Cendron, L., Nietzel, T., Fussl, M., Doccula, F.G., Navazio, L., Fricker, M.D., Van Aken, O., Finkemeier, I., Meyer, A.J., Szabo, I., Costa, A., and Schwarzlander, M. (2015). The EF-hand Ca^{2+} binding protein MICU choreographs mitochondrial Ca^{2+} dynamics in Arabidopsis. Plant Cell **27,** 3190-3212.

Warui, D.M., Sil, D., Lee, K.-H., Neti, S.S., Esakova, O.A., Knox, H.L., Krebs, C., and Booker, S.J. (2022). *In vitro* demonstration of human lipoyl synthase catalytic activity in the presence of NFU1. ACS Bio & Med Chem Au **2,** 456-468.

Watanabe, M., Mochida, K., Kato, T., Tabata, S., Yoshimoto, N., Noji, M., and Saito, K. (2008). Comparative genomics and reverse genetics analysis reveal indispensable functions of the serine acetyltransferase gene family in Arabidopsis. Plant Cell **20,** 2484-2496.

Weger, B.D., Weger, M., Görling, B., Schink, A., Gobet, C., Keime, C., Poschet, G., Jost, B., Krone, N., Hell, R., Gachon, F., Luy, B., and Dickmeis, T. (2016). Extensive regulation of diurnal transcription and metabolism by glucocorticoids. PLoS Genet. **12,** e1006512.

Wirtz, M., Droux, M., and Hell, R. (2004). *O*-acetylserine (thiol) lyase: an enigmatic enzyme of plant cysteine biosynthesis revisited in *Arabidopsis thaliana*. J. Exp. Bot. **55,** 1785-1798.

Yi, X., and Maeda, N. (2005). Endogenous production of lipoic acid is essential for mouse development. Cell. Mol. Biol. **25,** 8387-8392.

Zhang, H., Zhang, T.T., Liu, H., Shi, D.Y., Wang, M., Bie, X.M., Li, X.G., and Zhang, X.S. (2018). Thioredoxin-mediated ROS homeostasis explains natural variation in plant regeneration. Plant Physiol. **177,** 434-434.

Zhang, X., Xin, Y., Chen, Z., Xia, Y., Xun, L., and Liu, H. (2021). Sulfide-quinone oxidoreductase is required for cysteine synthesis and indispensable to mitochondrial health. Redox Biol. **47,** 102169.

SUPPLEMENTAL DATA

Supplemental Information includes 20 Figures and 6 Tables.

A

Line	Full line name	Genetic background	Reference
WT	Wild type	Col-0	
grxs15-1	*grxs15-1*	SALK_112767	Ströher *et al.*, 2016; Moseler *et al.*, 2021
amiR	GRXS15^{amiR}	Col 0	Ströher et *al.*, 2016
K83A #3	*grxs15-3 UBQ10pro:GRXS15 K83A #3*	GK-837C05	Moseler et *al.*, 2015
K83A #4	*grxs15-3 UBQ10pro:GRXS15 K83A #4*	GK-837C05	Moseler *et al.*, 2015

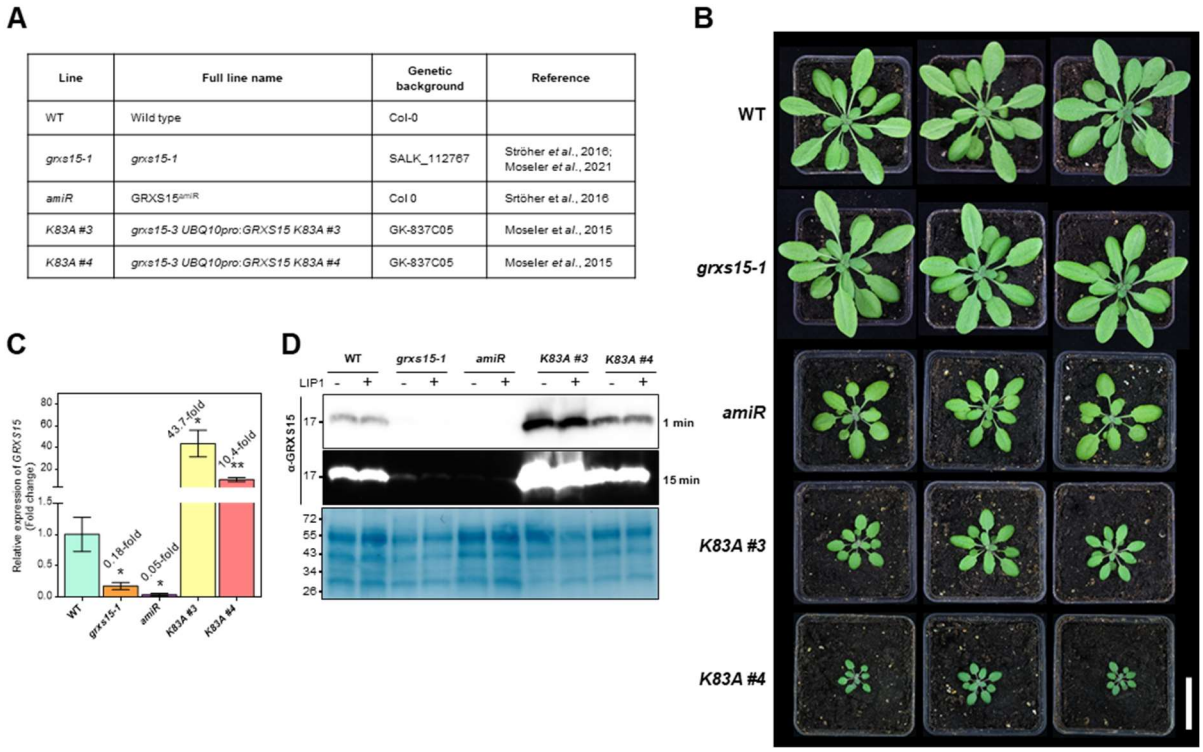

Supplemental Figure S1. Phenotypes of different *grxs15* mutants. A, The mutant collection includes two knock-down lines, *grxs15-1* and GRXS15^{amiR} (*amiR*), with decreased amounts of *GRXS15* transcript of about 18 % and 5 %, respectively. In a complementary approach, GRXS15 K83A protein variants were used to rescue the embryo lethal *grxs15-3* (GK-837C05) null mutant in line *#3* and *#4* are driven by a strong ubiquitous promoter (Moseler *et al.*, 2015). **B,** Representative photos of 5-week-old plants grown on soil under long-day conditions. Scale bar: 3 cm. **C**, Relative expression level of *GRXS15* transcripts determined by qRT-PCR in wild type (WT) and the four *grxs15* mutants shown in panel b. The presented data are means ± SEM (n = 3). Student's t-test (α = 0.05) has been performed for all mutants (pairwise comparison to wild type) and significant differences are indicated at P < 0.1 (*) and P < 0.01 (**). Changes in comparison to expression in the wild type are shown in fold-changes. *P*-values: Supplemental Data Set 6. **D,** Protein gel blot analysis with primary antibodies raised against GRXS15. 15 µg of mitochondria isolated from seedlings grown in hydroponic culture were used. The blot is shown with two exposure times. Exposure for 15 minutes allows detection of minute amounts of GRXS15 in *grxs15-1* and *amiR*. Amido Black staining of the PVDF membrane serves as loading control. The plant phenotypes (panel b) and the blot exposed for 1 min are also shown in Figure 3 of the main manuscript.

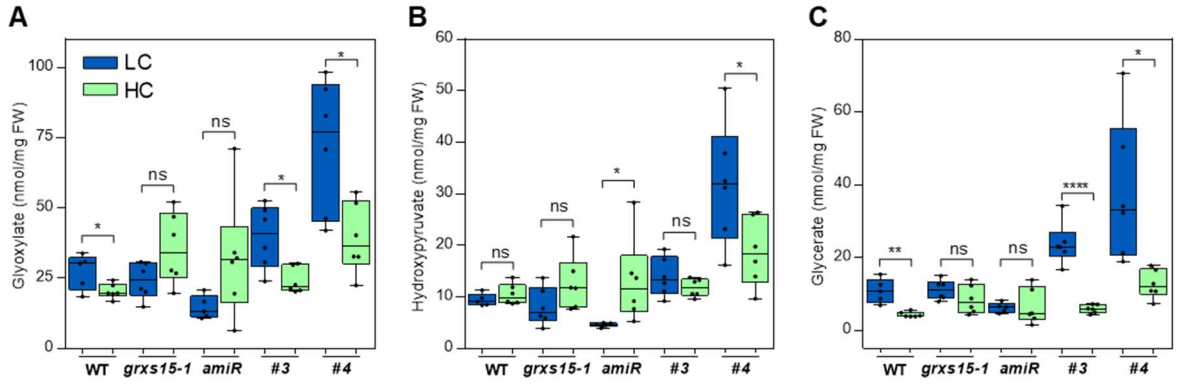

Supplemental Figure S2. Suppression of photorespiration has an impact on photorespiratory intermediates glyoxylate, hydroxypyruvate and glycerate in mutants complemented with GRXS15 K83A. *Metabolic amounts of 8-week-old plants of hydroxypyruvate (**A**), glycerate (**B**) and glyoxylate (**C**) in wild type and grxs15 mutants grxs15-1, amiR, K83A #3 and #4 grown in low carbon dioxide condition (LC: 390 ppm CO_2) and high carbon dioxide condition (HC: 5,000 pm CO_2). Box plots show the median as centre line with the box for the first to the third quartile and whiskers indicating min and max values of the whole dataset (n = 5-6). Asterisks represent significant differences (*=P ≤ 0.1, ****= P ≤ 0.0001, ns: not significant) calculated according to* Student's *t*-test (α = 0.05). *P*-values: Supplemental Data Set 7.

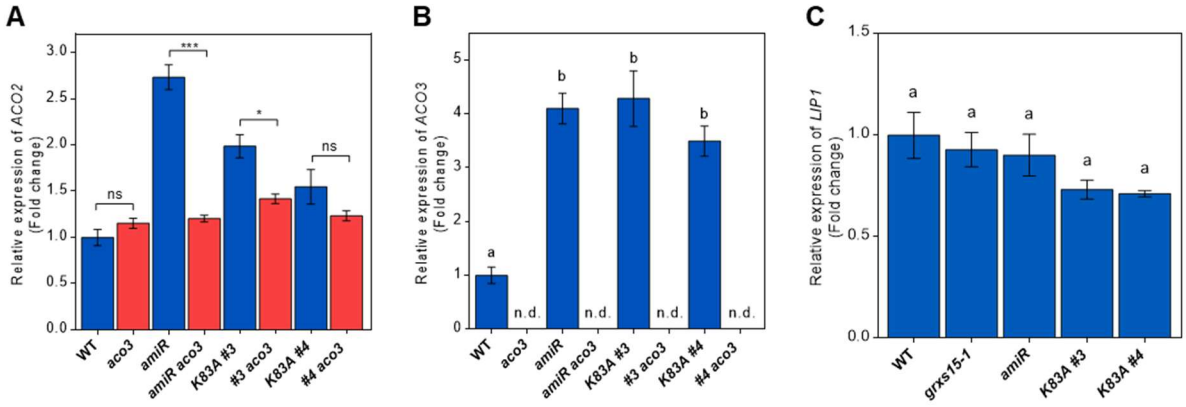

Supplemental Figure S3. Expression level of *ACO2*, *ACO3* and *LIP1* in the *grxs15* mutants. Relative expression level of *ACO2* (**A**), *ACO3* (**B**) and *LIP1* (**C**) transcripts determined by qRT-PCR in wild type and the four *grxs15* mutants. The presented data are means ± SEM (*n* = 3). Student's *t*-test has been performed for all mutants against the wild type (α = 0.05), different letters indicate significant statistically different groups and asterisks indicate P < 0.1 (*), P < 0.001 (***), *ns: not significant and n.d.: not detected*. *P*-values: Supplemental Data Set 8.

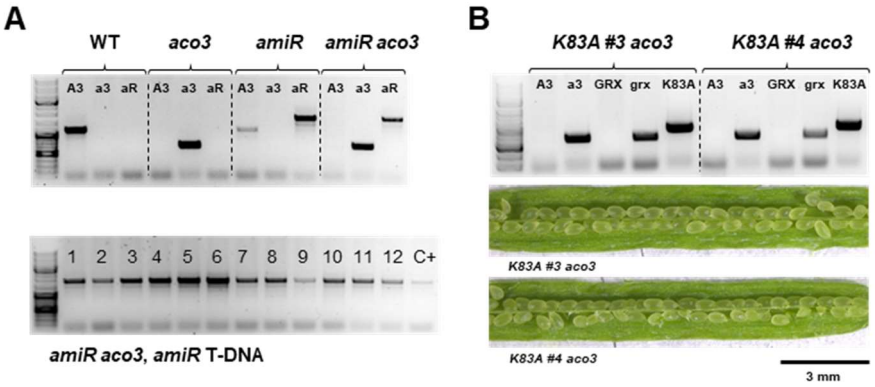

Supplemental Figure S4. Confirmation of genotypes for crosses of *aco3* and *grxs15.* A, Genotyping of the cross *amiR* × *aco3*. A3: *ACO3* WT allele, a3: *aco3* T-DNA; aR: *amiR* T-DNA. The panel at the bottom shows PCR results for 12 independent plants to confirm the selected line *amiR* × *aco3* as homozygous for *amiR*. **B,** Genotyping of the crosses *K83A #3* and *#4* × *aco3*. GRX: *GRXS15* WT allele; K83A: T-DNA carrying the lysine mutation. The panels at the bottom show opened siliques to confirm the absence of aborted seeds.

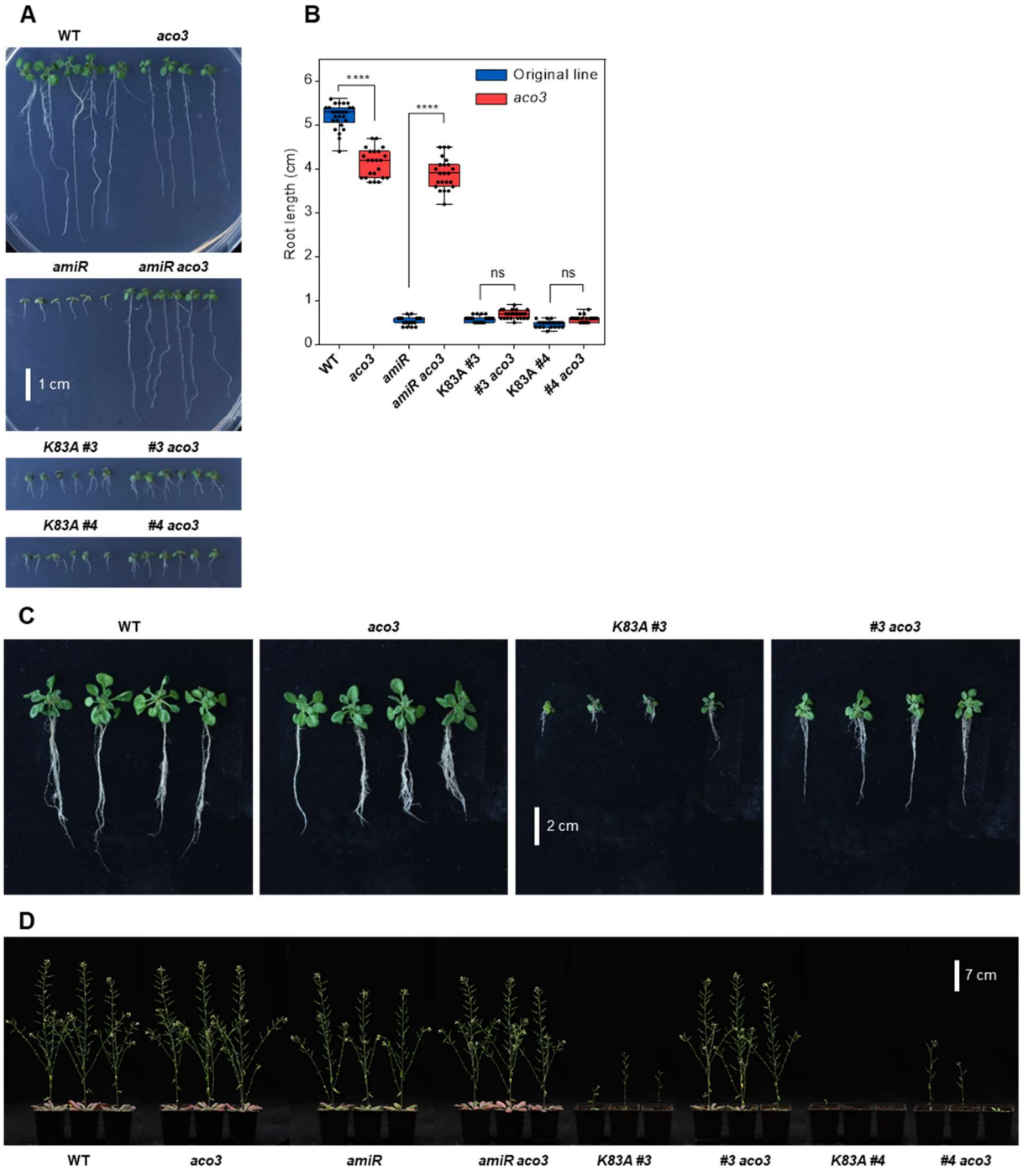

Supplemental Figure S5. Loss of *ACO3* partially suppressed the dwarfism in *grxs15* mutants. A, 10-day-old seedlings grown on ½ MS vertical agar plates under long-day conditions. **B,** Root length analysis (*n* = 22-26). Data for WT and the different *grxs15* mutants are shown in blue, data for *aco3* and the respective crosses are shown in red. Asterisks indicate P < 0.0001 (****) and ns: not significant, calculated according to Student's *t*-test (α = 0.05). *P*-values: Supplemental Data Set 9. **C,** 17-day-old seedlings grown on vertical agar plates under long-day conditions. **D,** Photo of three representative 8-week-old plants of *aco3* and crosses compared with their respective parental lines. All plants were grown on soil under long-day conditions.

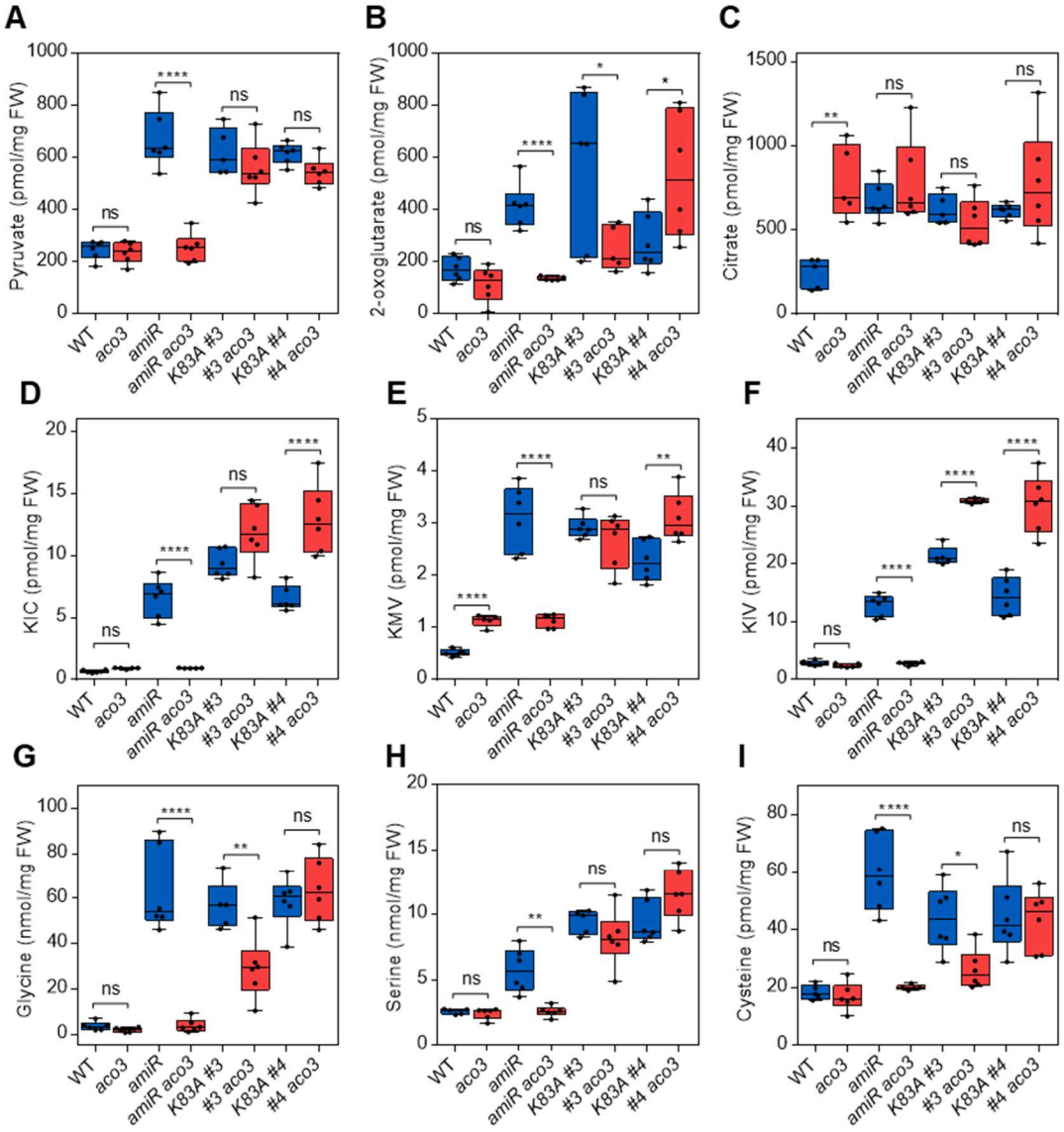

Supplemental Figure S6. Loss of *ACO3* has an impact on the metabolite signature. Metabolite signatures of 8-day-old seedlings. Analysis of TCA cycle metabolites pyruvate (**A**) and 2-OG (**B**), which are substrates of PDC and OGDC, respectively, and citrate (**C**), which is converted by aconitases; three branched chain α-keto acids (KIC, KMV and KIV) (**D-F**), which are all degraded by BCDHC, and the amino acids glycine (**G**) and serine (**H**) that are linked to photorespiration, and the activity of the mitochondrial glycine dehydrogenase complex (GDC). Cysteine (**i**) is synthesized from its immediate precursor serine. All box plots show the median as centre line with the box for the first to the third quartile and whiskers indicating min and max values of the whole dataset (n = 5-6). Asterisks represent significant differences (*=$P \leq 0.1$, **= $P \leq 0.01$ ***= $P \leq 0.001$ ****= $P \leq 0.0001$, ns: not significant) calculated according to one-way ANOVA with Tukey's multiple comparisons test (α = 0.05). Data for WT and the different *grxs15* mutants are shown in blue, data for *aco3* and the respective crosses are shown in red. *P*-values: Supplemental Data Set 10.

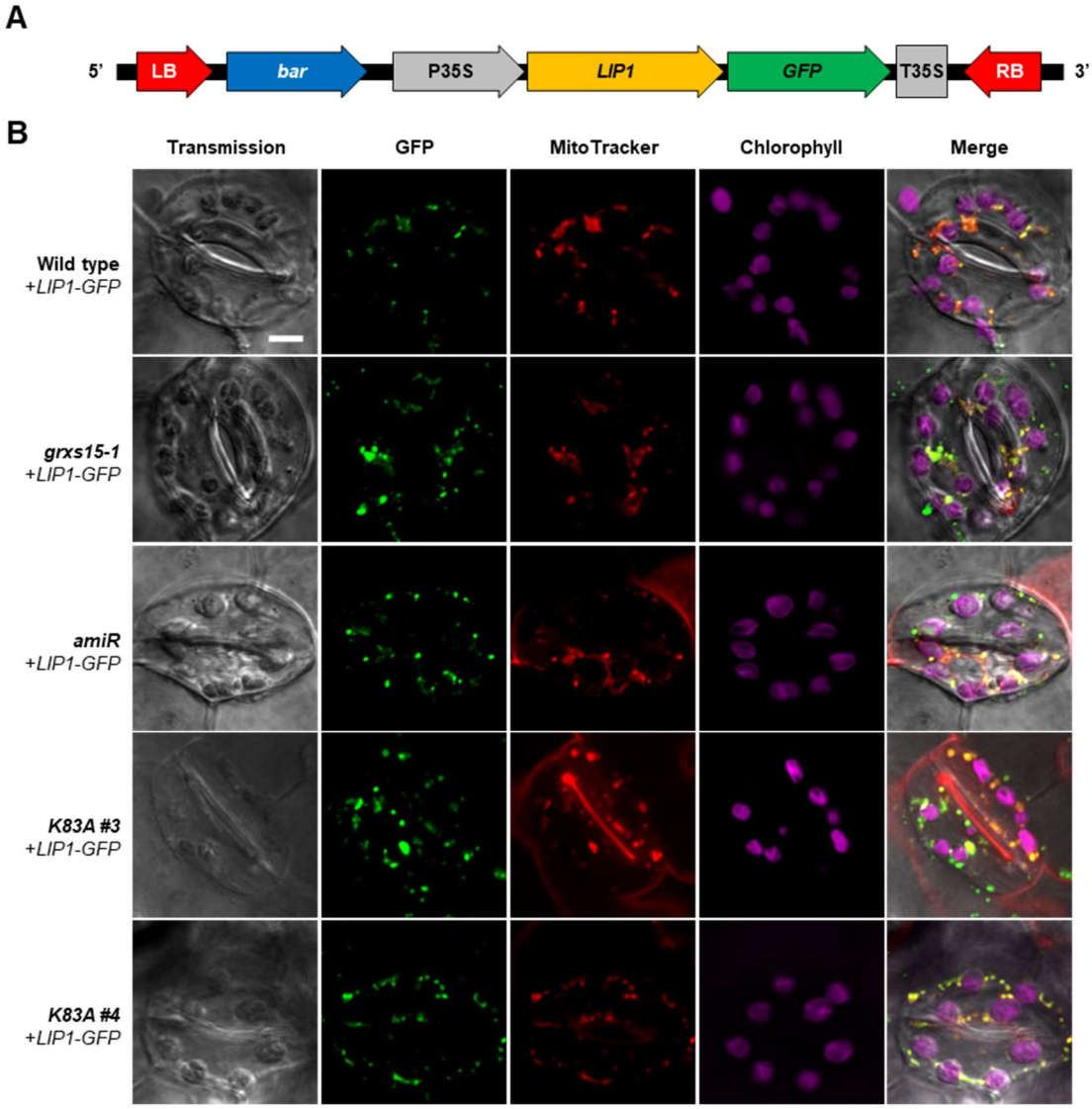

Supplemental Figure S7. Transformed plants expressed LIP1-GFP in mitochondria. A, Representation of the construct used for the overexpression of LIP1 with a C-terminal GFP for the subcellular localization. The gene coding for *LIP1* includes the original signal peptide for mitochondrial targeting. **B,** Confocal microscopy images show stomata from 7-day-old seedlings stably expressing LIP1-GFP in different genetic backgrounds (wild type, *grxs15-1*, *amiR*, *K83A #3* and *#4*). The figure shows transmission images, GFP fluorescence (λ_{ex} = 488 nm; λ_{em} = 520 nm), MitoTracker Orange staining for mitochondria (λ_{ex} = 543 nm; λ_{em} = 597 nm), chlorophyll autofluorescence (λ_{ex} = 633 nm; λ_{em} = 675 nm) and the merged images. For each line one representative set of images selected from three independent transgenic lines is shown. Scale bar: 5 µm.

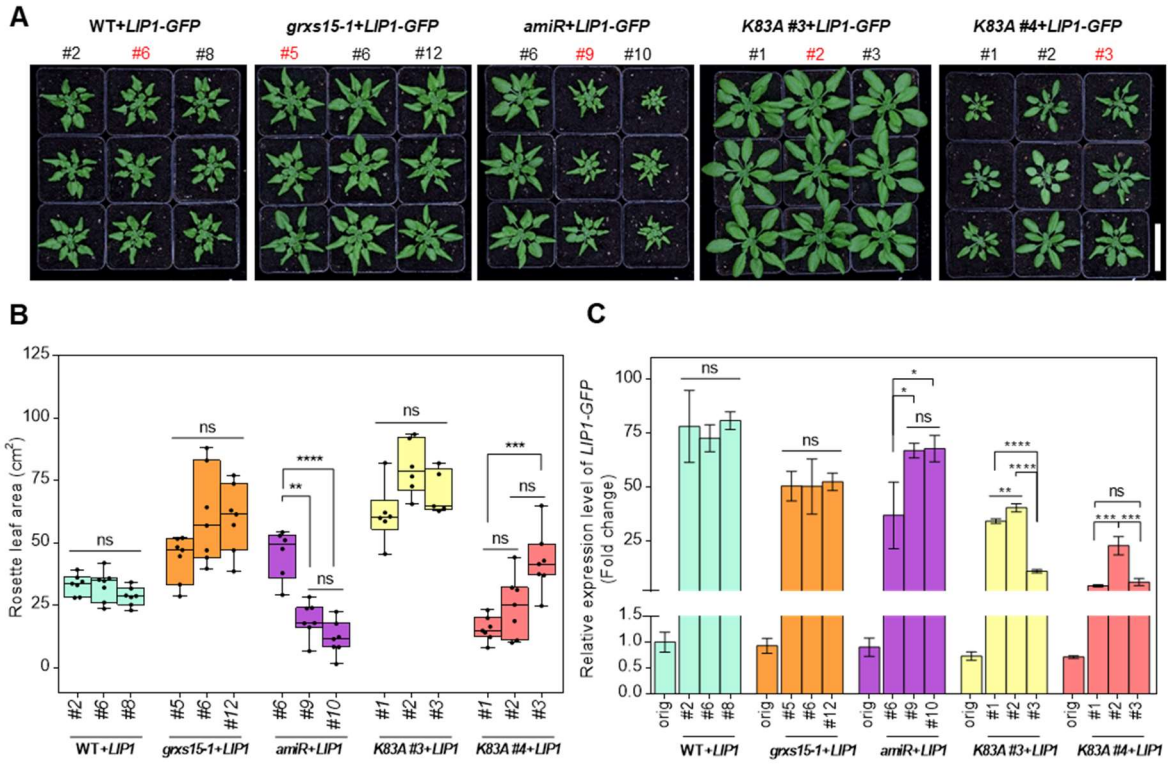

Supplemental Figure S8. Overexpression of *LIP1-GFP* results in phenotypic effects that depend on the respective genetic background and vary in several independent lines. A, 5-week-old plants of three independent stable lines transformed with pSS01_*35S*$_{pro}$*:LIP1-GFP* grown under long-day conditions (wild type+*LIP1-GFP*: numbers #2, #6, #8; *grxs15-1+LIP1-GFP*: #5, #6, #12; *amiR+LIP1-GFP*: #6, #9, #10; *K83A #3+LIP1-GFP*: #1, #2, #3, and *K83A #4+LIP1-GFP*: #1, #2, #3). *LIP1* overexpression lines chosen for all further phenotypic characterization, metabolite analyses and transformation with *OAS-TL C* are indicated with red numbers. Scale bar: 5 cm. **B,** Rosette area of the three independent stable lines after four weeks on soil under log-day conditions (*n* = 8). Box plots show the median as center line with the box for the first to the third quartile and whiskers indicating min and max values of the whole dataset. **C,** Relative expression level of *LIP1* transcripts determined by qRT-PCR in wild type and the four *grxs15* mutants. RNA was isolated from 10-day-old seedlings. The presented data are means ± SEM (*n* = 3). Different letters indicate significantly different groups calculated according to one-way ANOVA with Tukey's multiple comparisons test separately for each genotype plus the respective genetic background (orig) (α = 0.05). *P*-values: Supplemental Data Set 11.

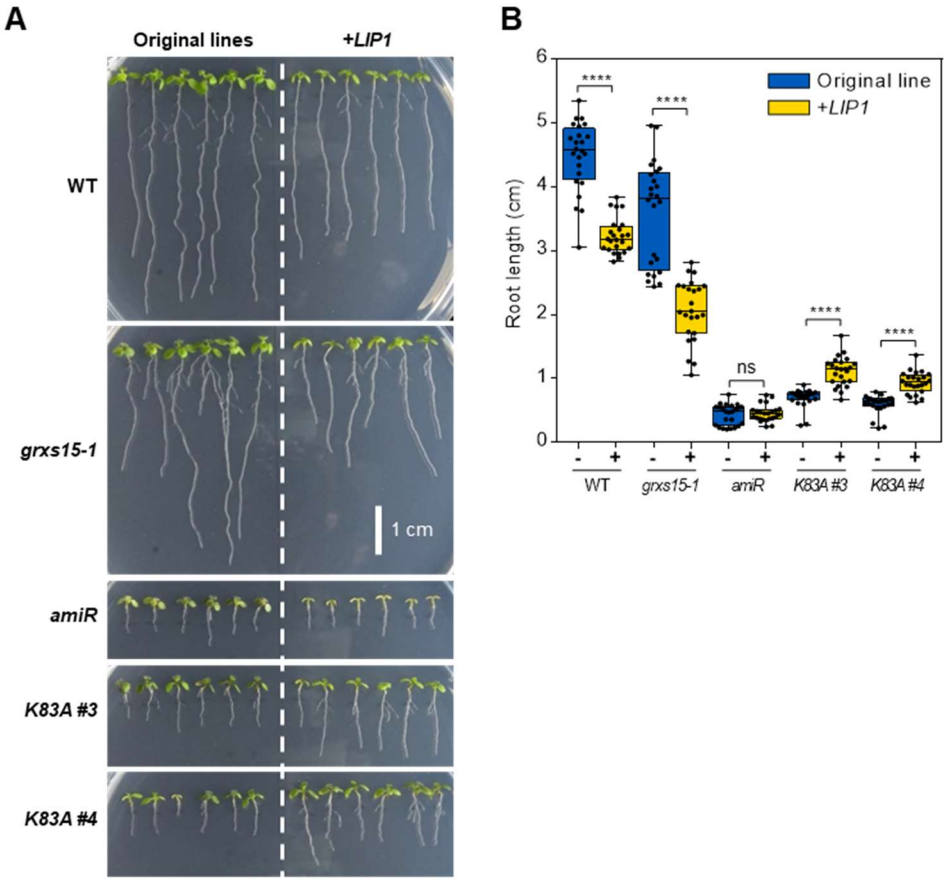

Supplemental Figure S9. *LIP1* overexpression affects root length. A, 10-day-old seedlings grown on ½ MS vertical agar plates in long-day conditions. **B,** Analysis of root length of *LIP1-GFP* overexpression lines compared with their respective genetic background. The b*ox plot shows the median as centre line with the box for the first to the third quartile and whiskers indicating min and max values of the whole dataset (n = 24).* Asterisks indicate P < 0.0001 (****) and ns: not significant, calculated according to Student's *t*-test (α = 0.05). *P*-values: Supplemental Data Set 12.

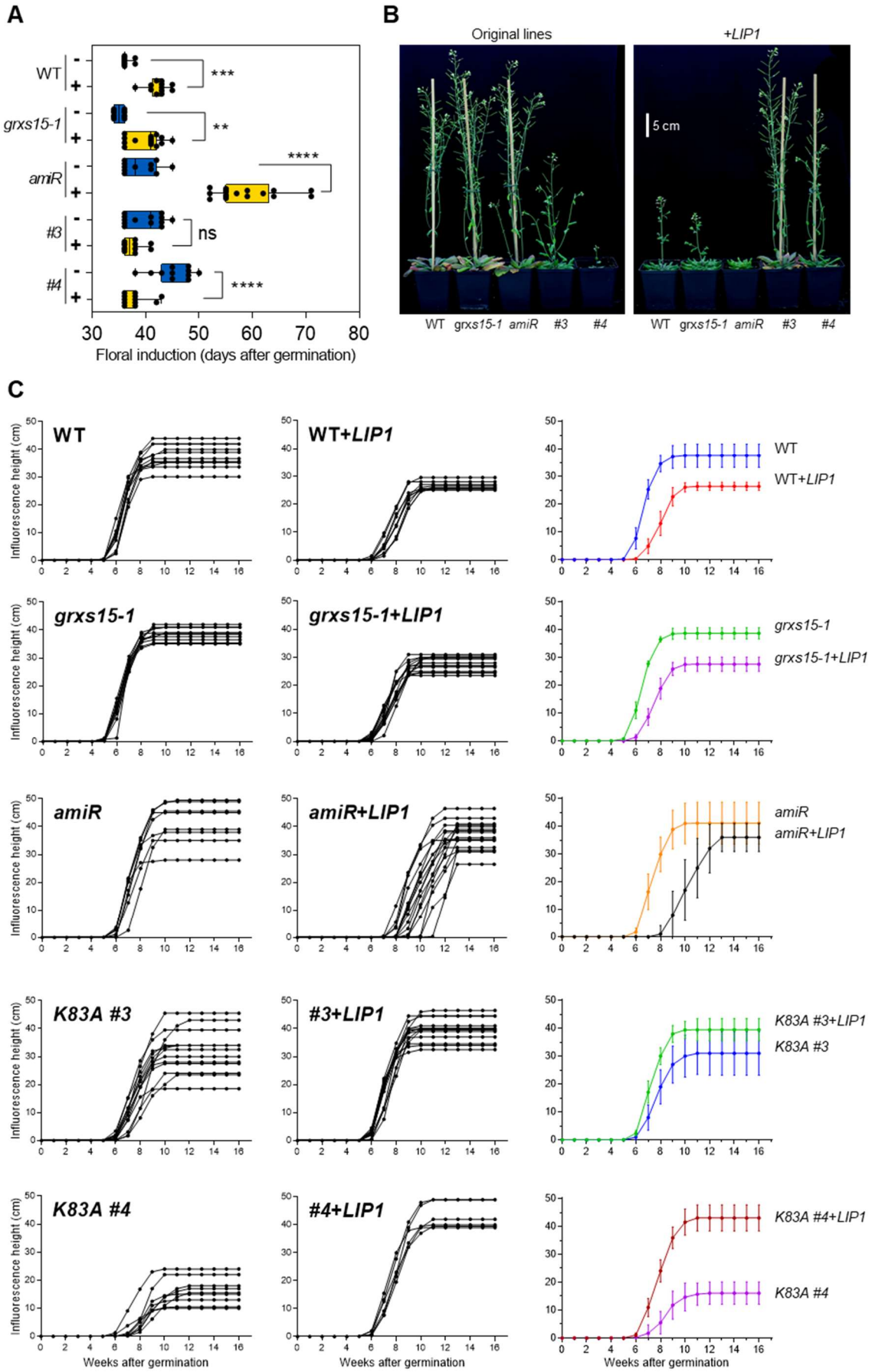
A
WT
grxs15-1
amiR
#3
#4
***
**
****
ns
****
30 40 50 60 70 80
Floral induction (days after germination)
B
Original lines
+LIP1
5 cm
WT grxs15-1 amiR #3 #4
WT grxs15-1 amiR #3 #4
C
WT
WT+LIP1
grxs15-1
grxs15-1+LIP1
amiR
amiR+LIP1
K83A #3
#3+LIP1
K83A #3+LIP1
K83A #3
K83A #4
#4+LIP1
K83A #4+LIP1
K83A #4
Influorescence height (cm)
Weeks after germination

Supplemental Figure S10. *LIP1* overexpression affects floral induction and inflorescence development. A, Floral induction. The data show the time after germination when the developing flower bud became visible. *The box plot shows the median as centre line with the box for the first to the third quartile and whiskers indicating min and max values of the whole dataset (n = 11-17). Asterisks represent significant differences (**= P ≤ 0.01, ***= P ≤ 0.001, ****= P ≤ 0.0001, ns: not significant) calculated according to* one-way ANOVA with Tukey's multiple comparisons test (α = 0.05). Data for WT and the different *grxs15* mutants are shown in blue, data for the respective lines overexpressing *LIP1* are shown in yellow. **B** and **C,** Documentation of inflorescence development. (**B**) Flower stalk height nine weeks after germination for non-transformed control plants (left) and plants overexpressing *LIP1-GFP* (right). All plants were grown on soil under long-day conditions. (**C**) Development of the main inflorescence. Plants were grown continuously under long-day conditions and measured three times per week. Panels on the right show the average inflorescence height ± SD calculated from data for individual plants shown on the left (*n* = 6-17). *P*-values: Supplemental Data Set 13.

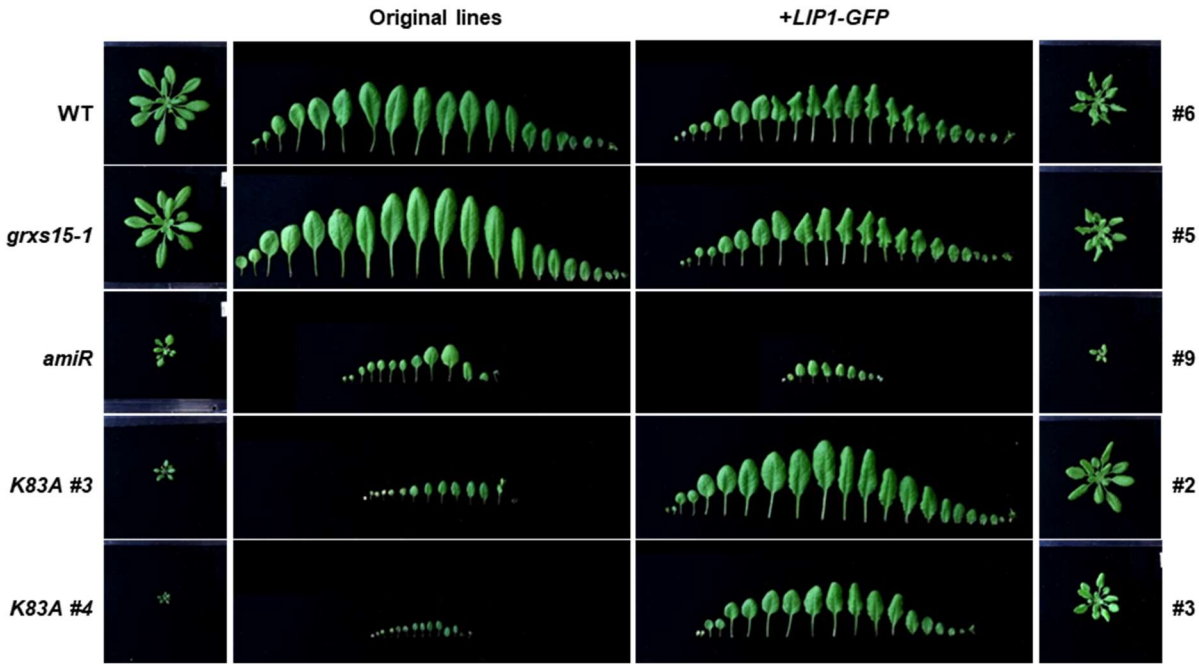

Supplemental Figure S11. *LIP1* overexpression induced a curly leaf phenotype. Plants stably overexpressing *LIP1-GFP* were grown on soil under long-day conditions for 32 days. At the time of harvest, the root system was removed and rosettes were dissected to isolate all leaves according to their developmental age from the older leaves on the left to the youngest leaves on the right. The numbers on the right identify the selected lines (see Supplemental Figure S8A).

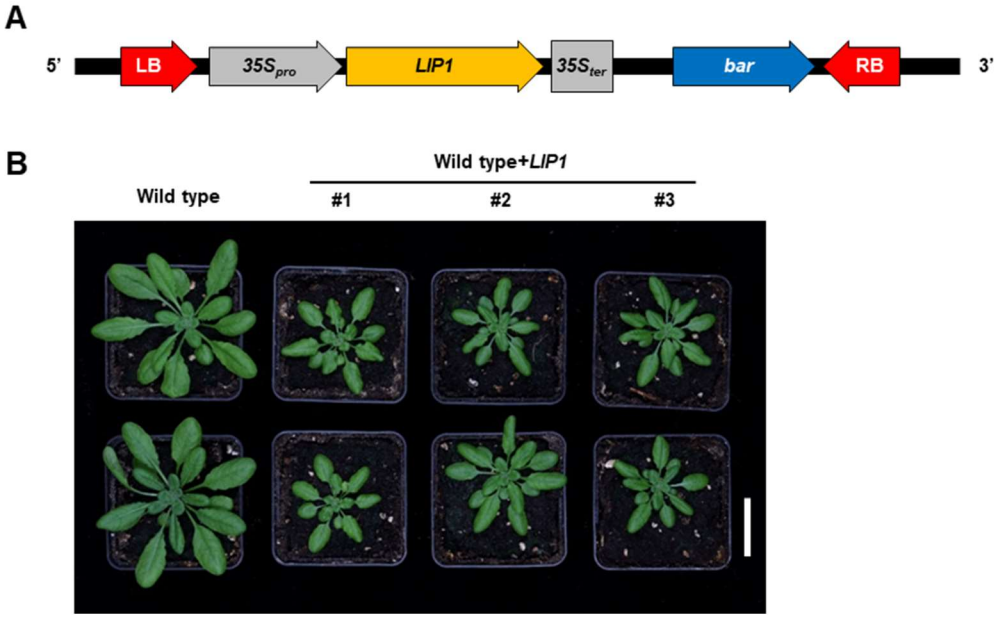

Supplemental Figure S12. Overexpression of *LIP1* without a GFP tag is deleterious. A, Schematic representation of the construct used for the overexpression of *LIP1* without GFP. The T-DNA is 3,890 bp long and uses the vector pB7WG2 as backbone (Karimi *et al.*, 2002). **B,** Representative images of three independent stable lines transformed with pB7WG2_$35S_{pro}$:*LIP1* grown for five weeks under long-day conditions. Scale bar: 3 cm.

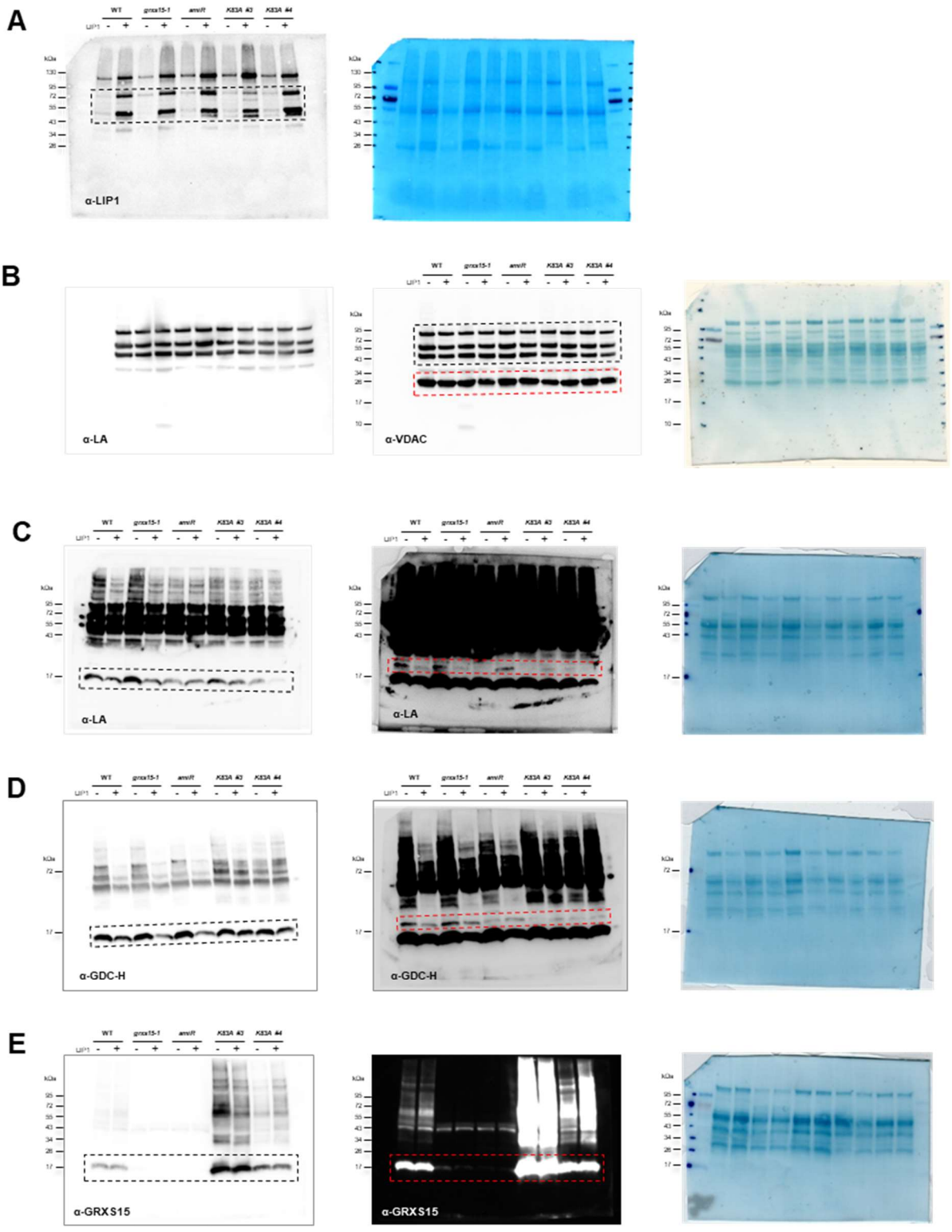

Supplemental Figure S13. Uncropped western blot images. A, 15 µg of proteins extract from mitochondria isolated from plants grown on soil were transferred with semidry blotting on PVDF membrane which was incubated with a 1:1,000 dilution of primary antibody raised against LIP1 (Moseler *et al.*, 2021) for 2 h at room temperature. The dashed rectangle delineates the area shown in Figure 3G. **B,** 15 µg of protein extracted from mitochondria isolated from seedlings grown in hydroponic were transferred with semidry blotting on PVDF membrane which was incubated with a 1:1,000 dilution of primary antibody raised against lipoylated proteins (Abcam, ab58724) over-night at 4 °C. The same membrane was re-incubated with 1:5,000 dilution of primary antibody raised against VDAC1-5 HRP-conjugated (Agrisera, AS07 201-HRP). The dotted rectangles delineate the areas for lipoylated proteins

(grey) and VDAC (red) shown in Figure 3G. **C,** 20 µg of protein extracted from mitochondria isolated from seedlings grown in hydroponics were transferred by wet blotting onto a PVDF membrane, which was incubated with a 1:500 dilution of primary antibody raised against lipoylated proteins for 3 h at room temperature. The dotted rectangles delineate the areas shown in Figure 3G. The grey line shows the lipoylated GDC-H isoforms 1 and 3 and in the red line part of the same blot after prolonged exposure time to highlight the isoform GDC-H2. **D,** Similar to c, 20 µg of protein extracted from mitochondria isolated from seedlings grown in hydroponic were transferred with wet blotting on PVDF membrane which was incubated with a 1:5,000 dilution primary antibody raised against GDC-H proteins (Agrisera As05 074) for 3 h at room temperature. The grey dashed rectangle highlights GDC-H isoforms 1 and 3 and the red rectangle a prolonged exposure time to highlighted the isoform GDC-H2. Both areas are shown in Figure 3G. **E,** 20 µg of protein extracted from mitochondria isolated from seedlings grown in hydroponic were transferred with wet blotting on PVDF membrane which was incubated with a 1:2,500 dilution of primary antibody raised against GRXS15 (Moseler *et al.*, 2015) for 2 h at room temperature. The dotted rectangle delineates the area shown in Figure 3G and Supplemental Figure S1. Highlighted in red is the same part of the blot with an extended exposure time as displayed in Supplemental Figure S1.

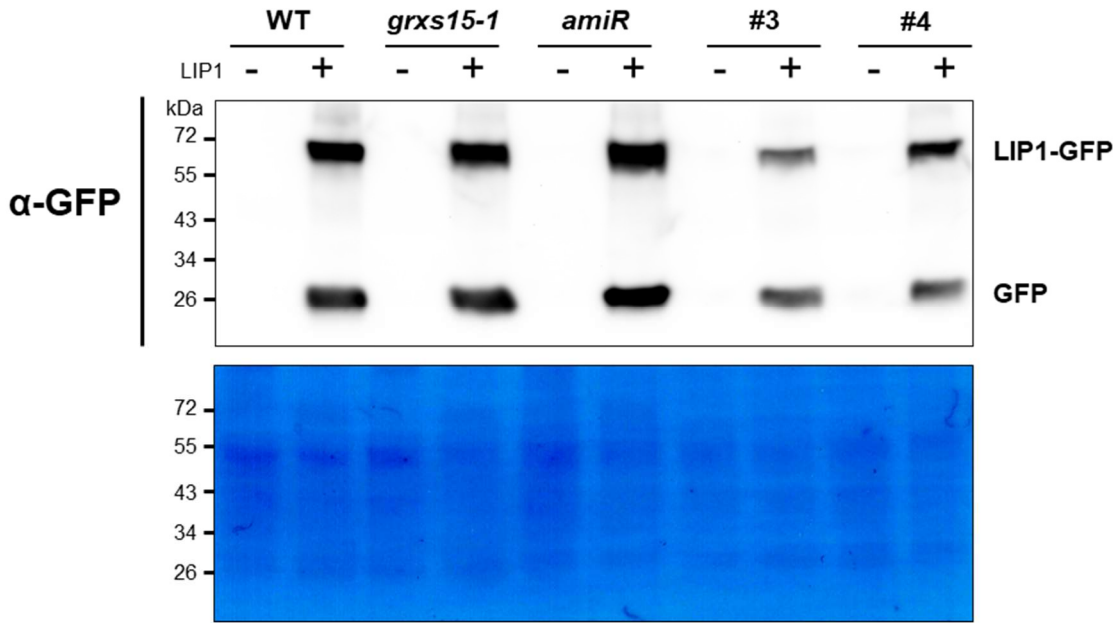

Supplemental Figure S14. Protein gel blot analysis with antiserum raised against GFP. Protein gel blot analysis with primary antibodies raised against GFP (Thermo, A-6455). 15 µg of protein extracted from mitochondria isolated from seedlings grown in hydroponic culture were loaded. Amido Black staining of the PVDF membrane serves as loading control. The two bands indicate that a fraction of the LIP1-GFP fusion protein got cleaved.

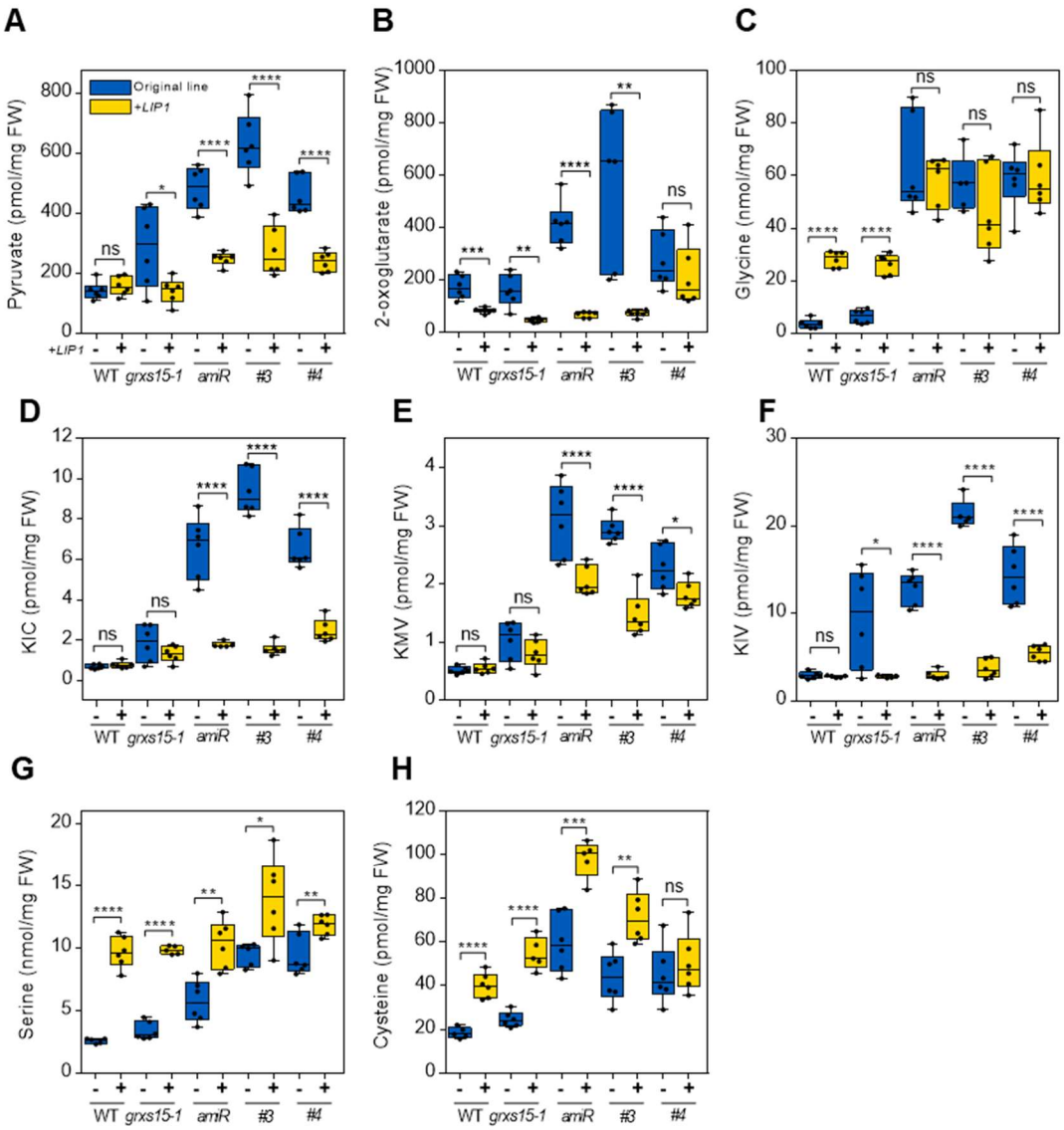

Supplemental Figure S15. Overexpression of *LIP1* causes pronounced metabolic changes. A-F, Concentration of substrates of LA-dependent mitochondrial enzymes: pyruvate as the substrate of PDC (**A**), 2-oxoglutarate as the substrate of OGDC (**B**), glycine as the substrate of GDC (**C**), and three branched chain α-keto acids (**D-F**), which are all metabolized by BCDHC. **G** and **H,** Serine and cysteine, which are formally derived in parts from glycine. Metabolites were extracted from 8-day-old seedlings *grown under long-day conditions. The box plots show the median as centre line with the box for the first to the third quartile and whiskers indicating min and max values of the whole dataset (n = 5-6).* Asterisks represent significant differences (*=$P \leq 0.1$, **= $P \leq 0.01$, ***= $P \leq 0.001$, ****= $P \leq 0.0001$, ns: not significant) calculated according to Student's *t*-test (α = 0.05). *P*-values: Supplemental Data Set 14. Data for WT and the different *grxs15* mutants are shown in blue (-), data for the respective lines overexpressing *LIP1* are shown in yellow (+).

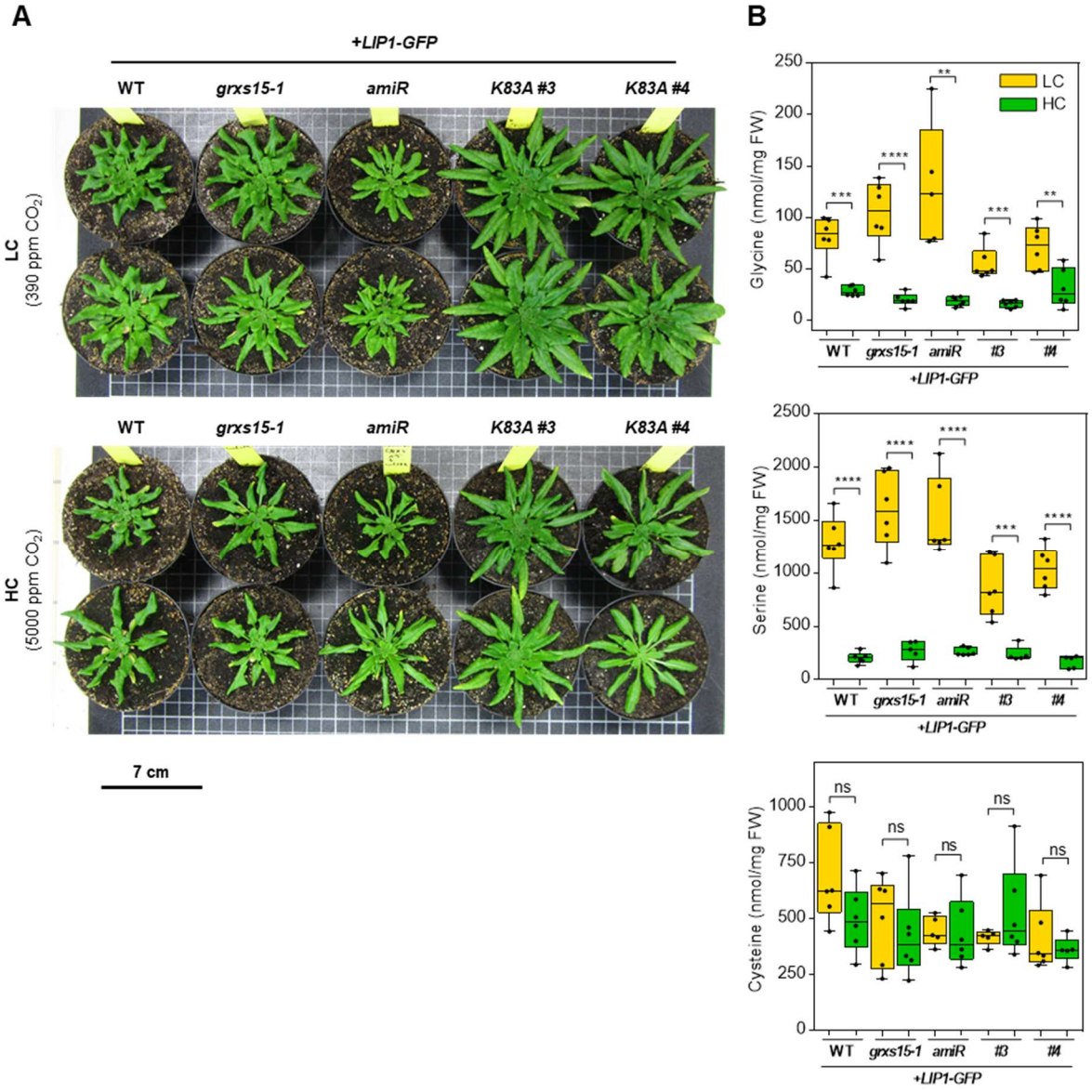

Supplemental Figure S16. High CO_2 has no beneficial effect on *LIP1* overexpression lines. A, Phenotype comparison between 8-week-old wild type (WT) and *grxs15* mutants stably overexpressing *LIP1-GFP* grown in normal air and high CO_2 (390 and 5,000 ppm, respectively) and a 12/12-hour day/night light regime. **B,** Content of glycine, serine and cysteine of 8-week-old plants grown in low (LC, shown in yellow) and high carbon dioxide condition (HC, shown in green) (n = 5-6) (for absolute values see P-values: Supplemental Data Set 15). Asterisks represent significant differences (**= $P \leq 0.01$ ***= $P \leq 0.001$ ****= $P \leq 0.0001$, ns: not significant) calculated according to Student's t-test ($\alpha = 0.05$).

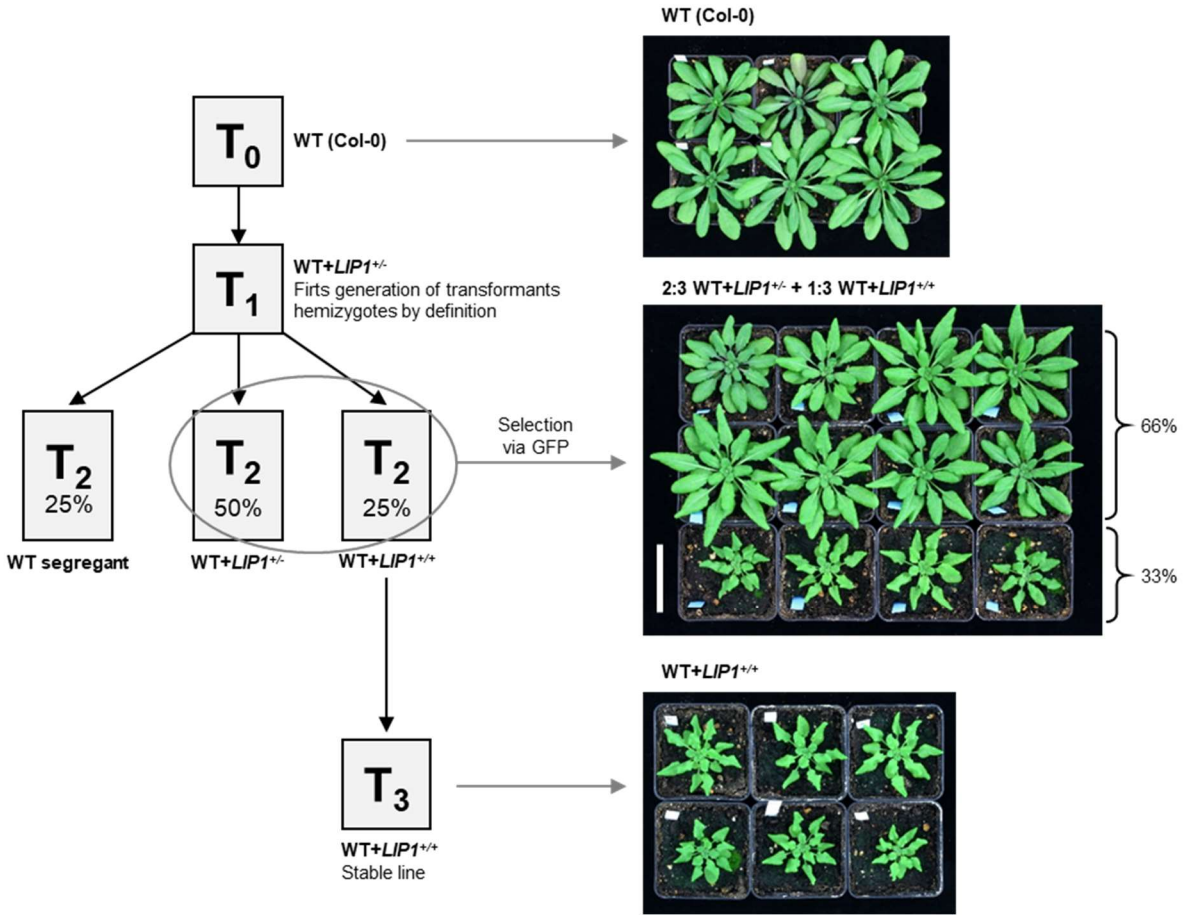

Supplemental Figure S17. Overexpression of *LIP1* has a gene dosage-dependent effect on wild type (WT) plants. Representative picture of 5-week-old WT plants overexpressing *LIP1-GFP* in homozygosis (+/+) and hemizygosis (+/-) compared with the original WT. T_0 WT plants were transformed for *LIP1-GFP* overexpression, T_1 plants were selected via herbicide resistance (BASTA). T_2 segregated and transformants were selected by visual inspection for GFP fluorescence. Non-fluorescent WT segregants (25 %) were removed and the remaining fluorescent individuals selected (75 %) subsequently phenotypically separated into two classes presumed to be hemizygous (66 %) and homozygous (33 %) for the *LIP1-GFP* overexpression. Homozygosity was confirmed in T_3 populations. Scale bar: 5 cm.

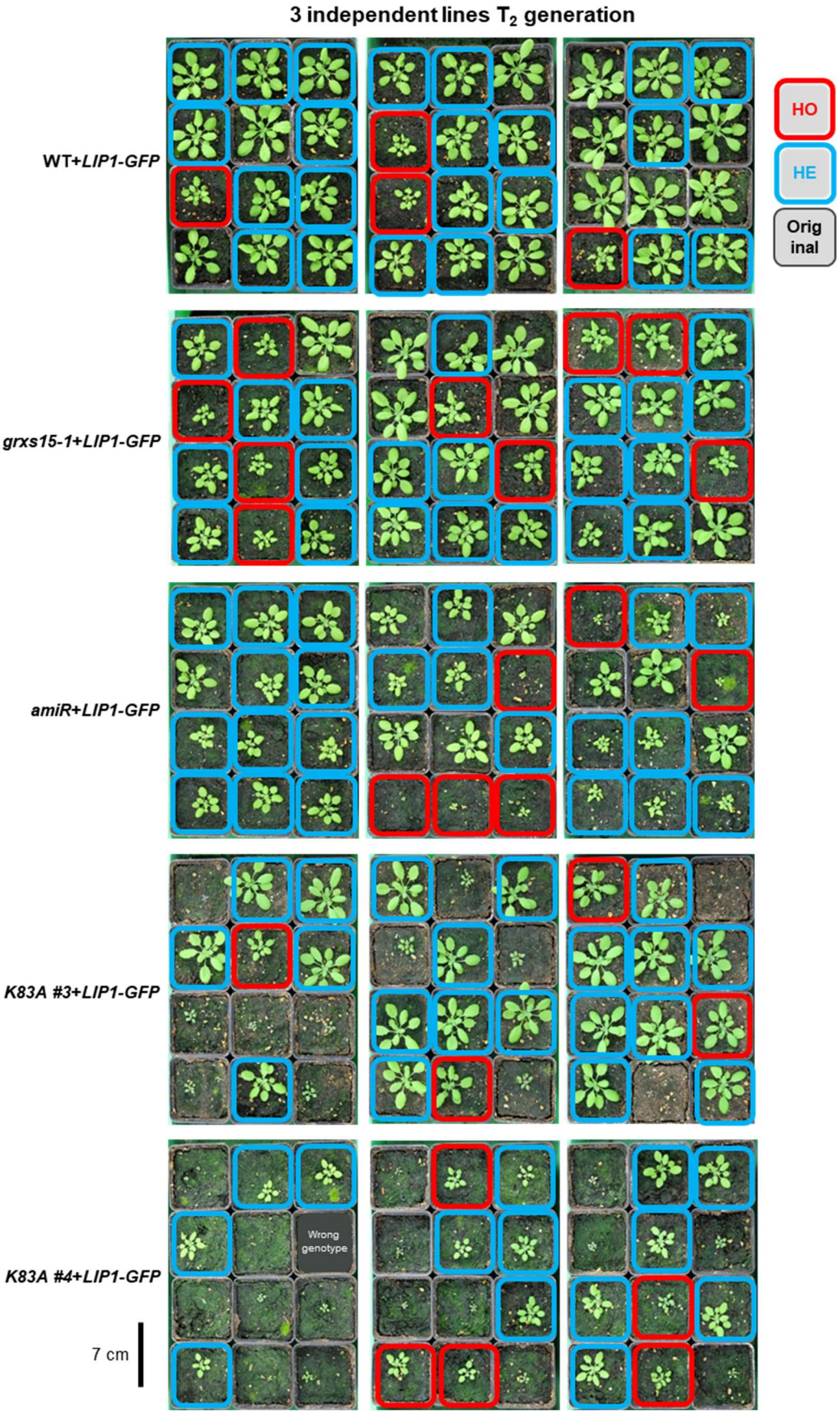
3 independent lines T2 generation
WT+LIP1-GFP
grxs15-1+LIP1-GFP
amiR+LIP1-GFP
K83A #3+LIP1-GFP
K83A #4+LIP1-GFP
Wrong genotype
7 cm
HO
HE
Orig inal

Supplemental Figure S18. Overexpression of *LIP1* has a gene dosage-dependent effect on WT and GRXS15-deficient mutants. Photos of 4-week-old plants from the screening of the second generation (T_2) for *LIP1-GFP* overexpression. Twelve plants of each independent line selected per genotype were grown on soil in standard long-day conditions. The next generation (T_3) was then analysed via GFP to determine the zygosity of the respective mother plant (100 % fluorescent seedlings: homozygotes; 75 % fluorescent seedlings: hemizygotes; 0 % fluorescent seedlings: WT segregants). Scale bar: 7 cm.

A

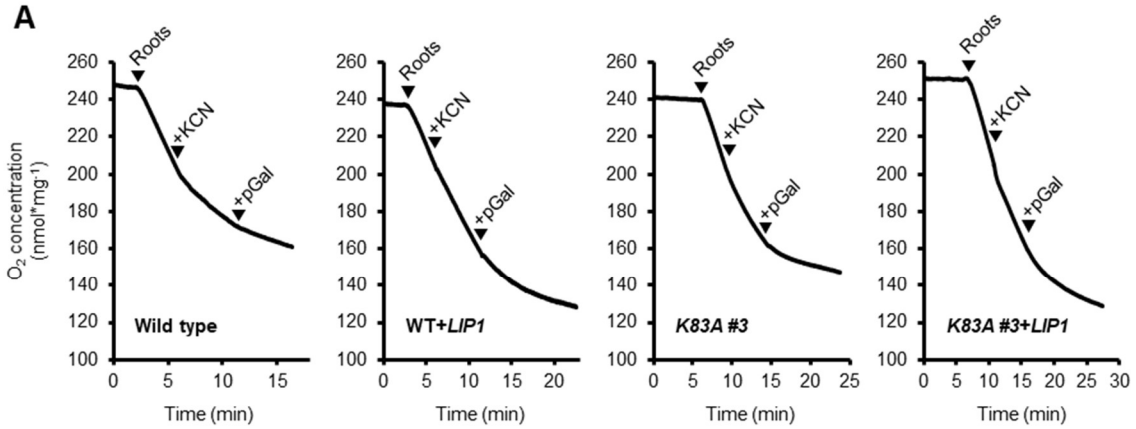

B

Line	Repl.	DW (mg)	Baseline	Roots	KCN	pGal
WT	#2	5.9	0.08	2.10	0.75	0.31
	#3	4.3	0.01	1.77	0.91	0.19
	#4	6.3	0.10	1.35	0.64	0.15
	#5	7.7	0.06	1.06	0.55	0.19
WT+*LIP1*	#1	6.2	0.05	3.20	2.41	0.27
	#2	4.8	0.08	1.92	1.77	0.19
	#3	5.3	0.05	2.06	1.56	0.22
	#4	10.3	0.04	2.00	1.58	0.08
K83A #3	#1	5.6	0.08	1.85	1.34	0.24
	#2	5.5	0.02	2.37	1.10	0.21
	#3	9.2	0.04	1.79	0.73	0.07
	#4	6.3	0.09	1.23	0.48	0.14
	#5	5.4	0.11	2.21	0.92	0.22
#3+LIP1	#1	7.2	0.04	0.90	0.58	0.10
	#2	6.9	0.04	1.20	0.60	0.09
	#3	8	0.03	1.59	0.94	0.18
	#4	7.9	0.04	1.16	0.59	0.07
	#5	6.9	0.04	1.62	1.03	0.14

C

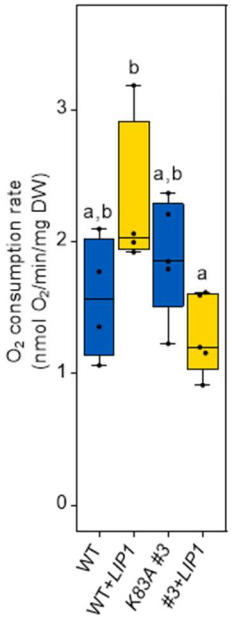

Supplemental Figure S19. Overexpression of *LIP1* has an impact on respiration of roots. A, Exemplary respirograms of four genotypes (absolute values highlighted in grey, on table in (**B**). Roots were cut from 16-day-old seedlings grown on ½ MS vertical agar plates and oxygen consumption was followed by time with a Clark-type oxygen electrode. After recording the basal root respiration without inhibitors (baseline), arrows indicate the addition of roots, KCN (potassium cyanide; final concentration 4 mM) for inhibition of COX and pGal (propyl gallate; final concentration 200 µM) to inhibit AOX. After the measurements, the roots were incubated O/N at 60 °C to dry. **B,** Rates of respiration were calculated in a window of 1 minute, directly before the addition of roots or KCN and the end of the measurement after pGal addition by the software Oxygraph Plus (Hansatech Instruments Ltd). The table shows the absolute values of respiration measurements shown in Figure 4E, normalized on the dry weight (DW). For each of the four genotypes four or five replicates were done. **C,** Basic root respiration of all four genotypes (*n* = 4-5). The box plot shows the median as centre line with the box for the first to the third quartile and whiskers indicating min and max values of the whole dataset. Different letters indicate significant differences between treatments calculated according to one-way ANOVA with Tukey's multiple comparisons test (α = 0.05). Supplemental Data Set 16. Data for WT and *K83A #3* are shown in blue, data for the respective lines overexpressing *LIP1* are shown in yellow.

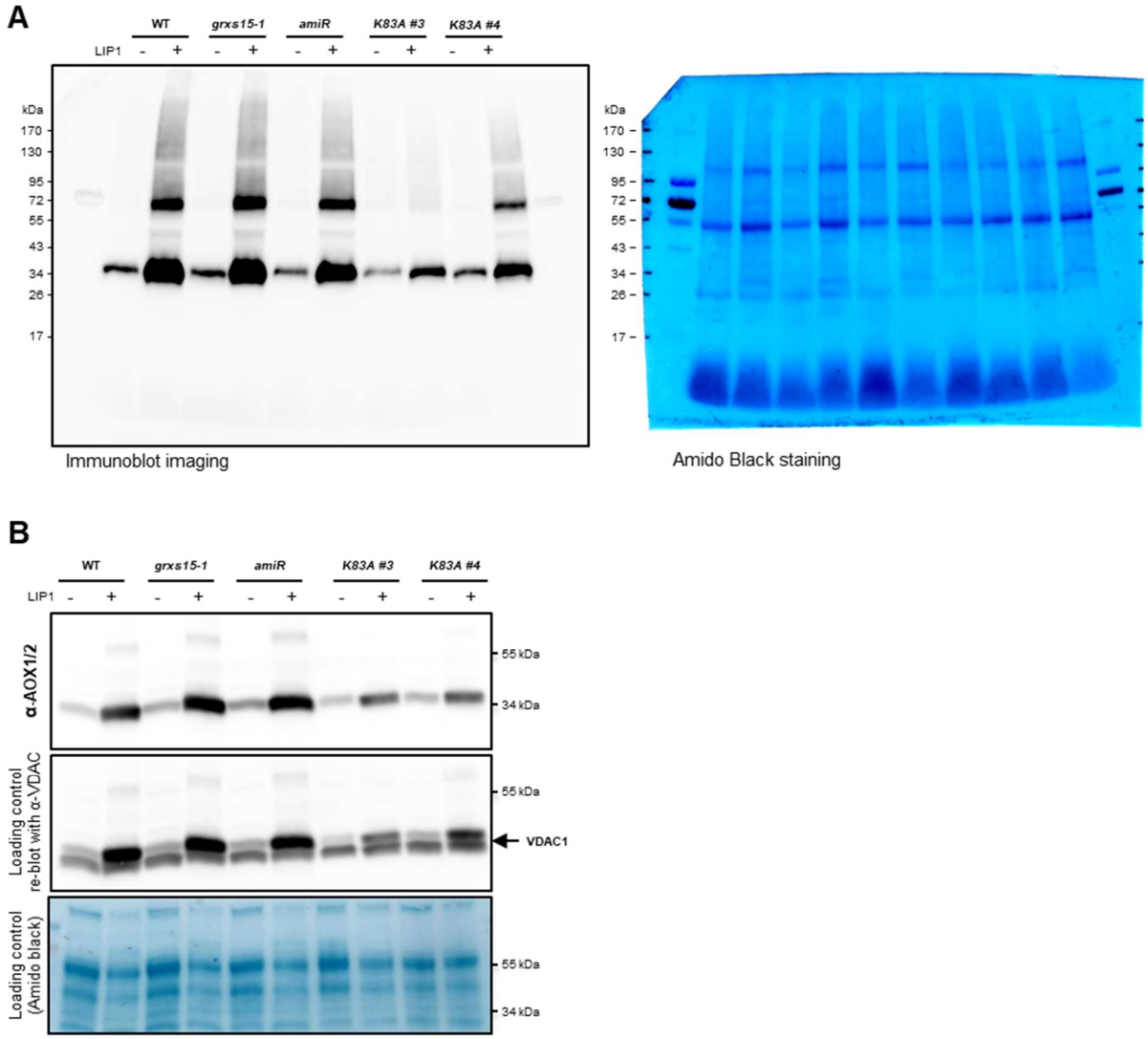

Supplemental Figure S20. Overexpression of *LIP1* has an impact on the regulation of AOX expression. A, Protein gel blot analysis with primary antibodies raised against AOX1/2 (AS04 054; Agrisera). 15 µg of proteins extracted from mitochondria isolated from leaves of 7-week-old soil-grown plants. Amido Black stain serves as loading control. **B,** Similar to (**A**), protein gel blot analysis with primary antibodies raised against AOX1/2 with 15 µg of protein extracted from mitochondria isolated from seedlings grown in hydroponic culture for 16 days. Re-blot with antibody raised against VDAC1 and Amido black stain serves as loading control.

Supplemental Table S1. Primers for genotyping

Line name and ID	Allele type	Primer ID	Sequence (5' → 3')
grxs15-1	WT	#2710	GGAGATTCAGGGACACCTTTC
(SALK_112767)		#2711	ATGGTCCACTTCGTATGTTGG
	T-DNA	#1401	ATTTTGCCGATTTCGGAAC
		#2711	ATGGTCCACTTCGTATGTTGG
amiR (Ströher *et al.*, 2016)	T-DNA	#3791	CGGCAACAGGATTCAATCTTAAG
		#4428	CGCACAATCCCACTATCCTT
grxs15-3	WT	#2708	TGAAGCATACTTTTGGGATGG
(GK-837C05)		#2709	ATTCAAAACCATACGCTCACG
	T-DNA	#2709	ATTCAAAACCATACGCTCACG
		#432	CCCATTTGGACGTGAATGTAGACAC
K83A T-DNA (Moseler *et al.*, 2015)	T-DNA	#2842	AGGGACACCAGCCATGTAGAT
		#3613	GTTTTCCCAGTCACGACGTTGT
aco3	WT	#4974	CACTGTCTCATCGCTTCTTCC
(SALK_014661)		#4975	TCCAACAAAATCAATCCCTTG
	T-DNA	#4975	TCCAACAAAATCAATCCCTTG
		#1401	ATTTTGCCGATTTCGGAAC
+OAS-TL C	T-DNA	#5127	CGATGATCATGGCTTCAAGG
(pMDC32_*35S$_{pro}$*:*OAS-TL C*)		#3791	CGGCAACAGGATTCAATCTTAAG

Supplemental Table S2. Primers used for cloning

Gene	Purpose	Primer ID	Sequence (5' → 3')
LIP1 (AT2G20860)	Cloning in pSS01	#4874	GGGGACAAGTTTGTACAAAAAAGCAGGC TTAATGCATTCGCGCTCCGCC
		#4877	GGGGACCACTTTGTACAAGAAAGCTGGG TGCGGGGATGTAGAAGGAGAAG
	Cloning in pB7WG2	#4874	GGGGACAAGTTTGTACAAAAAAGCAGGC TTAATGCATTCGCGCTCCGCC
		#4876	GGGGACCACTTTGTACAAGAAAGCTGGG TCTACGGGGATGTAGAAGGAGA

Primer #4874 includes a start codon and part the DNA coding for the original signal peptide for mitochondrial targeting. Primer #4877 lacks a stop codon to allow translational fusion of LIP1 with a C-terminal GFP. Primer #4876 includes the stop codon.

Supplemental Table S3. *grxs15* mutants overexpressing *LIP1-GFP* show a Mendelian segregation

Genetic background	Line	*n*	BASTA-resistant	BASTA-sensitive	Resistant/total (%)	□²
WT+LIP1-GFP	**#2**	235	176	59	74.9	0.001
WT+LIP1-GFP	**#6**	207	157	50	75.8	0.079
WT+LIP1-GFP	**#8**	105	83	22	79.0	0.917
grxs15-1+LIP1-GFP	**#5**	182	134	48	73.6	0.183
grxs15-1+LIP1-GFP	**#6**	155	116	39	74.8	0.002
grxs15-1+LIP1-GFP	**#12**	182	139	43	76.4	0.183
amiR+LIP1-GFP	**#6**	285	220	65	77.2	0.731
amiR+LIP1-GFP	**#9**	104	80	24	76.9	0.205
amiR+LIP1-GFP	**#10**	183	137	46	74.9	0.002
K83A #3+LIP1-GFP	**#1**	148	117	31	79.1	1.297
K83A #3+LIP1-GFP	**#2**	179	132	47	73.7	0.151
K83A #3+LIP1-GFP	**#3**	104	80	24	76.9	0.205
K83A #4+LIP1-GFP	**#1**	104	79	25	76.0	0.051
K83A #4+LIP1-GFP	**#2**	260	191	69	73.5	0.328
K83A #4+LIP1-GFP	**#3**	151	111	40	73.5	0.179

All three independent lines for overexpression of *LIP1-GFP* in *WT*, *grxs15-1*, *amiR*, *K83A #3,* and *#4* segregated with a ratio of about 3:1 for resistance of T_2 plants to BASTA after 10 days. □² was calculated on an expected segregation of 3:1 (α = 0.05).

Supplemental Table S4 | Wild type lines overexpressing *LIP1* without GFP tag have a Mendelian segregation

Genetic background	Line	*n*	BASTA-resistant	BASTA-sensitive	Resistant/total (%)	□²
WT+LIP1	**#1**	181	129	52	71.3	1.343
WT+LIP1	**#2**	168	133	35	79.2	1.556
WT+LIP1	**#3**	196	149	47	76.0	0.109

All three independent lines for overexpression of *LIP1* in WT segregated with a ratio of about 3:1 for resistance of T_2 plants to BASTA after 10 days. □² was calculated on an expected segregation of 3:1 (α = 0.05).

Supplemental Table S5 | WT+*LIP1* lines overexpressing *OAS-TL C* show Mendelian segregation of *OAS-TL C*

Genetic background	Line	*n*	T-DNA (*OAS-TL C*) positive	T-DNA negative	T-DNA positive/total (%)	□²
WT+*LIP1+OAS-TL C*	**#1**	12	8	4	66.7	0.444
WT+*LIP1+OAS-TL C*	**#2**	24	18	6	75.0	0.000
WT+*LIP1+OAS-TL C*	**#3**	12	10	2	83.3	0.444

All three independent lines for overexpression of *OAS-TL C* in WT *and* WT+*LIP1* segregated with a ratio of about 3:1 for the presence of the *OAS-TL C* construct (primers #5127 and #2791, Supplementary Table 1). χ^2 was calculated on an expected segregation of 3:1 (α = 0.05).

Supplemental Table S6 | Primers used for quantitative assessment of expression levels by qRT-PCR

Gene	Primer ID	Sequence
LIP1	#5199	CACCAGATGCCTTCGAGAGGTA
AT2G20860	#5200	TCTCCCGCTTTGTACGACGAC
ACO3	#5252	ATGCTTGTTGTGCCTCCTGG
AT2G05710	#5253	TCTGGGTAGAGAAGGCCTTTGG
ACO2	#5254	CAAGCTAGGAATTCCACTCCGGTT
AT4G26970	#5255	TCTCCACCACCAGGTTTAGGAAGA
GRXS15	#5256	CGCTGTGAAATCCTTCAGCCAC
AT3G15660	#5257	GCTCCAATTCACCTTCCTTGTGC
TIP41	#3892	AATGCGTTTGACGCACTAGC
AT4G34270	#3893	GAGACGGCTTGCTCCTGAAT
SAND	#2895	CCATATTGCAAGAAGTTTGCGCGTCTG
AT2G28390	#2896	GCAAGTCATCGGGATGGAGAGACG

Supplemental references

Karimi, M., Inze, D., and Depicker, A. (2002). GATEWAY vectors for Agrobacterium-mediated plant transformation. Trends Plant Sci. 7, 193-195.

Moseler, A., Aller, I., Wagner, S., Nietzel, T., Przybyla-Toscano, J., Mühlenhoff, U., Lill, R., Berndt, C., Rouhier, N., Schwarzländer, M., and Meyer, A.J. (2015). The mitochondrial monothiol glutaredoxin S15 is essential for iron-sulfur protein maturation in Arabidopsis thaliana. Proc. Natl. Acad. Sci. U.S.A. 112, 13735-13740.

Moseler, A., Kruse, I., Maclean, A.E., Pedroletti, L., Franceschetti, M., Wagner, S., Wehler, R., Fischer-Schrader, K., Poschet, G., Wirtz, M., Dörmann, P., Hildebrandt, T.M., Hell, R., Schwarzländer, M., Balk, J., and Meyer, A.J. (2021). The function of glutaredoxin GRXS15 is required for lipoyl-dependent dehydrogenases in mitochondria. Plant Physiol. 186, 1507-1525.

Ströher, E., Grassl, J., Carrie, C., Fenske, R., Whelan, J., and Millar, A.H. (2016). Glutaredoxin S15 is involved in Fe-S cluster transfer in mitochondria influencing lipoic acid-dependent enzymes, plant growth, and arsenic tolerance in Arabidopsis. Plant Physiol. 170, 1284-1299

6 | Conclusions and outlook

In general, this thesis contributes to an integrated understanding of iron–sulfur (Fe–S) cluster biogenesis in plant mitochondria. Based on published data, the current knowledge about the processes of Fe–S clusters assembly and distribution via glutaredoxin S15 (GRXS15) was summarised and used to compile an updated working model for the respective processes (Fig. 7.1A). Furthermore, it was emphasised that the continuous turnover of mitochondrial Fe–S clusters-containing proteins implies that clusters are set free and most likely disintegrate due to their instability in the free form. This leads to the release of sulfide and iron ions. By combining different datasets on protein abundance and protein degradation rates, the amount of Fe–S clusters required/destroyed daily per single mitochondrion was estimated. In the same way, the concomitant amount of sulfide released in the mitochondrial matrix was estimated. The role of biotin synthase (BIO2) and lipoyl synthase (LIP1) in the overall sulfide release was also examined. Since both of these enzymes sacrifice Fe–S clusters as sulfur sources, it is hypothesised that their activity contributes to the total amount of sulfide that is set free in plant mitochondria (Fig. 7.1B). Considering the overall Fe–S cluster-protein turnover and the destructive catalytic activity of BIO2 and LIP1, it was speculated that every day more than 31,000 sulfur atoms are set free in a single mitochondrion. To prevent the poisoning of complex IV of the electron transport chain (ETC), it is assumed that an efficient sulfide detoxification system is needed within the mitochondrion (Fig. 7.1C).

In plant mitochondria, GRXS15 is an essential protein that can bind Fe–S clusters. In contrast with other organisms, plant mitochondria contain only GRXS15, as a single class II GRX. To understand the biological reason underlying the lack of class I GRXs in plant mitochondria and to explore whether GRXS15 can substitute their functions, the distinct biochemical roles of these two classes were examined. Initially, the structural differences between class I and class II GRXs were investigated *in vitro*, using human *Hs*Grx2 and *Hs*Grx5 as models for class I and class II GRXs, respectively. It was demonstrated that the sequence of either two or seven amino acids between a highly conserved lysyl residue and the active site cysteine defines different loop structures. These domains are named type-I or type-II loops, respectively, and are the main discriminant between class I and II GRXs. Absence or presence of the loop structure impacts on the orientation of the side chain of the preceding lysyl residue, which in turn affects positioning and probably also the protonation state of the active site cysteine. More specifically, while the absence of the extended type-II loop is the key to efficient redox activity, its presence influences the structure of the holo-dimer GRX-[2Fe–2S]-GRX. The conformational changes of the holo-dimer may have a negative impact on its cluster-transferring properties.

These novel insights were exploited to further investigate the oxidoreductase activities of GRXS15 *in vitro*. It was confirmed that GRXS15 has a slow oxidation activity and lacks reduction abilities with roGFP2 as a substrate protein. After truncation of GRXS15 by deleting its type-II loop, GRXS15-loop was still not able to reduce roGFP2 but showed enhanced oxidation activity. Moreover, it was shown that GRXS15 spontaneously forms homodimers through intermolecular disulfide bonds involving cysteine residues in the active site. However, it remains unresolved whether GRXS15 has a significant oxidoreductase activity within the mitochondrion or whether its activity is strictly confined to that as a [2Fe–2S] cluster transferase. Thus, the reasons for the absence of catalytically active class I GRXs in plant mitochondria remain an open question.

Subsequently, the *in planta* role of GRXS15 and the physiological consequences of its reduced activity were investigated. GRXS15 is an essential mitochondrial protein, and null mutants are embryo-lethal. Therefore, *grxs15* knockdowns and lines partially complemented with the less functional GRXS15 K83A were examined, despite being remarkably dwarf. By analysing several pathways reliant on mitochondrial Fe–S clusters, it was unravelled that the main metabolic consequence of diminished GRXS15 activity is an impairment in all four lipoyl-dependent mitochondrial dehydrogenase complex activities (Fig. 7.1D).

Based on these observations, it was hypothesised that the main role of GRXS15 is to shuttle [2Fe–2S] clusters from the first assembly machinery to the second (Fig. 7.1A) and that LIP1 is the primary enzyme affected by a bottleneck caused by the insufficient cluster-transfer activity of GRXS15 in severe *grxs15* mutants. The facts that LIP1 with just 85 copies per mitochondrion is very low abundant and that it needs a constant supply of [4Fe–4S] clusters for its catalytic activity, makes this enzyme a pronounced sink for clusters (Fig. 7.1B). Therefore, the current evidence suggested that LIP1 is unable to compete with other more abundant enzymes when the pool of Fe–S clusters is limited.

In this work, it is shown that it is possible to manipulate the distribution of the mitochondrial Fe–S clusters. Specifically, the flux of clusters towards aconitase 3 (ACO3) or to LIP1 was genetically altered by changing the abundance of the respective proteins (Fig. 7.1E). ACO3 knockout allowed more clusters to be provided to LIP1, suppressing the dwarf phenotype of the *grxs15* mutants. With the opposite principle, overexpression of LIP1 generated a new sink for clusters (Fig. 7.1B), which suppressed the dwarf phenotype of the most severely affected *grxs15* mutants.

Furthermore, this study has led to a completely unexpected observation: overexpression of LIP1 turned out to be deleterious for wild-type plants, macroscopically visible as significantly reduced growth, a curly leaf phenotype, delayed development and shorter inflorescences. After characterizing this novel dwarf mutant, the results indicated that there was no impairment in

the lipoyl-dependent dehydrogenases nor any hyper-lipoylation (Fig. 7.1G). Instead, it was demonstrated that overexpression of LIP1 causes the release of toxic levels of sulfide that intoxicate complex IV of the ETC (Fig. 7.1F). This may be due to the sacrificial disintegration of the auxiliary [4Fe–4S] cluster by LIP1. However, it cannot be excluded that the auxiliary cluster may fall apart if it is not used immediately, *e.g.*, in case of substrate shortage for LIP1 or increased LIP1 abundance.

Finally, the role of mitochondrial cysteine biosynthesis was examined. To prevent complex IV intoxication by sulfide (Fig. 7.1F), evolution exploited two mechanisms of scavenging. While animal cells and some fungi oxidise sulfide by the inner mitochondrial membrane protein SQR (sulfide:quinone reductase), plants use sulfide for cysteine biosynthesis in the mitochondrial matrix by the enzyme *O*-acetylserine-(thiol)-lyase C (OAS-TL C) (Fig. 7.1C). The observations of this study demonstrate that the toxic effect of overexpression of LIP1 can be at least partially alleviated by enhancing the capacity of sulfide fixation through the overexpression of OAS-TL C. This suggests that the main role of the plant mitochondrial cysteine biosynthesis is not to produce cysteine but rather to scavenge sulfide released by the mitochondrial metabolism, *e.g.*, from Fe–S clusters disassembly.

Taken together, the results achieved in this thesis provide strong evidence that the mitochondrial [4Fe–4S] cluster-dependent pathway relies on GRXS15 (Fig. 7.1A) and that LIP1 is the first enzyme that experiences a cluster shortage when the upstream delivery system is impaired (Fig. 7.1B). Moreover, the potential release of toxic sulfide by LIP1 sets the need for local cysteine biosynthesis in the matrix as a sulfide detoxification system (Fig. 7.1C). Altogether, this thesis contributes to expanding our knowledge of Fe–S cluster-dependent metabolism and allows refinement of the model for the cluster distribution within plant mitochondria (Fig. 7.1).

Overall, this study provides a starting point for future research, especially by opening the door to understanding how mitochondria counter sulfide intoxication. Eventually, this may help answer the question of why plants possess a cysteine biosynthesis complex within the mitochondrion in contrast to animals and fungi and why by far largest fraction of of *O*-acetylserine is synthesized in the matrix. Moreover, since overexpression of LIP1 causes sulfide release within the mitochondrion, it offers a suitable tool to study the physiological implications of sulfide toxicity in this subcellular compartment *in vivo*.

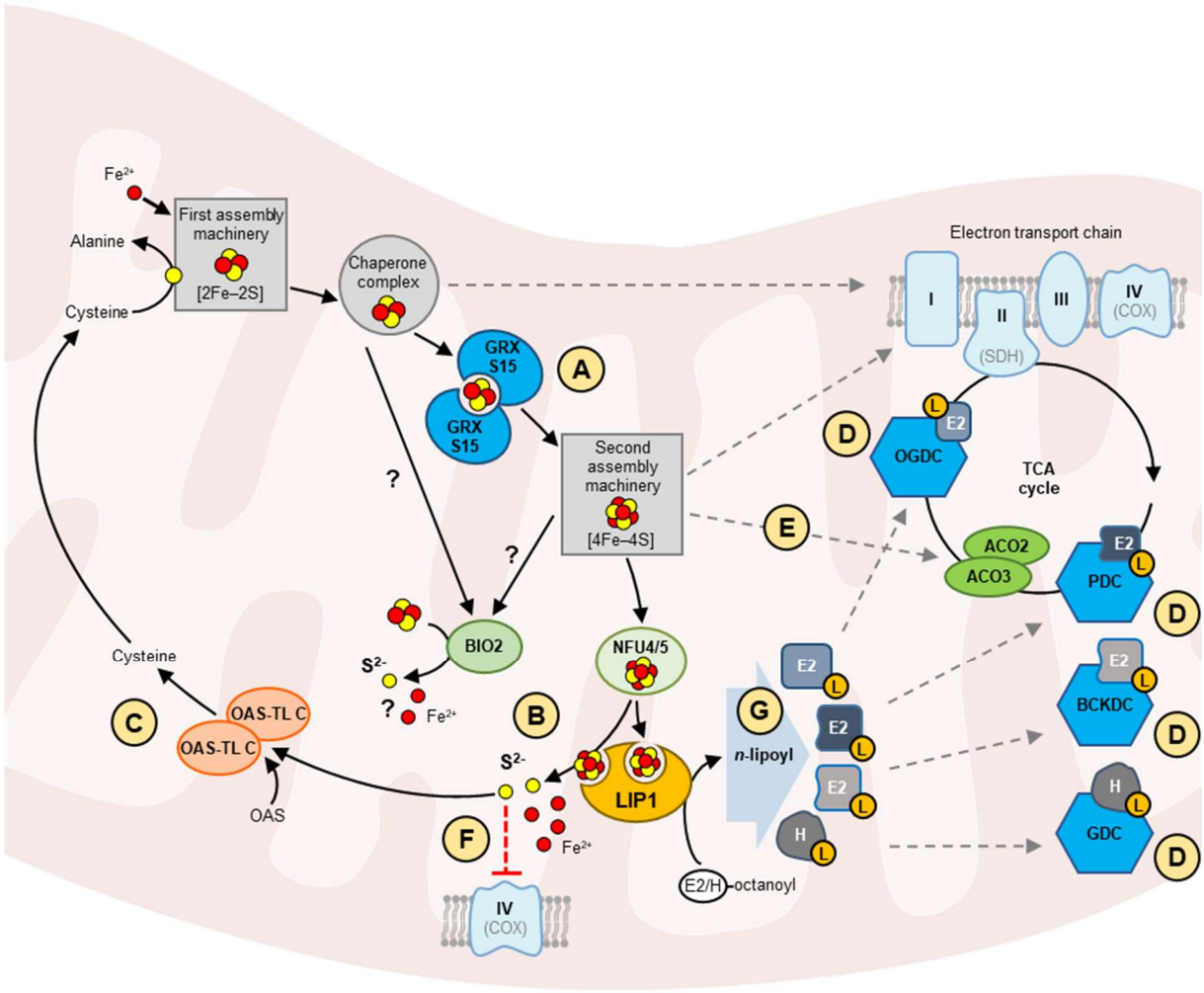

Fig. 7.1 | Working model of Fe–S cluster assembly and distribution in plant mitochondria. On the top left, a simplification of the first assembly machinery, which utilises cysteine as sulfur source (yellow circles) and iron (red circles) to build [2Fe–2S] clusters, is depicted. After assembly, a chaperone complex acts as a hub for further delivery of [2Fe–2S] clusters to target proteins such as subunits of complexes I, II and III in the mitochondrial electron transport chain (ETC) and to glutaredoxin S15 (GRXS15). GRXS15 is the key protein for transferring [2Fe–2S] clusters from the first assembly machinery to the second, where [4Fe–4S] clusters are being built (**A**). These are then distributed to target proteins such as ETC complexes, aconitases 2 and 3 (ACO2/3) (**E**), biotin 2 (BIO2) and lipoyl synthase (LIP1) (**B**). Delivery of [4Fe–4S] to LIP1 relies on the NifU-like proteins NFU4/5. Both BIO2 and LIP1 require one [4Fe–4S] cluster for their catalytic activity and use a second "auxiliary" cluster (one [2Fe–2S] for BIO2 and one [4Fe–4S] for LIP1) as sulfur source to synthesise biotin and lipoyl cofactors. Specifically for LIP1, two sulfur atoms are transferred from the auxiliary cluster to the *n*-octanoyl residue attached to the dehydrogenase subunits E2 or H for its conversion to the *n*-lipoyl prosthetic group Ⓛ (**G**). lipoyl cofactor is necessary for the activity of four mitochondrial dehydrogenase complexes glycine decarboxylase (GDC), pyruvate dehydrogenase (PDC), 2-oxoglutarate dehydrogenase (OGDC), and branched-chain α-keto acid dehydrogenase (BCKDC) (**D**). In the absence of any established repair mechanism, the remnants of the auxiliary clusters are assumed to disintegrate and release sulfide. Similarly, entire auxiliary clusters may fall apart if they are not used immediately, *e.g.*, in case of substrate shortage for LIP1 or increased LIP1 abundance. To prevent poisoning of cytochrome *c* oxidase (COX, complex IV) (**F**), the toxic sulfide is utilised by *O*-acetylserine-(thiol)-lyase C (OAS-TL C) to synthesise cysteine (**C**), which can be reused for a new round of Fe–S cluster assembly.

Acknowledgements

After over four and half years of this PhD project, as I look back, I realize just how many people were a part of this adventure. Without all the invaluable help and support from so many people, I would not have come this far.

First and foremost, I want to express my deep gratitude and appreciation to my supervisor, **Andreas**. Thank you for constantly and patiently having guided me throughout my entire PhD journey. I am thankful for your trust and immense support, as well as our sometimes very long but incredibly engaging scientific discussions. Your encouragement to be scientifically autonomous and creative has been invaluable. Additionally, I'm grateful for the numerous opportunities you provided for me to participate in meetings, conferences, and build collaborations. Your enthusiasm and encouragement were instrumental in making this PhD challenge a success. I am further grateful to **Peter Dörmann** for offering to co-supervise as well as to **Christiane Dahl** and **Ulrich Schweizer** for kindly agreeing to examine my thesis.

I want to express my deepest thanks to my closest lab/desk mates. I consider you more than just colleagues; you are my friends. Thanks **Anna-Lena** and **Finja**, for the huge help in the lab and for guiding me at the very beginning of my time in Germany. Thanks **Michelle**, for your constant positive energy and the encouragement to give our best. Thanks, **Taheb**, and **Ling**, I appreciate the time you've shared with me, the support in the lab, and our enjoyable discussions about life, food and different cultures. Thanks **Yan**, I've lost count of all the beers we've shared together!

I'd like to extend my gratitude to my other (more experienced) lab-friends. Thanks **José**, you have been a true mentor for me, always kind and encouraging, providing infinite precious recommendations. Thanks **Anna** for all your help, not just with the science but also for supporting me through the challenges of the PhD. Thanks also to you, **Stephan**, even though you've "just" joined us, I can't emphasize enough how supportive you've been in this short time. And, looking back, I cannot forget all the assistance and kindness I received from **Stefanie Müller-Schüssele** and from former colleagues **Philippe**, **Sophie**, **Steffi W.** as well as all the other students who have been part of the lab.

Furthermore, I wish to thank our fantastic technicians, **Maria** and **Claudia** (but also **Vera**, **Krista**, **Alexa**, **Helmut**, **Britta**) for their fundamental assistance and positivity.

A very special thank goes to "my" students, **Pravallika**, **Zamiga**, **Giosué**, **Lisa** and **Jeremy** but also **Juan Carlos**, **Sophia** and **Sarah**. However, I'd like to give particular credit to **Timon**, "my" first master student I've ever supervised. You have been a loyal and fantastic student and

friend. Your curiosity and creativity were invaluable, not only for this project but also as a source of encouragement throughout the entire PhD journey.

Moreover, I'd like to extend my appreciation to **Frank Hochholdinger** and all the (present and former) members of the **Crop Functional Genomics group**. You are too many to mention one by one (!) but you need to know I appreciated every single moment with you, from scientific advice to café breaks, wurst day, hanging out, sharing food and an incredible amount of cakes!

I'd also like to express my thanks to our secretaries **Frau Jessen**, **Frau Kreitz** and **Frau Skamel**. I consider myself fortunate to have received the utmost efficient and supportive assistance in navigating bureaucratic challenges.

I want to extend my gratitude to the visiting students **Alberto**, and **Jacopo**. Even though for a short time, I remember you with affection. In particular, I want to thank the amigo **Thomaz**. The “corona time” would have been much more challenging without your presence and our conversations about food and life.

Moreover, I'd like to express my deep appreciation for our collaborators in Nancy: **Nicolas Rouhier**, **Jeremy Couturier** and my colleague **Loïc Christ**, who have shared with me both the passion and challenge of working with glutaredoxins. Additionally, I am thankful to all our other collaborators **Christopher Lillig** from Greifswald, **Stefan Timm** from Rostock, **Markus Wirtz**, **Rüdiger Hell**, **Gernot Poschet** and **Elena Sturm** from Heidelberg. I would also like to extend my gratitude to **Tatjana Hildebrandt**, **Jannis Moormann** and **Björn Heinemann** from Köln, **Harvey Millar** from Perth, **Roland Lill** and **Ulrich Mühlenhoff** from Marburg, **Janneke Balk** from Norwich. Thanks to all of you for the stimulating scientific discussion and for helping me to put all the pieces of my results together.

Without all of you, I would have probably achieved less than half of what I realized during my PhD.

Besides science, I’d also like to express my most sincere gratitude to my **family** (grazie per tutto quello che avete fatto e che continuate a fare per me) and all of my friends that supported me during my time in Germany. **Giada**, my personal hashira. **Giordano** my true and sincere friend. **Vale**, grazie per tutti i bei ricordi che mi porterò dietro. **Lea** and **Jacob**, I’ll never forget all the fun and drama we had together. **Piet**, **Karoline** and **Günter** from my taijiquan group (my mind stayed healthy thanks to Taiji, too!). And all the **amici** che non che non ho lo spazio per citare tutti ma che non hanno mai smesso di supportarmi anche se ero lontano.

References

Abdalla, M. *et al.* (2016) ‘Crystal structure of yeast monothiol glutaredoxin Grx6 in complex with a glutathione-coordinated [2Fe-2S] cluster’, *Acta Crystallographica*, 72(10), pp. 732–737. doi: 10.1107/S2053230X16013418.

Abdalla, M., Eltayb, W. A. and Yousif, A. (2018) ‘Comparison of structures among Saccharomyces cerevisiae Grxs proteins’, *Genes and Environment*, 40(1), pp. 1–9. doi: 10.1186/s41021-018-0104-5.

Aller, I., Rouhier, N. and Meyer, A. J. (2013) ‘Development of roGFP2-derived redox probes for measurement of the glutathione redox potential in the cytosol of severely glutathione-deficient rml1 seedlings’, *Frontiers in Plant Science*, 4(DEC), pp. 1–12. doi: 10.3389/fpls.2013.00506.

Alvarez, B. and Salinas, G. (2022) ‘Basic concepts of thiol chemistry and biology’, *Redox Chemistry and Biology of Thiols*. Elsevier Inc., pp. 1–18. doi: 10.1016/B978-0-323-90219-9.00026-1.

Atkinson, A. *et al.* (2011) ‘The LYR protein Mzm1 functions in the insertion of the rieske Fe/S protein in yeast mitochondria’, *Molecular and Cellular Biology*, 31(19), pp. 3988–3996. doi: 10.1128/mcb.05673-11.

Azam, T. *et al.* (2020) ‘The Arabidopsis mitochondrial glutaredoxin GRXS15 provides [2Fe-2S] clusters for ISCA-mediated [4Fe-4S] cluster maturation’, *International Journal of Molecular Sciences*, p. 9237. doi: 10.3390/ijms21239237.

Balk, J. and Pilon, M. (2011) ‘Ancient and essential: the assembly of iron – sulfur clusters in plants’, *Trends in Plant Science*. Elsevier Ltd, 16(4), pp. 218–226. doi: 10.1016/j.tplants.2010.12.006.

Batool, S. *et al.* (2018) ‘Sulfate is incorporated into cysteine to trigger ABA Production and stomatal closure’, *The Plant Cell*, 30(12), pp. 2973–2987. doi: 10.1105/tpc.18.00612.

Bauwe, H. (2023) ‘Photorespiration – Rubisco’s repair crew’, *Journal of Plant Physiology*. Elsevier GmbH, 280(November 2022), p. 153899. doi: 10.1016/j.jplph.2022.153899.

Begas, P., Staudacher, V. and Deponte, M. (2015) ‘Systematic re-evaluation of the bis(2-hydroxyethyl)disulfide (HEDS) assay reveals an alternative mechanism and activity of glutaredoxins’, *Chemical Science*. Royal Society of Chemistry, 6(7), pp. 3788–3796. doi: 10.1039/c5sc01051a.

Beinert, H. (2000) ‘Iron-sulfur proteins: ancient structures, still full of surprises’, *Journal of Biological Inorganic Chemistry*, 5(1), pp. 2–15. doi: 10.1007/s007750050002.

Bellí, G. *et al.* (2002) ‘Structure-function analysis of yeast Grx5 monothiol glutaredoxin defines essential amino acids for the function of the protein’, *Journal of Biological Chemistry*, 277(40), pp. 37590–37596. doi: 10.1074/jbc.M201688200.

Booker, S. J. and Lloyd, C. T. (2022) ‘Twenty years of radical SAM! the genesis of the superfamily’, *ACS Bio and Med Chem Au*, 2(6), pp. 538–547. doi: 10.1021/acsbiomedchemau.2c00078.

Bradford, M. M. (1976) ‘A rapid and sensitive method for the quantification of microgram quantities of protein utilizing the principle of protein-dye binding’, *Analytical Biochemistry*, 72(1976), pp. 248–254. doi: doi.org/10.1016/0003-2697(76)90527-3.

Brancaccio, D. *et al.* (2014) ‘Formation of [4Fe-4S] clusters in the mitochondrial iron–sulfur cluster assembly machinery’, *Journal of the American Chemical Society*. American Chemical Society, 136(46), pp. 16240–16250. doi: 10.1021/ja507822j.

Braymer, J. J. *et al.* (2021) ‘Mechanistic concepts of iron-sulfur protein biogenesis in Biology’, *Biochimica et Biophysica Acta - Molecular Cell Research*. Elsevier, 1868(1), p. 118863. doi: 10.1016/j.bbamcr.2020.118863.

Buchanan, B. B. and Balmer, Y. (2005) ‘Redox regulation: A broadening horizon’, *Annual Review of Plant Biology*, 56, pp. 187–220. doi: 10.1146/annurev.arplant.56.032604.144246.

Bych, K. *et al.* (2008) ‘The iron-sulphur protein Ind1 is required for effective complex I assembly’, *EMBO Journal*, 27(12), pp. 1736–1746. doi: 10.1038/emboj.2008.98.

Camaschella, C. *et al.* (2007) ‘The human counterpart of zebrafish shiraz shows sideroblastic-like microcytic anemia and iron overload’, *Blood*. American Society of Hematology, 110(4), pp. 1353–1358. doi: 10.1182/blood-2007-02-072520.

Christ, L., Couturier, J. and Rouhier, N. (2022) ‘Relationships between the reversible oxidation of the single cysteine residue and the physiological function of the mitochondrial glutaredoxin S15 from *Arabidopsis thaliana*’, *Antioxidants*, 12(1). doi: 10.3390/antiox12010102.

Cicchillo, R. M. *et al.* (2004) ‘*Escherichia coli* lipoyl synthase binds two distinct [4Fe−4S] clusters per polypeptide’, *Biochemistry*. American Chemical Society, 43(37), pp. 11770–11781. doi: 10.1021/bi0488505.

Couturier, J. *et al.* (2013) ‘The iron-sulfur cluster assembly machineries in plants: Current knowledge and open questions’, *Frontiers in Plant Science*, 4(JUL), pp. 1–22. doi: 10.3389/fpls.2013.00259.

Couturier, J., Jacquot, J. P. and Rouhier, N. (2013) ‘Toward a refined classification of class I

dithiol glutaredoxins from poplar: Biochemical basis for the definition of two subclasses', *Frontiers in Plant Science*, 4(DEC), pp. 1–14. doi: 10.3389/fpls.2013.00518.

Deponte, M. (2013) 'Glutathione catalysis and the reaction mechanisms of glutathione-dependent enzymes', *Biochimica et Biophysica Acta - General Subjects*. Elsevier B.V., 1830(5), pp. 3217–3266. doi: 10.1016/j.bbagen.2012.09.018.

Douce, R. *et al.* (2001) 'The glycine decarboxylase system: A fascinating complex', *Trends in Plant Science*, 6(4), pp. 167–176. doi: 10.1016/S1360-1385(01)01892-1.

Dumanović, J. *et al.* (2021) 'The Significance of Reactive Oxygen Species and Antioxidant Defense System in Plants: A Concise Overview', *Frontiers in Plant Science*, 11(January). doi: 10.3389/fpls.2020.552969.

Fernandes, A. P. *et al.* (2005) 'A novel monothiol glutaredoxin (Grx4) from *Escherichia coli* can serve as a substrate for thioredoxin reductase', *Journal of Biological Chemistry*, 280(26), pp. 24544–24552. doi: 10.1074/jbc.M500678200.

Fernandes, A. P. and Holmgreen, A. (2004) 'Glutaredoxins: glutathione-dependent redox enzymes with functions far beyond a simple thioredoxin backup system', *Antioxidants and Redox Signaling*, 6(February), pp. 63–74. doi: doi: 10.1089/152308604771978354.

Foye, C. H. and Noctor, G. (2013) 'Redox signaling in plants', *Antioxidants and Redox Signaling*, 44(June), pp. 2087–2090. doi: doi/10.1089/ars.2013.5278.

Fuchs, P. *et al.* (2020) 'Single organelle function and organization as estimated from Arabidopsis mitochondrial proteomics', *The Plant Journal*, 101(2), pp. 420–441. doi: 10.1111/tpj.14534.

Gao, X. H. *et al.* (2010) 'Biochemical characterization of glutaredoxins from *Chlamydomonas reinhardtii*: Kinetics and specificity in deglutathionylation reactions', *FEBS Letters*. Federation of European Biochemical Societies, 584(11), pp. 2242–2248. doi: 10.1016/j.febslet.2010.04.034.

Garcia, bP. S. *et al.* (2022) 'An early origin of iron–sulfur cluster biosynthesis machineries before Earth oxygenation', *Nature Ecology & Evolution*, 6(10), pp. 1564–1572. doi: doi.org/10.1038/s41559-022-01857-1.

Gravina, S. A. and Mieyal, J. J. (1993) 'Thioltransferase is a specific glutathionyl mixed disulfide oxidoreductase', *Biochemistry*, 32(13), pp. 3368–3376. doi: 10.1021/bi00064a021.

Gupta, V. and Carroll, K. S. (2014) 'Sulfenic acid chemistry, detection and cellular lifetime', *Biochimica et Biophysica Acta - General Subjects*. Elsevier B.V., 1840(2), pp. 847–875. doi: 10.1016/j.bbagen.2013.05.040.

Hagen, K. S., Holm, R. H. and Reynolds, J. G. (1981) 'Definition of reaction sequences resulting in self-assembly of $[Fe_4S_4(SR)_4]^{2-}$ clusters from simple reactants', *Journal of the American Chemical Society*, 103(14), pp. 4054–4063. doi: 10.1021/ja00404a013.

Hanson, G. T. *et al.* (2004) 'Investigating mitochondrial redox potential with redox-sensitive green fluorescent protein indicators', *Journal of Biological Chemistry*, 279(13), pp. 13044–13053. doi: 10.1074/jbc.M312846200.

Heeg, C. *et al.* (2008) 'Analysis of the Arabidopsis O-acetylserine(thiol)lyase gene family demonstrates compartment-specific differences in the regulation of cysteine synthesis', *The Plant cell*, 20(January), pp. 168–185. doi: 10.1105/tpc.107.056747.

Herrero, E., Belli, G. and Casas, C. (2011) 'Structural and functional diversity of glutaredoxins in yeast', *Current Protein & Peptide Science*, 11(8), pp. 659–668. doi: 10.2174/138920310794557637.

Hoff, K. G. *et al.* (2009) '*In vivo* fluorescent detection of Fe-S clusters coordinated by human GRX2', *Chemistry and Biology*. Elsevier Ltd, 16(12), pp. 1299–1308. doi: 10.1016/j.chembiol.2009.11.011.

Holmgreen, A. and Aslund, F. (1995) 'Glutaredoxin', *Methods in Enzymology*, 252(1995), pp. 283–292. doi: 10.1016/0076-6879(95)52031-7.

Holmgren, A. (1976) 'Hydrogen donor system for *Escherichia coli* ribonucleoside diphosphate reductase dependent upon glutathione', *Proceedings of the National Academy of Sciences of the United States of America*, 73(7), pp. 2275–2279. doi: 10.1073/pnas.73.7.2275.

Imlay, J. A. (2013) 'The molecular mechanisms and physiological consequences of oxidative stress: Lessons from a model bacterium', *Nature Reviews Microbiology*. Nature Publishing Group, 11(7), pp. 443–454. doi: 10.1038/nrmicro3032.

Ivanova, A. *et al.* (2019) 'A mitochondrial LYR protein is required for complex I assembly', *Plant Physiology*, 181(4), pp. 1632–1650. doi: 10.1104/pp.19.00822.

Iwema, T. *et al.* (2009) 'Structural basis for delivery of the intact [Fe2S2] cluster by monothiol glutaredoxin', *Biochemistry*, 48(26), pp. 6041–6043. doi: 10.1021/bi900440m.

Johansson, C. *et al.* (2007) 'Reversible sequestration of active site cysteines in a 2Fe-2S-bridged dimer provides a mechanism for glutaredoxin 2 regulation in human mitochondria', *Journal of Biological Chemistry*, 282(5), pp. 3077–3082. doi: 10.1074/jbc.M608179200.

Johansson, C. *et al.* (2011) 'The crystal structure of human GLRX5: Iron-sulfur cluster co-ordination, tetrameric assembly and monomer activity', *Biochemical Journal*, 433(2), pp.

303–311. doi: 10.1042/BJ20101286.

Kelley, L. A. *et al.* (2016) ‘The Phyre2 web portal for protein modeling, prediction and analysis’, *Nature Protocols*. Nature Publishing Group, 10(6), pp. 845–858. doi: 10.1038/nprot.2015-053.

Laemmli, U. K. (1970) ‘Cleavage of Structural Proteins during the Assembly of the Head of Bacteriophage T4’, *Nature*, 227, pp. 680–685. doi: doi.org/10.1038/227680a0.

Lanz, N. D. and Booker, S. J. (2015) ‘Auxiliary iron-sulfur cofactors in radical SAM enzymes’, *Biochimica et Biophysica Acta - Molecular Cell Research*. Elsevier B.V., 1853(6), pp. 1316–1334. doi: 10.1016/j.bbamcr.2015.01.002.

Leaden, L., Busi, M. V and Gomez-casati, D. F. (2014) ‘The mitochondrial proteins AtHscB and AtIsu1 involved in Fe–S cluster assembly interact with the Hsp70-type chaperon AtHscA2 and modulate its catalytic activity’, *MITOCH*, 19, pp. 375–381. doi: 10.1016/j.mito.2014.11.002.

Lemaire, S. *et al.* (2004) ‘New thioredoxin targets in the unicellular photosynthetic eukaryote *Chlamydomonas reinhardtii*’, 101(19), pp. 7475–7480. doi: 10.1073/pnas.0402221101.

Li, H. and Outten, C. E. (2012) ‘Monothiol CGFS glutaredoxins and BolA-like proteins: [2Fe-2S] binding partners in iron homeostasis’, *Biochemistry*, 51(22), pp. 4377–4389. doi: 10.1021/bi300393z.

Li, L. *et al.* (2010) ‘Structure of Arabidopsis chloroplastic monothiol glutaredoxin AtGRXcp’, *Acta Crystallographica*, 66(6), pp. 725–732. doi: 10.1107/S0907444910013119.

Li, L. *et al.* (2017) ‘Changes in specific protein degradation rates in *Arabidopsis thaliana* reveal multiple roles of Lon1 in mitochondrial protein homeostasis’, *The Plant Journal*. John Wiley & Sons, Ltd, 89(3), pp. 458–471. doi: https://doi.org/10.1111/tpj.13392.

Li, S. *et al.* (2009) ‘Nuclear activity of ROXY1, a glutaredoxin interacting with TGA factors, is required for petal development in Arabidopsis thaliana’, *The Plant Cell*, 21(2), pp. 429–441. doi: 10.1105/tpc.108.064477.

Lill, R. *et al.* (2015) ‘The role of mitochondria and the CIA machinery in the maturation of cytosolic and nuclear iron–sulfur proteins’, *European Journal of Cell Biology*, 94(7), pp. 280–291. doi: 10.1016/j.ejcb.2015.05.002.

Lill, R. and Freibert, S.-A. (2020) ‘Mechanisms of mitochondrial iron-sulfur protein biogenesis’, *Annual Review of Biochemistry*, 89(1), p. 1. doi: 10.1146/annurev-biochem-013118-111540.

Lillig, C. H. *et al.* (2005) ‘Characterization of human glutaredoxin 2 as iron-sulfur protein: A

possible role as red ox sensor', *Proceedings of the National Academy of Sciences of the United States of America*, 102(23), pp. 8168–8173. doi: 10.1073/pnas.0500735102.

Lillig, C. H., Berndt, C. and Holmgren, A. (2008) 'Glutaredoxin systems', *Biochimica et Biophysica Acta - General Subjects*, 1780(11), pp. 1304–1317. doi: 10.1016/j.bbagen.2008.06.003.

Luthman, M. and Holmgren, A. (1982) 'Rat Liver Thioredoxin and Thioredoxin Reductase: Purification and Characterization', *Biochemistry*, 21(26), pp. 6628–6633. doi: 10.1021/bi00269a003.

Maio, N. *et al.* (2014) 'Cochaperone binding to LYR motifs confers specificity of iron sulfur cluster delivery', *Cell Metabolism*, 19(3), pp. 445–457. doi: 10.1016/j.cmet.2014.01.015.

Maio, N. *et al.* (2016) 'Disease-causing SDHAF1 mutations impair transfer of Fe-S clusters to SDHB', *Cell Metabolism*. Elsevier, 23(2), pp. 292–302. doi: 10.1016/j.cmet.2015.12.005.

Maio, N. *et al.* (2017) 'A single adaptable cochaperone-scaffold complex delivers nascent iron-sulfur clusters to mammalian respiratory chain complexes I–III', *Cell Metabolism*, 25(4), pp. 945-953.e6. doi: 10.1016/j.cmet.2017.03.010.

Martin, J. L. (1995) 'Thioredoxin - a fold for all reasons', *Current Biology*, 131(3), pp. 245–250.

McCarthy, E. L. and Booker, S. J. (2017) 'Destruction and reformation of an iron-sulfur cluster during catalysis by lipoyl synthase', *Science*, 358(6361), pp. 373–377. doi: 10.1126/science.aan4574.

McLaughlin, M. I. *et al.* (2016) 'Crystallographic snapshots of sulfur insertion by lipoyl synthase', *Proceedings of the National Academy of Sciences of the United States of America*, 113(34), pp. 9446–9450. doi: 10.1073/pnas.1602486113.

Melber, A. *et al.* (2016) 'Role of Nfu1 and Bol3 in iron-sulfur cluster transfer to mitochondrial clients', *eLife*, 5, p. e15991. doi: 10.7554/eLife.15991.

Mesecke, N. *et al.* (2008) 'Two novel monothiol glutaredoxins from *Saccharomyces cerevisiae* provide further insight into iron-sulfur cluster binding, oligomerization, and enzymatic activity of glutaredoxins', *Biochemistry*, 47(5), pp. 1452–1463. doi: 10.1021/bi7017865.

Meyer, A. J. *et al.* (2007) 'Redox-sensitive GFP in Arabidopsis thaliana is a quantitative biosensor for the redox potential of the cellular glutathione redox buffer', *The Plant Journal*, 52(5), pp. 973–986. doi: 10.1111/j.1365-313X.2007.03280.x.

Møller, I. M., Jensen, P. E. and Hansson, A. (2007) 'Oxidative modifications to cellular

components in plants', *Annual Review of Plant Biology*, 58, pp. 459–481. doi: 10.1146/annurev.arplant.58.032806.103946.

Morgan, B. and Schwarzländer, M. (2016) 'Fluorescent protein sensors for the redox regulation in living cells', *BioSpektrum*, 22(3), pp. 260–263. doi: 10.1007/s12268-016-0683-2.

Moseler, A. *et al.* (2015) 'The mitochondrial monothiol glutaredoxin S15 is essential for iron-sulfur protein maturation in *Arabidopsis thaliana*', *Proceedings of the National Academy of Sciences of the United States of America*, 112(44), pp. 13735–13740. doi: 10.1073/pnas.1510835112.

Moseler, A. (2017) *Functional characterisation of glutaredoxin S15 from Arabidopsis thaliana*. PhD dissertation - University of Bonn. Available at: https://bonndoc.ulb.uni-bonn.de/xmlui/handle/20.500.11811/7314.

Moseler, A. *et al.* (2021) 'The function of glutaredoxin GRXS15 is required for lipoyl-dependent dehydrogenases in mitochondria', *Plant Physiology*, 186(3), pp. 1507–1525. doi: 10.1093/PLPHYS/KIAB172.

Mrozek, P. *et al.* (2023) 'Molecular basis for the enzymatic inactivity of class III glutaredoxins on standard glutathionylated substrates', *Nature Portfolio (Under review)*. doi: 10.21203/rs.3.rs-3029785/v1.

Mühlenhoff, U. *et al.* (2011) 'Specialized function of yeast Isa1 and Isa2 proteins in the maturation of mitochondrial [4Fe-4S] Proteins', *Journal of Biological Chemistry*, 286(48), pp. 41205–41216. doi: 10.1074/jbc.M111.296152.

Müller-Schüssele, S. J., Schwarzländer, M. and Meyer, A. J. (2021) 'Live monitoring of plant redox and energy physiology with genetically encoded biosensors', *Plant Physiology*, 186(1), pp. 93–109. doi: 10.1093/plphys/kiab019.

Na, U. *et al.* (2014) 'The LYR factors sdhaf1 and SDHAF3 mediate maturation of the iron-sulfur subunit of succinate dehydrogenase', *Cell Metabolism*, 20(2), pp. 253–266. doi: 10.1016/j.cmet.2014.05.014.

Nicholls, P. *et al.* (2013) 'Sulfide inhibition of and metabolism by cytochrome *c* oxidase', *Biochemical Society Transactions*, 41(5), pp. 1312–1316. doi: 10.1042/BST20130070.

Nietzel, T. *et al.* (2019) 'The fluorescent protein sensor roGFP2-Orp1 monitors *in vivo* H2O2 and thiol redox integration and elucidates intracellular H2O2 dynamics during elicitor-induced oxidative burst in Arabidopsis', *New Phytologist*, 221(3), pp. 1649–1664. doi: 10.1111/nph.15550.

Ogata, F. T. *et al.* (2021) 'Glutaredoxin: Discovery, redox defense and much more', *Redox*

Biology. Elsevier B.V., 43(April), p. 101975. doi: 10.1016/j.redox.2021.101975.

Pandey, A. K. *et al.* (2019) 'Mitochondria export iron-sulfur and sulfur intermediates to the cytoplasm for iron-sulfur cluster assembly and tRNA thiolation in yeast', *Journal of Biological Chemistry*, 294(24), pp. 9489–9502. doi: 10.1074/jbc.RA119.008600.

Pedroletti, L., Moseler, A. and Meyer, A. J. (2023a) 'Assembly, transfer, and fate of mitochondrial iron-sulfur clusters', *Journal of Experimental Botany*, 74(11), pp. 3328–3344. doi: 10.1093/jxb/erad062.

Pedroletti, L. *et al.* (2023b) 'Altered iron-sulfur cluster transfer in Arabidopsis mitochondria reveals lipoyl synthase as a Janus-faced enzyme that generates toxic sulfide', *The Plant Cell (Under review)*. doi: doi.org/10.1101/2023.08.30.55557.

Pettersen, E. F. *et al.* (2004) 'UCSF Chimera - A visualization system for exploratory research and analysis', *Journal of Computational Chemistry*, 25(13), pp. 1605–1612. doi: 10.1002/jcc.20084.

Picciocchi, A. *et al.* (2007) 'CGFS-type monothiol glutaredoxins from the cyanobacterium *Synechocystis PCC6803* and other evolutionary distant model organisms possess a glutathione-ligated [2Fe-2S] cluster', *Biochemistry*, 46(51), pp. 15018–15026. doi: 10.1021/bi7013272.

Przybyla-Toscano, J. *et al.* (2021) 'Iron–sulfur proteins in plant mitochondria: roles and maturation', *Journal of Experimental Botany*, 72(6), pp. 2014–2044. doi: 10.1093/jxb/eraa578.

Przybyla-Toscano, J. *et al.* (2022) 'Protein lipoylation in mitochondria requires Fe–S cluster assembly factors NFU4 and NFU5', *Plant Physiology*, 188(2), pp. 997–1013. doi: 10.1093/plphys/kiab501.

Rodríguez-Manzaneque, M. T. *et al.* (1999) 'Grx5 glutaredoxin plays a central role in protection against protein oxidative damage in *Saccharomyces cerevisiae*', *Molecular and Cellular Biology*, 19(12), pp. 8180–8190. doi: 10.1128/mcb.19.12.8180.

Rodríguez-Manzaneque, M. T. *et al.* (2002) 'Grx5 is a mitochondrial glutaredoxin required for the activity of iron/sulfur enzymes', *Molecular Biology of the Cell*, 13(4), pp. 1109–1121. doi: 10.1091/mbc.01-10-0517.

Rouhier, N. *et al.* (2007) 'Functional, structural, and spectroscopic characterization of a glutathione-ligated [2Fe-2S] cluster in poplar glutaredoxin C1', *Proceedings of the National Academy of Sciences of the United States of America*, 104(18), pp. 7379–7384. doi: 10.1073/pnas.0702268104.

Rouhier, N. *et al.* (2010) ‘Glutaredoxins: roles in iron homeostasis’, *Trends in Biochemical Sciences*, 35(1), pp. 43–52. doi: 10.1016/j.tibs.2009.08.005.

Rouhier, N., Couturier, J. and Jacquot, J. P. (2006) ‘Genome-wide analysis of plant glutaredoxin systems’, *Journal of Experimental Botany*, 57(8), pp. 1685–1696. doi: 10.1093/jxb/erl001.

Rouhier, N., Gelhaye, E. and Jacquot, J. (2004) ‘Plant glutaredoxins: still mysterious reducing systems’, *Cellular and Molecular Life Sciences*, 61, pp. 1266–1277. doi: 10.1007/s00018-004-3410-y.

Scalcon, V. *et al.* (2019) ‘Dimers of glutaredoxin 2 as mitochondrial redox sensors in selenite-induced oxidative stress’, *Metallomics*. Royal Society of Chemistry, 11(7), pp. 1241–1251. doi: 10.1039/c9mt00090a.

Schlößer, M. *et al.* (2023) ‘Localization of four class I glutaredoxins in the cytosol and the secretory pathway and characterization of their biochemical diversification’, *bioRxiv*, [Preprint], pp. 1–34. doi: doi.org/10.1101/2023.09.01.555924.

Schwarzländer, M. *et al.* (2008) ‘Confocal imaging of glutathione redox potential in living plant cells’, *Journal of Microscopy*, 231(2), pp. 299–316. doi: 10.1111/j.1365-2818.2008.02030.x.

Sheftel, A. D. *et al.* (2009) ‘Human Ind1, an iron-sulfur cluster assembly factor for respiratory complex I’, *Molecular and Cellular Biology*. American Society for Microbiology, 29(22), pp. 6059–6073. doi: 10.1128/MCB.00817-09.

Solmonson, A. and DeBerardinis, R. J. (2018) ‘Lipoic acid metabolism and mitochondrial redox regulation’, *Journal of Biological Chemistry*, 293(20), pp. 7522–7530. doi: 10.1074/jbc.TM117.000259.

Ströher, E. *et al.* (2016) ‘Glutaredoxin S15 is involved in Fe-S clustebr transfer in mitochondria influencing lipoic acid-dependent enzymes, plant growth, and arsenic tolerance in Arabidopsis’, *Plant Physiology*, 170(3), pp. 1284–1299. doi: 10.1104/pp.15.01308.

Tamarit, J. *et al.* (2003) ‘Biochemical characterization of yeast mitochondrial Grx5 monothiol glutaredoxin’, *Journal of Biological Chemistry*, 278(28), pp. 25745–25751. doi: 10.1074/jbc.M303477200.

Taylor, N. L. *et al.* (2004) ‘Lipoic acid-dependent oxidative catabolism of keto acids in mitochondria provides evidence for branched-chain amino acid catabolism in arabidopsis’, 134(February), pp. 838–848. doi: 10.1104/pp.103.035675.the.

The Arabidopsis Genome Initiative (2000) ‘Analysis of the genome sequence of Arabidopsis

thaliana', *Nature*, 408(December), pp. 796–815.

Trnka, D. *et al.* (2020) 'Molecular basis for the distinct functions of redox-active and FeS-transfering glutaredoxins', *Nature Communications*. Springer US, 11(1). doi: 10.1038/s41467-020-17323-0.

Ugalde, J. M. *et al.* (2021) 'Chloroplast-derived photo-oxidative stress causes changes in H_2O_2 and EGSH in other subcellular compartments', *Plant Physiology*, 186(1), pp. 125–141. doi: 10.1093/plphys/kiaa095.

Ugalde, J. M. *et al.* (2022) 'Live monitoring of ROS-induced cytosolic redox changes with roGFP2-based sensors in plants', in *Humana Press Inc.*, pp. 65–85. doi: 10.1007/978-1-0716-2469-2_5.

Uzarska, M. A. *et al.* (2013) 'The mitochondrial Hsp70 chaperone Ssq1 facilitates Fe/S cluster transfer from Isu1 to Grx5 by complex formation', *Molecular Biology of the Cell*, 24(12), pp. 1830–1841. doi: 10.1091/mbc.E12-09-0644.

Wächtershäuser, G. (1992) 'Groundworks for an evolutionary biochemistry: The iron-sulphur world', *Progress in Biophysics and Molecular Biology*, 58(2), pp. 85–201. doi: 10.1016/0079-6107(92)90022-X.

Warui, D. M. *et al.* (2022) '*In vitro* demonstration of human lipoyl synthase catalytic activity in the presence of NFU1', *ACS Bio & Med Chem Au*. American Chemical Society, 2(5), pp. 456–468. doi: 10.1021/acsbiomedchemau.2c00020.

Weiler, B. D. *et al.* (2020) 'Mitochondrial [4Fe-4S] protein assembly involves reductive [2Fe-2S] cluster fusion on ISCA1–ISCA2 by electron flow from ferredoxin FDX2', *Proceedings of the National Academy of Sciences of the United States of America*. Proceedings of the National Academy of Sciences, 117(34), pp. 20555–20565. doi: 10.1073/pnas.2003982117.

Wingert, R. A. *et al.* (2005) 'Deficiency of glutaredoxin 5 reveals Fe-S clusters are required for vertebrate haem synthesis', *Nature*, 436(7053), pp. 1035–1039. doi: 10.1038/nature03887.

Wydro, M. M. *et al.* (2013) 'The evolutionarily conserved iron-sulfur protein INDH1 Is required for complex i assembly and mitochondrial translation in Arabidopsis', *The Plant Cell*, 25(10), pp. 4014–4027. doi: 10.1105/tpc.113.117283.

Xing, S., Rosso, M. G. and Zachgo, S. (2005) 'ROXY1, a member of the plant glutaredoxin family, is required for petal development in *Arabidopsis thaliana*', *Development*, 132(7), pp. 1555–1565. doi: 10.1242/dev.01725.

Xing, S. and Zachgo, S. (2008) 'ROXY1 and ROXY2, two Arabidopsis glutaredoxin genes,

are required for anther development', *The Plant Journal*, 53(5), pp. 790–801. doi: 10.1111/j.1365-313X.2007.03375.x.

Xu, X. M. *et al.* (2009) 'Dual localized AtHscB involved in iron sulfur protein biogenesis in Arabidopsis', *PLoS ONE*, 4(10). doi: 10.1371/journal.pone.0007662.

Zaffagnini, M. *et al.* (2008) 'Biochemical characterization of glutaredoxins from *Chlamydomonas reinhardtii* reveals the unique properties of a chloroplastic CGFS-type glutaredoxin', *Journal of Biological Chemistry*, 283(14), pp. 8868–8876. doi: 10.1074/jbc.M709567200.

Zaffagnini, M. *et al.* (2019) 'Redox homeostasis in photosynthetic organisms: novel and established thiol-based molecular mechanisms', *Antioxidants and Redox Signaling*, 31(3), pp. 155–210. doi: 10.1089/ars.2018.7617.

Zannini, F. *et al.* (2019) 'The thioredoxin-mediated recycling of Arabidopsis thaliana GRXS16 relies on a conserved C-terminal cysteine', *Biochimica et Biophysica Acta - General Subjects*, 1863(2), pp. 426–436. doi: 10.1016/j.bbagen.2018.11.014.

Zimmermann, J. *et al.* (2020) 'One cysteine is enough: A monothiol Grx can functionally replace all cytosolic Trx and dithiol Grx', *Redox Biology*, 36(April), p. 101598. doi: 10.1016/j.redox.2020.101598.

Appendix 1

Appendix 1.1 | DNA and protein sequences of GRXS15 and variants

CDS of Arabidopsis GRXS15 (AT3G15660)

ATGGCGGCTTCTTTATCGAGCAGACTTATAAAAGGAATCGCTAATCTCAAAGCTGTTCGTTCTAGCAGATTGACG
TCTGCATCAGTCTACCAAAATGGGATGATGAGATTTTCCTCAACAGTGCCAAGTGATTCAGATACACATGATGAT
TTCAAGCCTACACAAAAAGTCCCTCCCGATTCTACGGACTCACTTAAAGATATCGTTGAGAATGATGTGAAGGAT
AATCCTGTTATGATCTACATGAAAGGTGTCCCTGAATCTCCTCAGTGTGGGTTTAGCTCACTAGCCGTCAGAGTT
TTGCAGCAATATAATGTTCCTATCAGTTCTAGAAACATTCTAGAAGACCAAGAGTTGAAAAACGCTGTGAAATCC
TTCAGCCACTGGCCTACGTTTCCACAGATCTTCATTAAGGGAGAGTTCATTGGCGGCTCAGACATCATCCTTAAC
ATGCACAAGGAAGGTGAATTGGAGCAGAAGCTTAAAGACGTCTCCGGAAACCAAGATTGA

Codes for the mitochondrial targeting peptide; AAA: lysine 83; TGT: cysteine 91

CDS of Arabidopsis GRXS15 in pETG10a

ATGaaacatcaccatcaccatcaccccatgacaagtttgtacaaaaaagcaggctttTCAACAGTGCCAAGTGAT
TCAGATACACATGATGATTTCAAGCCTACACAAAAAGTCCCTCCCGATTCTACGGACTCACTTAAAGATATCGTT
GAGAATGATGTGAAGGATAATCCTGTTATGATCTACATGAAAGGTGTCCCTGAATCTCCTCAGTGTGGGTTTAGC
TCACTAGCCGTCAGAGTTTTGCAGCAATATAATGTTCCTATCAGTTCTAGAAACATTCTAGAAGACCAAGAGTTG
AAAAACGCTGTGAAATCCTTCAGCCACTGGCCTACGTTTCCACAGATCTTCATTAAGGGAGAGTTCATTGGCGGC
TCAGACATCATCCTTAACATGCACAAGGAAGGTGAATTGGAGCAGAAGCTTAAAGACGTCTCCGGAAACCAAGAT
TGA

AAA: lysine 83; TGT: cysteine 91

Protein sequence of Arabidopsis GRXS15 in pETG10a

MKHHHHHHPMTSLYKKAGFSTVPSDSDTHDDFKPTQKVPPDSTDSLKDIVENDVKDNPVMIYMKGVPESPQCGFS
SLAVRVLQQYNVPISSRNILEDQELKNAVKSFSHWPTFPQIFIKGEFIGGSDIILNMHKEGELEQKLKDVSGNQD

K: lysine 83; CGFS: active site with cysteine 91

Number of amino acids: 150; **Molecular weight:** 16.96 kDa

CDS of Arabidopsis GRXS15 K83A in pETG10a

ATGaaacatcaccatcaccatcaccccatgacaagtttgtacaaaaaagcaggctttTCAACAGTGCCAAGTGAT
TCAGATACACATGATGATTTCAAGCCTACACAAAAAGTCCCTCCCGATTCTACGGACTCACTTAAAGATATCGTT
GAGAATGATGTGAAGGATAATCCTGTTATGATCTACATGGCTGGTGTCCCTGAATCTCCTCAGTGTGGGTTTAGC
TCACTAGCCGTCAGAGTTTTGCAGCAATATAATGTTCCTATCAGTTCTAGAAACATTCTAGAAGACCAAGAGTTG
AAAAACGCTGTGAAATCCTTCAGCCACTGGCCTACGTTTCCACAGATCTTCATTAAGGGAGAGTTCATTGGCGGC
TCAGACATCATCCTTAACATGCACAAGGAAGGTGAATTGGAGCAGAAGCTTAAAGACGTCTCCGGAAACCAAGAT
TGA

GCT: alanine 83; TGT: C91

Protein sequence of Arabidopsis GRXS15 K83A in pETG10a

MKHHHHHHPMTSLYKKAGFSTVPSDSDTHDDFKPTQKVPPDSTDSLKDIVENDVKDNPVMIYMAGVPESPQCGFS
SLAVRVLQQYNVPISSRNILEDQELKNAVKSFSHWPTFPQIFIKGEFIGGSDIILNMHKEGELEQKLKDVSGNQD

A: alanine 83

Number of amino acids: 150; **Molecular weight:** 16.90 kDa

CDS of Arabidopsis GRXS15 C91S in pETG10a

ATGaaacatcaccatcaccatcaccccatgacaagtttgtacaaaaaagcaggctttTCAACAGTGCCAAGTGAT
TCAGATACACATGATGATTTCAAGCCTACACAAAAAGTCCCTCCCGATTCTACGGACTCACTTAAAGATATCGTT
GAGAATGATGTGAAGGATAATCCTGTTATGATCTACATGAAAGGTGTCCCTGAATCTCCTCAGTCTGGGTTTAGC
TCACTAGCCGTCAGAGTTTTGCAGCAATATAATGTTCCTATCAGTTCTAGAAACATTCTAGAAGACCAAGAGTTG
AAAAACGCTGTGAAATCCTTCAGCCACTGGCCTACGTTTCCACAGATCTTCATTAAGGGAGAGTTCATTGGCGGC
TCAGACATCATCCTTAACATGCACAAGGAAGGTGAATTGGAGCAGAAGCTTAAAGACGTCTCCGGAAACCAAGAT
TGA

TCT: serine 91

Protein sequence of Arabidopsis GRXS15 C91S in pETG10a

MK*HHHHHH*PMTSLYKKAGFSTVPSDSDTHDDFKPTQKVPPDSTDSLKDIVENDVKDNPVMIYMKGVPESPQSGFS
SLAVRVLQQYNVPISSRNILEDQELKNAVKSFSHWPTFPQIFIKGEFIGGSDIILNMHKEGELEQKLKDVSGNQD

S: Serine 91

Number of amino acids: 150; **Molecular weight:** 16.94 kDa

CDS of Arabidopsis GRXS15-loop in pETG10a

ATGaaacatcaccatcaccatcaccccatgacaagtttgtacaaaaaagcaggctttTCAACAGTGCCAAGTGAT
TCAGATACACATGATGATTTCAAGCCTACACAAAAAGTCCCTCCCGATTCTACGGACTCACTTAAAGATATCGTT
GAGAATGATGTGAAGGATAATCCTGTTATGATCTACATGAAACCTCAGTGTGGGTTTAGCTCACTAGCCGTCAGA
GTTTTGCAGCAATATAATGTTCCTATCAGTTCTAGAAACATTCTAGAAGACCAAGAGTTGAAAAACGCTGTGAAA
TCCTTCAGCCACTGGCCTACGTTTCCACAGATCTTCATTAAGGGAGAGTTCATTGGCGGCTCAGACATCATCCTT
AACATGCACAAGGAAGGTGAATTGGAGCAGAAGCTTAAAGACGTCTCCGGAAACCAAGATTGA

Protein sequence of Arabidopsis GRXS15-loop in pETG10a (ΔG84V85P86E87S88)

MKHHHHHHPMTSLYKKAGFSTVPSDSDTHDDFKPTQKVPPDSTDSLKDIVENDVKDNPVMIYMKPQ**C**GFSSLAVR
VLQQYNVPISSRNILEDQELKNAVKSFSHWPTFPQIFIKGEFIGGSDIILNMHKEGELEQKLKDVSGNQD

Number of amino acids: 145; **Molecular weight:** 16.49 kDa

Appendix 1.2 | DNA and protein sequences of GRXC1 and roGFP2

CDS of Arabidopsis GRXC1 in pET16b

ATGggccatcatcatcatcatcatcatcatcacagcagcggccatatcgaaggtcgtcatATGGGTTCAATG
TTCAGTGGAAACCGAATGAGCAAGGAAGAGATGGAGGTGGTGGTGAACAAGGCTAAAGAGATCGTCTCTGCTTAT
CCCGTTGTTGTCTTCAGCAAGACATACTGTGGTTATTGCCAGAGGGTGAAGCAGTTACTGACGCAGCTAGGAGCA
ACTTTTAAAGTACTTGAGCTCGATGAAATGAGTGATGGAGGTGAGATCCAATCAGCTTTATCAGAGTGGACTGGA
CAGACCACAGTTCCAAACGTCTTCATCAAAGGAAACCACATCGGTGGATGCGATAGAGTGATGGAGACCAACAAG
CAAGGCAAGCTTGTGCCTCTACTTACTGAAGCTGGGGCTATTGCAGATAACTCTTCTCAACTTTGA

Protein sequence of Arabidopsis GRXC1 in pET16b

MGHHHHHHHHHHSSGHIEGRHMGSMFSGNRMSKEEMEVVVNKAKEIVSAYPVVVFSKTY**C**GY**C**QRVKQLSTQLGA
TFKVLELDEMSDGGEIQSALSEWTGQTTVPNVFIKGNHIGGCDRVMETNKQGKLVPLLTEAGAIADNSSQL

CGY**C**: class II GRXs active site

Number of amino acids: 146; **Molecular weight:** 16.11 kDa

CDS of roGFP2 in pET30b

ATGcaccatcatcatcattcttctggtctggtgccacgcggttctggtatgaaagaaaccgctgctgctaaa
ttcgaacgccagcacatggacagcccagatctgggtaccgacgacgacgacaaggccATGGTGAGCAAGGGCGAG
GAGCTGTTCACCGGGGTGGTGCCCATCCTGGTCGAGCTGGACGGCGACGTAAACGGCCACAAGTTCAGCGTGTCC
GGCGAGGGCGAGGGCGATGCCACCTACGGCAAGCTGACCCTGAAGTTCATCTCCACCACCGGCAAGCTGCCCGTG
CCCTGGCCCACCCTCGTGACCACCCTGACCTACGGCGTGCAGTGCTTCAGCCGCTACCCCGACCACATGAAGCAG
CACGACTTCTTCAAGTCCGCCATGCCCGAAGGCTACGTCCAGGAGCGCACCATCTTCTTCAAGGACGACGGCAAC
TACAAGACCCGCGCCGAGGTGAAGTTCGAGGGCGACACCCTGGTGAACCGCATCGAGCTGAAGGGCATCGACTTC
AAGGAGGACGGCAACATCCTGGGGCACAAGCTGGAGTACAACTACAACTGCCACAACGTCTATATCATGGCCGAC
AAGCAGAAGAACGGCATCAAGGTGAACTTCAAGATCCGCCACAACATCGAGGACGGCAGCGTGCAGCTCGCCGAC
CACTACCAGCAGAACACCCCCATCGGCGACGGCCCCGTGCTGCTGCCCGACAACCACTACCTGAGCACCTGCTCC
GCCCTGAGCAAAGACCCCAACGAGAAGCGCGATCACATGGTCCTGCTGGAGTTCGTGACCGCCGCCGGGATCACT
CTCGGCATGGACGAGCTGTACAAGTAA

ACCTACGGC: Chromophore TYG; TGC: cysteine 147; TGC: cysteine 204

Protein sequence of roGFP2 in pET30b

MHHHHHHSSGLVPRGSGMKETAAAKFERQHMDSPDLGTDDDDKAMVSKGEELFTGVVPILVELDGDVNGHKFSVS
GEGEGDATYGKLTLKFISTTGKLPVPWPTLVTTLTYGVQCFSRYPDHMKQHDFFKSAMPEGYVQERTIFFKDDGN
YKTRAEVKFEGDTLVNRIELKGIDFKEDGNILGHKLEYNYNCHNVYIMADKQKNGIKVNFKIRHNIEDGSVQLAD
HYQQNTPIGDGPVLLPDNHYLSTCSALSKDPNEKRDHMVLLEFVTAAGITLGMDELYK

TYG: chromofore; C: cysteines 147 and 204

Number of amino acids: 283; **Molecular weight:** 31.77 kDa

Appendix 1.3 | Protein sequences of all class I and class II glutaredoxins in Arabidopsis

Different colour indicates subcellular localization: cytosol, endoplasmic reticulum, plastid, mitochondrion.

GRXC1
MGSMFSGNRMSKEEMEVVVNKAKEIVSAYPVVVFSKTYCGYCQRVKQLLTQLGATFKVLELDEMSDGGEIQSALSEWTGQTTV
PNVFIKGNHIGGCDRVMETNKQGKLVPLLTEAGAIADNSSQL

GRXC2.1
MAMQKAKEIVNSESVVVFSKTYCPYCVRVKELLQQLGAKFKAVELDTESDGSQIQSGLAEWTGQRTVPNVFIGGNHIGGCDAT
SNLHKDGKLVPLLTEAGAIAGKTATTSA

GRXC2.2
MDSIMCVSSWKFYTMNDSWMYLDAFVYQWMILSYLIGNFSGICSKTYCPYCVRVKELLQQLGAKFKAVELDTESDGSQIQSGL
AEWTGQRTVPNVFIGGNHIGGCDATSNLHKDGKLVPLLTEAGAIAGKTATTSA

GRXC3
MVDQSPRRVVVAALLLFVVLCDLSNSAGAANSVSAFVQNAILSNKIVIFSKSYCPYCLRSKRIFSQLKEEPFVVELDQREDGD
QIQYELLEFVGRRTVPQVFVNGKHIGGSDDLGAALESGQLQKLLAAS

GRXC4
MTMFRSISMVMLLVALVTFISMVSSAASSPEADFVKKTISSHKIVIFSKSYCPYCKKAKSVFRELDQVPYVVELDEREDGWSI
QTALGEIVGRRTVPQVFINGKHLGGSDDTVDAYESGELAKLLGVSGNKEAEL

GRXC5
MAVTAFNTLKLVSSSLDPIPSVSCSSYSFSLIYVGSPYKRCLKQSCSVRAMTSSSSAASSSSSSFGSRMEESIRKTVTENTVV
IYSKTWCSYCTEVKTLFKRLGVQPLVVELDQLGPQGPQLQKVLERLTGQHTVPNVFVCGKHIGGCTDTVKLNRKGDLELMLAE
ANGKNGQS

GRXS12.1
MVAATVNLANMTWTSLNSNPAISFSMLSGIRNLGMLPFRRCLKPTVIGIASWPPLRCSSVKAMSSSSSSSGSTLEETVKTTVA
ENPVVVYSKTWCSYSSQVKSLFKSLQVEPLVVELDQLGSEGSQLQNVLEKITGQYTVPNVFIGGKHIGGCSDTLQLHNKGELE
AILAEANGKNGQT

GRXS12.2
MVAATVNLANMTWTSLNSNPAISFSMLSGIRNLGMLPFRRCLKPTVIGIASWPPLRCSSVKAMSSSSSSSGSTLEETVKTTVA
ENPVVVYSKTWCSYSSQVKSLFKSLQVEPLVVELDQLVSLGKTSLPHDIGLKHLQKFWWFLAFPGSEGSQLQNVLEKITGQYT
VPNVFIGGKHIGGCSDTLQLHNKGELEAILAEANGKNGQT

GRXS14
MALRSVKTPTLITSVAVVSSSVTNKPHSIRFSLKPTSALVVHNHQLSFYGSNLKLKPTKFRCSASALTPQLKDTLEKLVNSEK
VVLFMKGTRDFPMCGFSNTVVQILKNLNVPFEDVNILENEMLRQGLKEYSNWPTFPQLYIGGEFFGGCDITLEAFKTGELQEE
VEKAMCS

GRXS15
MAASLSSRLIKGIANLKAVRSSRLTSASVYQNGMMRFSSTVPSDSDTHDDFKPTQKVPPDSTDSLKDIVENDVKDNPVMIYMK
GVPESPQCGFSSLAVRVLQQYNVPISSRNILEDQELKNAVKSFSHWPTFPQIFIKGEFIGGSDIILNMHKEGELEQKLKDVSG
NQD

GRXS16
MAAITISSSLHASASPRVVRPHVSRNTPVITLYSRFTPSFSFPSLSFTLRDTAPSRRRSFFIASAVKSLTETELLPITEADSI
PSASGVYAVYDKSDELQFVGISRNIAASVSAHLKSVPELCGSVKVGIVEEPDKAVLTQAWKLWIEEHIKVTGKVPPGNKSGNN
TFVKQTPRKKSDIRLTPGRHVELTVPLEELIDRLVKESKVVAFIKGSRSAPQCGFSQRVVGILESQGVDYETVDVLDDEYNHG
LRETLKNYSNWPTFPQIFVKGELVGGCDILTSMYENGELANILN

GRXS17
MSGTVKDIVSKAELDNLRQSGAPVVLHFWASWCDASKQMDQVFSHLATDFPRAHFFRVEAEEHPEISEAYSVAAVPYFVFFKD
GKTVDTLEGADPSSLANKVGKVAGSSTSAEPAAPASLGLAAGPTILETVKENAKASLQDRAQPVSTADALKSRLEKLTNSHPV
MLFMKGIPEEPRCGFSRKVVDILKEVNVDFGSFDILSDNEVREGLKKFSNWPTFPQLYCNGELLGGADIAIAMHESGELKDAF
KDLGITTVGSKESQDEAGKGGGVSSGNTGLSETLRARLEGLVNSKPVMLFMKGRPEEPKCGFSGKVVEILNQEKIEFGSFDIL
LDDEVRQGLKVYSNWSSYPQLYVKGELMGGSDIVLEMQKSGELKKVLTEKGITGEQSLEDRLKALINSSEVMLFMKGSPDEPK
CGFSSKVVKALRGENVSFGSFDILTDEEVRQGIKNFSNWPTFPQLYYKGELIGGCDIIMELSESGDLKATLSE

Appendix 2

Appendix 2.1

The molybdenum cofactor (Moco) is not only associated with nitrogen metabolism (see Chapter 4 and the attached manuscript) but it is also essential for AAO3 (abscisic acid aldehyde oxidase), the enzyme that catalyses the last step in the biosynthesis of the abscisic acid (ABA). ABA is a crucial hormone to regulate stomata closure, preventing water loss and thus plays a key role in drought stress (Batool *et al.*, 2018). Since Moco biosynthesis is dependent on the Fe–S cluster enzyme CNX2 (cofactor of nitrate reductase and xanthine dehydrogenase 2, see Chapter 2 and Chapter 4) in the mitochondrion, we hypothesized that restricted Fe–S cluster supply in *grxs15* mutants may reduce Moco, and eventually ABA, synthesis. Such a deficiency would potentially affect stomatal closure and thus water retainment of the plant, with potential consequences on drought tolerance (Appendix 2 Fig. 1).

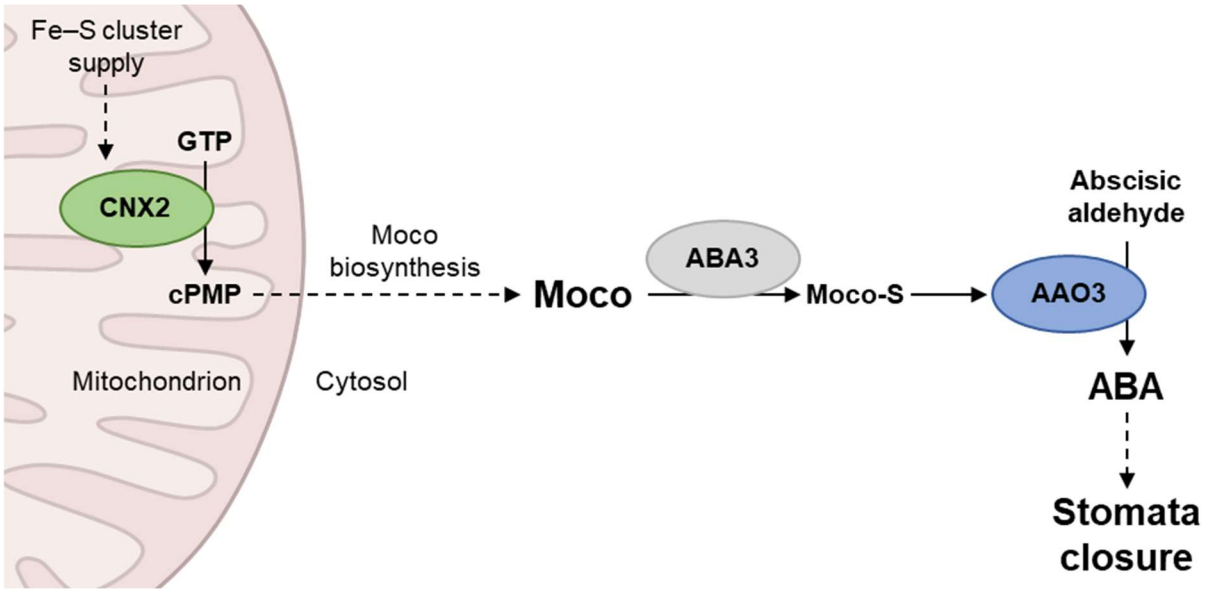

Appendix 2 Fig. 1. Working model for the function of Moco in ABA biosynthesis and stomatal closure. [4Fe–4S] cluster is delivered to CNX2 (cofactor of nitrate reductase and xanthine dehydrogenase 2) which catalyses the conversion of GTP (guanosine triphosphate) to cPMP (cyclic pyranopterin monophosphate). Mitochondrial cPMP is exported to the cytosol and processed to Moco (molybdenum cofactor) in several steps (not shown). Moco is then sulfurated by ABA3 (molybdenum cofactor sulfurase) and inserted into AAO3 (ABA aldehyde oxidase) which can catalyse the conversion of abscisic aldehyde to abscisic acid (ABA). ABA can finally induce stomatal closure.

Since most *grxs15* mutants (*amiR*, *grxs15 K83A #3* or *#4*) have comparatively small rosettes, and thus transpire less, we compared drought stress symptoms of wild-type plants with the *grxs15-1* mutant, that has reduced levels of GRXS15 but no growth phenotype (see Supplemental Figure S1 in Chapter 4 and Chapter 5). The g*rxs15-1* mutant appeared to be more sensitive to drought after 2 weeks with no water (Appendix 2 Fig. 2a). However, after three days of re-watering, the mutant recovered similarly to wild type (Appendix 2 Fig. 2b). This

evidence suggested that impairment in GRXS15 may affect the water loss during drought. Nevertheless, further investigations and quantitative data are required to establish a direct connection between GRXS15, Moco biosynthesis, and ABA activity.

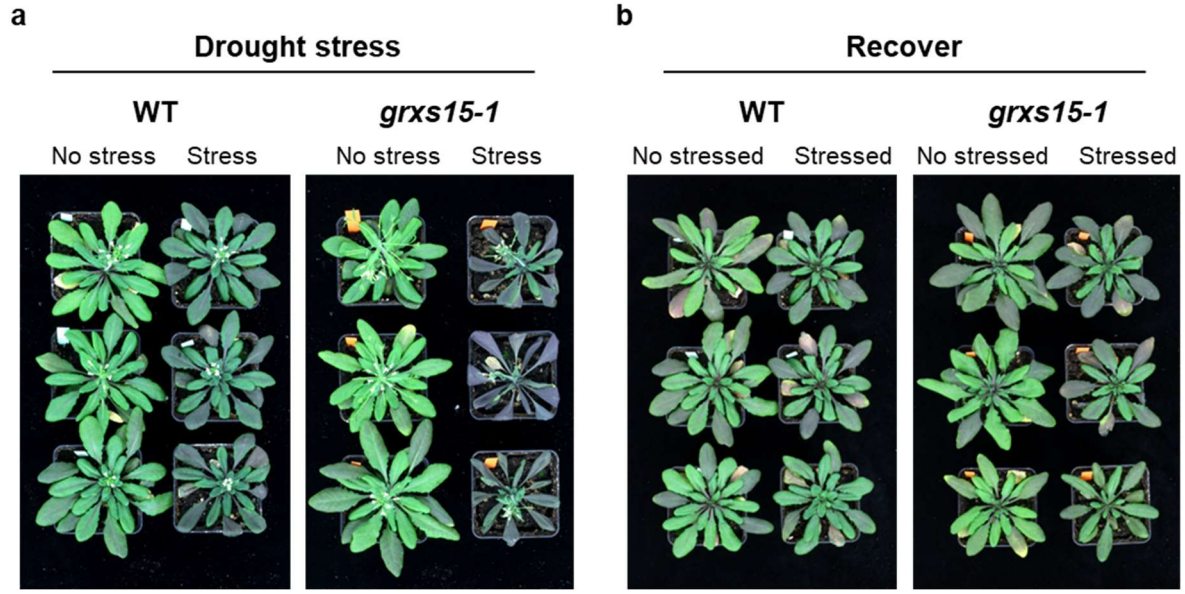

Appendix 2 Fig. 2 | The *grxs15-1* mutant is particularly sensitive to drought stress. a Representative photo of 6-week-old wild type and *grxs15-1* plants either normally watered or subjected to drought for 2 weeks. **b** The same plants in (**a**) 3 days after re-watering the stressed plants.

Appendix 2.2

As shown in Chapter 4 (Moseler *et al.*, 2021), *grxs15* mutants *amiR*, *K83A #3 and #4* develop a dwarf phenotype on standard soil containing no peat. We reported the observation that the phenotype of the *grsx15* mutants can sensibly change when the plants are grown on a different substrate. When grown on peat pellets (Jiffy-7), the dwarfism was largely lifted (Appendix 2 Fig. 3a-c). After 7 weeks under long-day conditions, the rosette fresh weight of amiR and grxs15-1 plants exhibited an increase when grown on peat pellets compared to standard soil, although there was no significant difference observed when compared to the wild type. However, the phenotype changes of *K83A #3* and *#4* between the two substrates were remarkable, with a massive increment of rosette fresh weight of 30-fold and 100-fold, respectively (Appendix 2 Fig. 3d).

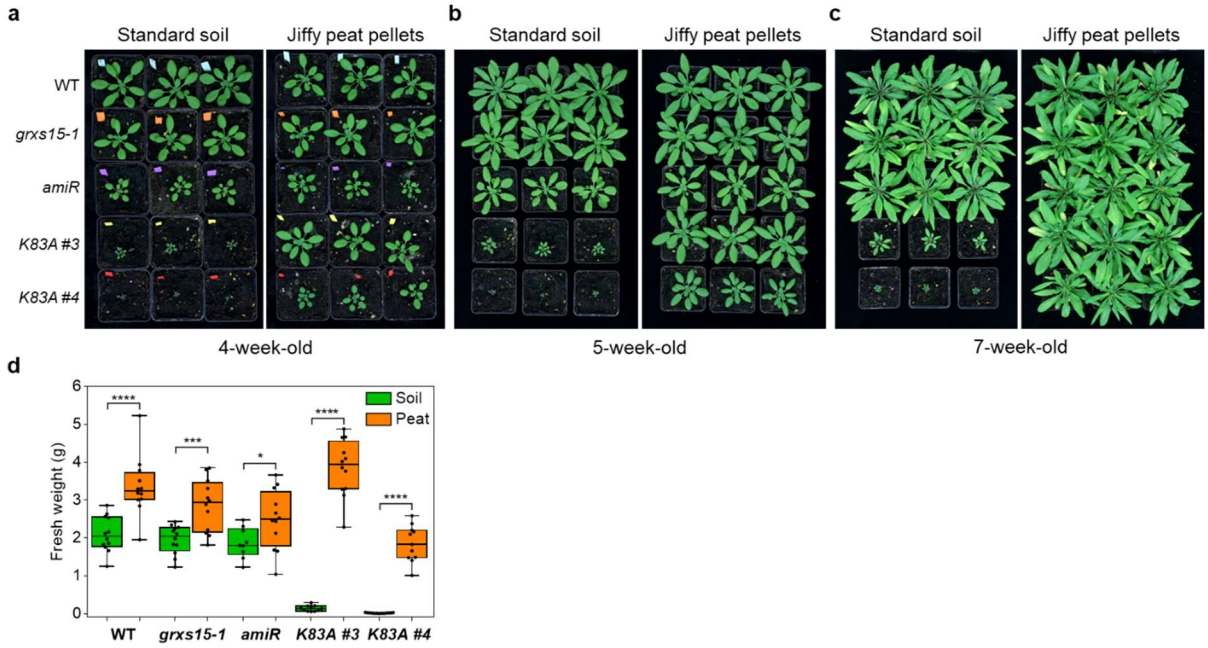

Appendix 2 Fig. 3 | *grxs15* mutants grow better on peat than on soil. Representative photo of 4-week-old (**a**), 5-week-old (**b**) and 7-week-old (**c**) wild-type plants compared with *grxs15* mutants growing on standard soil mixture (Floradur B-seed, Perlite Perligran 0-6 and quartz sand in a ratio of 10:1:1, respectively) and peat pellet (Jiffy-7; Jiffy Products International AS, DK). **d** Shoot fresh weight of 7-week-old plants (n = 9-14). Box plots show the median as centre line with the box for the first to the third quartile and whiskers indicating min and max values of the whole dataset. Asterisks represent significant differences (*=$P \leq 0.1$, ***= $P \leq 0.001$, ****= $P \leq 0.0001$) calculated according to Student's t-test ($\alpha = 0.05$).